University of Ferrara

PhD course in
"PHYSICS"

CYCLE XXX

COORDINATOR Prof. Vincenzo Guidi

Innovative chemoresistive materials for gas sensing and development of silicon and quartz MEMS devices

Disciplinary Scientific Sector FIS/01

PhD student
Andrea Gaiardo

Supervisor
Prof. Vincenzo Guidi

Second supervisor
Dr. Pierluigi Bellutti

Years 2014/2017

Index

Declarations

The work described in this thesis is entirely original and my own, except where otherwise indicated. Parts of this work have been published in the scientific literature:

[A.1] Gaiardo, A., Fabbri, B., Giberti, A., Guidi, V., Bellutti, P., Malagù, C., Valt, M., Pepponi, G., Gherardi, S., Zonta, G., Martucci, A., Sturaro, M., Landini, N. ZnO and Au/ZnO thin films: Room-temperature chemoresistive properties for gas sensing applications (2016) Sensors and Actuators, B: Chemical, 237, pp. 1085-1094.

[A.2] Gaiardo, A., Fabbri, B., Guidi, V., Bellutti, P., Giberti, A., Gherardi, S., Vanzetti, L., Malagù, C., Zonta, G. Metal sulfides as sensing materials for chemoresistive gas sensors (2016) Sensors (Switzerland), 16 (3).

[A.3] Giberti, A., Gaiardo, A., Fabbri, B., Gherardi, S., Guidi, V., Malagù, C., Bellutti, P., Zonta, G., Casotti, D., Cruciani, G. Tin(IV) sulfide nanorods as a new gas sensing material (2016) Sensors and Actuators, B: Chemical, 223, pp. 827-833.

[A.4] Giberti, A., Casotti, D., Cruciani, G., Fabbri, B., Gaiardo, A., Guidi, V., Malagù, C., Zonta, G., Gherardi, S. Electrical conductivity of CdS films for gas sensing: Selectivity properties to alcoholic chains (2015) Sensors and Actuators, B: Chemical, pp. 504-510.

[A.5] Giberti, A., Fabbri, B., Gaiardo, A., Guidi, V., Malagù, C. Resonant photoactivation of cadmium sulfide and its effect on the surface chemical activity (2014) Applied Physics Letters, 104 (22), art. no. 222102.

Introduction

In 1938, Wagner and Hauffe discovered that atoms and molecules adsorbed onto the surface of a semiconductor influences its electrical properties [1]. Brattain and Bardeen have extended this knowledge with their study about germanium properties when exposed to electrolytes and gaseous molecules [2]. Afterwards, studies provided by Heiland [3], Bielanski et al. [4] and Seiyama et al. [5] about reaction effects between metal oxides and gaseous analytes, laid the basis to a possible development of a commercial device. Thus, the decisive step was taken when Taguchi introduced chemoresistive sensors based on metal-oxide semiconductors in an industrial product (Sajama-Taguchi sensors [6]). From then on, research about the chemoresistive sensors and, more generally, on the solid-state gas sensors has been increasing ever since. This interest rise has been pushed by an increased awareness about substances that are hazardous to health and that resulting in pollution [7]. Indeed, in the last years, air pollution is worrying because many inhaled substances are known to have adverse effects on our long-term health (for several years). The known effects of air pollution have further highlighted hazards in industrial environments (e.g. mining, chemical and manufacturing industries) and in urban (domestic) environments [8], which has led to extensive research to determine the acceptable safe levels of known airborne hazardous substances [9]. Legislation has implemented requiring that industrial activities and products cannot result in an unprotected person being exposed to harmful gas levels, introducing gas exposure parameters, such as Threshold Limit Value (TLV) and Short-Term Exposure Limit (STEL) as law references for human safety [10]. Hence, there has been a sudden growth in the number of applications requiring accurate detection of a wide variety of gases and vapours. In many cases, suitable methods to control or monitor these atmospheres were limited by sensor technology or analysis methods high costs. For this reason, companies and researchers paid high attention about chemoresistive gas sensors and their peculiar advantages, such as very low detection limit (in the range of ppb-ppm of gas concentrations), low manufacturing cost, small size and simple implementation on portable device [11]. These advantages allowed chemoresistive gas sensors to get a market share, despite existing of higher performance sensors such as optical sensors, which, anyway, are very expensive, bulky and technologically complex. Nowadays, there are many companies offering this type of sensors, such as Figaro, FIS, MICS, UST, CityTech, AppliedSensors, NewCosmos, etc. [12].

Over the years, the chemoresistive gas-sensor technology has focused mainly on the development of devices provided with a metal-oxide-semiconductor as receptor/sensing material and alumina substrates as transducer/mechanical support. Indeed, the coupling of them allows developing sensors with excellent properties, i.e. excellent sensitivity, fast response and recovery times, robustness, easy and relatively low-cost production [13, 14].

The research about chemoresistive gas sensors has allowed broadening knowledge of the capabilities of these devices, thus leading to an increase of their properties control and a refinement of the production process. Moreover, the ever-greater awareness of the sensing worth of these devices has allowed the development of increasingly technologically advanced systems, such as the electronic nose, which let extended application fields of the chemoresistive gas sensors from the environmental monitoring, to safety and security, quality control of food production and medical diagnosis [15-17]. However, despite such great advantages, the in-depth study of these devices has highlighted some important unsolved drawbacks that still limit their use in many application fields. Among these disadvantages, the incomplete selectivity and lack of stability sometimes result in unreliable responses [18, 19]. Moreover, these devices often need a significant amount of energy to support chemical reactions at the MOX surface, activated at high temperatures [20]. These limits represent a problem, but they are also the boost for researchers to expand knowledge on chemoresistive gas

sensors and to explore new frontiers about technological development of this device, introducing studies about new kind of substrates and sensing materials.

The aim of this thesis is to contribute to the innovation of both fundamental parts of chemoresistive gas sensors, i.e. the sensing material and the substrate. Different approaches are exploited to face the challenge, including studies of not conventional semiconductors as sensing materials and optimization of Micro-Electro-Mechanical Systems (MEMS) quartz and silicon devices as transducers.

An introduction on the generalities of semiconducting inorganic material, including the main charge transport methods known so far and a description of their operation principles, as well as the principal factors influencing their performance, is given in **Chapter 1**. Moreover, limits of MOX semiconductors as chemoresistive gas sensing materials are explained.

In **Chapter 2** interesting features about innovative chemoresistive materials studied are described to motivate our choice. Then, synthesis and chemical, structural and morphological characterizations of semiconductors prepared are reported. Afterwards, electrical characterization both in thermo- and photo-activation modes of sensing materials used are showed and discussed.

Theory and state of the art of MEMS microheaters are presented in **Chapter 3**. Main problems with the common substrate for chemoresistive gas sensors are highlighted to introduce the goal of MEMS quartz and silicon devices that we developed in the Bruno Kessler Foundation of Trento. In the sector part of chapter 3 is illustrates the design, the microfabrication process and characterizations carried out on silicon and quartz devices produced. Particular care was dedicated to the development of a suitable insulating material, deposited by means of PECVD technique, with the important role of electrical insulator between the heater and the open circuit of the sensing material.

The main conclusions of every single study presented, as well as the outlooks for future projects, are summarized in the last chapter, **Conclusions and Outlook.**

Bibliography

[1] C. Wagner, K. Hauffe, The stationary state of catalysts in homogeneous reactions, Ztschr. Elektrochem. 33 (1938) 172

[2] W.H. Brattain and J. Bardeen, Surface properties of germanium, Bell Syst. Tech. J., 32 (1953) 1

[3] G. Heiland, Zum Einfluss von Wasserstoff auf die elektrische Leitfahigkeit von ZnO-Kristallen, Zeit. Phys. 138 (1954) 459–464

[4] A. Bielanski, J. Deren, J. Haber, Electric conductivity and catalytic activity of semiconducting oxide catalysts, Nature 179 (1957) 668–669

[5] T. Seiyama, A. Kato, K. Fujiishi, M. Nagatani, A new detector for gaseous components using semiconductive thin films, Anal. Chem. 34 (1962) 1502

[6] N. Taguchi, U.S. Patent 3,631,436 (1971)

[7] N. de Nevers, Air Pollution Control Engineering, McGraw-Hill, New York, 1995

[8] R.M. Harrison, A Fresh Look at Air, Chemistry in Britain, December 1994, 987-1000

[9] Health and Safety Executive, EH40/96 Occupational Exposure Limits 1996, HMSO, London, 1996

[10] ACGIH Site. Available online: http://www.acgih.org/ (accessed October 2017).

[11] Neri, G. First Fifty Years of Chemoresistive Gas Sensors. Chemosensors 2015, 3, 1-20

[12] N. Barsan, D. Koziej, U. Weimar, Metal oxide-based gas sensor research: How to? Sensors and Actuators B: Chemical, Volume 121, Issue 1, 2007, Pages 18-35

[13] Yamazoe, N. Toward innovation of gas sensor technology. Sens. Actuators B 2005, 108, 2–14.

[14] Bochenkov, V.E.; Sergeev, G.B. Sensitivity, Selectivity, and Stability of Gas-Sensitive Metal-Oxide Nanostructures. In Metal Oxide Nanostructures and Their Applications; American Scientific Publishers: Valencia, CA, USA, 2010; pp. 31–52

[15] G. Zonta, G. Anania, B. Fabbri, A. Gaiardo, S. Gherardi, A. Giberti, V. Guidi, N. Landini, C. Malagù, Detection of colorectal cancer biomarkers in the presence of interfering gases, Sensors and Actuators B: Chemical, Volume 218, 2015, Pages 289-295

[16] Moon, H.G., Jung, Y., Han, S.D., Shim, Y.-S., Shin, B., Lee, T., Kim, J.-S., Lee, S., Jun, S.C., Park, H.-H., Kim, C., Kang, C.-Y. Chemiresistive Electronic Nose toward Detection of Biomarkers in Exhaled Breath (2016) ACS Applied Materials and Interfaces, 8 (32), pp. 20969-20976

[17] Núñez Carmona, E., Sberveglieri, V., Ponzoni, A., Galstyan, V., Zappa, D., Pulvirenti, A., Comini, E. Detection of food and skin pathogen microbiota by means of an electronic nose based on metal oxide chemiresistors (2017) Sensors and Actuators, B: Chemical, 238, pp. 1224-1230.

[18] F. Hossein-Babaei, V. Ghafarinia, Compensation for the drift-like terms caused by environmental fluctuations in the responses of chemoresistive gas sensors, In Sensors and Actuators B: Chemical, Volume 143, Issue 2, 2010, Pages 641-648

[19] G. Korotcenkov, B.K. Cho, Instability of metal oxide-based conductometric gas sensors and approaches to stability improvement (short survey), In Sensors and Actuators B: Chemical, Volume 156, Issue 2, 2011, Pages 527-538

[20] Isolde Simon, Nicolae Bârsan, Michael Bauer, Udo Weimar, Micromachined metal oxide gas sensors: opportunities to improve sensor performance, In Sensors and Actuators B: Chemical, Volume 73, Issue 1, 2001, Pages 1-26.

1 Overview of nanostructured semiconductors

1.1 Electronic properties of a semiconductor

1.1.1 Semiconductor general properties

A semiconductor is a material characterized by the following properties:

- resistivity in the range of 10^{-2} and 10^{9} Ω * cm;
- dependence on electrical conductivity from temperature;
- Band-gap in the order of the eV.

Its specific properties are generally due to impurities such as stoichiometric reticulate defects or thermal excitation. To explain the electrical behaviour of these materials, it is necessary to introduce the electronic band pattern, and by solving the Schrödinger equation for a crystalline solid, it turns out that the electrons have only possible energies within certain energy bands.
These energy levels are quantized, but due to their proximity and number, they are considered as a continuous band and are referred to as "density of states", that is the number of energy levels per unit of energy. A not-permitted range of energy for electrons (i.e. the bandgap) separates electronic bands, which contribute essentially to the determination of the properties of a material.
Semiconductors behave as insulators at 0 K, while at rising temperatures they exhibit conduction effects as some electrons can have enough energy to pass from the valence band to the conduction band.
The operating principle behind chemoresistive solid-state sensors is based on two different phenomena: the change in the surface conductance and the variation of the bulk conductance. The bulk is the internal volume of the sensitive material, which constitutes the sensor. Now we are going to make a panoramic on the most relevant properties of semiconductors that have been applied for the realization of sensors.

1.1.2 Band structure: bulk and Fermi distribution

As reported by Madou and Morrison [1.1], electrons can assume only energy values within certain intervals inside a crystal, corresponding to the energy bands of the crystal itself. These energy bands are separated by band gaps, forbidden areas where electrons cannot exist.
Two energy bands allowed, in particular, characterize semiconductors:

• the valence band (**VB**), which according to the band structure, is the lowest in energy between the bands occupied by electrons;

• the conducting band (**CB**), the higher band between those that can be occupied by electrons.

The **CB** is separated from **VB** by a gap energy in the order of the thermal energy ($E_g \sim k_b T$).
In a perfect crystal at absolute zero temperature, the conduction band is completely empty. Obviously real crystals present in nature have some imperfections and the absolute zero cannot be reached. Therefore, in the conduction band, we can still find some electrons, the same that are absent in the valence band. In conditions of thermal equilibrium, electrons inside energy levels follow the Fermi distribution (Eq. 1.1):

$$f = \frac{1}{1 + e^{\frac{E - E_F}{k_b T}}} \qquad Eq.\,1.1$$

where k_b is the Boltzmann constant, T the absolute temperature and E_F the Fermi level (it is a different concept than the Fermi energy because the second one is defined as the energy that well separates empty levels from filled levels, a useful concept for metals and degenerate semiconductors). That determines the level of occupation probability of $\frac{1}{2}$, so the probability to find a level empty or not, is the same at this energy. This distribution does not derive from the band structure of the crystal and, depending on the energy value, we can make the following considerations:

- if $E << E_F$, the distribution $f \to 1$;
- the probability to find an empty level becomes appreciable only if $E \simeq E_F$;
- if $E - E_F \ll k_b T$ the function assumes the form of the Maxwell-Boltzmann distribution.

If E_F is inside the forbidden band, the Maxwell-Boltzmann approximation can be used to indicate the electron density in the **CB** or, analogously, the density of holes in the **VB**.

1.1.3 Intrinsic and extrinsic semiconductors

Semiconductors can be of two types, depending on the position of the E_F with respect to the forbidden band of the crystal. If E_F is located very close to the centre of the gap, we have the same number of carriers in the **VB** and in the **CB**; in this case, we can talk about intrinsic semiconductor. On the other hand, if we add some impurities or if the crystal has structural imperfections, the E_F can be shifted from the middle of the gap, and the semiconductor is now called extrinsic and the number of holes and electrons is different. Sometimes the crystal can be so much doped that the Fermi energy can enter in the conduction or in the valence band. In this case, the semiconductor is degenerate and the Fermi level has almost the same meaning of the Fermi energy for metals because it well separates the empty zones from the filled ones and the semiconductor behaves like a metal.

Considering the extrinsic, non-degenerate case, we should have:

- p-type semiconductors if the number of holes in the valence band is bigger than the number of electrons in the conduction band and the Fermi level is moved below the middle of the gap;
- n-type semiconductors if the number of holes in the valence band is less than the number of electrons in the conduction band and the Fermi level is shifted above the middle of the gap.

The creation of extrinsic semiconductors can take place via the doping technique, a method which consists in the introduction of foreign atoms which replace those proper of the material. If they provide electrons to the material they are called donors. An example of the donor is P, which has a valence electron more than Si. It creates a defect in the periodical structure of the silicon crystal, placing an electron next to the conduction band. It is sufficient a little thermal excitation (and so a small energy) to send the electron towards the **CB** ionizing the donor, which assumes a positive charge; on the other hand, if the foreign atoms introduced via the doping provide holes to the material they are called acceptors. An example of the acceptor is B which has only three valence electrons. In a silicon crystal, it creates a defect slightly above the **VB** and with a little thermal excitation, an electron can jump from the valence band to the acceptor, conferring it a negative charge. In a typical lattice, the number density of atoms is of the order of 1023 cm^{-3}, while the density in the volume of

donors (or acceptors) is N_d~$10^{16\div18}$cm^{-3}. If we want to know the density of electrons in the conduction band and the density of holes in the valence band, it is necessary to use, as stated above, the Maxwell-Boltzmann distribution. Indeed:

- Assuming E_C-E_F > 2 k_bT, we find that $n=N_C e^{\frac{E_C-E_F}{k_bT}}$, where E_C is the energy of the edge of the conduction band and N_C is the effective density of states in a neighbourhood of the **CB** bottom;
- Assuming E_F-E_V > 2 k_bT, we find that $p = N_V e^{\frac{E_F-E_V}{k_bT}}$, where E_V is the energy of the edge of the valence band and N_V is the effective density of states in a neighbourhood of the **VB** top.

1.1.4 Surface states

At the external surface of a real crystal, there is a sudden interruption of the regular reticular structure. This gives birth to mechanisms of rearrangement in the crystal structure that produces an increased reactivity of superficial atoms or ions with respect to those of the bulk. There is essentially a perturbation which acts on the periodicity of the lattice on the surface; this perturbation is strong enough to create new localized electronic energy states, namely intrinsic. Most of the metal-inorganic semiconductors are ionic compounds. Superficial ions are not coupled to the corresponding ion of opposite charge: metallic cations attract electrons acting as acceptors, while oxygen anions give up electrons acting as donors. The unpaired electron represents an orbital, partially extended outside the surface of the semiconductor (see dandling bonds, paragraph 1.2.4).

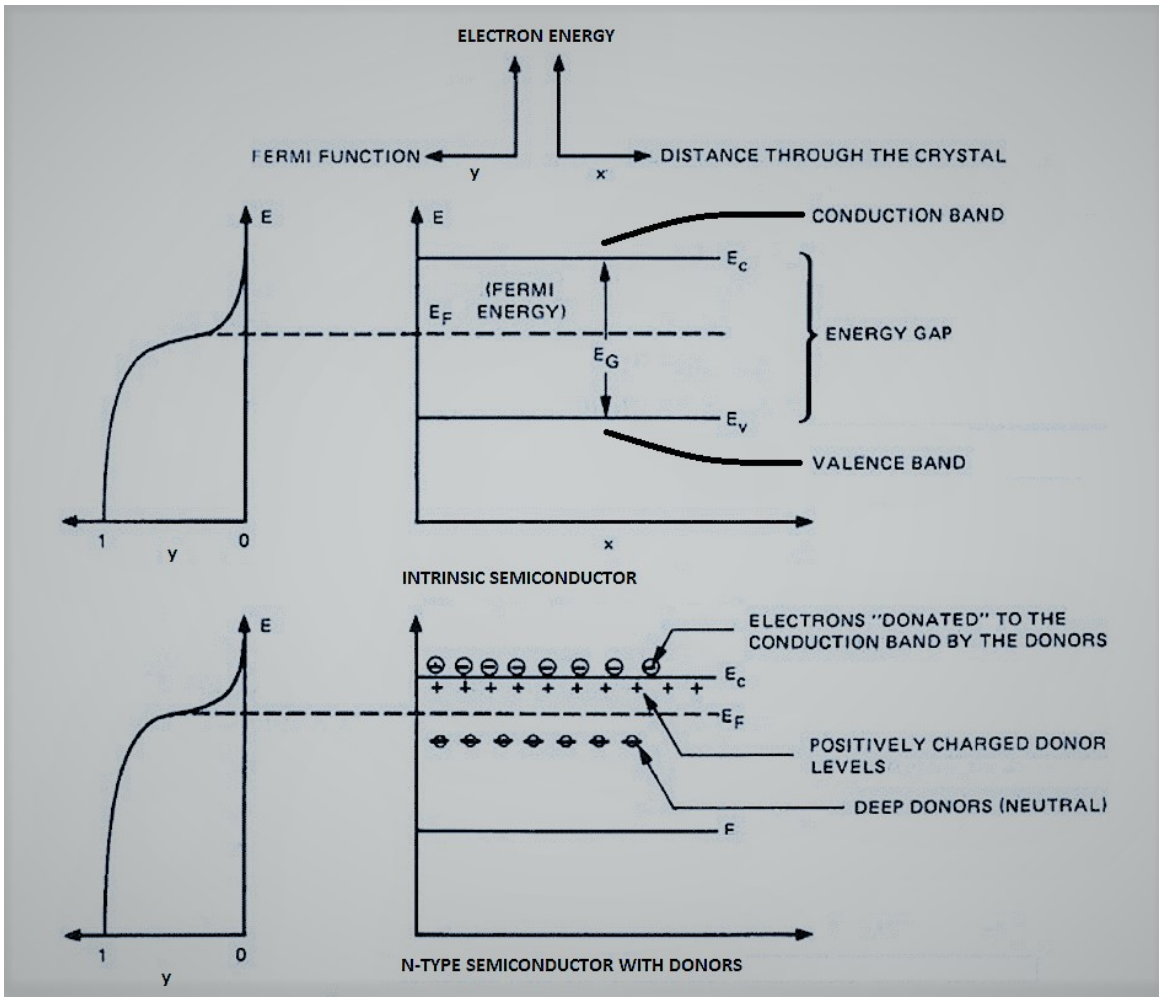

Figure 1.1: Fermi function and band diagram for an intrinsic *a*) and an extrinsic *b*) semiconductor [adapted from 1.1].

In a similar situation, the unpaired electron can capture another electron to form a pair, or it can enter the *bulk* of the crystal freeing a surface state. At this point, it is easy to understand why at the surface there are both acceptors that donors, as we can see in the band model of surface states in Figure 1.2 (for simplicity here is illustrated the case of "flat band").

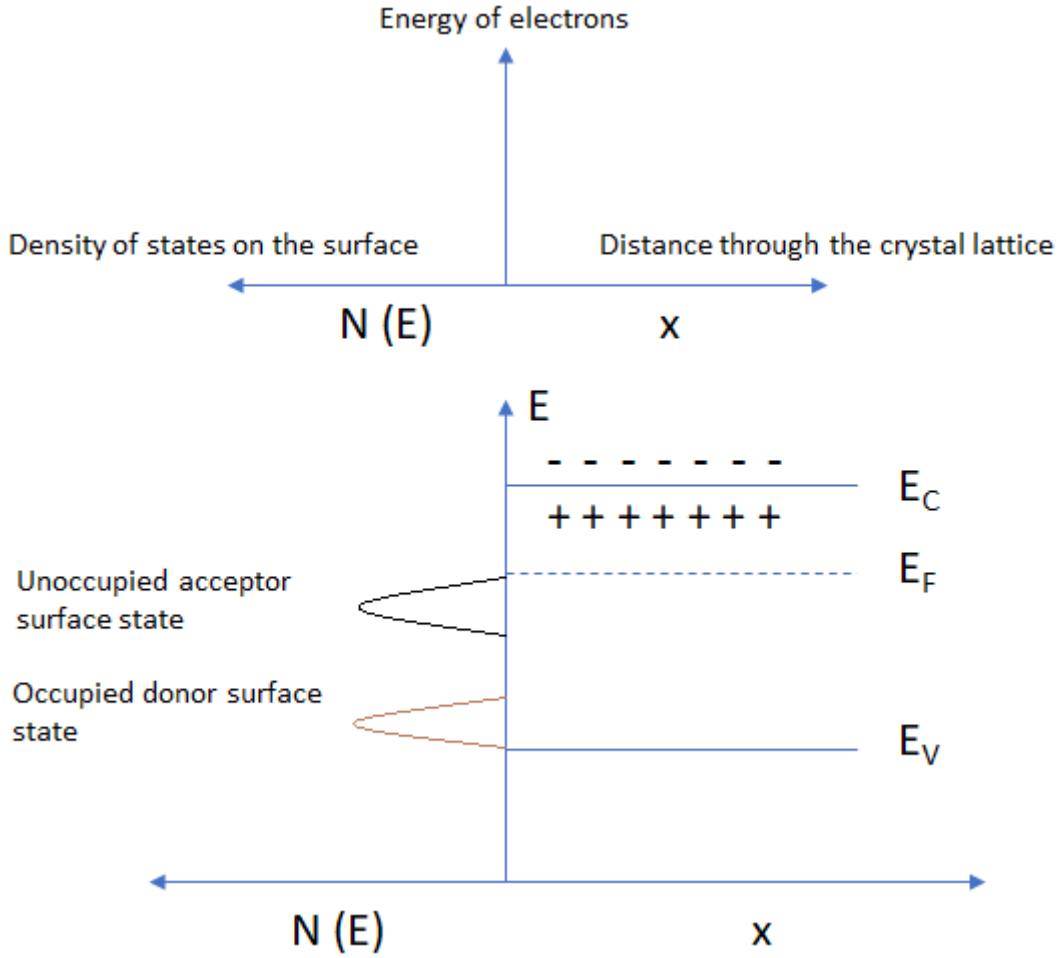

Figure 1.2: Neutral surface states in an n-type semiconductor: donors are occupied while acceptors are not. In the schematic representation, energy bands are represented for simplicity as a single level [adapted from 1.1].

1.1.5 Double layer

We can easily guess that the "flat band" configuration is far from equilibrium. Electrons in the **CB** are characterized by a higher energy level than that of superficial acceptors (Figure 1.2). When acceptor states are totally empty, while donors totally filled, the E_F should necessarily be in an intermediate position. Therefore, the electrochemical potential of electrons inside surface states is smaller than the electrochemical potential which characterizes the **CB**, and electrons here tend to migrate towards surfaces states, to minimize the energy of the system. This phenomenon leads to the formation of an accumulation layer of surface charge, balanced by the charge of donor ions located inside the bulk.

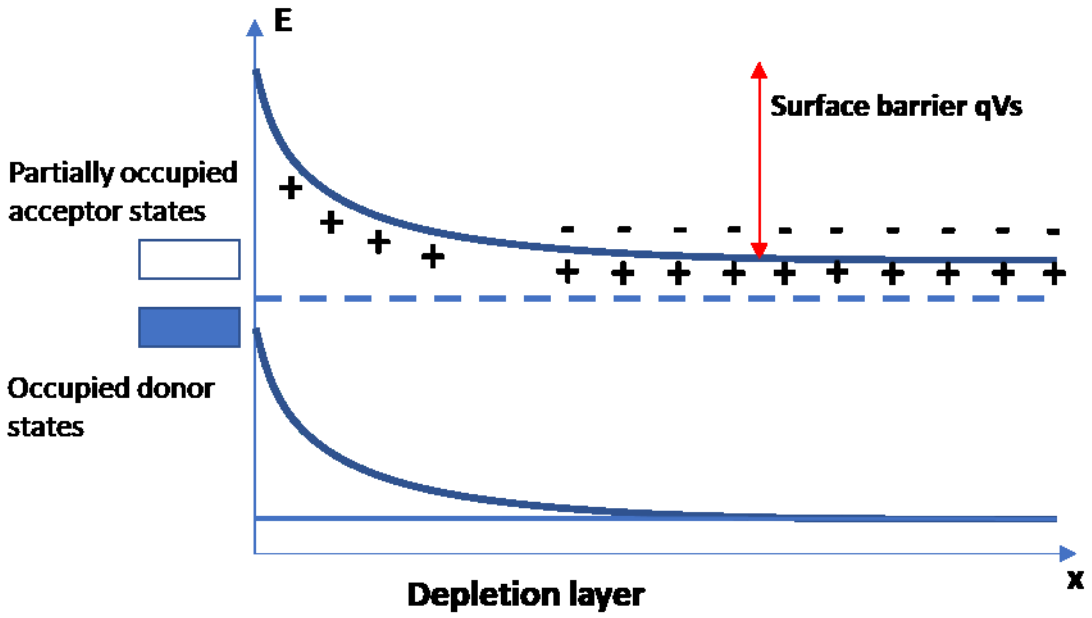

Figure 1.3: Double layer. Electrons in the conduction band are captured from surface states, creating a negative surface that contrasts the presence of positively charged donors just below it [adapted from 1.1].

Figure 1.3 represents schematically the charge migration of donor ions towards an n-type semiconductor. There is the formation of the so-called "double layer", consisting of positively charged donor ions which acts as a spatial charge, located at one side and, on the other side, of negatively charged states displaced on a plane. So, the relative electric field arises in the external region. Now it can be introduced the concept of the depletion layer, a region in which the only uncompensated charges present are donors, with a density $N_i = N_d - N_a$ (where N_d and N_a are respectively the density of donors and acceptors). All mobile carriers inside the depletion layer are inevitably led to migrate towards the surface.

Figure 1.4 represents intuitively the effects of absorption of oxidizing chemical species on the surface of the semiconducting grain: the contribution to the formation of a superficial charged layer is responsible for the creation of an intergranular potential barrier which electrons must surpass to cross multiple grains.

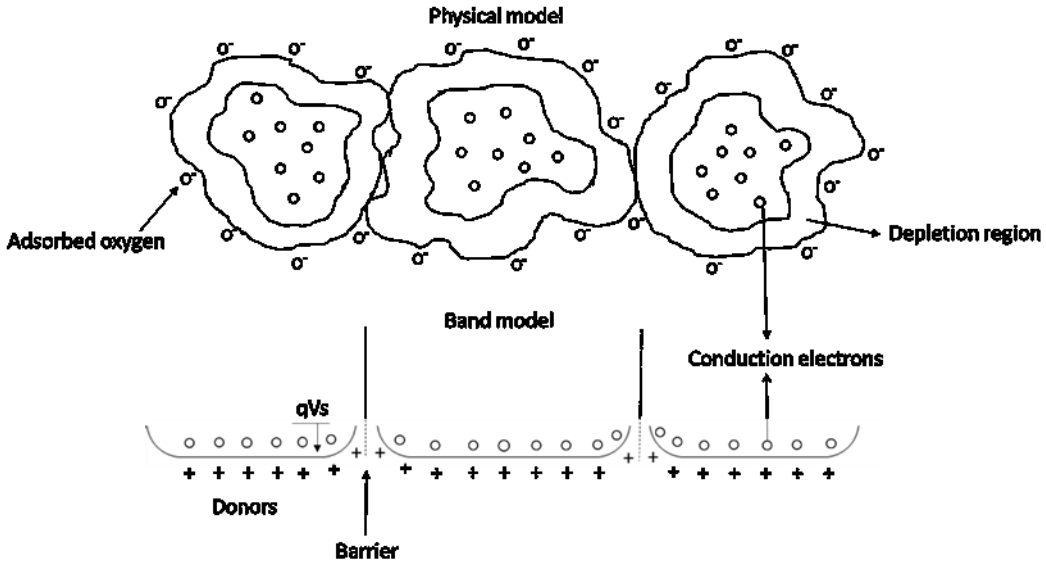

Figure 1.4: the potential barrier between grains [adapted from 1.1].

1.1.6 Poisson equation and Depletion Approximation

The unidimensional Poisson equation links the potential to the charge density. In this case (depletion approximation, **DA**), it assumes the following form:

$$\frac{d^2\phi}{dx^2} = \frac{qN_i}{\varepsilon_r\varepsilon_0} \qquad Eq.\ 1.2$$

where ϕ is the electric potential, depending on the distance x from the surface; N_i is the density of ions in the space charge region; ε_r is the relative dielectric constant of the material and ε_0 is that of vacuum. If the material is homogeneously doped, the density of donors (or acceptors) is independent of x and N_i is constant in the equation 1.2. To interpret the functional form of the equation 1.2, it is convenient to make a coordinate transformation to introduce the energy owned by an electron instead of the electric potential. The function V is defined as:

$$V(x) = \phi_b - \phi(x) \qquad Eq.\ 1.3$$

where ϕ_b is the bulk potential of the semiconductor. Substituting the function 1.3 in the equation 1.2 and then integrating we obtain:

$$\frac{dV}{dx} = \frac{qN_i(x - x_0)}{\varepsilon_r\varepsilon_0} \qquad Eq.\ 1.4$$

where x_0 is the thickness of the space charge region, determined by the need to totally compensate the layer of surface charge. Imposing the boundary condition for the electric field $\left[\frac{dV}{dx}\right]_{x=x_0} = 0$ at the equation 1.4, the semiconductor is discharged for $x \geq x_0$. Inside n-type materials, the number of electrons per unit surface, extracted from the superficial region of thickness x_0 is given by:

$N_d x_0 = N_i x_0$. This value should equally be referred to electrons that are migrated towards the surface, so $N_i x_0 = N_s$, in neutrality condition, where N_s is the density of charged surface states. Integrating another time, the equation 1.2 and imposing the boundary condition $V = 0$ for $x = x_0$, we obtain:

$$V(x) = \frac{qN_i(x - x_0)^2}{2\varepsilon_r\varepsilon_0} \qquad Eq.\ 1.5$$

Calculating the value of 1.5 at $x = 0$, we obtain the so-called Schottky relation, that expresses the value of the surface barrier Vs (that is the potential V at $x = 0$):

$$V_S = \frac{qN_i x_0^2}{2\varepsilon_r\varepsilon_0} \qquad Eq.\ 1.6$$

Electrons must have an energy at least equal to qVs to migrate towards superficial energy levels. Remembering that $N_i x_0 = N_s$, the relation 1.6 can also be written in the following form:

$$V_S = \frac{qN_S^2}{2\varepsilon_r\varepsilon_0 N_i} \qquad Eq.\ 1.7$$

The relation 1.7 is of fundamental importance to quantify the potential difference between the surface and the bulk: the energetic gap, which separates surface-electrons from bulk-electrons as a function of N_s. The entire calculation has been done assuming a "clean" surface (with no adsorbed gas), but in a more general case V_s can also be related with the density of adsorbed oxygen ions (O^{2-} and O^-) and

of oxygen atoms still present in the atmosphere in a molecular form (O_2), interesting for sensors operating in air.

1.2 Adsorption and surface reactions

1.2.1 Surface interactions

In general, there is an effect due to interactions between gases and the semiconductor surface, namely bulk effect, according to which the semiconductor stoichiometry is modified by the presence of a gas or organic steam. A semiconductor in the air undergoes a stoichiometric change because of the interaction between air oxygen and the semiconductor, where the material captures part of the oxygen with consequent alteration of the semiconductor conductivity. This is at the basis of complex chemical-physical mechanisms linked to the variation in conductivity of the material itself.
To pass from grain to grain, electrons must cross the surface potential barrier at the external shell of all grains of the material. The electrical conductivity of semiconductors is proportional to the density of electrons n_s at the surface of grains and close to the superior limit of the potential barrier.
Furthermore, n_s exponentially varies following the surface barrier potential qVs. Indeed:

$$n_s = N_c e^{-\frac{qV_s + E_C - E_F}{k_b T}} = N_d e^{\frac{qV_S}{k_b T}} \qquad Eq.\ 1.8$$

where N_C is the effective density of energetic states near the **CB**. It is so necessary to present a model in order to describe variations of the density n_s due to the adsorption of the atmospheric oxygen on the surface of the semiconductor. For a complete treatment, we must take into account also other atmospheric (reducing or oxidizing) gases.
There is two main possible interaction between semiconductor surface and gases:

- Gas adsorption;
- Ionic adsorption.

1.2.2 Adsorption

Because of the increased reactivity of surface atoms, particles from the gaseous phases can be attracted and retained by the surface of the semiconductor. This phenomenon is named adsorption.
There are mainly two types of adsorption processes at the interface between the semiconductor and the atmosphere, which are distinguished by their binding energy:

• physisorption (bond energy < 6 kcal mole);

• chemisorption (bond energy > 15 kcal mole).

Physisorption is the first stage of interaction that is established without the formation of chemical bonds between the material surface and the gaseous species in the environmental atmosphere. It is the weakest form of solid-gas interactions because it is due to Van der Waals-type bonds.
The molecules of adsorbed gas undergo a slight polarization, which is also induced on the surface molecules. This type of interaction between dipoles, therefore, constitutes the so-called phenomenon of the physisorption, causing a decrease in the total energy of the system.
During the physisorption, there is no change in the positioning of the adsorbing atoms, which remain fixed in their positions. The energy of the system is represented as the function of the distance d between adsorbent material and molecules adsorbed, $d \to \infty \Rightarrow E_{interaction} \to 0$.

Subsequently, a dipole-dipole attraction is developed as the adsorbate approaches the surface, where for $d \rightarrow 0 \Rightarrow E \rightarrow \infty$. The physisorption (see Figure 1.5) is characterized by a small value of the so-called "adsorption heat" ΔH_{phys}, with a high coverage value θ for low temperatures and vice versa for high temperatures, characterized by a low coverage.
If the surface of the solid is uniform, i.e. with identical and uniformly distributed adsorption sites, the adsorption rate can be expressed as the difference between an adsorption and a desorption times:

$$\frac{dN}{dt} = k_2(N_t - N)P - k_1 N \qquad Eq.\,1.9$$

where N is the number of adsorbed molecules per unit of area, N_t the total density of available adsorption sites, P is the gas pressure, while k_1 and k_2 represent respectively the kinetic desorption and adsorption constants. As it can be seen, the adsorption time is directly proportional to the gas pressure and the number of adsorption sites, while the desorption time is related to the number of sites already occupied, i.e., the surface coating. The surface fraction coverage is defined as follow:

$$\theta = \frac{N}{N_t} \qquad Eq.\,1.10$$

equation valid for a monolayer of gas adsorbed molecules.
The chemisorption species can bind to the solid and this interaction can be described as a new phase. There are a displacement and a rearrangement of the surface atoms during the chemisorption. The phase change can be ascribed as the modify in the structure of surface bonds in the solid material. Indeed, such atoms show a change the bonds energy with the other surface atoms while interacting with adsorbed molecules.

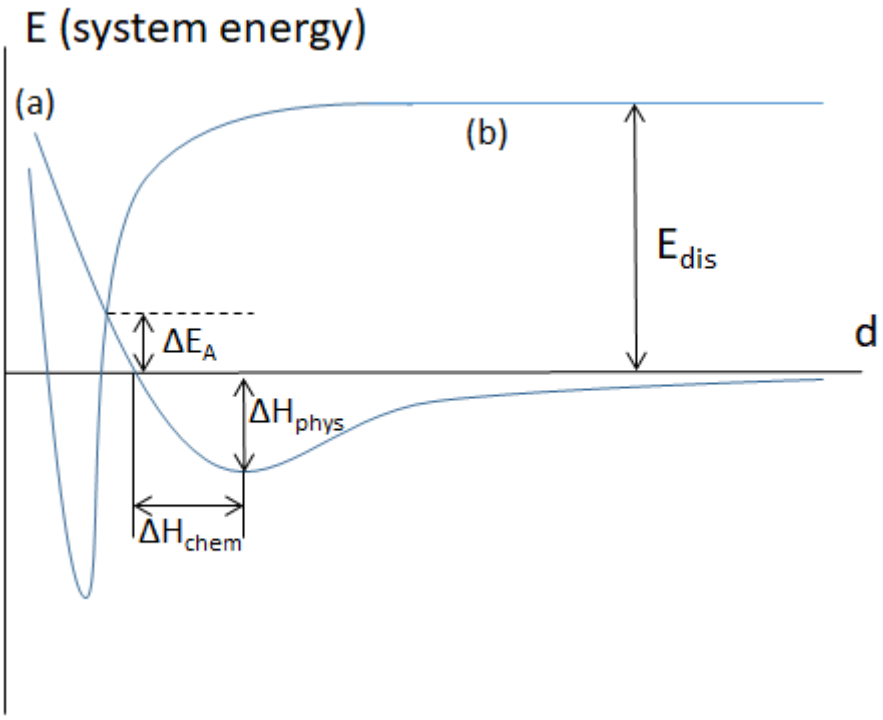

Figure 1.5: Model Lennard-Jones for: *a)* physisorption of a molecule, *b)* chemisorption of a molecule [adapted from 1.1].

At the equilibrium, equations 1.9 and 1.10 lead to Langmuir isotherm:

$$\theta = \frac{P}{(P + \frac{k_1}{k_2})} \qquad Eq.\,1.21$$

Which, for very low pressures, can be reduced to Henry's law:

$$\theta = P\frac{k_2}{k_1} \qquad Eq.\,1.32$$

This last equation, which can be used only as an approximation in experimental cases, claims that fractional coverage is proportional to gas pressure. The connection between physisorption and chemisorption can be understood by observing Figure 1.5, which is a graphical representation of the Lennard-Jones model. This model allows highlighting the ΔE_A activation energy of chemisorption, thus the energy that must be supplied in order to chemical adsorbs molecules over the material surface.

In the one hand, the curve (a) shows the energy of an adsorbed molecule as a function of distance d with respect to the adsorbent surface; you can notice a low minimum peak of that curve, corresponding to the heat (energy) of ΔH_{phys}. The curve (b), on the other hand, shows the energy as a function of the distance between the adsorbent and an adsorbed molecule of a dissociated adsorbate molecule in two atoms. The energy of dissociation (E_{dis}) for *d* values that tending to infinity represents the energy of dissociation; the pronounced peak for small distance values represents the desorption heat (ΔH_{chem}).

As it can be seen, the intersection between the two curves leads to a ΔE_A activation energy for chemisorption starting from a physical-adsorbed molecule: the ΔE_A is the energy required to dissociate a physisorbed molecule and that allows it to be chemisorbed. Instead of, the desorption process requires a $\Delta H_{chem} + \Delta E_A$ energy.

Contrarily to the physisorption process, the chemisorption is an activated process. The activation energy can be provided to the system both by heating and by a non-equilibrium process such as phot-activation.

Figure 1.6 highlights that a smaller amount of energy is needed to promote chemisorption starting from physical-adsorbed molecules in comparison with the energy that it is necessary to chemical-adsorb molecules directly from the gaseous phase. Indeed, in many cases, the physisorption process precedes the chemisorption, although this latter process can also be carried out directly starting from gaseous molecules.

The adsorption rate can be expressed as:

$$\frac{d\theta}{dt} = k_{ads}e^{-(\frac{\Delta E_A}{kT})} \qquad Eq.\,1.43$$

This last equation represents the case where ΔE_A is thermally supplied. Regarding desorption, it is represented by energy $\Delta H_{chem} + \Delta E_A$, so we can define the net adsorption rate as:

$$\frac{d\theta}{dt} = k_{ads}e^{\left(-E_A/k_BT\right)} - k_{des}\theta e^{\left(-E_A+\Delta H_{chem}/k_BT\right)} \qquad Eq.\,1.54$$

We can assume that $d\theta/dt = 0$ at the equilibrium, thus:

$$\theta = \frac{k_{ads}}{k_{des}}e^{\Delta H_{chem}/kT} \qquad Eq.\,1.65$$

θ decreases rapidly as the temperature rises. In this simple discussion, we assumed that θ is very low and therefore the availability of sites is not limited. In this way, the surface coverage of the chemical-

adsorbed molecules shows an apparent maximum with the rise of the temperature. Low values at low temperatures occur simply because the adsorption rate is negligible, and therefore the equilibrium is not reached in relatively long time. Furthermore, low values at high temperatures are obtained when an equilibrium in the chemisorption process is possible. In this way, the coverage rate decreases as the temperature rises.
The graph depicted in Figure 1.6 shows the dependence on the surface temperature of the physical- and chemical-adsorbed species on the semiconductor surface.

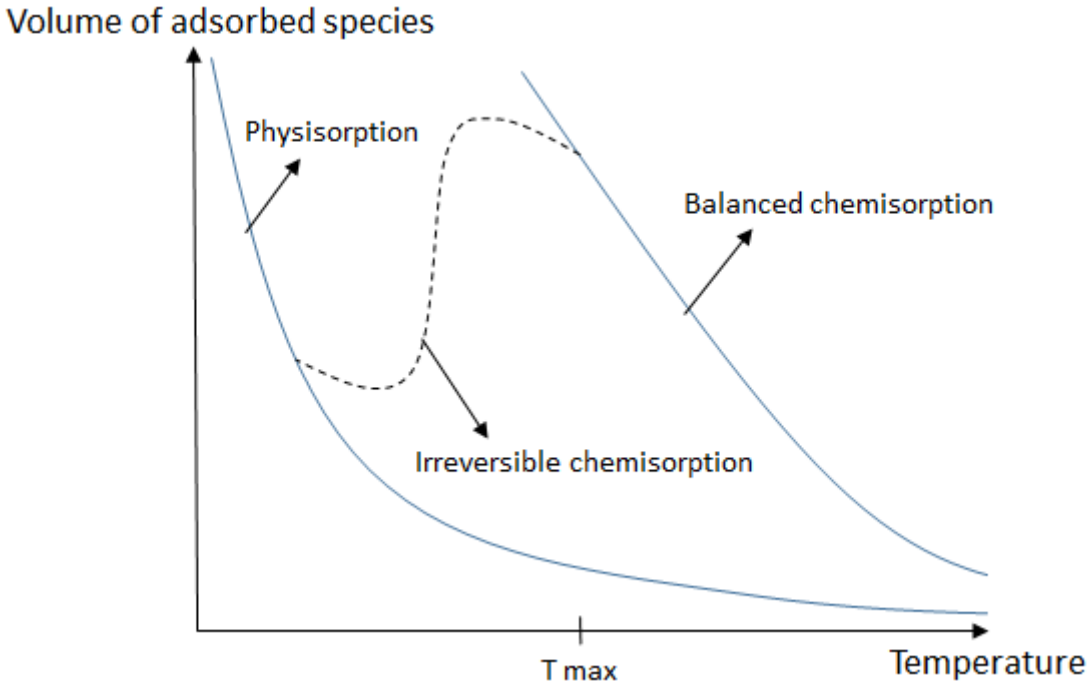

Figure 1.6: Typical isobar of adsorption [adapted from 1.1].

The maximum adsorption value is observed at T_{max} temperature, below this value the chemisorption is irreversible as the desorption rate (see equation 1.14) is negligible. Above this temperature, the desorption level, controlled by the activation energy $\Delta H_{chem} + \Delta E_A$, becomes appreciable, and an equilibrium of the adsorption is achieved, i.e. the adsorption rate equals the desorption rate. The surface coverage decreases as the temperature rises at a temperature higher than T_{max}.

1.2.3 Ionosorption

The ion sorption phenomenon occurs in principle when there are no bonds between the atoms of the adsorbate and surface atoms of the solid material, but the adsorbate acts as a superficial state by capturing an electron or a vacancy. Thus, it can be bonded to the surface by electrostatic attraction. Ion oscillation is of importance in the gas-sensing field, especially that of oxygen, which can be iono-adsorbed in various forms: O_2^-, O^- and O^{2-}. This latter form is not usually included among the adsorbed species because of the instability of the double-charged ions unless the surface site has a very high *Madelung's potential*.
The Madelung's potential equation is:

$$U = \frac{Ne^2\lambda}{R_0}\left(\frac{\rho}{R_0} - 1\right) \qquad Eq.\,1.76$$

where λ constant of Madelung, N number of ions, ρ potential range, R_0 such that $dU/dR|_{R0} = 0$

It was demonstrated that the potential request to form O^{2-} ions on the surface of a nanostructured semiconductor can be provided with thermal-activation. For common metal oxide, this temperature is over 400°C [1.2].

1.2.4 Dandling bonds

The description of the surface from the chemical-physical point of view leads to a more intuitive picture of the phenomena that occur.
In semiconductors such as metal oxides, metal sulphides and so on, different types of surface bonds may be obtained depending on the polarity and geometry of the bonds in the material; in the specific case of semiconductors, dangling bonds play a decisive role, Dandling bonds are atomic orbitals that "protrude" from the surface, as can be seen in Figure 1.7, where an example about interaction between dandling *d* orbital of a transition metal and oxygen is reported.

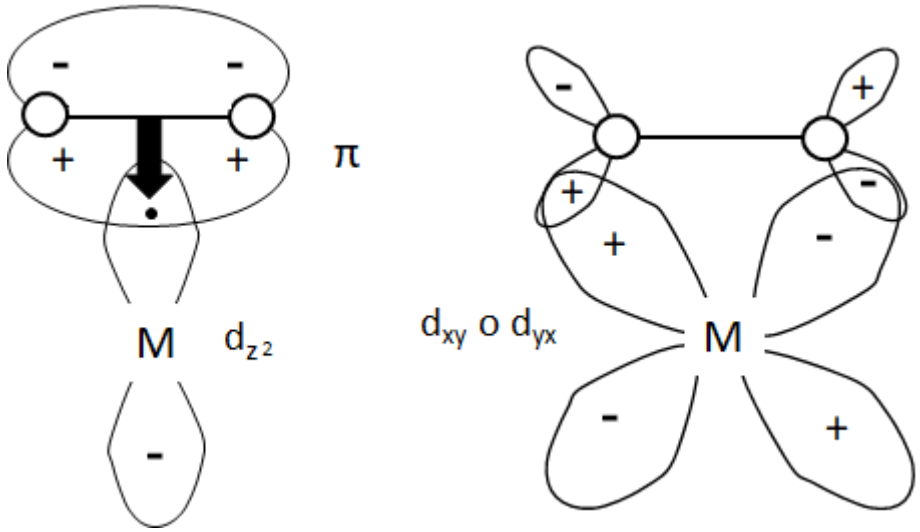

Figure 1.7: Chemisorption due to an electron interaction between a dangling bond of a transition metal and gaseous oxygen [adapted from 1.1].

It is impossible to have a complete coordination of each atom with its neighbouring atoms on a solid material surface. Hence, in materials such as silicon and carbon, hybrid sp^3 orbitals of dangling bonds remain available for interactions, whereas there are left accessible orbitals of *d* type if the atom with dangling bond is, as in our case, a transition metal. Usually, these are orbital containing an unpaired electron and, therefore, this atom is potentially able to both donate and receive electrons. In the case of transition metals, the number and shape of *d* orbitals allow complex reactions such as those in Figure 1.7.
The set of potential bonding points on the material surface are named surface states. The number of these surface states increase in the presence of irregularities and defects that further reduce the atoms coordination on the material surface. Irregularities can be originating from impurities, surface adsorbed, gradients, dislocations and grain edges (Figure 1.8).

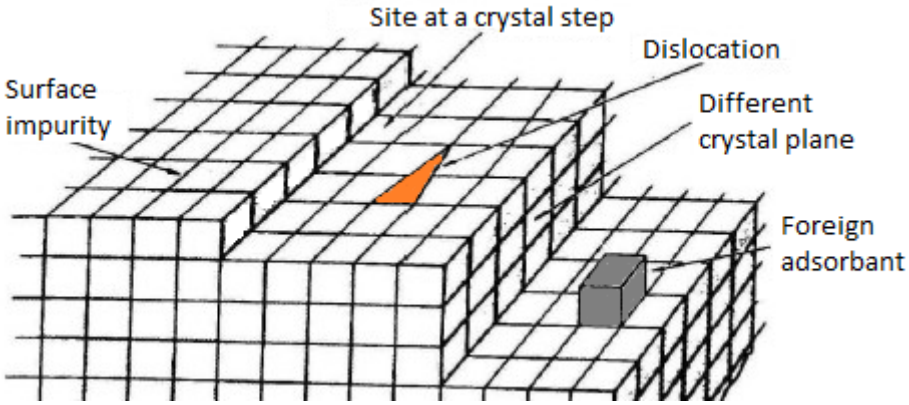

Figure 1.8: Representation of different types of defects present on a real surface.

1.2.5 Surface adsorption of oxygen

The oxygen is strongly ionized by the semiconductor exposed to the air, dominating the surface charge. Oxygen adsorption [1.3, 1.4, 1.5] produces a high increase in resistance in n-type semiconductors because it extracts electrons from the semiconductor by forming the depletion layer, so conduction electrons must cross this new insulating region. The oxygen adsorption process can be described by the following steps:

$$e^- + O_2 \leftrightarrow O_2^- \qquad Eq.\,1.87$$

$$O_2 \leftrightarrow 2O \qquad Eq.\,1.98$$

$$e^- + O \leftrightarrow O^- \qquad Eq.\,1.109$$

Where reagents are to be considered adsorbed. Let us assume for simplicity the validity of Henry's law, which shows that the amount of oxygen adsorbed is proportional to the partial pressure of oxygen in the atmosphere. By considering only the species O_2^-, we can write the adsorption rate as:

$$\frac{d[O_2^-]}{dt} = k_{ads} - n_S[O_2] - k_{ads}[O_2^-] \qquad Eq.\,1.20$$

and knowing that:

$$n_S = N_D e^{q^2[O_2^-]^2/2\varepsilon\varepsilon_0 kTN_i} \qquad Eq.\,1.21$$

it is possible to extrapolate that:

$$\Delta E_A = \frac{q^2[O_2^-]^2}{2\varepsilon\varepsilon_0 N_i} \qquad Eq.\,1.22$$

It is possible to conclude that the activation energy for adsorption increases rapidly with the increase of the adsorbed quantity. The simplest case of adsorption, without taking into account the local bonds, is that in which the energy is calculated by considering the difference between Fermi energy of the semiconductor and the oxygen energy (or the difference between their electrochemical potentials). From Figure 1.9 it can be noticed that, in the absence of surface charge, this energy difference is great (a). This difference decrease approaching the adsorption equilibrium (b).

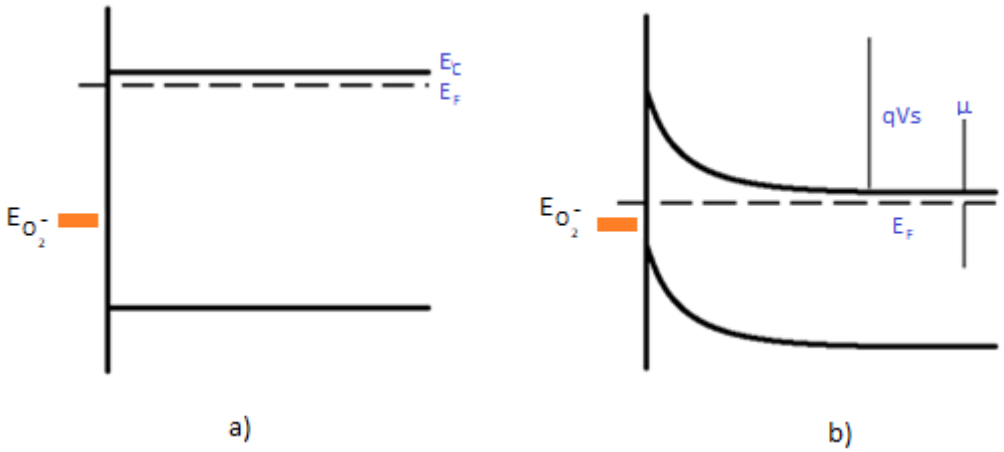

Figure 1.9: Difference between E_F and EO_2^- value at qV_S variation: a) flat band case, $qV_S = 0$, $[O_2^-] = 0$; b) equilibrium of adsorption [adapted from 1.1].

It is possible to calculate the total adsorption, by using the equations (1.17), (1.18) and (1.19) at equilibrium. Therefore, if we consider only the species concentration, applying the law of mass action to equation (1.18) and Fermi's statistics at (1.17) and (1.19), we obtain:

$$\frac{[O_2^-]}{[O_2]} = e^{-(E_{O_2}-E_F)/kT} \qquad Eq.\ 1.23$$

$$[O]^2 = [O_2]e^{-\frac{\Delta G}{kT}} \qquad Eq.\ 1.24$$

$$\frac{[O^-]}{[O]} = e^{-(E_0-E_F)/kT} \qquad Eq.\ 1.25$$

in which E_{O2} and E_O are the energy levels of the molecule and atom oxygens, respectively, and we assume, to simplify, that the receiving sites level remain unchanged, whether they are occupied or not. ΔG is the variation of free energy associated with the reaction (1.18), while the concentrations are indicated in square brackets. The atmospheric oxygen concentration $[O_2]$ is proportional to partial oxygen pressure in the air, P_{O2}.

Firstly, it is necessary to understand when it dominates the species O^- and when it dominates the species O_2^-. This is important because the former is more reactive than the latter. Therefore, the former is more sensitive than the latter to the variations in concentration of reducing or oxidizing gases. Secondly, it is also important to understand the dependence, of the surface density of charge, on the temperature and on the partial oxygen pressure, because it determines the resistance of the semiconductor, that is the measured value to detect atmospheric gases. From equations (1.23), (1.24) and (1.25) we get to:

$$\frac{[O_2^-]}{[O^-]} = [O_2]^{\frac{1}{2}}e^{-\frac{E_{O_2}-E_O-\Delta G/2}{kT}} \qquad Eq.\ 1.26$$

which let us affirm that the relative O^- concentration decreases as partial oxygen pressure increases and that the concentration increases as the temperature rises. Then, the adsorbed oxygen can interact with the gases present in the air, which is the basic effect that allows the operative working of common inorganic nanostructured semiconductors as chemoresistive sensors.
Indeed, for example, a gaseous molecule (A) can act as a reducing agent vs. adsorbed oxygen and, thus, vs. the semiconductor surface as follow:

$$A + O_2^- \rightarrow AO_2 + 1e^- \text{ (slow reaction)}$$

$$A + O^- \rightarrow AO + 1e^- \text{ (fast reaction)}$$

The released electron can return in the conduction band of the semiconductor, thus increase the conductance of the semiconductor. The relationship between the reducing gas concentration *[gas]* and the conductance *G* of a semiconductor is:

$$G = G_{air} * \alpha[gas]^{\beta} \qquad Eq.\,1.27$$

The gas can also behave in an oxidizing agent: in this way, it can interact directly with the surface or adsorbed oxygen, thus removing electrons from the conducting band of the semiconductor, thus decreasing the semiconductor conductance.

1.3 Chemoresistive gas-sensing catalysis

Many works in literature have highlighted that the operation of a chemoresistive gas sensor is based on reactions between the gas and the surface of the solid, reactions that have a direct effect on the conductance of the semiconductor; this process can be described as a reaction catalysed by the semiconductor itself.
Catalysis is of utmost importance in the chemoresistive gas-sensing field [1.6-1.11]. The presence in the semiconductor of catalytic additives can influence its selectivity by promoting a reaction rather than another, enhancing the selectivity of the sensor. Moreover, the catalytic process decreases the amount of energy required (named activation energy) for the chemical reaction, which involves, e.g., a decrease of the temperature necessary to thermo-activate the sensing process. Thus, the comprehension of the catalytic phenomena applied to this field is crucial to fully understand the interaction between gases and semiconductor surface, and hence the mechanisms of gas detection.

1.3.1 Activation mechanism

The activation energy of a chemical reaction is defined as the energy that must be provided to the system to allow the reaction mechanism. For example, in some reactions, it is necessary that the molecule is dissociated in the various parts (molecule fractions or ions) that compose it because they react exothermically with other ions or molecules. In this case, the activation energy can be identified by the dissociation energy of the molecule that should react. Therefore, since many reactions require an activation energy to take place, and that the operating principle of chemoresistive gas sensors is based on chemical reactions, it is clear that sensing a property of a semiconductor is strongly influenced by the activation energy necessary for the reaction.
The activation of chemical species in a reaction can be provided to promote, as already mentioned, a molecular dissociation, an ionization or some other intermediate reaction that "prepares" the species in a form that can involve to an exothermic reaction with the semiconductor surface. This activation energy is usually supplied by thermo-excitation, but can also be provided by photo-excitation (paragraph 1.4).
In general, a catalyst is a material that is introduced in the reaction environment to accelerate the chemical reaction. It acts through two main mechanisms in the chemoresistive gas sensor:

- the first is to concentrate the reagents by adsorption, which increases the probability of interaction between gas molecules and semiconductor surface;

- the second is to decrease the required reaction energy by activating one or more reagents.

Usually, pure metal-oxide semiconductor commonly used in the chemoresistive gas-sensing field is not a good catalyst, and an addition of suitable catalysts can greatly increase the sensitivity and the response velocity of the sensor. Furthermore, the catalyst can also increase the reaction rate for certain gaseous molecules, thus increasing the sensor selectivity [1.9-1.11].

1.3.2 Addition of supported catalysts

In chemoresistive gas sensors, support for catalysts is normally the semiconductor material itself, whose variation of resistance follows the laws described above.
They are dispersed in form of nanoclusters on the grains surfaces, which have a considerably greater size.
The common catalyst used in chemoresistive gas sensors are nanocluster of transition metals. There are many types of metal catalysts that can be provided on semiconductor sensors. Some are noble metals such as Au, Pd, Pt, others may be, for example, clusters of metal oxides.
The aim of the heterogeneous catalysis (i.e. between two different phases, for example, solid and gas) is to obtain a high surface area specific for the catalyst and to make it as stable as possible over time, even at high temperatures. With platinum, for example, a large dispersion on the surface of the material is attempted to maximize yield, so that each Pt atom (in principle) is available for interaction with gaseous reagents.
To explain how a catalyst can increase the sensitivity and selectivity of a sensor, let us refer to Figure 1.10, which shows some catalyst nanocrystals, deposited on grains of a semiconductor, which accelerate the oxidation of RH_2 species

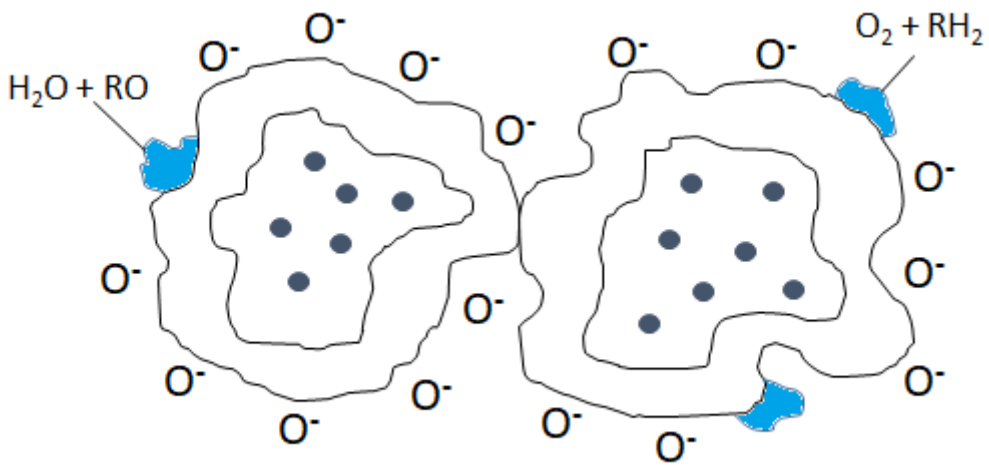

Figure 1.10: Oxidation of species RH_2 by catalyst nanoclusters, represented by black areas [adapted from 1.1].

The intergranular resistance of the support can be changed, thanks to catalyst support, by two mainly phenomena: spillover and Fermi energy control.

1.3.3 Support/catalyst interaction

- Spillover

The phenomenon of spillover is of great importance in catalysis, and thus in the chemoresistive gas-sensing field. Several studies have suggested that the atoms of oxygen, hydrogen and even carbon

monoxide, may be first activated and then flow ("Spillover") from the catalyst to the support (for example, a metal-oxide-semiconductor)

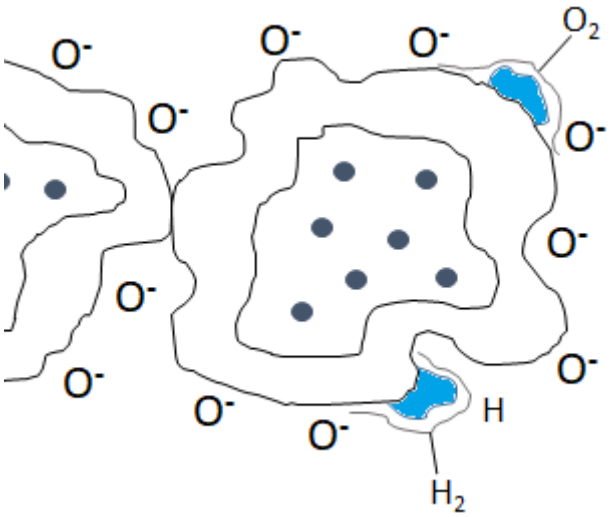

Figure 1.11: Spillover of hydrogen and oxygen molecules by the catalyst to the support [adapted from 1.1].

In Figure 1.11 we have reported a scheme of the described situation. Molecules of H_2 and O_2 are adsorbed by the catalyst nanoparticles, where they are activated and spillover to the support. If an oxidation reaction occurred only on the catalyst, it would have a minimal effect on the conductance of the material. Thanks to spillover mechanism, the reducing agent is forced by the catalyst to be rapidly oxidized and then transfer to the semiconductor by the presence of the metal catalyst dispersed as clusters over the semiconductor surface.

- Fermi energy control

The control of the Fermi energy means that the catalyst, supported on the semiconductor surface, "engages" the semiconductor Fermi energy and brings it to the Fermi energy level of the catalyst itself. The Fermi's energy is fixed to the surface in presence of superficial states with a density> $1012*cm^{-2}$. Figure 1.12 shows how a dispersed catalyst additive can "engage" Fermi's energy.

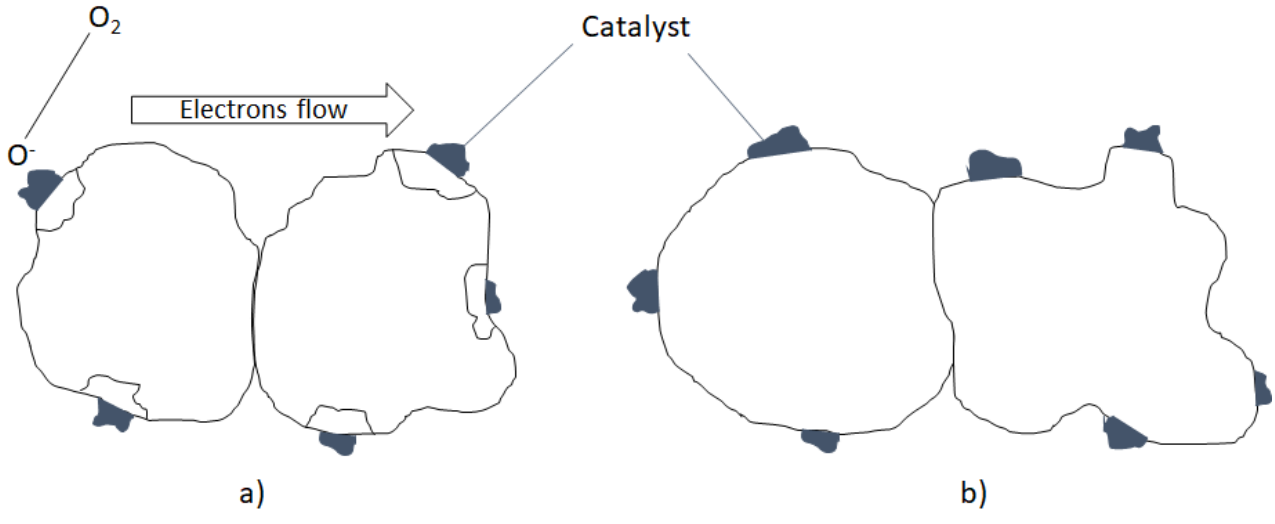

Figure 1.12: a) Low catalyst dispersion; b) Correct dispersion (separation between the clusters <50Å) [adapted from 1.1].

The spatial charge layer extends for about 100 Å from the surface within the semiconductor; hence we find out that the spatial charge layer derived from each of the catalyst nanocrystals extending for a radius of about 100 Å overlaps with the spatial charge layer of adjacent nanocrystals if they are spaced to a maximum of 50 Å. Therefore, it is easy to understand that a high catalyst concentration on the semiconductor surface is needed to exploit this phenomenon.
In the Figure 1.12 (a), each cluster controls the emptying layer in a hemisphere of about 100 Å, but within the space between the clusters the layer is again controlled by adsorbed oxygen and the catalyst effect is non-existent close to the particle-particle contacts. In the Figure 1.12 (b), we have a much larger dispersion of the catalyst on the surface, and the spatial charge is controlled at every point by the catalyst Fermi energy.
On the one hand, in Figure 1.13 (a), we can see the band structure for large size catalytic particles. In this situation, surface reactions do not, therefore, affect the bulk properties of the catalyst, nor the qVS barrier. If, on the other hand, the particles are small and well dispersed, as in Figure 1.13 (b), the effects of surface reactions cross the catalyst and directly affect the Fermi level energy of the semiconductor, thus influencing the qVS barrier directly.
Therefore, it is possible to affirm that if the catalyst dominates as a superficial state, replacing superficial N_S species (equation 1.7), it regulates the band curvature in the semiconductor, hence it controls semiconductor conductance in the same way of oxygen ions or any other species adsorbed in the model described for semiconductor sensors.

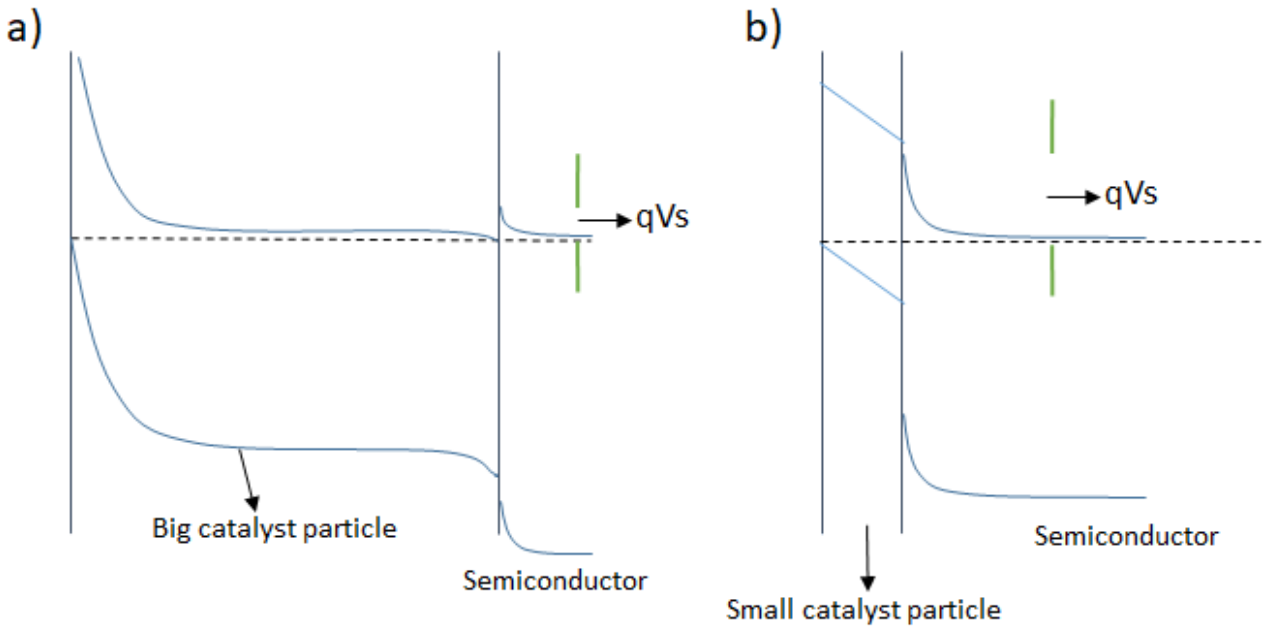

Figure 1.13: a) If catalyst particle is big (and dominated by adsorbed species), the spatial charge layer associated with adsorption does not affect the spatial charge layer of the semiconductor. Therefore, it does not affect the resistance of the intergranular contacts of the semiconductor. *b)* If the catalyst particle is small and highly dispersed, the effect of adsorbed species on the spatial charge layer of semiconductor is well defined [adapted from 1.1].

In conclusion, we can claim that there are two main points that control Fermi energy:

- The Fermi energy of the catalyst cluster at the interface with the semiconductor depends on the absorption of oxygen;

- The catalyst dispersion must guarantee a maximum distance between two nanocrystals of 100 Å.

1.4 Activation of a nanostructured semiconductor

Nanostructured semiconductors usually need to be "activated" to highlight chemoresistive properties. Indeed, without any activation, these materials suffer two main drawbacks that limited their functionality:

- the low number of charge carries, which results in a high resistance of the semiconductor;
- low surface reactivity, which limits the catalytic effect of the semiconductor in a gas-solid interaction.

Principal methods used to activate a nanostructured semiconductor as a chemoresistive gas sensor are an excitation by means of radiation (photo-activation mode) or thermal heating (thermo-activation mode).

1.4.1 Thermo-activation mode and grain size role

Consider a semiconductor film without intergranular resistance. Its variation of surface conductivity is defined as:

$$\Delta\sigma_x = q\mu_c\Delta n + q\mu_p\Delta p \qquad Eq.\,1.28$$

with σ volumetric conductivity, μ_c and μ_p mobility of electrons and holes, i.e. their velocity rate per unit of electric field, linked to the temperature by the following relation:

$$\mu\ \alpha\ T^{3}/_{2} \qquad Eq.\,1.29$$

where Δp and Δn indicate the holes per unit area in the depletion layer and the change in the actual number of electrons. It is assumed, however, that the variation in the number of holes is negligible and that the surface mobility of the electrons coincides with that of the bulk.

The conductance of a crystal width W, thickness t and length L is defined as:

$$G = \sigma W\frac{t}{L} \qquad Eq.\,1.30$$

The dependence of the charge carriers density on temperature is a function of the energy levels of the dominant donors. If the donor levels are close to the conduction band, donor ions will be completely ionized at room temperature. In this case, as temperature increases, the electron density in the conduction band remains unchanged. If the donor levels are deeper, the electrons will not be fully excited to the conduction band at room temperature; instead, above this temperature, the density of the conducting electrons increases exponentially with the temperature.

It is possible to produce defects in the lattice that alter the conductivity at sufficiently high temperatures, irrespective of the depth of the donor levels.

The carriers of charge move forced by an electric field imposed by the outside, and by diffusion associated with a concentration gradient. In the one-dimensional case, the current density flow is defined as:

$$J_i = \sigma_i E - \Delta_i z_i e\frac{dc_i}{dx} \qquad Eq.\,1.31$$

with E external electric field, Δ_i diffusion coefficient of i-th species, z_i the number of electronic charges on the i-th particle and c_i the concentration of the i-th species.

Considering a semiconductor oxide in the presence of gases in the atmosphere, the conductance variation is expressed as the difference between bulk conductance, G_{Xo}, and conductance loss (or gain) due to surface effects, G_0, i.e.,

$$G_{x_0} - G_0 = \Delta n \frac{W_u}{L} \qquad Eq.\,1.32$$

By knowing the conductance at $V_S = 0$ (V_S represents the value of the superficial barrier) and by measuring the variation of the conductance G_{Xo}-G_0, it is possible to calculate directly the variation of the actual number of electrons, Δn.

Conductivity loss due to surface effects is a small fraction of the bulk conductance, unless the sample is very thin, i.e. with a thickness similar to the depletion layer.

In order to increase the sensitivity to the gas, surface fluctuation variability should be prevalent, increasing the surface/volume ratio. This is achieved by creating a very fine grain superficial morphology, thus creating a strong porosity.

This leads to introducing the conduction mechanisms that provide electrical signals measured by the sensor. The gas sensors used are constituted of a porous layer composed of partially sintered granules of the sensitive material, so the electrons are obliged to cross the surface barrier formed in the intergranular contacts. The porous morphology of the material as described above allows the gas to reach a certain thickness of the surface material and consequently the surface of interaction with the gas is wide.

It cannot be assumed that all intergranular contacts are at the Schottky barrier. It is possible to distinguish two different types of intergranular contacts:

- “open neck” contact: surface states cause a depletion layer extending to the depth (Figure 1.14 a); in this case conductivity is mostly due to the non-emptied layer at the centre of the neck. The conductance is determined by the activation energy of the electrons of the donor states in the bulk and it will be changed by the gaseous atmosphere only by variations in the channel width;
- "closed neck" contact: depletion layers of the two surfaces overlap while leaving a strip through the centre with greater resistance (Figure 1.14 b). This geometry may result from an incomplete sintering that leaves a narrower neck or it can be produced by an open neck in which the depletion layer is modified by a gaseous atmosphere variation. In this case, the conductance would be determined by the activation energy of the electrons of the surface states in the conduction band; the influence of the gaseous atmosphere would be directly on the occupation of superficial states.

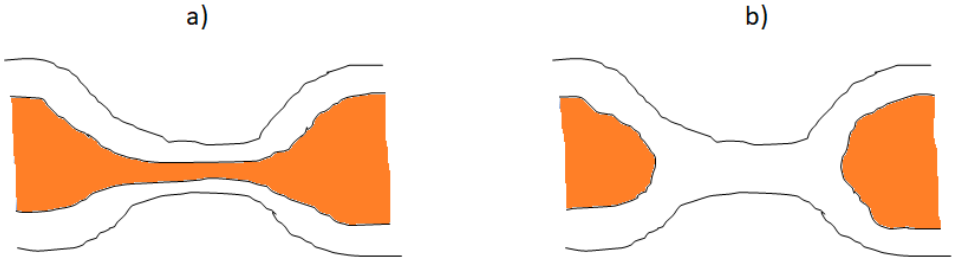

Figure 1.14: a) Open neck and b) closed neck [adapted from 1.1].

Inside the semiconductor grains the behaviour is ohmic with the Schottky barrier Contact, but in the contact points, due to surface charge, a Schottky barrier is formed. In this latter type of contact the conductivity will be limited by the charge transport through the barrier resulting:

$$\sigma \approx \cos(t)\, e^{\frac{-q\Delta V_S}{kT}} \qquad Eq.\ 1.33$$

This situation represents a limit case of the two previous ones; the activation energy for conductance will be directly related to the surface charge of the species present in the gaseous environment and, therefore, it is a function of the composition of the atmosphere. The exponential factor takes on great importance in polycrystalline materials with many intergranular contacts and consequently a high surface/volume ratio. In the intergranular contacts, the electrical resistance increases because in the area close to the surface there is the depletion layer. It turns out that just intergranular contact will be responsible for most of the resistance provided by the sample since chargers will be forced to cross the V_S potential barrier to switching from one grain to another. To obtain an equation that provides an approximate expression of the conductance of a polycrystalline semiconductor oxide film, we assume G0 as proportionality constant, the function of the bulk and geometric parameters of the device. Thus, we obtain:

$$G = G_0 e^{\frac{-qV_S}{kT}} \qquad Eq.\ 1.34$$

The capture of electrons by ion-adsorbed oxygen raises significantly V_S potential barrier, causing a variation in conductance. The activation energy for conductance, qV_S, is influenced by the charge and by the coverage fraction of superficial species and, thus, it is a function of the composition of the atmospheric gases. Given the fundamental role played by surface effects in the operation of gas chemical sensors, it is clearly necessary to realize polycrystalline semiconductor films in which the grains are as small as possible. Indeed, the small grain size increases the surface/volume ratio, inversely proportional to the radius, making superficial effects dominant over bulk ones.

1.4.2 Photo-activation mode

Therefore, via photo-excitation, it is possible to obtain the promotion of an electron (e) to the conduction band (CB) and the consequent formation of a hole (h +) in the valence band (VB). The result is an electrical conduction of the semiconductor (Figure 1.15).

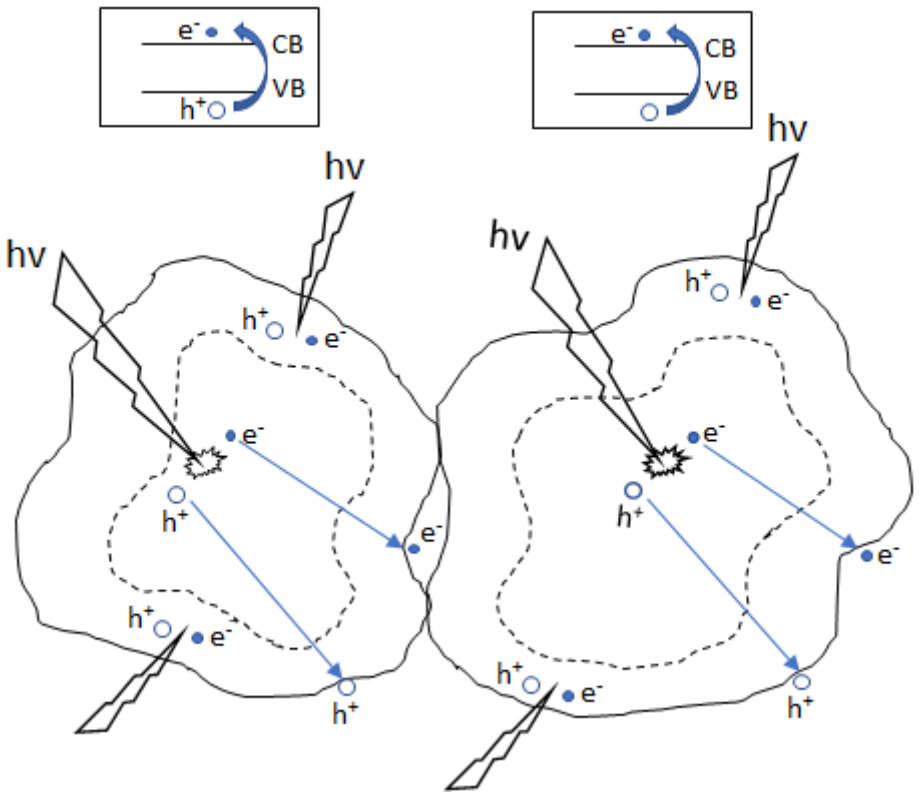

Figure 1.15: Representation of two semiconductor crystallites in contact and the formation of electron-gap pairs after lighting with energy equal to or greater than the band-gap energy [adapted from 1.12].

In this situation, in the presence of a gaseous or liquid phase at the semiconductor interface, a spontaneous adsorption of atmosphere gas molecules occurs according to the energy level (or potential redox) of each adsorbate. The catalytic processes involve these "free" holes and electrons, which can react with species adsorbed by an aqueous solution or air on the surface of the semiconductor.

Once the electron and gap excitation occurs, there is a lifetime of the nanosecond order in which photoelectron and photo-hole can transfer their energy to superficial states adsorbed by a liquid or gaseous phase on the surface of the semiconductor. If the semiconductor stays intact and the charge transfer to the adsorbed species on the surface is continuous and exothermic, then it is possible to obtain a process named heterogeneous photocatalysis [1.13]. There will be a transfer of photoelectrons to accepting molecules (oxidizing gases) and photo-holes towards molecules of electron donating gases (reducing agents), as shown in the following reactions and in Figure 1.15:

$$hv + (SC) \rightarrow e^- + h^+$$

$$A_{ads} + e^- \rightarrow A_{ads}^-$$

$$D_{ads} + h^+ \rightarrow D_{ads}^+$$

where SC indicates the semiconductor.
Each ion coming that have interacted on the surface can subsequently react with other molecules present in the atmosphere to form intermediate and final compounds of the photocatalytic reaction [1.14].
The use of photocatalytic reactions offers several advantages over others conventional techniques:
1. reactions can also occur at a low ambient temperature and pressure concentrations;
2. the treatment is economical, allowing potentially to use solar energy;

3. monitoring is also possible for thermo-degradable gases.

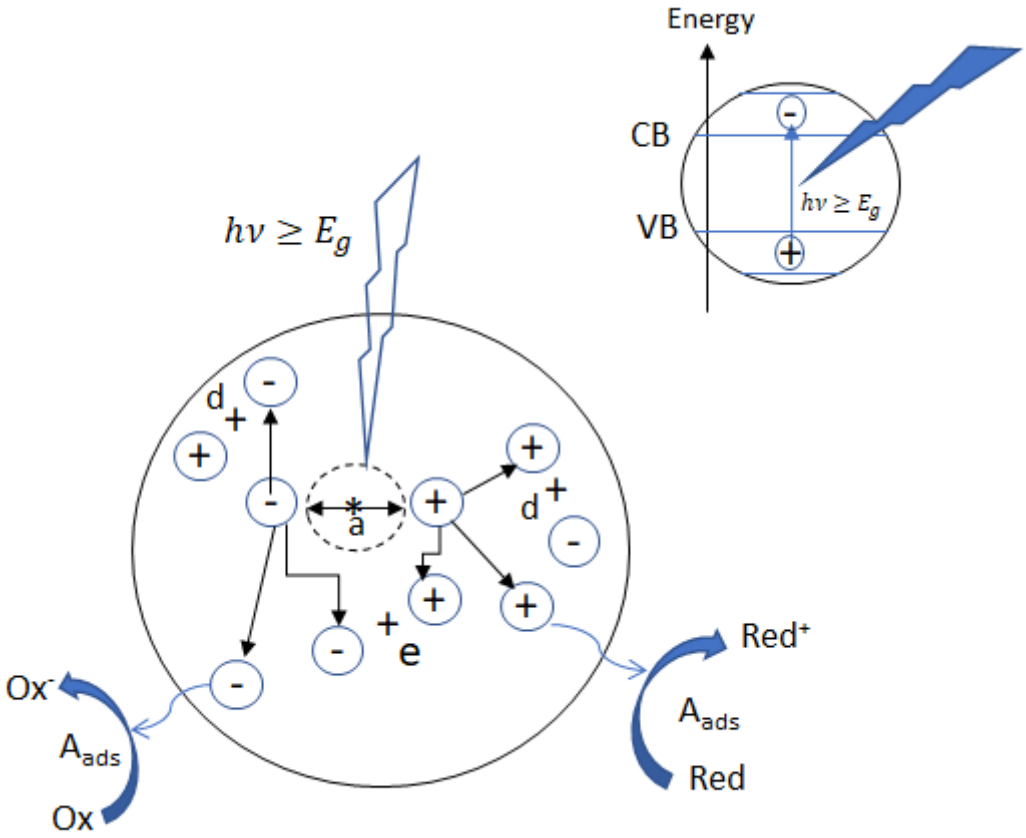

Figure 1.16: Illustration of the phenomenon of photo excitement in a semiconductor nanoparticle. The main processes described are: a) formation of the electron/hole pair; b) Oxidation of donor D; c) Reduction of AC; d) and e) recombination of the electron-hole pair respectively on the surface and on the bulk [adapted from 1.15].

There is also the possibility of recombination between the conduction band electrons and holes created by the photo-excitation. This inconvenient phenomenon of recombination is favoured by so-called "trap sites", which can be on the surface or on the bulk. In particular, it occurs when surface oxygen vacations and lattice defects provide new localized energy states that are not available in the "perfect" crystal. Furthermore, the surface represents a sudden discontinuity of the crystal, so it also provides a high density of energy states, located precisely in the surface region, which behaves as a trap state for the electrons.

Bibliography

[1.1] Marc J. Madou, Stanley Roy Morrison, Chemical Sensing with Solid State Devices, the University of Michigan. Academic Press, 1989.
[1.2] Barsan, N., Weimar, U. Conduction model of metal oxide gas sensors (2001) Journal of Electroceramics, 7 (3), pp. 143-167.
[1.3] N. Matsunaga, G. Sakai, K. Shimanoe, N. Yamazoe, "Diffusion equation based study of thin film semiconductor gas sensor-response transient", Sens. Actuators B, 83 (2002) 216-221.
[1.4] S. Nakata, K. Takemura, N. Ojima, T. Hiratani, S. Yamabe, "Mechanism of non-linear responses of a semiconductor gas sensor", Instrum. Sci. Technol., 28 (2000) 241-251.
[1.5] H. Lu, W. Ma, J. Gao, J. Li, "Diffusion-reaction theory for conductance response in metal oxide gas sensing thin films", Sens. Actuators B, 66 (2000) 228-231.
[1.6] A. Cabot, J. Arbiol, J. R. Morante, U. Weimar, N. Barsan, W Göpel, Analysis of the noble-metal catalytic additives introduced by impregnation of as obtained SnO_2 sol-gel nanocrystals for gas sensors, Sensors and Actuators B 70 (2000), 87-100.
[1.7] A. Cabot, A. Vilà, J. R. Morante, Analysis of the catalytic activity and electrical characteristics of different modified SnO_2 layers for gas sensors, Sensors and Actuators B 4210 (2002), 1-9.
[1.8] A. Cabot, A. Diéguez, A. Romano Rodrìguez, J. R. Morante, N. Barsan, Influence of the catalytic introduction procedure on the nano-SnO_2 gas sensors performances. Where and how stay the catalytic atoms? Sensors and Actuators B 4008 (2001), 1-9.
[1.9] G. Martinelli and M. C. Carotta, A study of the conductance and capacitance of pure and Pd-doped SnO_2 thick films, Sensors and Actuators B 18-19 (1994), 720-723.
[1.10] K. D. Shierbaum, U. Weimar, R. Kowalkowsky, W. Gopel, Conductivity, work function and catalytic activity of SnO_2-based sensors, Sensors and Actuators B 3 (1991), 205-214.
[1.11] M. Caldararu, D. Sprinceana, V. T. Popa, N. I. Ionescu, Surface dynamics in tin dioxide-containing catalysts II. Competition between water and oxygen adsorption on polycrystalline tin dioxide, Sensors and Actuators B 30 (1996), 35-4.
[1.12] M.C. Carotta, A. Cervi, A. Fioravanti, S. Gherardi, A. Giberti, B. Vendemiati, D. Vincenzi, M. Sacerdoti, A novel ozone detection at room temperature through UV-LED-assisted ZnO thick film sensors, Thin Solid Films, 2011, 1-8.
[1.13] Amy L. Linsebigler, Guangquan Lu, John T. Yates, Jr. Photocatalysis on TiO_2 Surfaces: Principles, Mechanisms, and Selected Results, Chem. Rev. 1995, 95, 735-758.
[1.14] Herrmann Jean Marie, Environmental photocatalysis: Perspectives for China, Science China Chemistry, 53 (2010), 1831-1843.
[1.15] Mills A, Le Hunte S. J Photochem Photobiol A: Chem 1997; 108:1.

2 Chemoresistive gas sensing material

In this part of the work will be presented innovative materials for chemoresistive gas-sensing devices studied during these 3 years of PhD. The choice of analysing materials that have been poorly studied so far has been driven by the limits shown by the common metal oxides used in this research field, including the lack of selectivity and stability in the long-term period. Materials investigated were chosen because of their peculiar characteristics, reported in the relevant paragraphs, which made them attractive for their characterization from a chemoresistive point of view.
For a standard sensor development, nanostructured materials were firstly synthesized and deeply characterized from the morphological, structural and chemical point of view, to optimise the powder production. Once a suitable powder was obtained, i.e. having a high purity and stability, it was deposited onto appropriate substrates and then electrical characterized to study its chemoresistive properties, both in thermo- and in photo-activation mode. All sensing characterizations were carried out by following the "3s rule", which encloses the three fundamental properties that a material sensitive to gaseous interactions must possess to be truly called "sensor", and therefore attractive for sensing applications: Selectivity, Sensitivity and Stability [2.1].

Parts of this chapter have been published in [A.1-A.5].

2.1 Chemical, morphological and structural analysis

The preparation of pure nanostructured powders is a crucial step to obtaining high-performance thick films. It is very important to obtain regular and nanoscale structures, since a large number of atoms on the surface and the effective Van der Waals, Coulombic and interatomic coupling significantly modifies the physical and chemical properties of low dimensional materials. Nanostructures characterized by a small size and high surface-to-volume ratio are the best candidates to improve the capability of detecting chemical and biological species [2.2]. For this reason, a deepened characterization of the obtained products is fundamental to improving the synthesis process and to achieve an optimised sensing material.

2.1.1 Scanning Electron Microscope – Energy-Dispersive X-ray spectroscopy

A scanning electron microscope (SEM) is an electron microscope that generates images of a sample by scanning the surface with a focused electrons beam. The electrons interact with sample atoms, producing various signals that contain information about the sample surface topography and composition. The electron beam is scanned in a raster scan pattern, and the beam position is linked with the detected signal to produce an image. The last versions of SEM, provided with the least technological development, can achieve resolution better than 1 nanometer.

The most common SEM mode is the detection of secondary electrons emitted by atoms excited by the electron beam. The number of secondary electrons that can be detected depends, among other things, on specimen topography. By scanning the sample and collecting the secondary electrons that are emitted using a special detector, an image displaying the topography of the surface is created. Samples can be observed in high vacuum in conventional SEM, or in low vacuum or wet conditions in variable pressure or environmental SEM, and at a wide range of cryogenic or elevated temperatures

by means of specialized instruments [2.3]. Moreover, the SEM instruments are typically coupled with the Energy-Dispersive X-ray spectroscopy (EDS or EDX), an analytical technique used for the elemental analysis or chemical characterization of a sample.
The study of powder morphology is very important in the chemoresistive gas sensing field. Indeed, it is an evidence in scientific literature that different morphology of the same semiconductor, e.g. nanorods, nanobeads or nanowire, shows great differences in sensing properties. These variations are mainly due to two causes, i.e. different grain size that results in a variation of the semiconductor surface available for interaction with the gaseous molecules, and a percentage change of the depletion layer in the presence of the same gas concentration between two different morphologies. [2.3].
We used two different type of SEM in our analysis:

- A Jeol JSM-7401F, available at the FBK, was produced by Joel and is equipped with a Bruker EDX detector to perform composition analyses. The instrument (installed in February 2005) is equipped with a cold field emission source, with Secondary Electron detectors (SE) and Backscattered Electron Detectors (BSE) both "in the lens" and "in the chamber", which offers a nominal resolution of 0,8nm at 30kV and 1,5 nm at 1kV. A special sample bias reduces the effective beam energy and enhances the resolution at low kV (0.1 kV), thus improving performances while charging effects are minimized. An EDS system (Oxford INCA 350) with the ultra-thin window is also available for elemental detection starting from Boron. This instrument offers a state-of-the-art capability for microstructural surface characterization using an electronic beam [2.4].

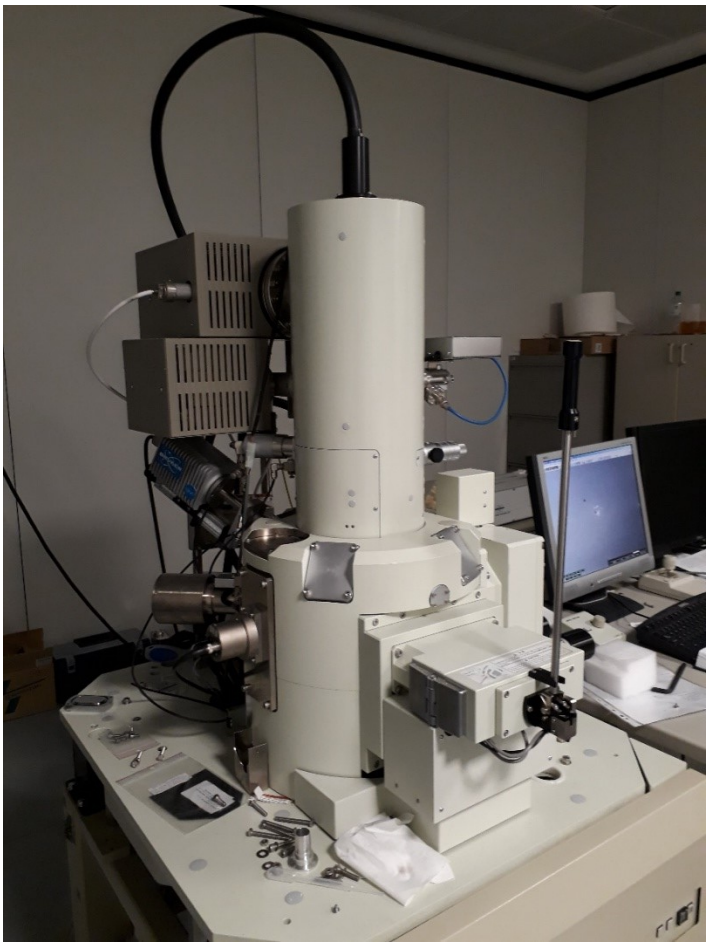

Figure 2.1: SEM-EDX Jeol model JSM-7401F available at the FBK.

- An SEM Zeiss EVO 40 (available at the microscope centre of Ferrara), which allows analysing surface morphology or topography from zooming in very large areas (one-millimetre side) up to sub micrometric dimensions. The microscope is provided with a LaB6 source with a maximum acceleration voltage of 30 kV. Identification of the chemical elements present in user-selected areas and particle sizes not smaller than micron is possible thanks to the energy dispersion spectrometer (EDS), coupled with the instrument, and suitable for X-ray microanalysis. The microscope can operate both conventionally in high vacuum or with variable pressure (SEM XVP), with a maximum pressure of 6 torrs [2.5].

Figure 2.2: SEM Zeiss model EVO 40, available at the microscope centre of Ferrara [2.5].

2.1.2 Transmission Electron Microscopy - Selected Area (Electron) Diffraction

Transmission Electron Microscopy (TEM) allows having an additional morphological information of powders studied in this work. TEM is a microscopy technique in which a beam of electrons is transmitted through a sample to form an image. The specimen is most often an ultrathin section less than 100 nm thick or a suspension on a grid. An image is formed from the interaction of the accelerated electrons with the sample as the beam is transmitted through the specimen. The image is then magnified and focused onto an imaging device, such as a fluorescent screen, a layer of photographic film, or a sensor such as a charge-coupled device.
Transmission electron microscopes are capable of imaging at a significantly higher resolution than other microscopes types, owing to the smaller de Broglie wavelength of electrons. This enables the instrument to capture fine details, even as small as a single column of atoms, which is thousands of times smaller than a resolvable object seen in a light microscope.
At lower magnifications TEM image contrast is due to differential absorption of electrons by the material due to differences in composition or thickness of the material. At higher magnifications, complex wave interactions modulate the intensity of the image, requiring expert analysis of observed images. Alternate modes of use allow for the TEM to observe modulations in chemical identity, crystal orientation, electronic structure and sample induced electron phase shift as well as the regular absorption based imaging. With TEM it is also possible to perform the Selected Area (Electron) Diffraction (SAED), a crystallography technique that information about crystallinity of specific

nanometric areas. This is possible because the wavelength of high-energy electrons is a few thousandths of a nanometer, and the spacing between atoms in a solid is about a hundred times larger, the atoms act as a diffraction grating to the electrons, which are diffracted. Some fraction of them will be scattered to specific angles, determined by the crystal structure of the sample, while others continue to pass through the sample without deflection [2.6]. It is possible to calculate the interplanar distance by means of the formula:

$$d = \lambda \frac{L}{R}$$

where λ is the wavelength of electrons, L is the camera length, R the radius of the diffraction rings and d the interplanar distance.
We used in this work two different TEM instruments:

- A Hitachi model H 800, available at the microscope centre of Ferrara. It is provided with a tungsten source and a maximum acceleration tension of 200 kV. Images are impressed on photographic plates

Figure 2.3: TEM Hitachi model H 800, available at the microscope centre of Ferrara.

- An FEI Tecnai F20T microscope, available at CNR-IMM centre of Bologna. The instrument is provided with a Field Emission Gun (FEG) cathode, and it is equipped whit EDS x-ray microanalysis, PEELS detector and HAADF detector for STEM operation. It is possible to carry out conventional analysis of materials, such as conventional diffraction contrast imaging, HREM imaging and analysis, micro- and nanodiffraction, STEM imaging and quantitative analysis, EDS X-ray elemental microanalysis and mapping in STEM mode [2.7].

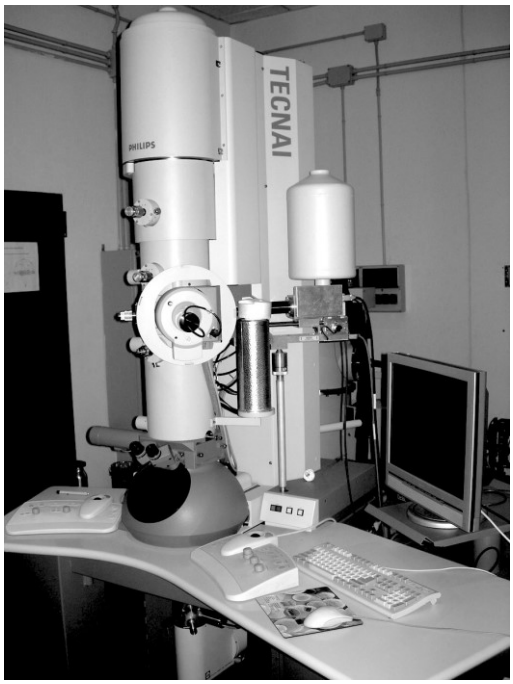

Figure 2.4: The TEM FEI Tecnai F20T microscope, available at CNR-IMM centre of Bologna [2.7].

2.1.3 X-ray Powder Diffraction

X-ray Powder Diffraction (XRPD) is an analytical technique primarily used for phase identification of a crystalline material and can provide information on unit cell dimensions. The analysed material is finely ground, homogenized, and average bulk composition is determined. X-ray diffraction is based on constructive interference of monochromatic X-rays and a crystalline sample. These X-rays are generated by a cathode ray tube, filtered to produce monochromatic radiation, collimated to concentrate, and directed toward the sample. The interaction of the incident rays with the sample produces constructive interference when conditions satisfy Bragg's Law. This law relates the wavelength of electromagnetic radiation to the diffraction angle and the lattice spacing in a crystalline sample. These diffracted X-rays are then detected, processed and counted. By scanning the sample through a range of 2θ angles, all possible diffraction directions of the lattice should be attained due to the random orientation of the powdered material. Conversion of the diffraction peaks to d-spacings allows identification of the mineral because each mineral has a set of unique d-spacings. Typically, this is achieved by comparison of d-spacings with standard reference patterns [2.8].
The crystalline form of the sample is a property with important influence in the gas sensing response. For instance, Jiménez et al. reported in their work how different crystal phases of WO_3 show change in sensing properties of this material vs. two target gases, i.e. H_2S and NO_2 [2.9].
The XRD instrument used in our work is a power Bruker X-Ray Diffraction model D8 Advance diffractometer, with an X-ray tube operating at 40 kV and 40 mA, and equipped with a Si(Li) solid-state detector (SOL-X) set to measure CuKα1,2 radiation. Powder samples were side-loaded on an aluminium holder, and zero-background holder respectively. Measuring conditions were from 5 through 95 ° 2θ range, 0.02 °2θ scan rate, counting time per step 4 and 6 s for all powders analysed. The phase identification was achieved by search-match using the EVA v.14.0 program by Bruker and the Powder Diffraction File database (PDF) v. 9.0.133. The crystallite size of the as-synthesized nanopowder was determined by the Rietveld method, as implemented in TOPAS v.4.1 program by Bruker AXS [2.10]. The fundamental parameters approach was used for the line-profile fit [2.11-

2.13]. The determination of crystallite size by TOPAS was accomplished by the DoubleVoigt approach [2.14].

Figure 2.5: a) Bruker D8 diffractometer at the Department of Earth Science (University of Ferrara); *b)* Bruker D8 diffractometer goniometer; X-ray tube *(a)*; Sample *(b)*; Detector *(c)*; Sled *(d)*.

2.1.4 Thermo-Gravimetric Analysis

The ThermoGravimetric Analysis (TGA) is a characterization with a crucial relevance in the standard chemoresistive gas-sensing device, where the receptor needs to be thermo-activated to operate in optimum condition [2.15]. Indeed, through this analysis, it is possible to determinate the thermal stability of the material used, including both chemical and structural stability [2.16].
Generally, Thermogravimetric analysis is a method of thermal analysis in which the mass of a sample is measured over time as the temperature changes. This measurement provides information about physical phenomena, such as phase transitions, absorption and desorption; as well as chemical phenomena including chemisorptions, thermal decomposition, and solid-gas reactions (e.g., oxidation or reduction) [2.17].
Standard TGA instrument is coupled with Differential Thermal Analysis (or DTA). In DTA, the material under study and an inert reference are made to undergo identical thermal cycles, while recording any temperature difference between sample and reference [2.18]. This differential temperature is then plotted against time, or against temperature. Changes in the sample, either exothermic or endothermic, can be detected relative to the inert reference. Thus, a DTA curve provides data on the transformations that have occurred, such as glass transitions, crystallization, melting and sublimation. The area under a DTA peak is the enthalpy change and is not affected by the heat capacity of the sample.
The TGA used in this dissertation is a Netzsch model 409 PC Luxx TG/DTA thermal analyser, available at the Department of Earth Science of the University of Ferrara. For almost all samples, about 70 mg of semiconductor powders were filled in a nickel crucible and analysed in the range of 20-900 °C, with a heating rate of 10 °C min^{-1} under an air flow of 20 ml h^{-1}.

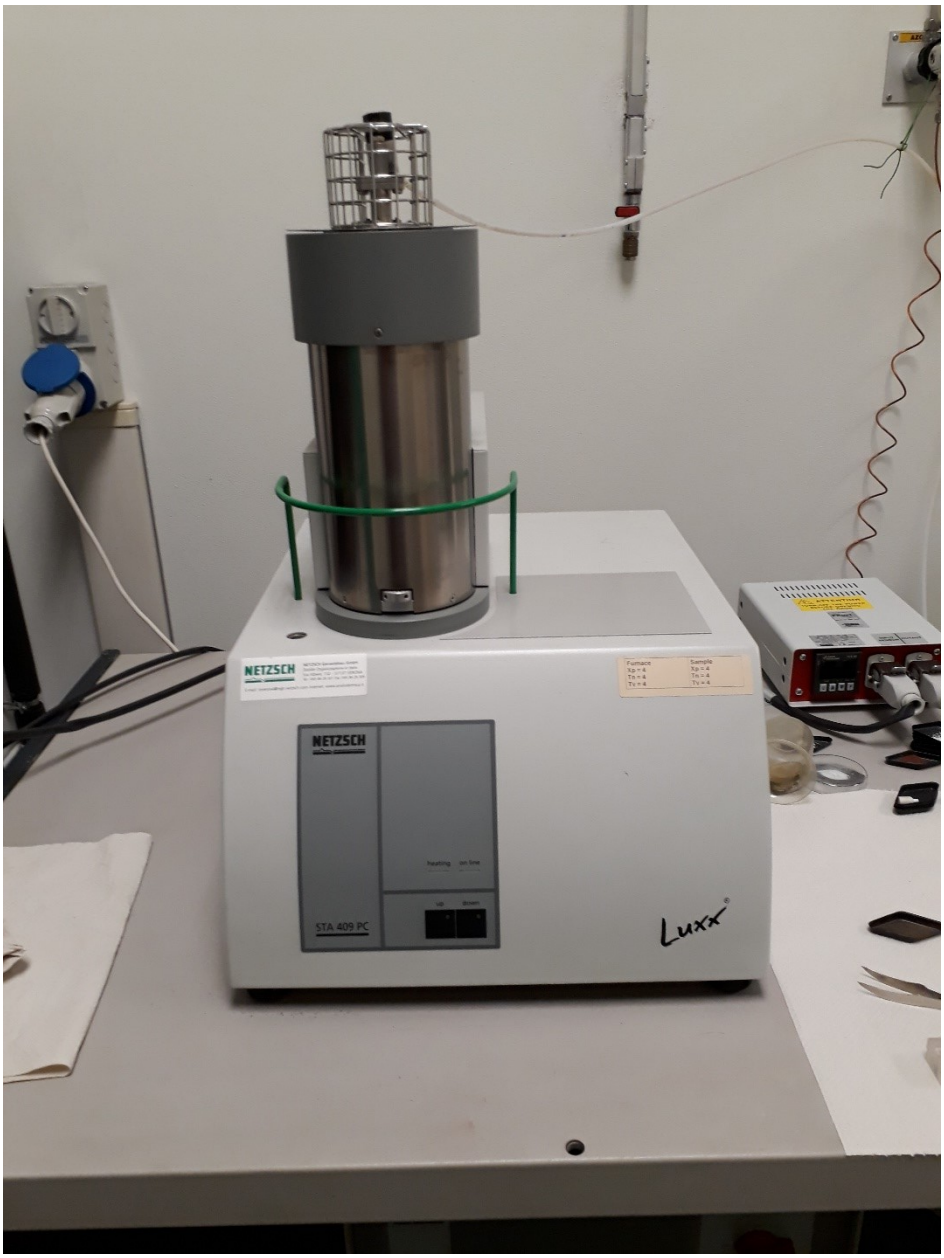

Figure 2.6: Netzsch model 409 PC Luxx TG/DTA thermal analyser, available at the Department of Earth Science of the University of Ferrara

2.1.5 X-ray Photoelectron Spectroscopy

X-ray photoelectron spectroscopy (XPS) is a quantitative spectroscopic technique that allows measurements of the empirical formula, the elemental composition at the parts per thousand range, chemical state and electronic state of the elements that exist within a material. XPS spectra are obtained by irradiating a material with a beam of X-rays while simultaneously measuring the kinetic energy and number of electrons that escape from the top 0 to 10 nm of the material being analysed. XPS requires usually high or ultra-high vacuum conditions [2.19].

The XPS can be used to analyse the surface chemistry of a material in its as-received state, or after some treatments. Contrarily the other analysis techniques proposed in this work, XPS analysis is specific to detect the change in the composition of about the firsts 10 nm of a nanopowder sample. Regarding chemoresistive gas sensors, the processes of greater interest that need a XPS surface

analysis to verify the material composition or stability are: exposure to heat to study the changes due to heating; exposure to reactive gases or solutions; exposure to ultraviolet light; decoration of the semiconductor with other nanoparticles (e.g. noble metal nanoparticles) [2.20]
Elemental identification is possible (except for H and He) for core level photoemission (5-1 at%, the typical detection limit for most elements). Relative elements abundance can be calculated in semi-quantitative or quantitative mode. Information on chemical bonds is derived either from core level shifts or from changes in the valence band electronic structure [2.21].
XPS spectra were recorded using a Scienta Esca-200 system equipped with a monochromatized Al Ka (1486.6 eV) source. The powders were attached to the sample holder using a double-sided carbon tape. An overall energy resolution of 0.4 eV was routinely used. The emission angle between the axis of the analyser and the normal to the sample surface was negligible. For each sample, Charge compensation was achieved using a flood gun and all core level peak energies were referenced to the saturated hydrocarbon in C 1 s at 285.0 eV. The XPS instrument used is available at the FBK.

Figure 2.7: Scienta Esca-200 XPS available at the FBK.

2.1.6 X-ray Fluorescence spectroscopy

X-ray fluorescence (XRF) is an analysis that allows detecting the emission of characteristic "secondary" X-rays from a material that has been excited by bombarding with high-energy X-rays or gamma rays. The phenomenon is widely used for elemental analysis and chemical analysis.
The instrument ionizes materials by means of short-wavelength X-rays or to gamma rays. The ionization consists of the ejection of one or more electrons from the atom and may occur if the atom is exposed to radiation with an energy greater than its ionization energy. X-rays and gamma rays can be energetic enough to expel tightly held electrons from the inner orbitals of the atom. The removal of an electron in this way makes the electronic structure of the atom unstable, and electrons in higher orbitals "fall" into the lower orbital to fill the hole left behind. In falling, energy is released in the form of a photon, the energy of which is equal to the energy difference between the two orbitals

involved. Thus, the material emits radiation, which has energy characteristic of the atoms present. The term fluorescence is applied to phenomena in which the absorption of radiation of specific energy results in the re-emission of radiation of a different energy. The limitation of this technique regards X-ray yields for the light elements. Indeed, it is often difficult to quantify elements lighter than sodium (Z = 11), unless background corrections and very comprehensive inter-element corrections are made [2.22].
This chemical analysis gives a huge contribution to the quantification of sample impurities, because of the very low detection limit (ppm) vs. atoms heavier than sodium. For this reason, the XRF analysis is used in the chemoresistive gas-sensing field to detect impurities with a high atomic number (inter alia transition metals) or to quantify the semiconductor doping or decoration [2.23].
The XRF instrument used in this work, available at the FBK, is a homemade Grazing Incidence X-Ray Fluorescence (GI-XRF), provided with a KETEK GMBH detector.

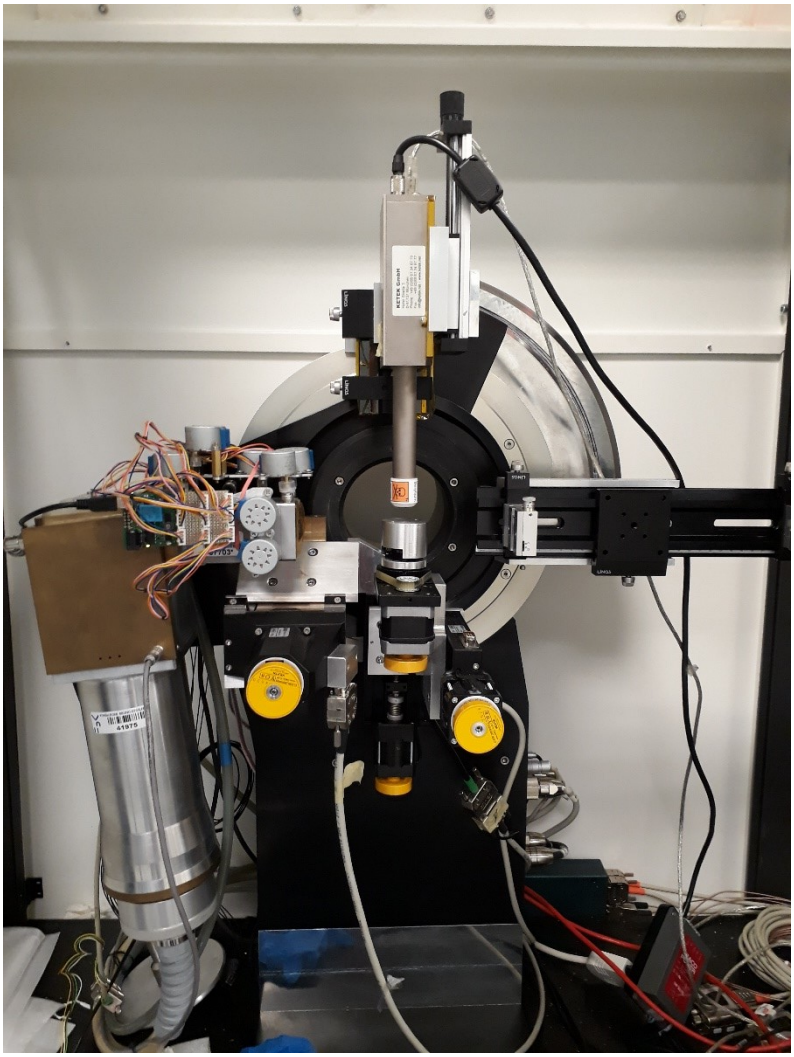

Figure 2.8: The GI-XRF available at the FBK.

2.1.7 Proton Transfer Reaction - Mass Spectrometry

PTR-MS is the abbreviation for Proton Transfer Reaction - Mass Spectrometry. The technology is based on reactions of ion donors (usually H_3O^+), which perform non-dissociative proton transfer to all VOCs with higher proton affinity. These characteristics result in sensitivity for VOCs in the air down to few pptv detection.

The very soft ionization technique avoids mass fragmentation, which enhances the interpretability of mass spectra. A TOF-MS linked to the PTR system offers real-time, high time resolution, high sensitivity detection of all analysed species in parallel. There is no need for time-consuming sample preparations or chromatographic separation before injection into the PTR-MS inlet. Furthermore, the opportunity to use Kr^+ as electron capturer allows detecting species with low proton affinity, enlarging possible applications of this technique.
The instrument utilized in this work is a KORE Technology, installed in FBK in 2011, and provided with PTR/APCI (Proton Transfer Reaction/Atmospheric Pressure Chemical Ionisation) source. It is equipped with a TOF-RA (Time Of Flight Reflectron Analyser for parallel detection) analyser, which allows reaching a mass resolution of 1300 *M/dM*. [2.24].

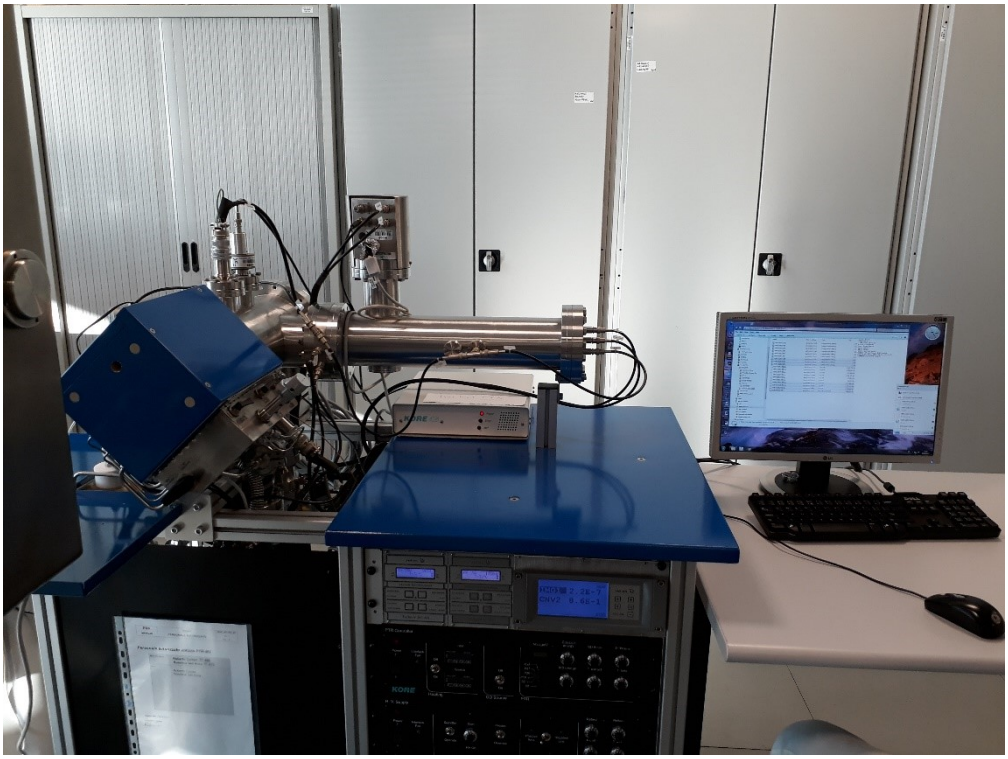

Figure 2.9: The KORE Technology PTR-MS available at the FBK.

2.2 Chemoresistive gas sensor development

The use of nanocrystalline material, combined with the serigraphic technology allows the production of sensitive films of the ceramic type, electrically stabilized at high temperature that, however, retain the nanometric grain structure.

2.2.1 Production process

To understand the process of preparation of thick film sensors is necessary a synthesis of all crucial aspects of the fabrication process. A classification of the chemoresistive gas sensors is based on the type of deposition used to obtain the sensing film:

- thin-film technology, a technique used to achieve layer thickness lower than 1 μm;
- thick-film technology, a technique used to achieve layer thickness higher than 1 μm.

Regarding thin film, there are various deposition methods that allow obtaining layers with a suitable thickness, such as Chemical Bath Deposition (CBD), Chemical Vapor Deposition (CVD), Plasma enhanced CVD (PECVD), dip coating, sputtering, spin coating and so on [2.25-2.27]. Among these techniques, the one that better-fitted nanopowder syntheses that we used were the spin-coating deposition, that allows depositing a nanostructured material mixed with a suitable solution (e.g. ethanol) on a flat substrate. The spin-coating technique is based on an instrument that, after solution drop deposition, spread the solution by centrifugation at a high velocity over the substrate. The speed at which the solution is spun and the viscosity of the solution determine the ultimate thickness of the deposited film. Repeated depositions can be carried out to increase the thickness of films as desired.

Chemoresistive thin-film gas sensors showed high interesting advantages, such as [2.28, 2.29]:

- high sensitivity;
- ultra-low detection limit;
- possibility to easily activated the thin sensing layers by means of various methods.

Despite these advantages, the great drawback of the instability of the thin-film sensor over the time, especially at relatively high temperature, limits its use in thermo-activation mode. For this reason, and since the thin film can be easily photo-activated with a high efficiency, we utilized chemoresistive thin-film gas sensor only in photo-activation mode, preferring thick-film deposition to obtain sensors suitable to thermo-activation.

Regarding thick-film technology, the major deposition method used is the screen-printing technique (which is one of the more ancient techniques of reproduction of graphic arts) introduced in the field of technology during the '70s to construct printed hybrid circuits [2.30]. It was applied for the construction of electronic components used in various sectors. Thick film hybrid circuits are famous for their multiple qualities as compactness, robustness and low cost [2.31]. Thick film technology is also relevant because it allows to build very precise geometries, so it is useful in the sensor field. In the last years, the screen printing technique is highly evolved even if the applied procedures have not substantially changed [2.32]. However, what makes the thick film technology suitable for the realization of sensors is its low cost combined with an easiness production process. Thick-film chemoresistive sensors, prepared by means of screen printing technique, showed the following advantageous properties:

- good sensitivity even at a low gas concentration;
- discrete reliability and repeatability of the measurement;
- small sizes;
- low cost;
- ease of automation;
- high performance;
- high stability.

However, a limitation of thick films in the chemoresistive gas sensors field is the deposition thickness, which not allows a high efficiency of sensors in photo-activated mode. Indeed, the extinction length of visible radiation provided by a commercial source (e.g. LED) is lower than 1 μm. Therefore, only a small fraction of the thick film is involved by photo-conductance and photo-activation of surface chemistry, making thin films more attractable to be studied for this application [2.29].

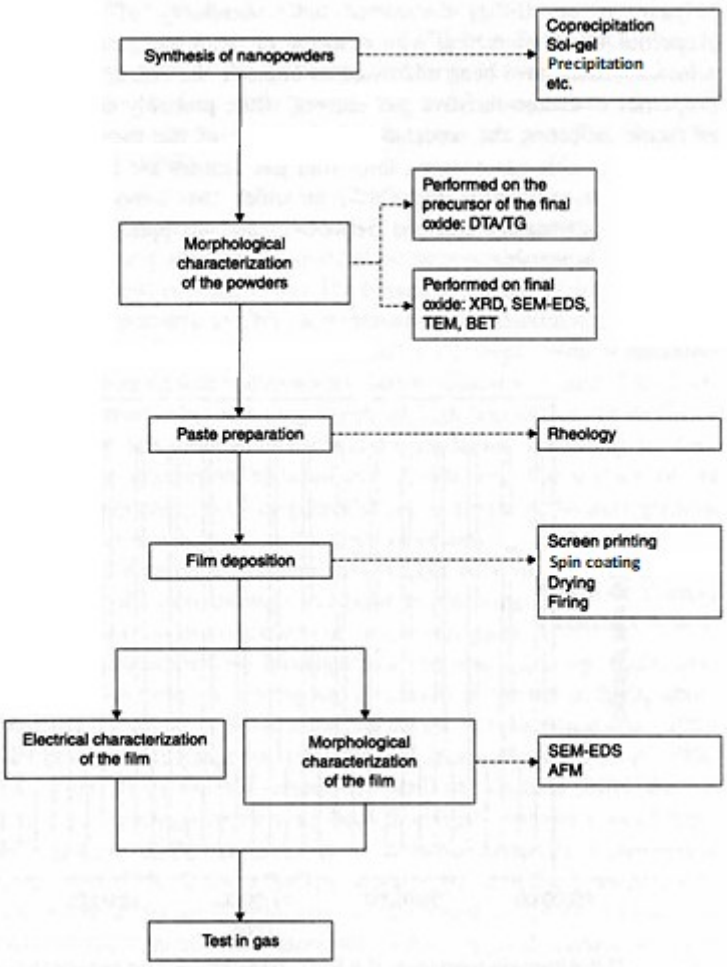

Figure 2.10: Scheme of the entire process to obtain thick films used as gas sensors [2.33].

2.2.2 Synthesis of a nanostructured semiconductor

The control of nanostructured semiconductor synthesis is the crucial step to prepare reliable chemoresistive gas sensor with high performance.

Nanostructured materials or nanomaterials are solid structural elements (particles or grains) whose characteristic dimension, in at least one of the three directions, is a few nanometers, generally from 1 to 100 [2.34]. Within this dimensional range, the size of the particles becomes comparable to the critical length scale of physical phenomena leading to new or improved physical properties. Among these, the mechanical, optical, magnetic, tribological, catalytic, and electrical properties are very appealing in the storage and conversion of energy [2.35] photonics, [2.36] chemical sensing [2.37], high-density magnetic recording [2.38], and catalysis [2.39]. The nanostructured materials can be classified up to date according to various criteria. According to the scheme proposed by [2.34] (Figure 2.11), nanomaterials can be classified according to both to the chemical composition and the shape of the microstructural constituents (crystallites and grain board form). Depending on the shape of crystallites, nanomaterials can be distinguished by layer-shaped structures, rod-shaped structures, or equiaxed crystallites. Based on their chemical composition, crystallites are distinguished in four different families. In the first, nanomaterials have the same chemical composition inside both the nanocrystal and the grain boundary; in the second, the crystallites differ in their chemical

composition; in the third, the composition of the crystallites differs from the grain areas; in the fourth, the materials for which crystallites are immersed in a matrix of different nature.

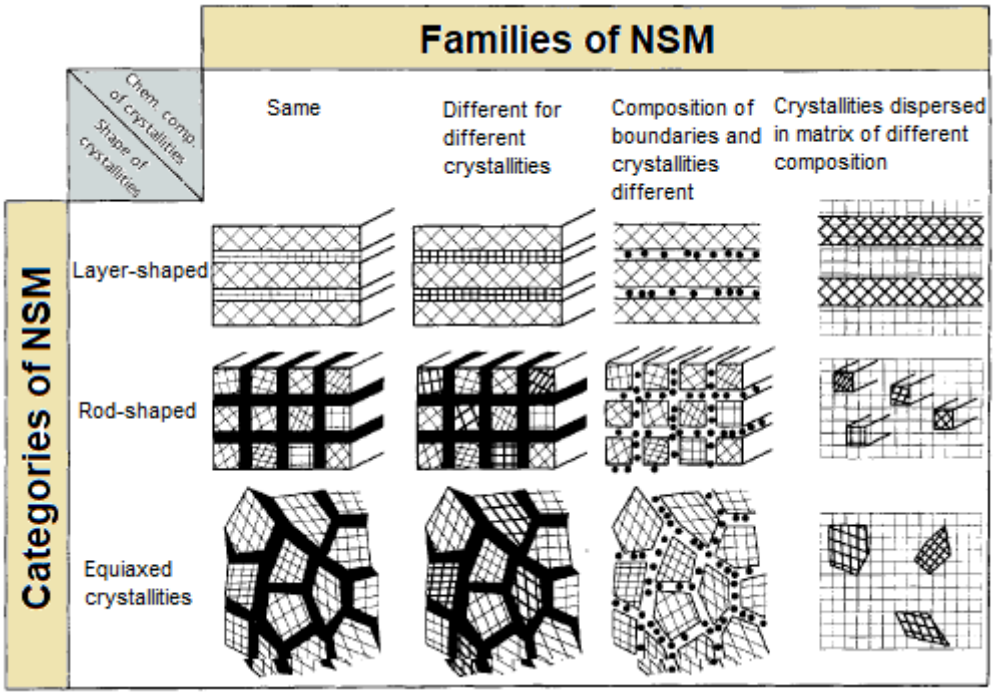

Figure 2.11: Classification of dwarf materials according to the morphology of microstructure constituents and chemical composition [adapted from 2.34].

Another effective and immediate classification [2.40] differentiates the nanomaterials based on their dimensional characteristics in four different classes (Figure 2.12):

• zero-dimensional, 0-D (nanoparticles),

• mono-dimensional, 1-D (nanotubes and nanowires);

• two-dimensional, 2-D (sheets);

• three-dimensional, 3-D (nanostructured nanoparticle materials such as constituent blocks).

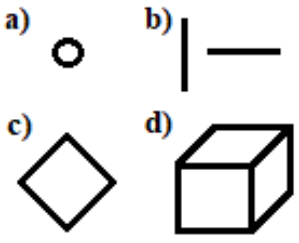

Figure 2.12: a) zero-dimensional, *b)* mono-dimensional, *c)* two-dimensional and *d)* three-dimensional nanostructure representations.

In recent years, the impetus to experiment with new synthesis methods in the nanopowder research field has received special attention due to the peculiar properties at the nanometric level and the ever-increasing demand for extremely fine powders with which is possible to obtain innovative ceramically products [2.41].
Despite the great steps forward carried out, the refinement of existing synthesis types is still a basic topic. Indeed, important steps still must be done to ensure that nanostructures with ideal features can be obtained [2.42].

In the synthesis processes of nanostructured powders, it is of crucial importance to control certain characteristics such as:

- particle size;
- particle shape;
- granulometric distribution;
- purity;
- agglomeration of nanoparticles.

In general, as with any other material synthesized, nanostructured materials depend on the preparation method, i.e. characteristics of the reagents used for preparation, the formation processes and synthesis parameters. A common problem for all synthesis processes is the production of powders that generally tend to be strongly agglomerated. Because of their high surface area and the great number of atoms located along grain edge areas and surface, nanoparticles are extremely reactive and tend easily to form bonds, thus creating agglomerates [2.43, 2.44]. This phenomenon is the main cause of low density and high porosity in finished products, thus compromising the benefits associated with the use of nanostructures. Therefore, among the goals that are currently being pursued in the production of nanomaterials, there is the development of increasingly accurate techniques and production methods that allow taking full advantage of the innovative properties of such materials, overcoming the disadvantages of their production [2.45].

The synthesis of nanostructured compounds can be divided into three main categories:

- gaseous phase synthesis;
- liquid phase synthesis;
- mechanical synthesis.

In this work, synthesis of nanostructured semiconductors was carried by means of liquid phase synthesis. Indeed, among preparation types, the synthesis in the liquid phase is an approach that allows controlling key requirements, since the kinetic and thermodynamic parameters of the chemical processes can be carefully monitored to yield inorganic nanoparticles with desired performance attributes. The main advantage of the liquid-phase synthesis is that this method permits the large-scale preparation of materials with nanoscale architectures without a significant modification of their morphology, which results in stable physical/chemical properties [2.46]. Moreover, liquid phase synthesis processes involve the preparation of an initial solution in which precursor materials are dissolved in solution and closely mixed at ionic and/or molecular level. This guarantees a high homogeneity of the final product. Other advantages of this technique regard the easiness and the low cost since usually, it is no necessary additional expensive instruments to control the reaction process [2.47]. However, the need for long process times and the high cost of some reagents result in the large use of this method in research laboratories but limit the preparation of large quantities of nanomaterial in the industry. Another negative aspect is the high toxicity of some metal salts used as reagents that restrict the preparation of biocompatible compounds.

There are four kinds of liquid phase syntheses, i.e. by precipitation or coprecipitation, microemulsion, sol-gel, and hydrothermal reactions in both polar and nonpolar media. During my PhD studies, it was decided to utilize mainly two of them, the sol-gel method to obtained metal oxides and precipitation for metal sulphides.

Precipitation of solid particles in solution is a dynamic process involving three stages: nucleation, growth, and coarsening/aggregation. Both of techniques used in this work allow a great control of all these steps, especially for the nucleation and the growth, thanks to the possible use during the synthesis of acid and bases to adjust pH, catalysts or complexing compounds. Furthermore, precipitation and sol-gel methods usually need room temperature and standard pressure to work properly, and this is a great advantage in term of simplicity and low cost.

2.2.2.1 Sol-gel method

Various works in the literature report the synthesis of nanoparticles through this method [2.48-2.53]. The formation of nanopowders via sol-gel technique is a process commonly used in the production of metal oxides, especially for small quantities. This synthesis method has the advantage of allowing preparation, in addition to nanoparticles, of materials of different shapes, such as film, aerogel and fibres. Figure 2.13 shows a schematic of the various products that can be obtained through the process. Sol-gel synthesis needs relatively low temperatures and it is easily reproducible. It also allows a high degree of homogenization when different phases are involved. However, it presents the typical disadvantages of wet processes: there are many steps required to obtain final products, it is generally necessary a medium/long-time of the process, the possibility of material contamination during the various phases, and often the high cost of reagents.

The method involves the formation of a "sol" (solid particles suspended within a continuous liquid phase) which subsequently freeze (liquid particles trapped within a solid continuous phase). Precursors are generally organometallic materials (e.g. alkoxides) which, dissolved in an appropriate solvent through hydrolysis reactions, are converted to the corresponding hydroxides. The subsequent step is the elimination of the solvent, which causes the condensation of the hydroxides and the formation of a three-dimensional lattice, the gel.

The reactions involved [2.54] initially involve the hydrolysis of the alkoxide where *R* is an alkyl group:

$$M(OR)_x + yH\text{-}OH \rightarrow M(OR)_{x-y}(OH)_y + yROH$$

Then, hydrolysed species form M-O-M bonds through condensation processes for the elimination of water and alcohol molecules:

$$\text{-M-OH + HO-M- } \rightarrow \text{ -M-O-M- + H-O-H}$$

$$\text{-M-OH + RO-M } \rightarrow \text{ -M-O-M- + ROH}$$

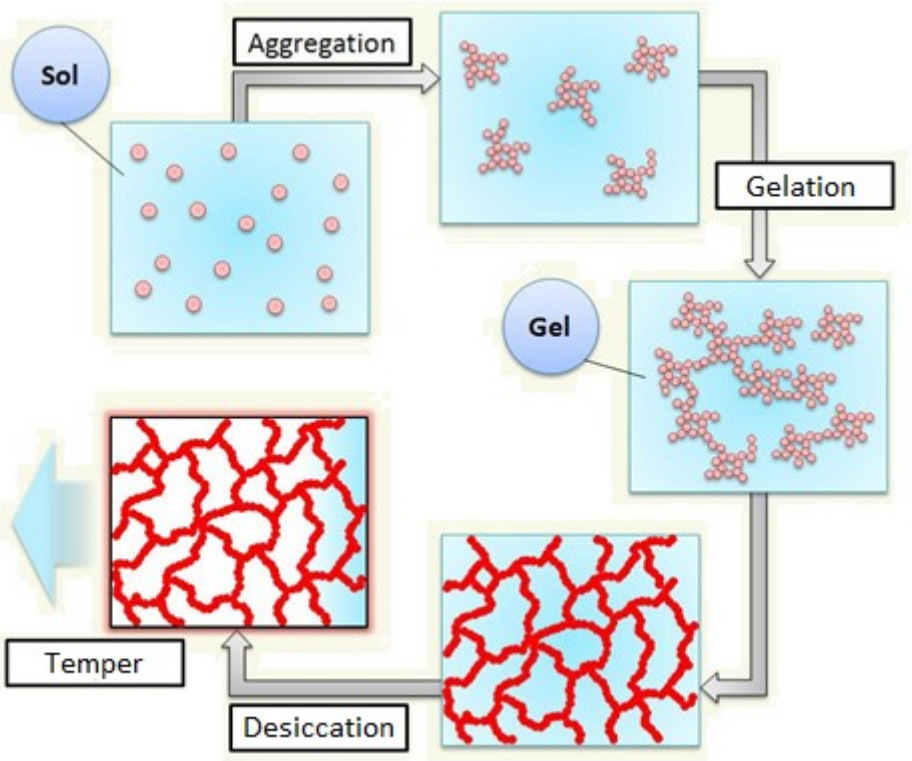

Figure 2.13: Schematic representation of sol-gel synthesis [adapted from 2.55].

2.2.2.2 Precipitation synthesis

This extremely simple method is used, in particular, in the production of powders with a single crystal phase. It consists in the preparation of a solution containing the desired cations (generally starting from metal salts such as chlorides, oxychlorides and nitrates) followed by mixing with a reagent containing a precipitating anion. Some parameters, such as temperature and pH, are very important in the precipitation synthesis, to achieve a good reaction yield. For this reason, these parameters need to be controlled strongly. The solution is usually kept in stirring to aid the formation of crystallites. There are two main phases of nanocrystals formed in the precipitation process: nucleation and crystal growth. The nucleation starts thanks to the formation of a nucleation centre, which is a nanoparticle, in a saturated or over-saturated solution, that through the mechanism of heterogeneous catalysis (biphasic system) activates weak links to the interface with the molecules in solution, promoting the crystallization reaction by the formation of a "crystalline germ" nanoparticle. This phenomenon occurs when it is thermodynamically favoured, i.e. when the Gibbs free energy is lower than zero in the following equation:

$$\Delta G = \Delta H - T\Delta S$$

There are two kinds of nucleation: homogeneous or heterogeneous.
The crystal growth consists in the addition of new atoms or ions to the nucleation centre, through electrostatic and chemical interactions. This step is pushed by a thermodynamic driving force, which could be supplied from outside (e.g. by means of heating or cooling) or already present inside the reaction environment (e.g. suitable ΔG). The crystal growth can be distinguished between two major mechanisms, i.e. Non-uniform or uniform lateral growth [2.56, 2.57].
It is possible that, due to an over-saturated solution, nucleation prevails on the growth, forming, in this case, a colloid that is inseparable from the rest of the solution by means of common separation techniques.
Once the precipitation of the product is obtained, it can be separated from the solution by physical filtration.
Both main steps of precipitation synthesis, listed above, strongly depend by parameters such as temperature, pressure, pH and use of catalysts. Through the suitable combination of these parameters, it is possible to control morphology, chemical purity and crystal structure of the product obtained.

2.2.3 Thick film sensors preparation

2.2.3.1 Sensing paste development

In this work, we deposited the nanostructured semiconductor used as an active material into a suitable transducer, i.e. the substrate, by means of screen printing technique. To achieve this goal, we added other substances to the sensing powder in order to give it an appropriate viscosity that allows printing the sensing material. Therefore, the sensing paste is composed of:

- the active material (nanostructured semiconductor);
- the fried;
- organic vehicles.

The active material consists of a nanometric powder of semiconducting particles with an average diameter smaller than 100 nm, which must be chosen depending on the type of gas to be detected

with the sensor. Preparation techniques used to synthesize nanostructured semiconductors are reported in section 2.2.2.
The fried is a powder formed by a mixture of glassy oxides based on silica (SiO_2) charged with alkaline-earth oxides or with oxides of the IV group, to modify its behaviour with temperature. Its function is to fix particles between them and to anchor the paste to the substrate. The first aspect is of fundamental importance in order to form a uniform network of particles and to obtain intergranular Schottky barriers; the second aspect is practical and is essential so that the film does not detach from the substrate. The fried needs temperature up to 500°C to work properly. The fried melted at this temperature, thus expressing its function. It was not possible to use the fried with all sensing materials tested in this work. Indeed, metal-sulphide semiconductors showed degradation at a temperature up to 350-400°C, thus we decided to not use fried with these materials. However, this has not led to excessive complications, and the pastes have shown satisfactory adhesion to the substrate even without "fried".
Organic vehicles are generally organic solvents in which are dissolved resins and surfactants in order to optimize the dispersion of solid particles and to regulate the viscoelastic behaviour of the paste. Their quantity varies in total from 50% and 80% in mass to the amount of the sensitive material powder, and depends on the desired dough consistency that is necessary reached for an optimal deposition. After the deposition, the organic vehicle is completely removed in the subsequent thermal treatment (paragraph 2.2.5).

2.2.3.2 Deposition of the sensing paste

The printing of the paste on the substrate is carried out with a screen printing machine (see figure 2.14).

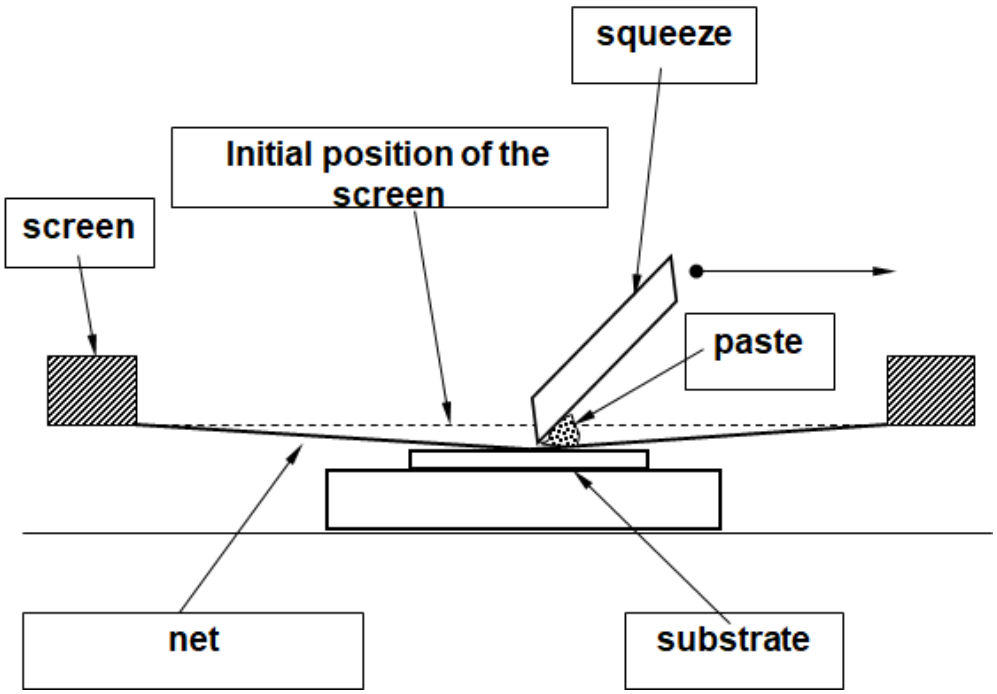

Figure 2.14: Screen printing, a lateral simplified section of the machine.

The essential components of a screen-printing machine are:

- screen, which shows the geometry of the design to be printed;

- squeegee, a spatula that, exerting pressure, allows the paste to cross the screen and to settle on the substrate, reproducing the design with high quality.

A typical screen consists of a network of finely twisted steel wires (of 100μm), stretched over a substrate. As shown in Figure 2.14, between cables there is an empty space; to characterize a printing screen a specific unit of measure, named mesh should be defined. The mesh number corresponds to the number of wires per linear inch that can be calibrated as a function of the required application. The cables network is covered by an UV-sensitive emulsion, on which is impressed photographically the design to be printed. Moreover, the screen presents some areas in which the emulsion is absent, through which the paste can be printed on the substrate. Therefore, the function of the printing screen is to define the design and to calibrate the quantity of paste. The paste must be a pseudo-plastic fluid, which varies its viscosity as a function of the applied stress. The squeegees must be resistant to solvents involved in the process and present in the paste. They are two: the first one forces the paste through the screen, the second one works in the opposite direction and reports the paste in the initial position for a new print.

2.2.4 Thin-film deposition

To deposit powders by means of thin-film technique, it was used an SPS spin coater model SPIN150i**.** Ethanol was the solvent used to give the suitable viscosity to the solution. After each deposition, thin films obtained were thermally stabilized at 100°C for 10 min in an air atmosphere. The process of spinning/stabilization was repeated many times until the desired film thickness was reached. Films thickness were measured by ellipsometry.

2.2.5 Drying and firing

Once printed, the ink undergoes two different treatments: the drying and the firing. The drying is a low-temperature treatment, around 100 – 150°C that serves to eliminate the most volatile organic solvents and to avoid the draining of the printed ink. It can be done in a common airy hotplate or in an infrared oven. The firing is a high-temperature process (up to 850°C) made in a muffle furnace or in an infrared oven. It serves to eliminate oil organic additive used to obtain the ink and to leave on the substrate only the film composed of the functional material and by the small percentages of fried. During these two processes, the temperature must be rigorously controlled to limit the formation of cracks on the handwork, which may prejudice conductive phenomena through the material.

2.2.6 Packaging

After the drying process, the printed substrate must be "bonded" into a special support, named "T039", which allows the protection of the sensor and the transmission of the electrical signal, thus completing the preparation process of the gas sensor, ready to be interfaced with the collected data system. These pins are welded, by thermo-compression or ball-bonding techniques, to the heater and to the contacts of the plate on which the film is deposited.

Figure 2.15: Bonded silicon substrate sensors, compared with a 2-cent money (left), and comparison between the bonded sensor and 1cent money (right).

This connection, powered by golden wires (99.99%) with a diameter of 0.06mm, is carried out via apparatus shown in Figure 2.16.

Figure 2.16: Instruments used for the "bonding" in Ferrara (left) and Trento (right)

2.2.7 Experimental setup for gas sensing measurements

As shown in Figure 2.17, the experimental setup consists mainly of:

- cylinders
- pneumatic system;
- gas-sensing chamber;
- an electronic system to read sensor signal
- data acquisition system

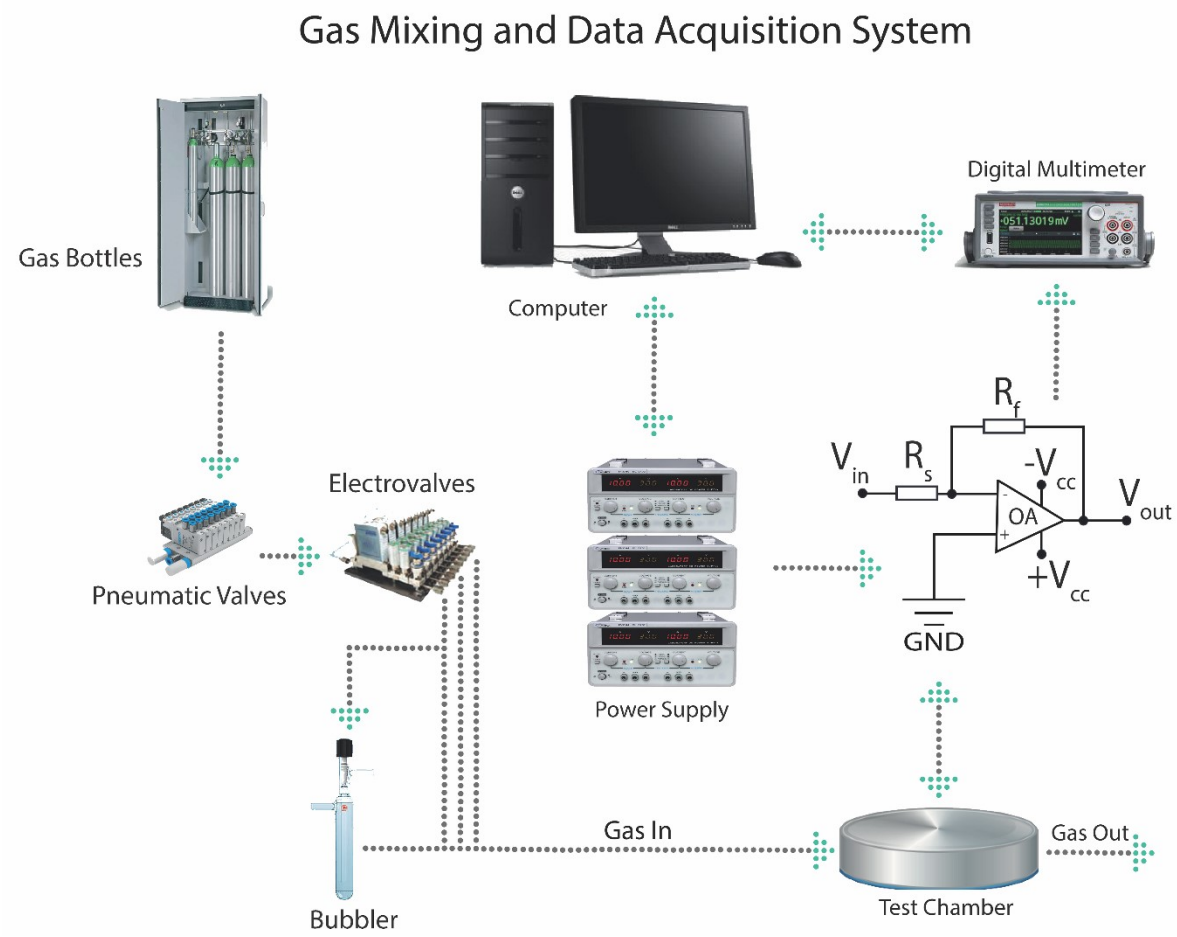

Figure 2.17: Schematic representation of the experimental setup.

The various components of the experimental setup are interfaced with each other in order to study sensing responses of gas sensors used, depending on the type and concentration of the gas mixture introduced into the gas-sensing chamber.

A detailing explanation the individual components is listed below.

2.2.7.1 Flow meters for gas mixing

The gas that we want to study is contained in gas cylinders, connected to flux meters that allow setting the flow. This flow is then sent to the measuring chambers, at which are connected through Teflon tubes. To know which flow is to be set, the following relation must be used:

$$F = \frac{F_{tot} C}{C_C}$$

where F_{tot} is the total flux that we inject in the gas chamber (in our case, 500 standard cubic centimetres per minute), C is the gas concentration of the target that we wanted to be analyzed in the chamber and C_C is the gas concentration in the cylinder (certified by the seller company).

2.2.7.2 Gas sensing chamber

We used two different gas-sensing chambers for measurements carried out in thermo- and in photo-activation mode. Indeed, the experimental setup in photo-activation is more complicated than in thermo-activation, because it needs suitable radiation source and a focusing apparatus.
In both cases, temperature and relative humidity inside the gas-sensing chamber were constantly controlled by means of a commercial HIH-4000 Honeywell humidity sensor and a commercial temperature sensor.

- **Thermo-activation mode**

The measurement chamber is the place in which sensors are positioned. It has a cylindrical shape, it is made of aluminium and hermetically sealed by a cover through bolts. At the centre of the chamber, there is the diffuser around which sensors are positioned. In every chamber, it is possible to place up to eight sensors together with the humidity sensor and the temperature sensor. Furthermore, it is important to specify that the gas is diffused uniformly inside the chamber in order to solicit sensors at the same time. The housing of devices was provided with four connections in order to give tension to both electrical circuits of the substrate. In all electrical characterizations, sensors were kept for 24 hours at the working temperature before sensing measurements, in order to stabilize sensors at such temperature.

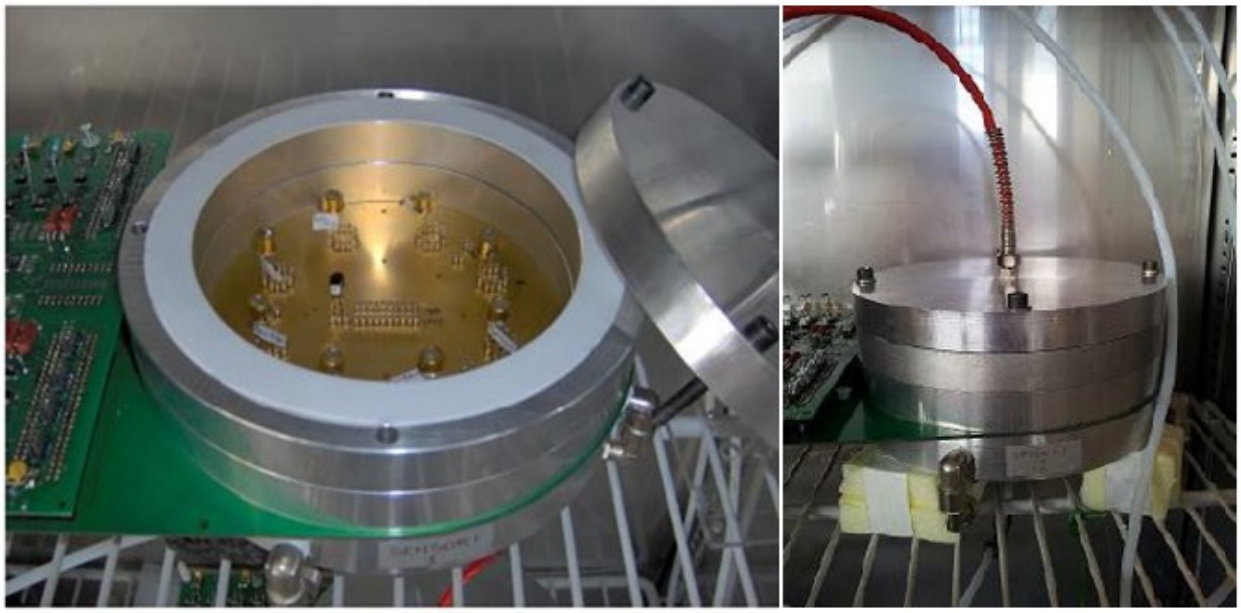

Figure 2.18: Sensor inside the chamber (left) and chamber hermetically sealed (right).

- **Photo-activation mode**

For the electrical characterization in photo-activation mode, the sensors were placed in a dedicated chamber provided with a glass window, through which the light emitted by a Light Emitting Diode (LED) was focused onto the films by means of an optical system (Figure 2.19). The sensor measurements were carried out at room temperature.

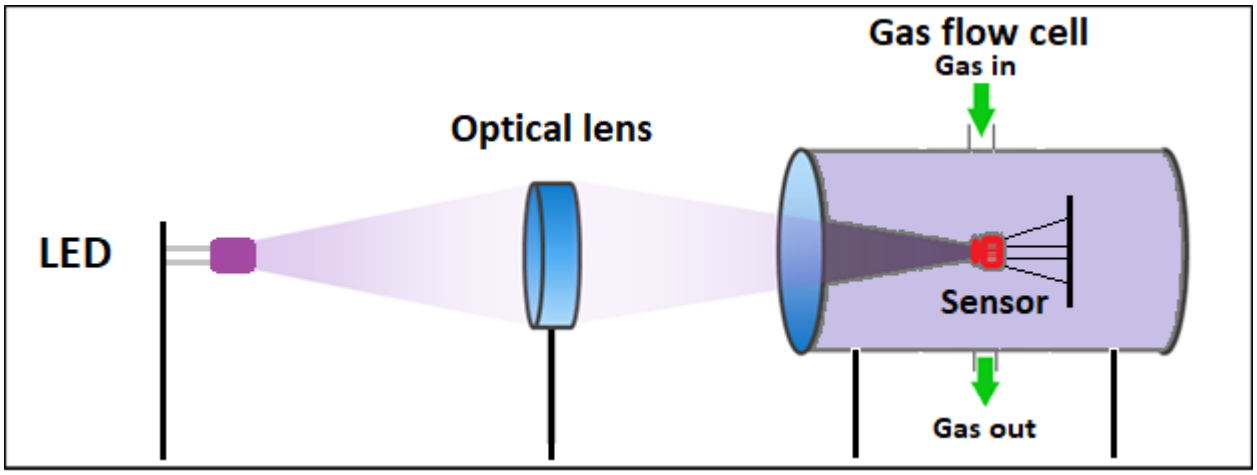

Fig 2.19: Schematic representation of the optical system and the gas chamber for measurements in photo-activation mode [adapted from A.5].

The commercial Hamamatsu LEDs (Figure 2.20) were quasi-monochromatic with an emission spectrum width of five nm. In order to achieve an overview of chemoresistive properties of sensing materials analysed, we decided to use different excitation wavelengths ranging from 385 to 645 nm. In particular:

• UV light, wavelength 385 nm;

• purple light, wavelength 405 nm;

• blue light, wavelength 468 nm;

• green light, wavelength 525 nm;

• yellow light, wavelength 592 nm;

• red light, wavelength 645 nm.

Fig 2.20: A commercial LED.

The radiations intensity was similar for all photodiodes used, and it was about 200 µW. In all electrical characterizations, sensors were kept exposed to the LED radiation the necessary time to reach a steady signal, in order to stabilize sensors at such excitation wavelength.

2.2.7.3 Electronic system to read sensor signals

In order to detect the changes in conductance of the sensor is necessary to insert it inside a circuit, represented in Figure 2.21:

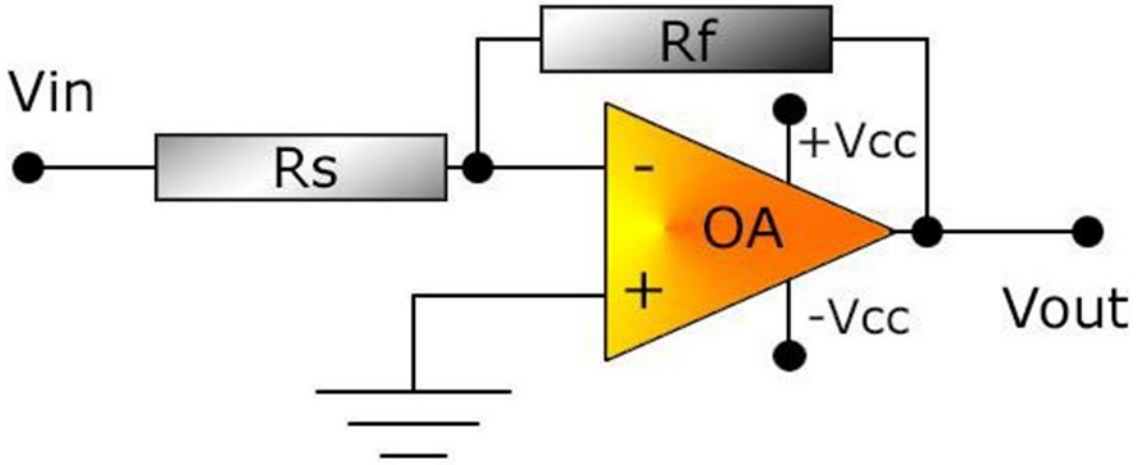

Figure 2.21: Circuit in which the sensor is inserted.

This is an inverting operational amplifier (OA), in fact, the input signal is connected at the negative entrance of the amplifier, while the positive one is grounded. At the ends of the resistors R_S and R_f we have respectively the voltage values V_{in} and V_{out}, so:

$$\frac{V_{out}}{R_f} = -\frac{V_{in}}{R_s}$$

The gain is given by:

$$\frac{V_{out}}{V_{in}} = -\frac{R_f}{R_s}$$

Fixing Vin = -5V, because of the virtual short circuit to the inputs of the OA, the inverting input terminal is at the same potential that the non-inverting input terminal. In this way, the sensor is subjected to a constant potential difference of 5V until the OA works far from saturation. Being the values of V_{in} and R_f known and constant, the output voltage V_{out} is then proportional to the conductance:

$$V_{out} = -R_f \cdot V_{in} \frac{1}{R_s} = -k \cdot G$$

where G is the conductance in the presence of the gas and G_{air} the conductance measured without the gas. Moreover, the expression of for response assumes a simple shape, independent from the circuit parameters:

$$\frac{G}{G_{air}} = \frac{V_{out}(gas)}{V_{air}}$$

where the wordings gas or air indicate the presence or not of the gas to measure.

Gas responses, for reducing and oxidizing gases, were defined for all sensing materials tested as follow:

$$R = \begin{cases} (G_{gas} - G_{air})/G_{air} & for\ reducing\ gases \\ (G_{gas} - G_{air})/G_{gas} & for\ oxidizing\ gases \end{cases}$$

For what concerns the heater, the circuit is represented in figure 2.22.

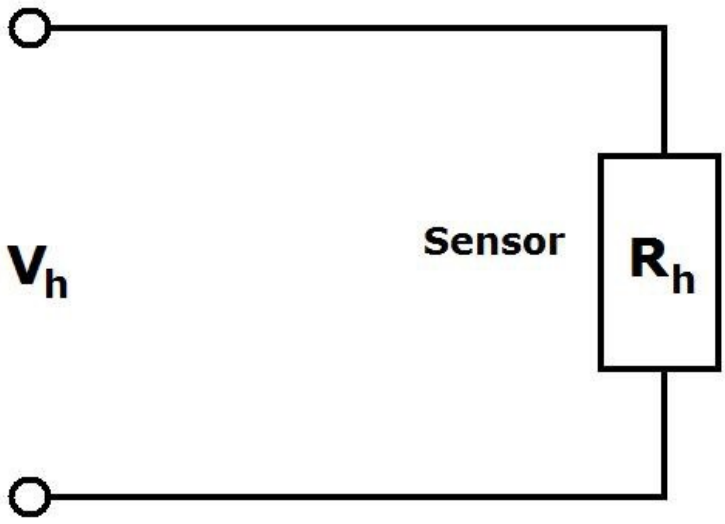

Figure 2.22: Heater circuit.

The heater is a thermal sensor and consists of a platinum coil in which resistance increases linearly with temperature. The relation between temperature and resistance is the following:

$$R_h = R_0(1 + \alpha T + \beta T^2)$$

in which R_h is the resistance at room temperature, R_0 is the resistance at 0°C, T is the temperature at which one wants to set the sensor, while α and β are two characteristic constants of the material. Constant α and β values depend on type of metal used and deposition characteristics.

Choosing the working temperature, it is possible to find the corresponding R_h. Applying a voltage V_h to the circuit the current that circulates, according to Ohm's law, will be:

$$R_h = \frac{V_h}{i} \qquad Eq.\,2.1$$

where V_h is established by the user and the current is measured by the feeder. It is so possible to control and directly modify R_h and so the temperature of sensors (modifying V_h).

2.3 Metal sulphides

2.3.1 Nanostructured metal sulphides

The great challenge of nanostructured materials lies in the control of their properties by the grain size, which combines bulk and surface effects [2.58-2.61]. Low-dimensional nanostructures have been

prepared with various morphologies and have attracted research attention because of their fundamental role in the comprehension of the quantum size effect and great potential applications [2.62, 2.63]. One-dimensional (1D) nanostructures are ideal for investigating the dependence of electrical transport, mechanical and optical properties on size and dimensionality [2.64]. Indeed, highly attractive properties and novel applications have resulted from well-aligned one-dimensional nanostructures on substrates, because they play a key role as both interconnections and functional components in improving the performance of technologically advanced devices [2.65, 2.66]. In recent years, many unique and excellent properties have already been demonstrated or proposed, such as superior mechanical toughness, lower turn-on voltage for field emitters, higher efficiency for solar cells, better electrochemical performance for lithium-ion batteries and enhancement of thermoelectric figure of merit [2.67, 2.68]. At the same time, two-dimensional (2D) nanostructures, i.e., nanosheets, nanoplates, and nanowalls, are suggested to be ideal components for nanoscale devices used in data storage, nanoswitches and biological sensors, due to their nanometre-scale thickness, high surface-to-volume ratio, and fascinating photocatalytic and optical activities [2.69].

In the last years, the variable features of colloidal nanocrystals, such as their size-dependent electronic, optical, magnetic, mechanical and chemical properties, which cannot be obtained in their bulk counterparts, have attracted the attention of researchers [2.70, 2.71]. Within colloidal semiconductors, metal chalcogenide nanocrystals have been extensively investigated due to their size-dependent photoemission characteristics and quantum confinement effects [2.72]. These nanomaterials can be used for different biological labelling and diagnostics, electroluminescent devices, lasers, photovoltaic devices, light-emitting diodes and single-electron transistors [2.73].

Metal sulfides are nanocrystals with great potential for investigation, due to their various types of structures. They are abundant and cheap because they exist in nature as minerals, i.e., heazlewoodite (Ni_3S_2), chalcocite (Cu_2S), pyrite (FeS_2) and others. The morphology of metal-sulfide nanostructures can be controlled by applying general solution methods and thermal evaporations, and their possible applications in energy conversion and storage were demonstrated. In the scientific literature, many papers have been reported to provide an overview of recent research and significant advances, ranging from synthesis to properties and applications, especially in energy conversion and storage, such as solar cells, lithium-ion batteries, piezoelectric nanogenerators and fuel-cells [2.74-2.76]. So far, in the gas sensing field, metal sulfides have been mainly studied in combination with metal oxides in order to modify the sensing activity of the latter [2.77, 2.78]. Metal sulfides as sensing materials for gas detection have been poorly studied, and the works published do not present an in-depth study of their sensing properties [2.79, 2.80]. On the contrary, the literature presents extensive investigations on metal-oxide semiconductors as sensing materials, due to their excellent sensitivity, fast response and recovery times, and low-cost [2.81, 2.82]. However, despite such important advantages, metal-oxides still exhibits unsolved drawbacks. Their incomplete selectivity and lack of stability sometimes result in unreliable responses [2.1, 2.83]. Moreover, these semiconductors often need a significant amount of energy to support chemical reactions at the surface, activated at high temperatures. By studying physical and chemical properties of nanostructured metal sulphides, it arose that such materials may be very good candidates to be further investigated in the chemoresistive gas sensing field. Indeed, by using these materials, we expect an improvement from an energy consumption point of view, both in thermal- and photo-activation modes, due to their lower band-gap than for metal-oxide semiconductors. This means that the activation of intrinsic surface reactions occurs at lower working temperatures, then the minor power supply is necessary. Due to this advantage, we were motivated in the search for potentially improved performance in terms of selectivity and stability. The absence of oxygen in the crystal lattice of metal sulphides leads to a different catalytic mechanism on the surface reaction with respect to metal oxides. In addition, this absence may solve the constant drift of the signal suffered by metal oxides and ascribed to the in/out-diffusion of oxygen vacancies,

which alters the doping level. For these reasons, we decided to focus our work on the use of metal sulfides for chemoresistive gas sensors by means of thick-film deposition technique [A.2].

2.3.2 Tin Disulphide

Parts of this paragraphs has been published in [A.2, A.3]. Tin (IV) sulphide is a mid-gap semiconductor (Eg = 2.35 eV), which can be synthesized as different types of nanostructures, e.g., nanoparticles, nanotubes, nanobelts, nanoflakes etc. [2.84-2.86]. The physical and chemical properties of this IV-VI semiconductor are very interesting due to their possible application, as solar cell material [2.87], lithium batteries [2.88], field-effect transistors [2.89] and optoelectronics [2.90]. Even though the list of application fields is undoubtedly wide, so far, the literature lacks investigations on tin disulfide as a material for chemical sensing. For this application, up to now, conductometric gas sensors are mostly based on metal oxides. Among metal-oxide semiconductors, the most studied up to now is the tin dioxide [291]. One of the SnO_2 drawbacks as the chemoresistive gas sensor is the long-term instability, a problem that could be related to a typical and characteristic defect of metal oxides: the oxygen vacancies [2.92, 2.93]. The mobility of these defects is linked to the lack of thermodynamic equilibrium of oxygen with the environment and it may be the reason for metal-oxides long-term instability. Therefore, the adoption of the metal sulphide counterpart of SnO^2, where sulphur atoms take place of the oxygen one, can pave the way to an alternative, more reliable, sensing material for gas detection. Recently, works about SnS^2 in the gas-sensing field were published. Ou *et al*. [2.94] have demonstrated the sensitivity of SnS_2 films to NO_2, by exploring the sensing behaviour of this material with five target gases (H_2, H_2S, CH_4, NO_2 and CO_2), whereas Shi *et al*. [2.80] prepared SnS_2 nanostructure through hydrothermal synthesis and they studied its sensing behaviour to ammonia at room temperature. A brief comparison between responses obtained at room temperature with SnO_2, SnS_2 and SnS_2-SnO_2 hybrid materials was carried out *vs.* ammonia by Xu *et al.* [2.79], but the grains of SnO_2 and SnS_2 which composed the films had different morphological features. Despite this, this material lacks in a deep investigation about its chemoresistive properties both in thermo- and photo-activation mode.

2.3.2.1 Synthesis

Various synthesis routes for SnS_2 have been proposed in the literature, including sol-gel processes, solid-state reactions, hydrothermal processes [2.95, 2.96], photo-catalysed synthesis [2.97] and so on. The advantage of using a solution precipitation solution compared to the ones listed above lies in lower costs, simplicity, time savings, and especially in the fact that no sophisticated and expensive tools are required. Therefore, it has been chosen for the synthesis of SnS_2 to use precipitation synthesis in a deionized water solution, at ambient temperature and pressure [2.98].

The sensing powder was synthesized by using Sigma Aldrich reagents. First, 2.3 mmol of $SnCl_4 \cdot 5H_2O$ were dissolved in a beaker with 2 mL of HCl (37% m/v). Then, to the resulting suspension were added distilled water, diluted in 80 mL. The solution was stirred for 10 minutes. Afterwards, 0.35 g of thioacetamide and 20 mL were added to this solution. The mixture obtained was stirred for further 3 h. The Tin (IV) Sulphide precipitated in this solution as brown nanoparticles, thus it was isolated by vacuum filtration and washed with water and methanol. At last, the product was dried for 6 h at 40 °C.

Among reagents used, tin tetrachloride pentahydrates were dissolved in HCl solution to provide the Sn^{4+} in the reaction environment.

$$SnCl_4*5H_20 + HCl \rightarrow Sn^{4+} + 5Cl^- + H^+ + 5H_2O$$

Thioacetamide was instead used to release the S^{2-} necessary to obtain stannic sulphide:

$$CH_3C(=S)NH_2 + H_2O \rightarrow CH_3C(=O)NH_2 + H_2S$$

The amide can also subsequently react with another molecule of water to form:

$$CH_3C(=O)NH_2+H_2O\rightarrow CH_3C(=O)O^-NH_4^+$$

Hydrogen disulphide, which is a weak acid, was in equilibrium in the water solution with the HS^- ion (which has a pKa = 6.9 in a water solution at 18 ° C) and with the S^{2-} ion.

$$H_2S + H_2O \leftrightarrow HS^- + H_3O^+ \qquad \text{Eq. 2.2}$$

$$HS^- + H_2O \leftrightarrow S^{2-} + H_3O^+ \qquad \text{Eq. 2.3}$$

These ions in solution can interact with the Sn^{4+} ion and lead to the formation of the product, the stannic sulphide, through the general reaction:

$$2H_2S + Sn^{4+} \rightarrow SnS_2 + 4H^+$$

To investigate role of acid and the possible used of a complexing agent in the synthesis reaction, three syntheses were carried out: without HCl (sample SnS_2(1)), with HCl as chemical to adjust reaction pH (pH = 3) (sample SnS_2(2)), and with the same quantity of HCl (pH = 3) and 3.3 mmol of o-phenylenediamine as complexing agent (sample SnS_2(3)).

2.3.2.2 Chemical, Structural and Morphological Characterization

To investigate the effect of o-phenylenediamine and the acid catalysis on the reaction method to synthesize SnS_2 nanopowders, it was decided to analyse the different products obtained (SnS_2(1), (2), (3)) with a preliminary SEM-EDX analysis. As can be seen in Figures 2.23-2.25, the use of o-phenylenediamine and the subsequent formation of the complex in water solution with Sn^{4+} ions did not lead to a real advantage for the synthesis route. In fact, the sample SnS_2(3) (Figure 2.23) obtained with the complex agents results in the formation of very large (≈ 10 μm) and impure grains that contain high levels of by-products identified with EDX chemical analysis, including compounds with chloride, nitrogen, oxygen and carbon.

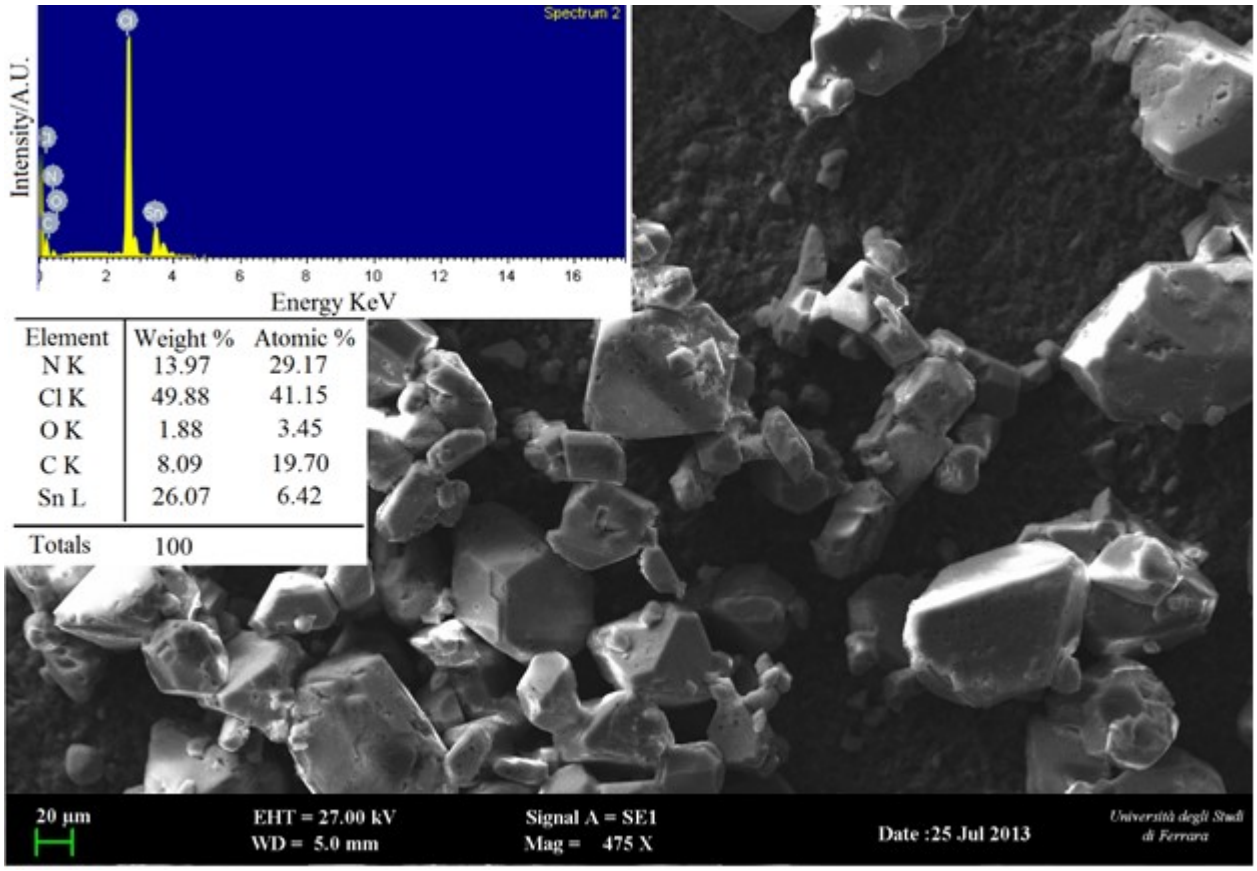

Figure 2.23: SEM-EDX analysis of SnS_2 powders sample $SnS_2(3)$ [adapted from A.2].

Conversely, the acid catalysis played a key role in the formation of pure and nanostructured SnS_2. Indeed, the product obtained in acidic solution ($SnS_2(2)$) achieved a better reaction yield (95%) than sample ST1 (83%). Moreover, the SEM-EDX characterization in Figure 2.24 showed that sample $SnS_2(2)$ exhibits a higher chemical purity and smaller nanostructured grains than $SnS_2(1)$, Figure 2.25 (average size of ≈ 300 nm and ≈1 µm, respectively). The role of acid in the synthesis could be attributed to the shift of the chemical equilibrium in the formation of S^{2-} ions. Indeed, thioacetamide reacts with the water solution to form hydrogen sulphide (Eq. 2.2 and 2.3) [2.99, 2.100]. The dissociation reaction of weak acid H_2S is one that provides at this moment ions S^{2-} to the solution.

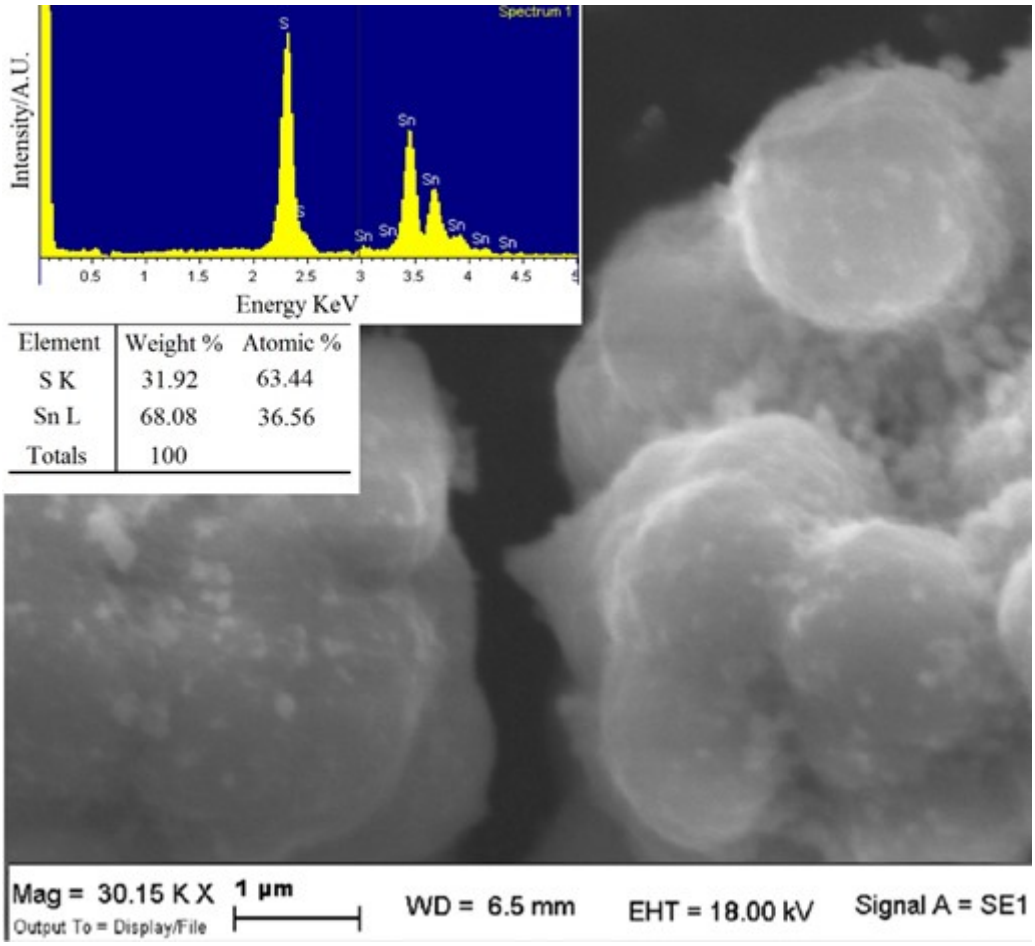

Figure 2.24: SEM-EDX analysis of SnS_2 powders sample SnS_2(2) [adapted from A.2].

The addition of hydrochloric acid shifted the equilibrium of the reaction towards the products according to the Le Chatelier principle. Consequently, the last reduces the H_2S dissociation and, hence, the S^{2-} available concentration. The slow release of sulphide ions thereby promoted the controlled growth of the SnS_2 grains.

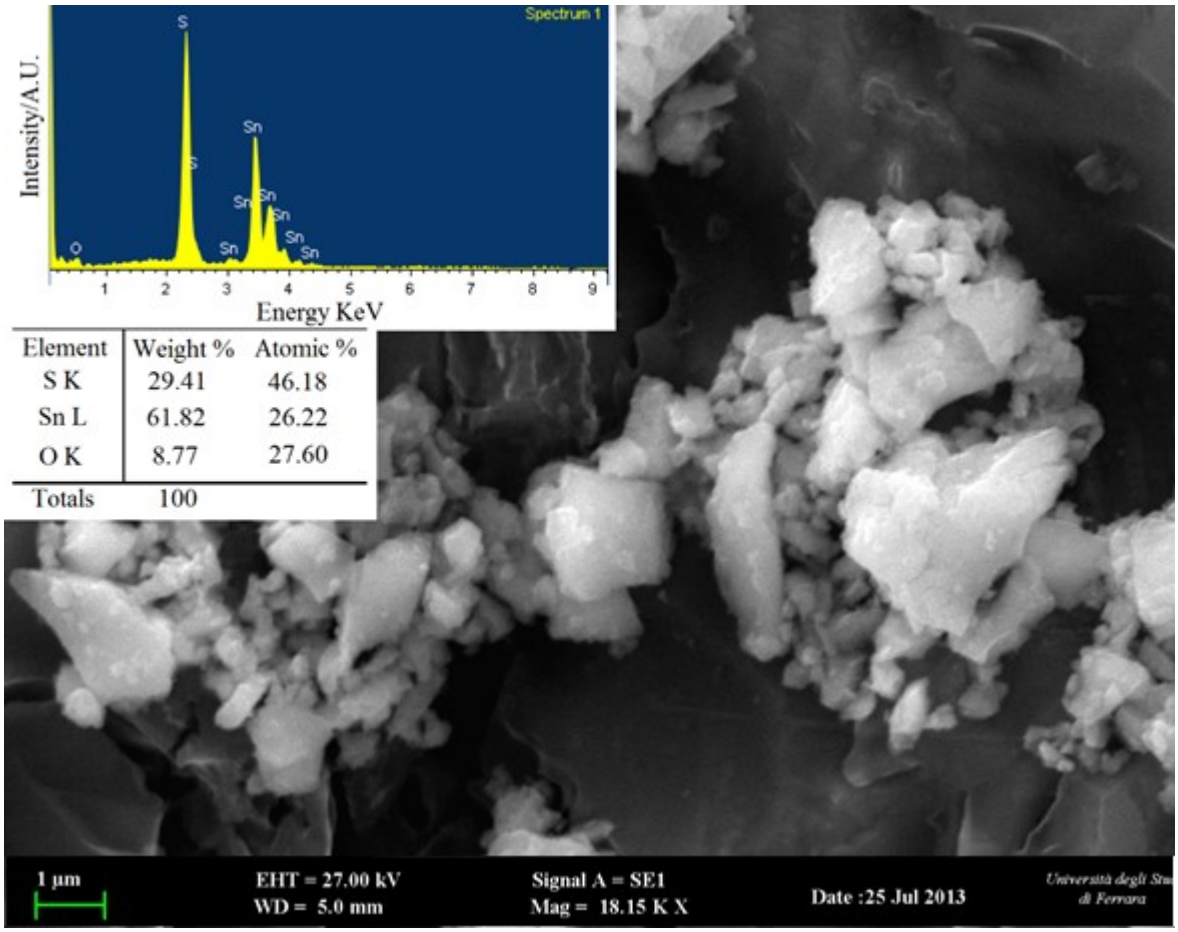

Figure 2.25: SEM-EDX analysis of SnS_2 powders sample $SnS_2(1)$ [adapted from A.2].

From the results obtained, it was decided to use the $SnS_2(2)$ powder as a sensing material and to perform the other characterizations only on this sample.

The results of XRD measurements of the synthesized nanopowder are shown in Fig. 2.26. From phase matching analysis, it turned out that the material is monophasic and the peaks correspond to Berndtite-2T (space group P-3m1), confirming that the synthesis method yielded very high purity SnS_2.

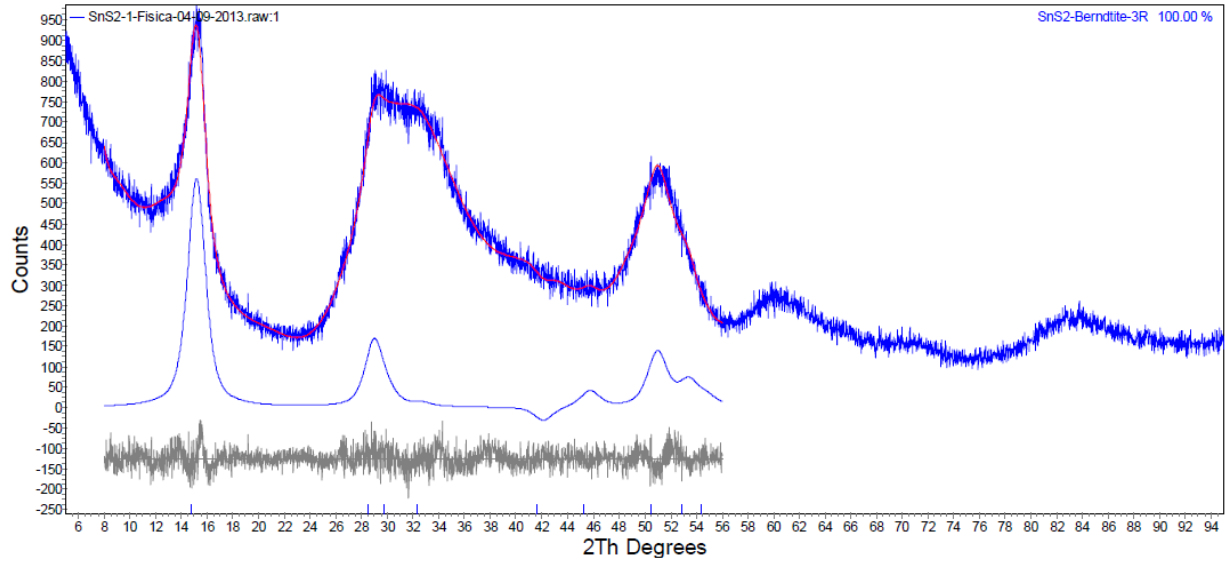

Figure 2.26: XRD pattern of the as-synthesized SnS_2 powder.

Crystallite size from Rietveld profile fitting resulted in (6.2 ± 0.4) nm.
TEM analysis, (see Figure 2.27), evidences that the clusters observed in SEM images are composed of structures with nanorod-like morphology. The average dimensions of nanorods are about 20-30 nm in length and 5 nm thick. Such quite small dimensions are due to the acidic character of the synthesis environment, which allows a slow release of sulphur ions. The inset in Fig. 3 shows the SAED diffraction pattern, which confirms the crystal phase determination of XRD measurements. The interplanar distances were found to be 3.20, 2.74 and 1.79 Å, knowing that electrons wavelength was 0.037 nm (at 100 kV), length of the camera (40 cm) and radius of the diffraction rings.

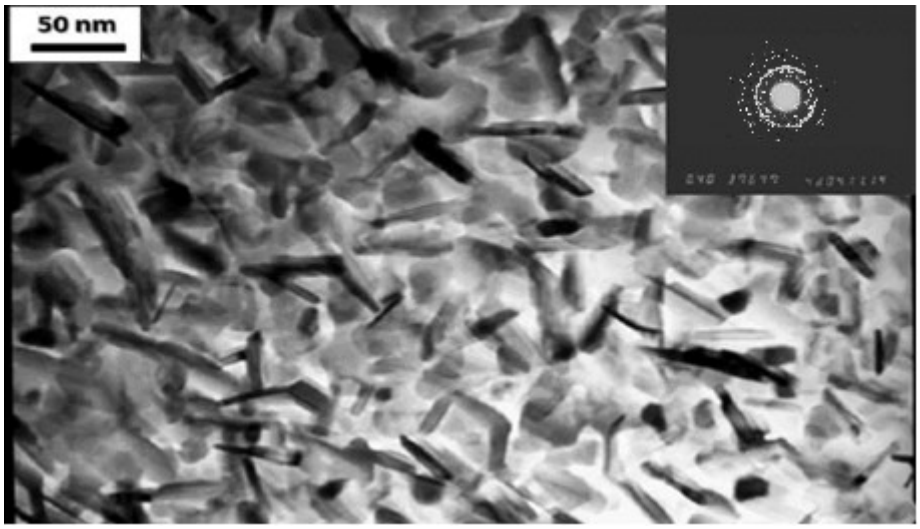

Figure 2.27: TEM image of the SnS_2 nanopowder [adapted from A.3].

Fig. 2.28 reports the TG/DTG/DTA analyses performed on the as-synthesized SnS_2 nanopowder. It can be observed an exothermic peak at about 120 °C, related to water loss until 135 °C. Another small weight loss starts from 135 °C until 300 °C, probably due to the evaporation of the last residuals of organic vehicles. At temperatures exceeding 450 °C, SnS_2 begins to transform into tin (II) oxide (SnS) and finally oxidizes to SnO_2, which corresponds to further weight loss [2.101].

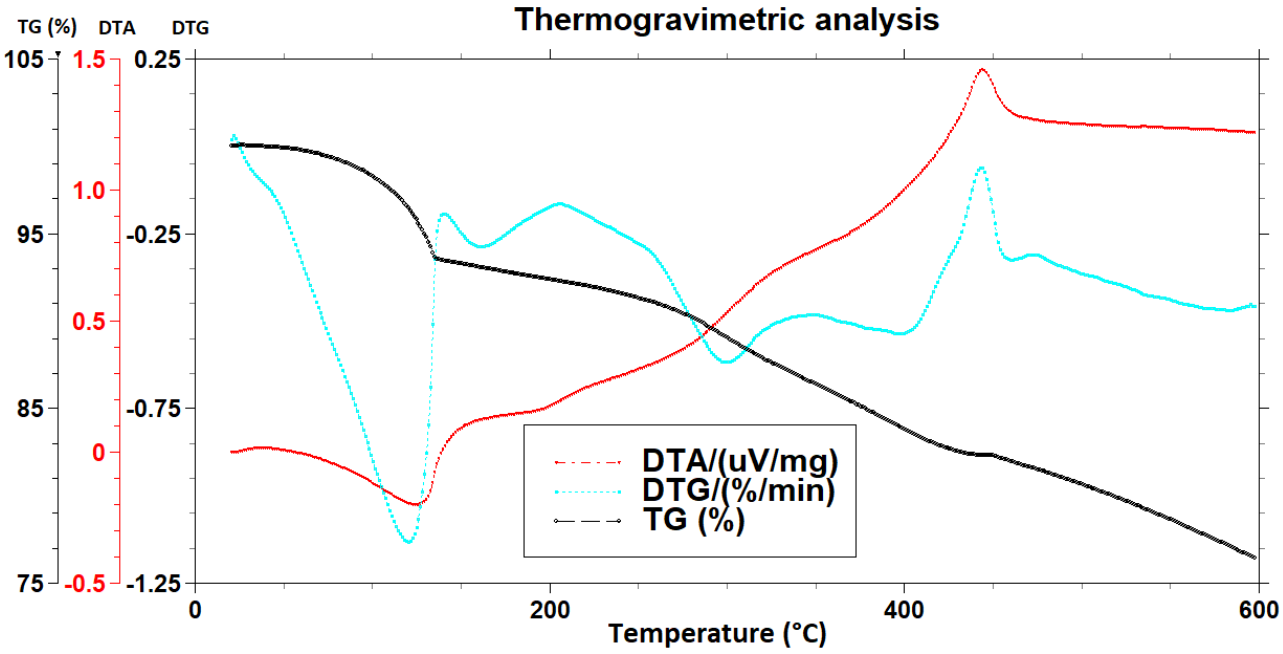

Figure 2.28: TG-DTG-DTA analysis of the as-synthesized SnS_2 powder [adapted from A.3].

2.3.2.3 Electrical Characterization

The electrical characterizations were carried out both in thermo- and photo-activation mode. Since the material did not show any chemoresistive properties in a photo-activation mode with all gases tested at the six different radiation wavelengths, we reported below only the electrical characterization in thermal-activation mode.
Since the thermogravimetric results, we decided to thermal stabilized the SnS_2 sensor, after screen printing deposition, at 300°C.
The responses of the sensors were investigated at operating temperatures between 150°C and 300°C. Much higher temperatures must be avoided with this material, since it oxidizes to SnO_2 [2.101], whereas temperatures lower than 250 °C proved to be not sufficient to activate surface chemistry. The tested gases represent different categories of molecules, to test the surface reactivity of this semiconductor with respect to gas molecules with important chemical differences. Gas concentrations have been chosen to take into account the corresponding Threshold Limit Values (TLV). Tests were performed with CO (1 ppm, 10 ppm), benzene (5 ppm), methane (2500 ppm), H2S (1 ppm, 10 ppm), NO (10 ppm), acetaldehyde (1 ppm, 10 ppm) and acetone (1 ppm, 10 ppm). The same measurements were performed in dry air carrier and wet air carrier, by means of a bubbling system. In wet air carrier, the relative humidity (RH%) was around 30%. After we verified that humidity levels larger than RH ~ 30% had no significant effects on the response of the samples, we opted to perform the wet measurements with this relatively low level of humidity, to have more leeway in the dry component of the carrier. Furthermore, sensing comparison with its metal-oxide counterpart (SnO_2) was carried out.

2.3.2.3.1 Thermo-Activation Mode

Results of the experiments for a SnS_2 sensor in dry condition are reported in Fig. 2.29. Firstly, at lower working temperature than 250°C not appreciable changes of the sensor conductance were obtained. Then, it can be noticed that at 250°C, the sensors were modestly responsive to the gases, R is in the range 0.05-0.5, and no selectivity was observed. Instead, at 300 °C, the responses were significantly improved. Indeed, at this operating temperature, the sensors strongly and selectively sensed the ketone and aldehyde, functional groups, with an increase in response by almost two orders of magnitude. The responses to the other all almost analytes under investigation were all negligible. However, hydrogen sulphide showed a modest response (less than 8% with respect to acetone).

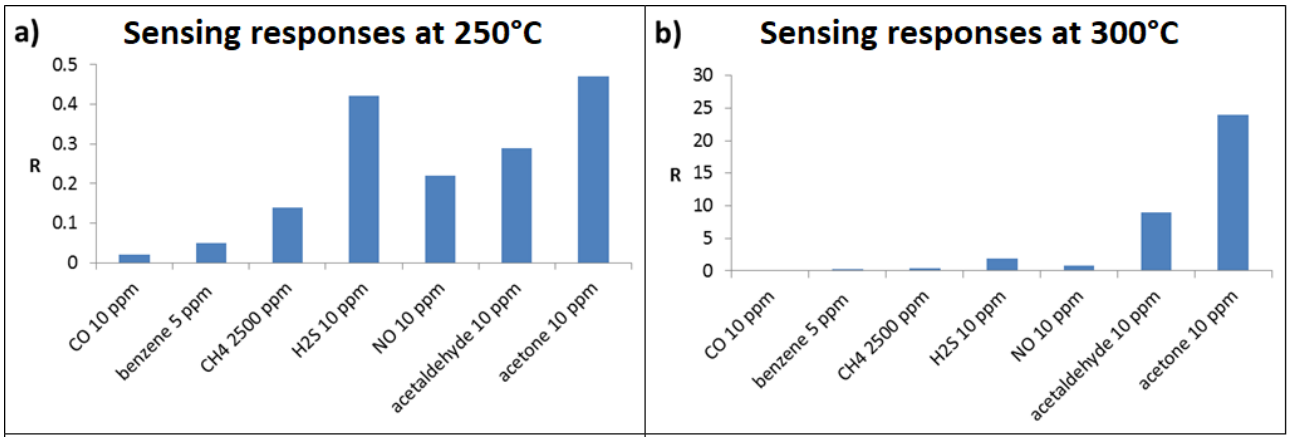

Figure 2.29: Histograms of sensing responses of SnS_2 sensors vs gases analysed at a) 250°C, b) 300°C) [adapted from A.2].

Further chemical and structural characterizations were carried out to confirm the material stability at the best working temperature of 300°C since thermogravimetric analysis highlighted that a transition of SnS_2 to SnO_2 begins at a temperature close to 350°C.
XRD analysis was carried out after six weeks of usage at 300 °C. The analysis, reported in Figure 2.30 (blue curve on which only a negligible trace of cassiterite can be detected), showed the absence of any significant phase and chemical changes, thus proving the substantial stability of SnS_2 at this working temperature [2.102]. For this reason, we safely considered 300 °C as operating temperature for SnS_2.

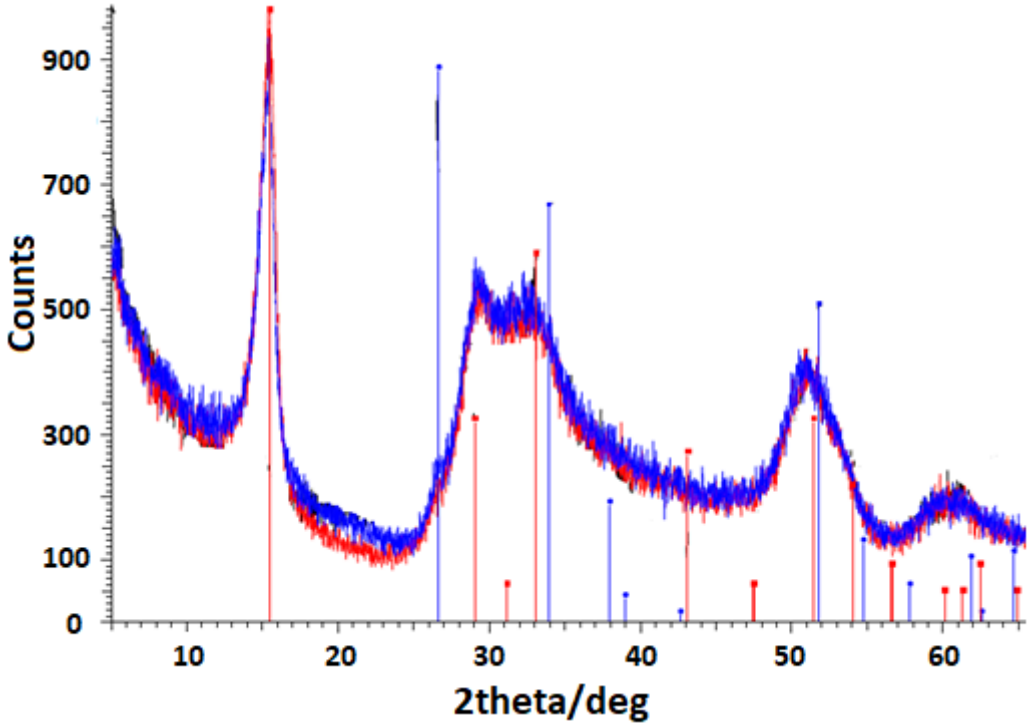

Figure 2.30: XRD analysis for the as synthesized (red line) and the thermally treated (blue line) SnS_2 nanopowder [adapted from A.3].

This stability was also confirmed, in Figure 2.31, by the XPS results. In fact, the line shape and peak position of Sn 3d and S 2p core levels (typical of SnS_2) did not change for the samples before and after the heat treatment at 300 °C for five days. On the contrary, these peaks changed with the treatment at 400 °C for five days. The shift of tin peaks is due to the transition of SnS_2 to SnO_2 occurs at this temperature. At the same time, the peak of sulphur almost disappeared confirming the ongoing chemical transitions to SnO_2.

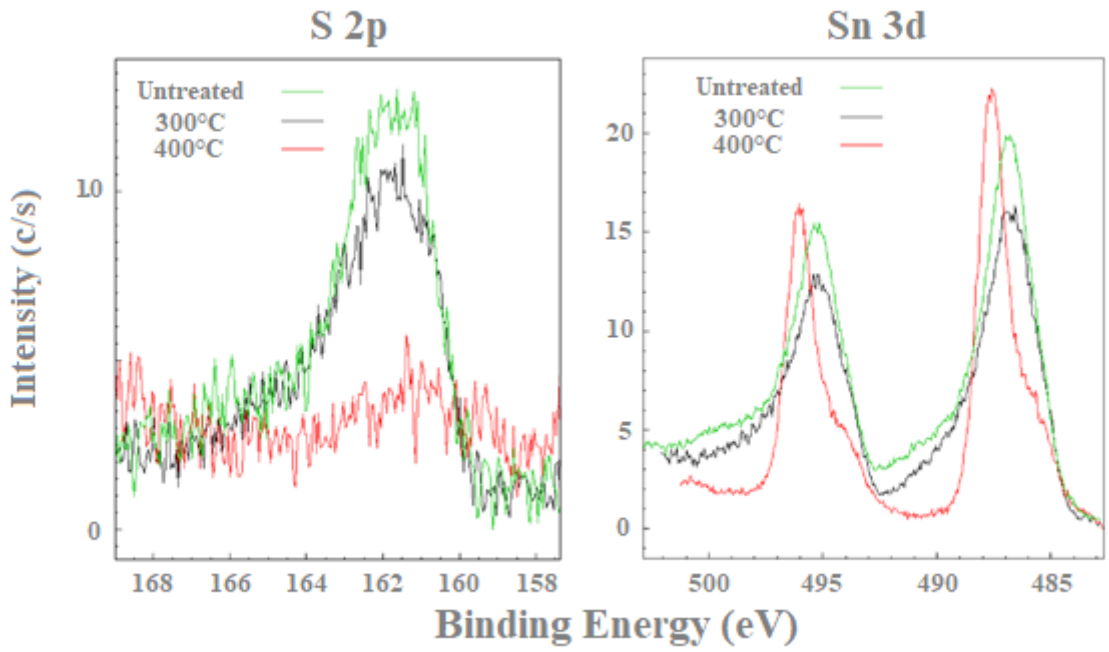

Figure 2.31: XPS characterizations of as-synthesized and thermal treated SnS_2 nanopowder. Position changes in 3d peaks for tin (left) and in 2p for sulphur (right) [adapted from A.2].

The performance of the sensing material was tested vs humidity. Fig. 2.32 a) and 2.32 b) show the dynamic responses of a SnS_2 thick-film sensor at 300 °C exposed to 10 ppm of acetone, 10 ppm of acetaldehyde and 10 ppm of H_2S in dry and wet conditions, respectively. The temperature inside the text chamber was 28°C. In Fig. 2.32 c) and 2.32 d), the dynamic responses of the same sample in presence of 1 ppm gas concentration are also shown.

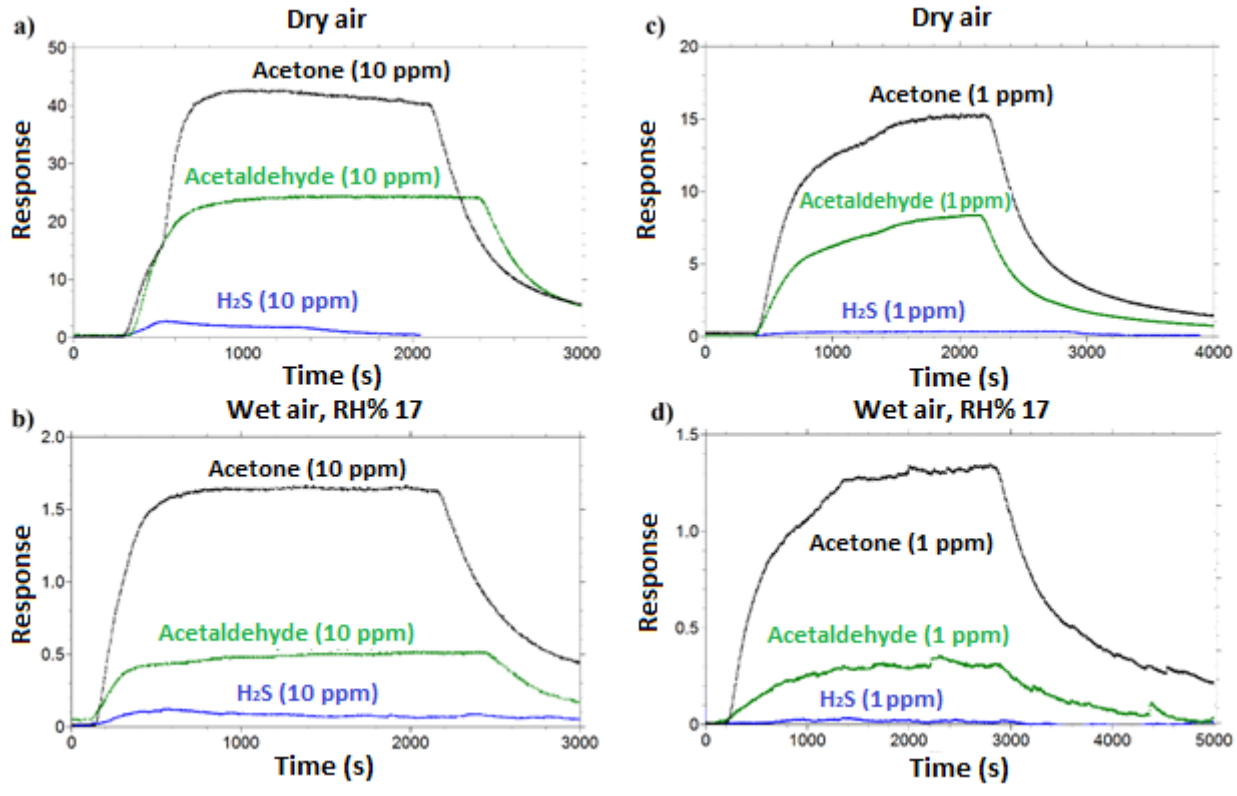

Figure 2.32: Dynamic responses of SnS_2 sensors vs acetone, acetaldehyde and hydrogen sulphide both in the dry and wet air, at 2 different concentration [adapted from A.3].

From these measurements, it is clearly observed that under wet conditions the response time is of the order of some minutes, whereas the recovery time is from two to three times longer, as under dry conditions, a feature similar to the behaviour of traditional metal-oxide films [2.103-2.105]. Therefore, it is possible to conclude that humidity reduces the response by more than one order of magnitude. It is worth noting that the reduction factor was almost independent of the gas, therefore the presence of water vapour diminishes the sensitivity but does not alter the selectivity obtained in dry air. Because of these measurements, it derives that the low detection limit for acetone falls in the sub-ppm range.
We also studied and compared the sensor sensitivity in the dry and wet air, to deeply investigate the humidity influence on the sensing response of the SnS_2 sensor.

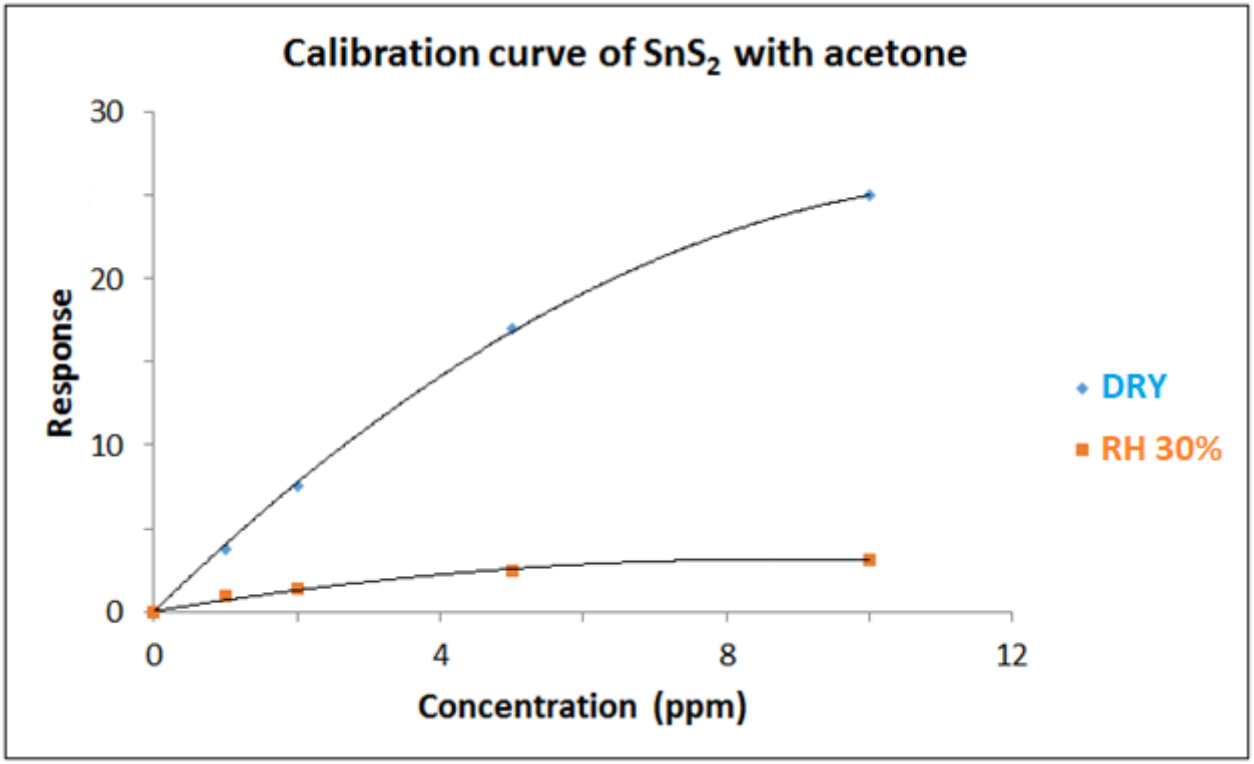

Figure 2.33: Sensitivity of CdS sensors both in the dry and wet air [adapted from A.2].

As can be seen in the last Figure, the trend demonstrated in calibration curves is in line with the trend of the common metal-oxide gas sensors [2.106, 2.107]. The humidity effect, to decrease the sensitivity of the SnS_2 sensor, could be due to a competitive interaction between the analyte and OH^- group on the sensing films [2.108-2.110].
A possible sensing mechanism for the acetone detection by SnS_2 could be proposed taking into consideration the possible oxidation of the molecule on the semiconductor surface, involving adsorbed oxygen ions and catalysed by the semiconductor itself:

$$CH_3COCH_3(g) + 8O^-(ads) \rightarrow 3CO_2(g) + 3H_2O(g) + 8e^- \quad \text{Eq. 2.4}$$

The function of the sulphur, in comparison to a metal, is to operate a different catalytic activity, resulting in different reaction steps and, as proved by the experiments, an improved selectivity.

In presence of water vapour, the reaction (Eq. 2.4) enters the competition with the reaction of acetone with weakly physisorbed hydroxyl groups (OH^-):

$$CH_3COCH_3(g) + OH^-(ads) \rightarrow CH_3COO^- + CH_4(g)$$

In this case, since there is no surface/gas charge transfer, the total conductance change is reduced, thus explaining the much weaker responses under humidity conditions. Given the high working temperature and the catalytic action of the sensitive material, the reaction may proceed to a further oxidation of the acetate ion formed.

We also carried out to interference tests to investigate the possible cross-sensitivity between acetone and other gases tested. In particular, we choose acetaldehyde since among the tested gases it yielded a considerable response. Furthermore, it is a possible interferer in many potential applications to reveal acetone. In this experiment, performed in wet condition, we measured the response to a mixture of 1 ppm of both acetone and acetaldehyde. The result is reported in 2.34.

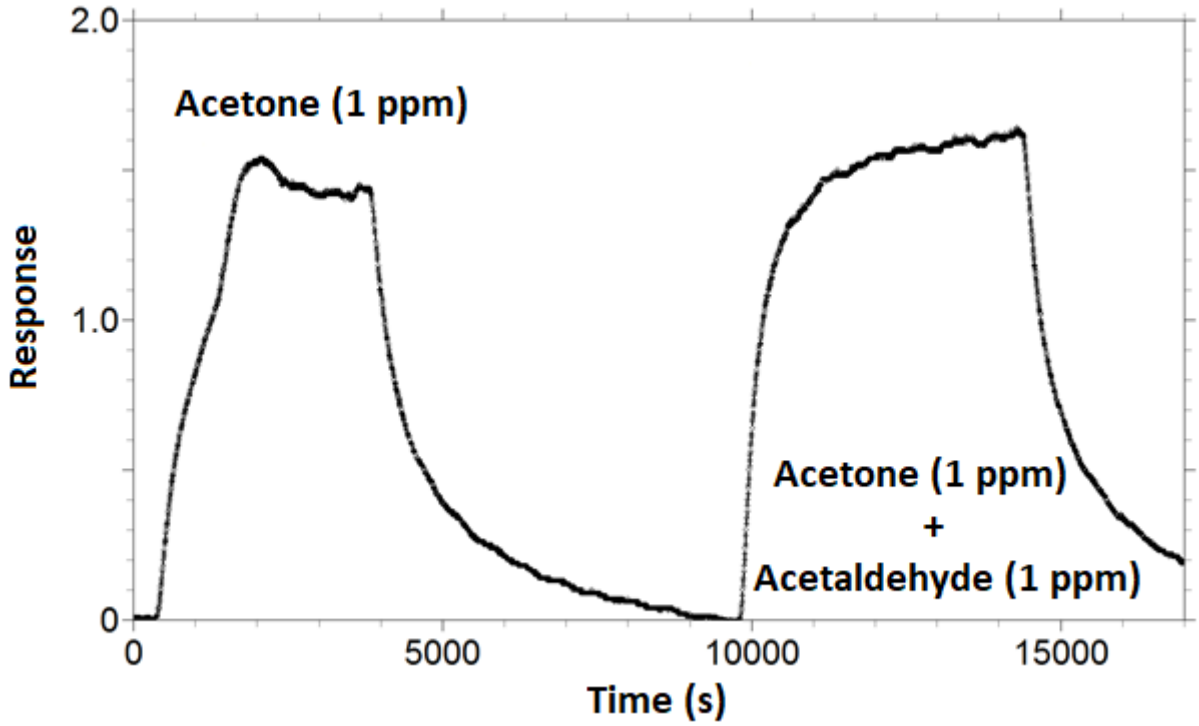

Figure 2.34: Cross selectivity measurements of SnS_2 sensors vs acetone and acetaldehyde [adapted from A.3].

As it can be seen, the presence of acetaldehyde affects lowly the response to acetone. This is a further evidence of the very good selectivity of this sensing material to acetone, as well as of the importance of the non-linearity of the responses to different gases in conductometric gas sensors. To verify the acetone response reproducibility over the time, SnS_2 sensors were tested by exposing them to 10 ppm of acetone at different times, in a period lasting six weeks. The result is reported in Figure 2.35 and they show quite interesting features of this material since both a modest response variation and the absence of a definite trend are the main characteristics.

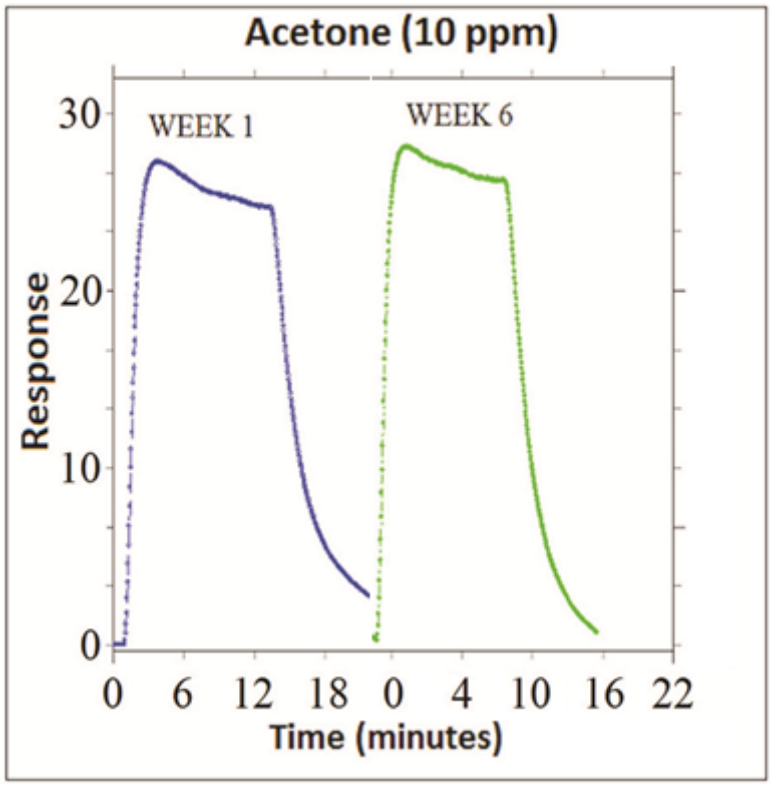

Figure 2.35: Characterization of the sensor stability in 6 weeks of measurements [adapted from A.2].

It is remarkable to notice that the in-diffusion of oxygen in SnO_2 annihilates oxygen vacancies, changing the doping level, whereas in SnS_2 it replaces the sulphur atoms and annihilates sulphur vacancies, transforming the material in tin dioxide. Tin dioxide long-time drift may be associated to this phenomenon [2.92, 2.93], which could be a problem because in SnO_2 the gas sensing achieves good performance at much higher working temperatures (> 400 °C), where oxygen in-out diffusion is highly efficient. On the contrary, SnS_2 shows very interesting performance at temperatures well below the critical temperature, probably circumventing in-out diffusion related instabilities.
Moreover, a comparison of the chemoresistive characteristics of SnS_2 with its metal-oxide counterpart SnO_2 was undertaken. Indeed, it is well known that, among the metal oxides widely studied, SnO_2 is deeply employed for gas sensing devices, thanks to its great chemical and physical properties [2.106, 2.11]. To obtain comparable measurements, the grains SnO_2 nanostructures must have the same size and shape to those of SnS_2 grains, respectively. The thickness of each film obtained through screen printing was ~ 30 μm.
Firstly, an electrical characterization vs. 2500 ppm of methane for SnS_2 and SnO_2 was carried out. The measurements, reported in Figure 2.36, highlight a similar trend for SnS_2 and SnO_2 sensors, even if SnS_2 worked at temperature 100°C lower than for SnO_2. In addition, the recovery time of SnS_2 was faster than for SnO_2. Meanwhile, SnO_2 sensor, thermo-activated at the same temperature of SnS_2, showed a lower sensing response and slower kinetics in the sensing response compared to the SnS_2 sensor.

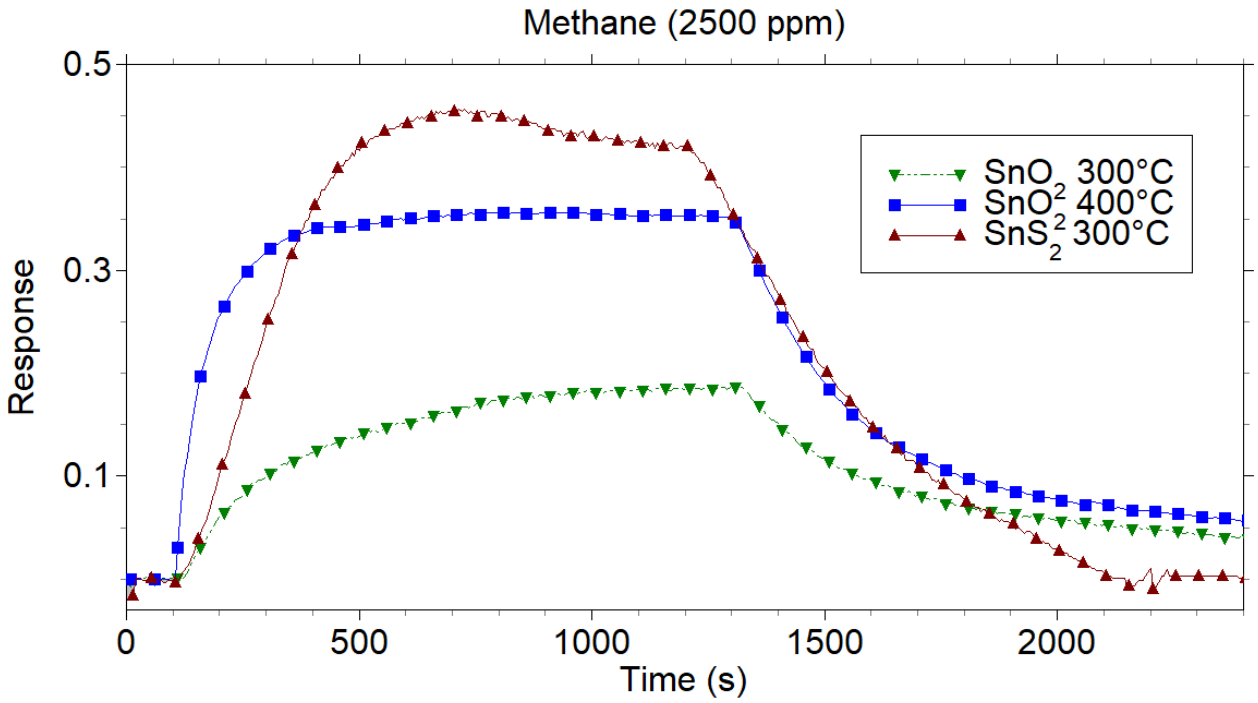

Figure 2.36: Comparison of sensing responses vs 2500 ppm of methane of SnO_2 and SnS_2 gas sensors [adapted from A.2].

Fig. 2.37 shows another interesting comparison about the conductance values measured for SnS_2 and SnO_2 films, exposed to dry airflow over a relatively long acquisition time. All the sensors tested were used for the first time. The main characteristics that can be observed are the drift of the signals for all the films, which represents the initial stabilization trend of these sensors over the first 10 days of use. However, the sensors based on SnS_2 tested at the best working temperature, highlighted a lower drift of the signal than for SnO_2 at its best working temperature (400°C). This superior signal stability of SnS_2 cannot be ascribed to the different operational temperatures. In fact, by repeating the measurements at a lower temperature for SnO_2 (300 °C), the drift of the signal was always larger than for SnS_2 at 300°C. This difference of signal drifts could be explained, again, through the in-out diffusion rate of oxygen vacancies that changes the doping level [2.112]. In the case of SnS_2, instead, the cause of *n*-type doping is still under investigation, however, until oxygen is not present in the lattice (temperatures lower than 670 K), the influence of oxygen partial pressure on the signal is expected to be weaker.

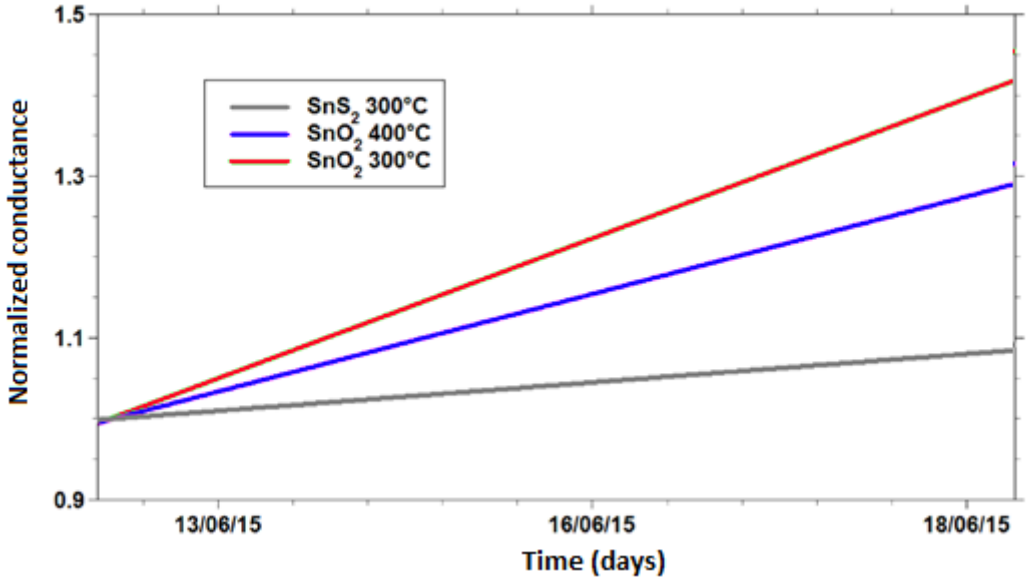

Figure 2.37: Measurements of SnS_2 and SnO_2 baseline drift in the first 5 days of sensing characterization in the dry air [adapted from A.2].

At least, the barrier height of SnS_2 and SnO_2 films was measured. With this aim, Arrhenius plots were obtained as reported in [2.127]. As it can be seen in the Figure 2.38 b), a very weak dependence on temperature was observed for SnS_2 with respect to SnO_2. The widely acknowledged behaviour of SnO_2, in the range of temperatures chosen [2.107], showed a net change of slope at temperatures (about 450 K) proper of the transition of O^{2-} chemisorbed species to O^- (which is expected to be more reactive in electron extraction), was not present in SnS_2 barrier curve. This feature explained the change in the slope above 450 K. However, the effect should not be present in SnS_2 and its intergrain barrier remains constant. From the comparison of the Arrhenius plots of SnO_2 and SnS_2, reported in Figure 2.38 a), it arose that the conductance G of the latter was always lower than for the former. However, the functional dependence of G on temperature T was more similar at higher temperatures than at the lower. In the temperature region of transition from SnS_2 to SnO_2 (about 670 K), a bump in conductance for SnS_2 appeared, ending in a similar slope to that of SnO_2 above 800 K. This was a confirmation of the transition of SnS_2 to SnO_2, in according to TG analysis.

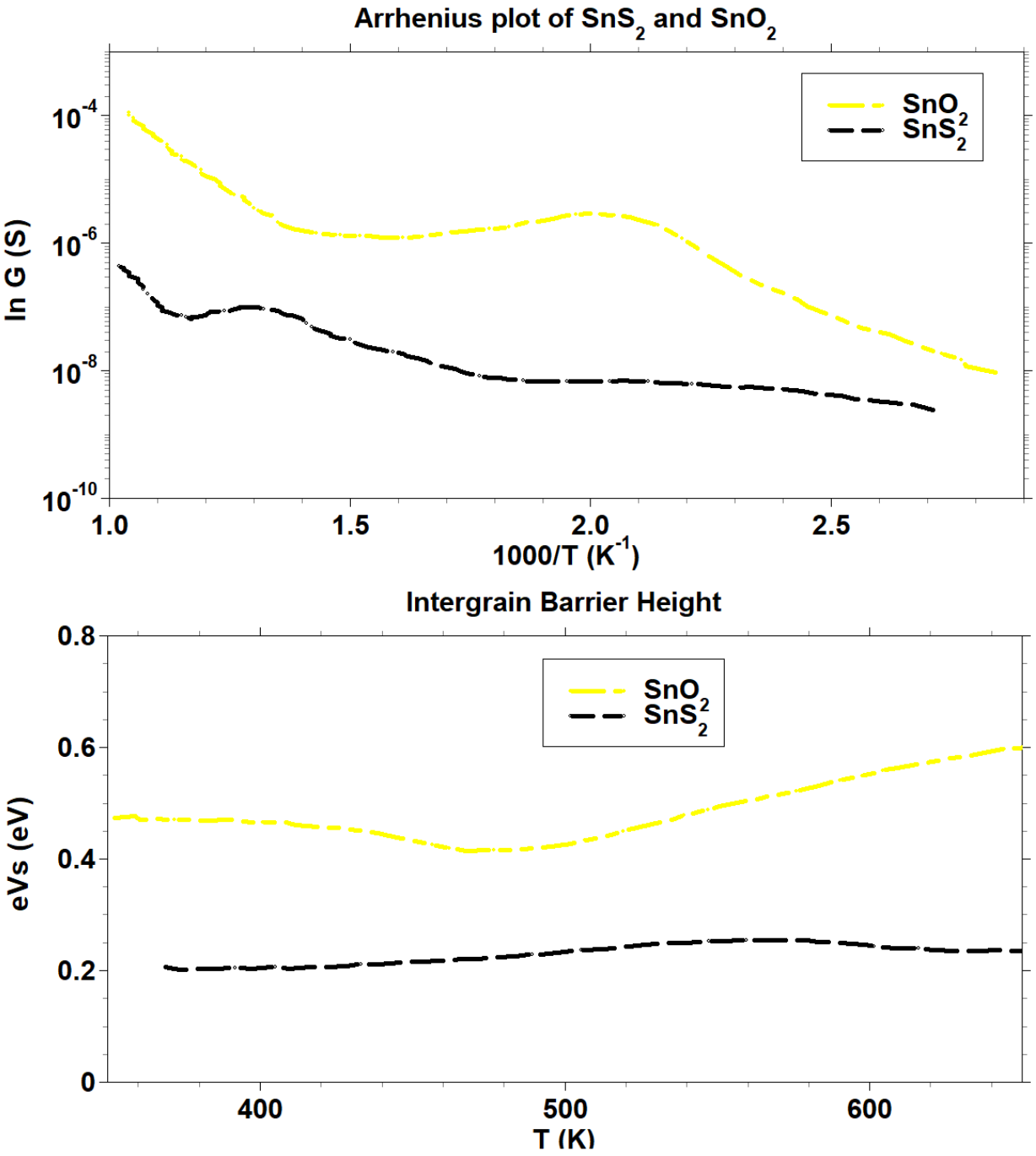

Figure 2.38: a) Arrhenius plot and *b)* intergrain barrier height of SnO_2 and SnS_2 sensors [adapted from A.2].

2.3.3 Cadmium Sulfide

Parts of this paragraphs has been published in [A.2, A.4 and A.5]. Cadmium sulfide (CdS) is a wide gap semiconductor (Eg = 2.40 eV), widely used in many fields of science and technology due to its interesting chemical and physical properties. In particular, this material shows piezoelectricity, photoconductivity, chemoresistivity and electroluminescence. These properties allowed the development of CdS-based devices that can be employed as solar cells, photoresistors, piezoelectric transducers and gas sensors [2.113-2.116]. A recent interesting example of a CdS-based gas sensor is reported in [2.117], where it is shown that a luminescent reaction between alcohol molecules and CdS surface can occur, and it can be employed as a basic mechanism for alcohols-selective luminescent

gas sensors. Regards studies of CdS as a chemoresistive gas sensor, recently Fu *et al.* [2.118] synthesized this material with leaf-like morphology through the hydrothermal method and studied its sensing properties exposed to four gases (isopropanol, methanol, acetone and ether) in thermo-activation mode. Other works on the use of CdS as gas sensors are present in the literature, but in these studies, the transduction of the signal depends on catoluminescence [2.119], Field Electron Transistor [2.120] and piezoelectric effects [2.121], and not on chemoresistive mechanisms. The lack of deepening study about CdS as chemoresistive gas sensor opens up to an investigation about its chemoresistive properties both in thermo- and photo-activation mode.

2.3.3.1 Synthesis

All chemicals employed in this work were from Sigma Aldrich. Cadmium Sulfide nanoparticles were obtained by precipitation method at room temperature and atmospheric pressure, in aqueous solution. In this synthesis, 10 mmol of cadmium acetate dihydrate and 20 mmol of o-phenylenediamine were dissolved in 100 mL of water and stirred for 2 h. Afterwards, 20 mmol of thioacetamide was added to the solution. The mixture obtained was stirred for 6 h. Hence, a precipitate of yellow-orange nanoparticles was formed. The product was isolated by vacuum filtration and washed several times with methanol and water. At last, CdS nanoparticles were dried for 4 h at 40 °C. The synthesis was performed in three different modes: without o-phenylenediamine (sample CdS(1)), with 10 mmol (sample CdS(2)), and with 20 mmol of o-phenylenediamine as complexing agent (sample CdS(3)).

2.3.3.2 Chemical, Structural and Morphological Characterization

In order to investigate the role of o-phenylenediamine and the advantages that could lead to the formation of nanostructured cadmium sulfide, it was decided to analyze the different products obtained (CdS(1), CdS(2) and CdS(3)) with SEM-EDX analysis. The results highlighted that the reaction methods, in which o-phenylenediamine was used, allows obtaining a product with a higher chemical purity and reaction yield (Figures 2.39, 2.40, 2.41). In fact, EDX analysis on sample CdS(1) (Figure 2.39) showed a high quantity of carbon and oxygen, in addition with an average size of the crystal grains (≈400 nm) greater than samples CdS(2) and CdS(3) (Figures 2.40 and 2.41, with an average size of ≈200 nm and ≈100 nm, respectively).

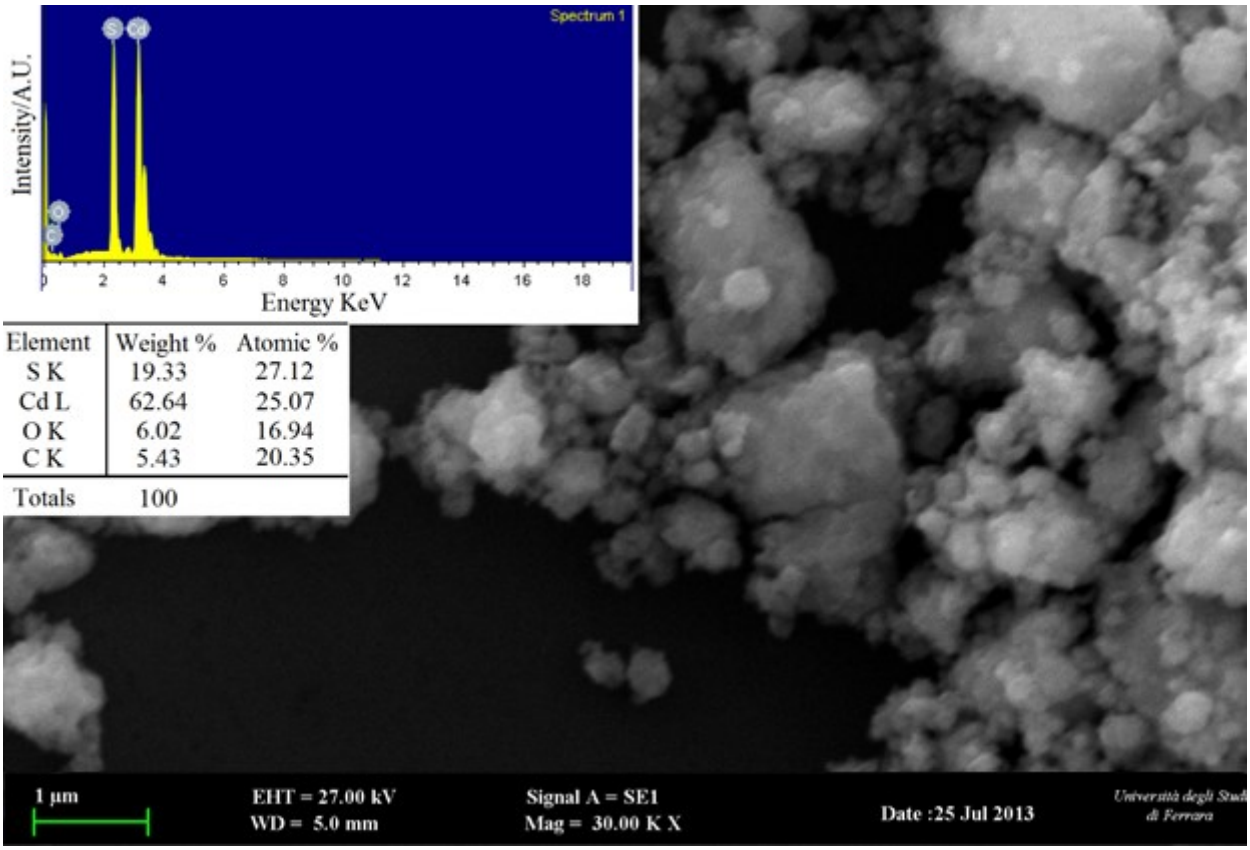

Figure 2.39: SEM-EDX analysis of the sample CdS(1) [adapted from A.4].

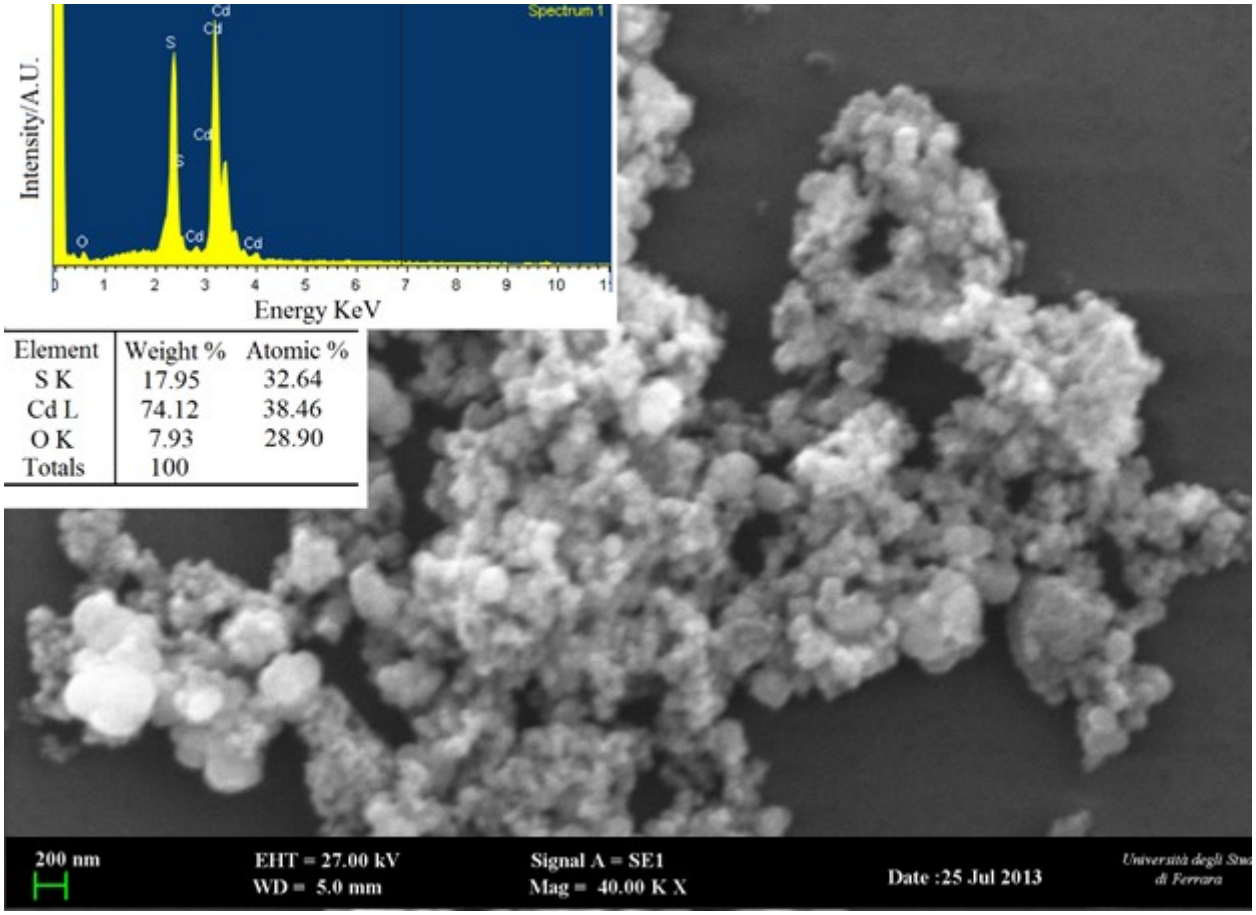

Figure 2.40: SEM-EDX analysis of the sample CdS(2) [adapted from A.4].

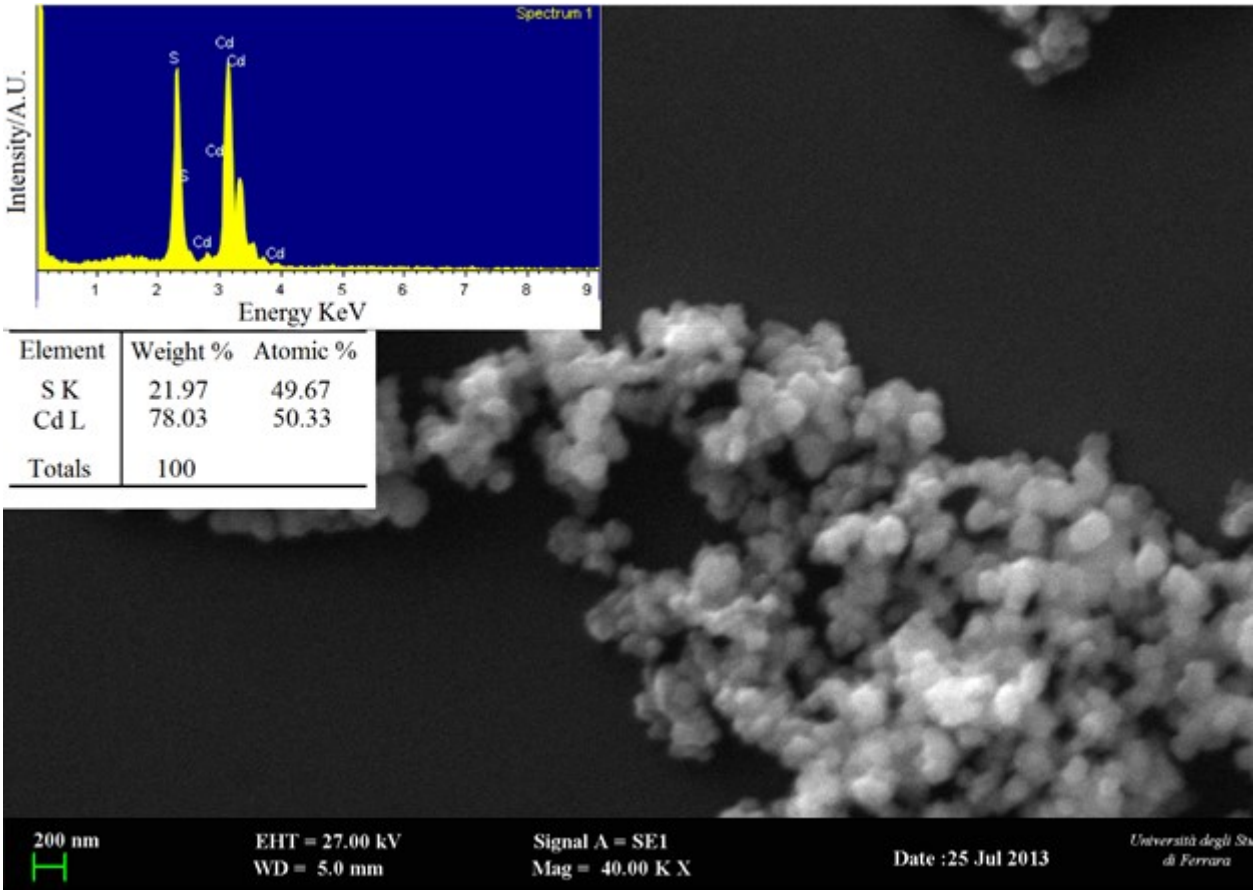

Figure 2.41: SEM-EDX analysis of the sample CdS(3) [adapted from A.4].

These results highlighted the important role of o-phenylenediamine as a complex agent. In fact, the chemical reaction was expected to occur as a two-stage process:

$$Cd^{2+} + 2\text{o-phenylenediamine} \rightarrow [Cd(\text{o-phenylenediamine})_2]^{2+}$$

In this step, cadmium acetate was dissolved in water to give the Cd^{2+} ions. O-phenylenediamine reacts at this time with Cd^{2+} ions, resulting in the formation of a metal-ligand complex. The thioacetamide was ready decomposed and acted as the sulfur source generating S^{2-} that allowed the formation of CdS nanoparticles

$$[Cd(\text{o-phenylenediamine})_2]^{2+} + S^{2-} \rightarrow CdS + 2\text{o-phenylenediamine}$$

The SEM-EDX results showed the importance of intermediate metal-ligand complex formation to nanocrystal arrested precipitation growth kinetics, particle stabilization, and, ultimately, their optical properties [2.122, 1.123]. At the same time, in Figures 2.39, 2.40 and 2.41, the difference between samples CdS(2) and CdS(3) can be noted. The latter exhibits a greater chemical purity, ideal stoichiometry and lower grain dimensions than the former. In addition, the reaction yield for sample CdS(3) (98, 5%) was better than sample CdS(2), with which 80% of the product was obtained compared to the theoretical value achievable. These data support the idea that specific cadmium complex formation modulates the crystal growth. The comparison between samples CdS(2) and CdS(3) has also provided further evidence to support the previous literature [2.124], in which it is suggested that o-phenylenediamine acts as a bidentate ligand with Cd^{2+} ions leading to the formation of a tetrahedral or square planar coordination complex. Therefore, in sample CdS(2) o-phenylenediamine behaves as a limiting reagent with respect to cadmium ions, and it failed to

coordinate completely Cd^{2+} ions [2.125]. From the obtained results, we decided to use the powder CdS(3) as a sensing material and to perform further characterizations on this sample only.

TEM analysis, reported in Figure 2.42, shows that the clusters previously observed with SEM analysis are composed of structures with nanobead-like morphology. The average size of clusters was about 100 nm, while the dimension of nanobeads is roughly a few tens of nanometers. SAED diffraction pattern is shown as an inset in Figure 2.42. The interplanar distances were 3.2, 2.1 and 1.7 Å, which confirmed XRD analysis results

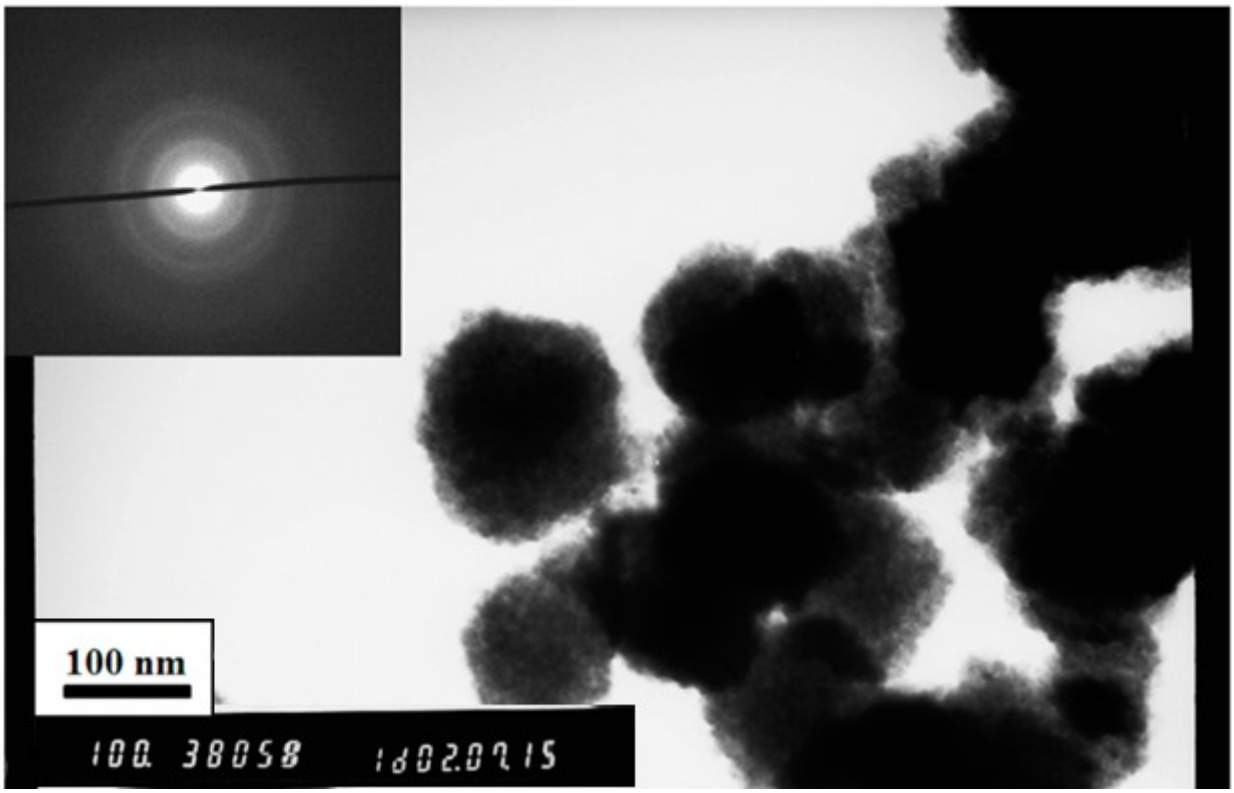

Figure 2.42: The TEM image of the CdS nanopowder. The inset shows the SAED diffraction pattern of the CdS sample [adapted from A.2].

The results of XRD measurements of the synthesized nanopowder are shown in Figure 2.43. From the analysis of the phase composition, as described in the section 2.1.3, it turns out that the material is monophasic and the peaks correspond to the cubic polymorph of cadmium sulfide, β-CdS/hawleyite (space group F − 43 m), confirming that the synthesis method yielded very high purity CdS.

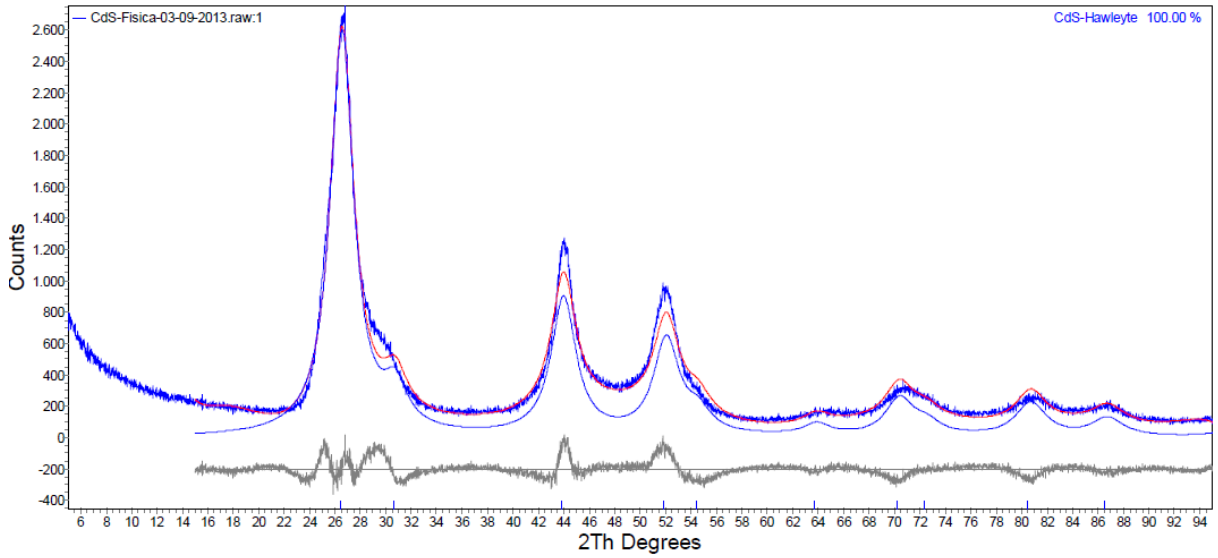

Figure 2.43: XRD pattern of the as-synthesized CdS powder.

The determined crystallite size resulted in 2.59 ± 0.14 nm.

In the Figure 2.44, it is reported the TG/DTG/DTA analysis performed on the screen-printing paste, in which we can observe an exothermic peak at about 200°C, due to the loss of the organic vehicle. The TG curve shows that no significant changes occur to the material up to about 500°C, this indicating stoichiometric and morphological stability. Above a temperature of about 550°C, a weight gain of the sample can be noticed.

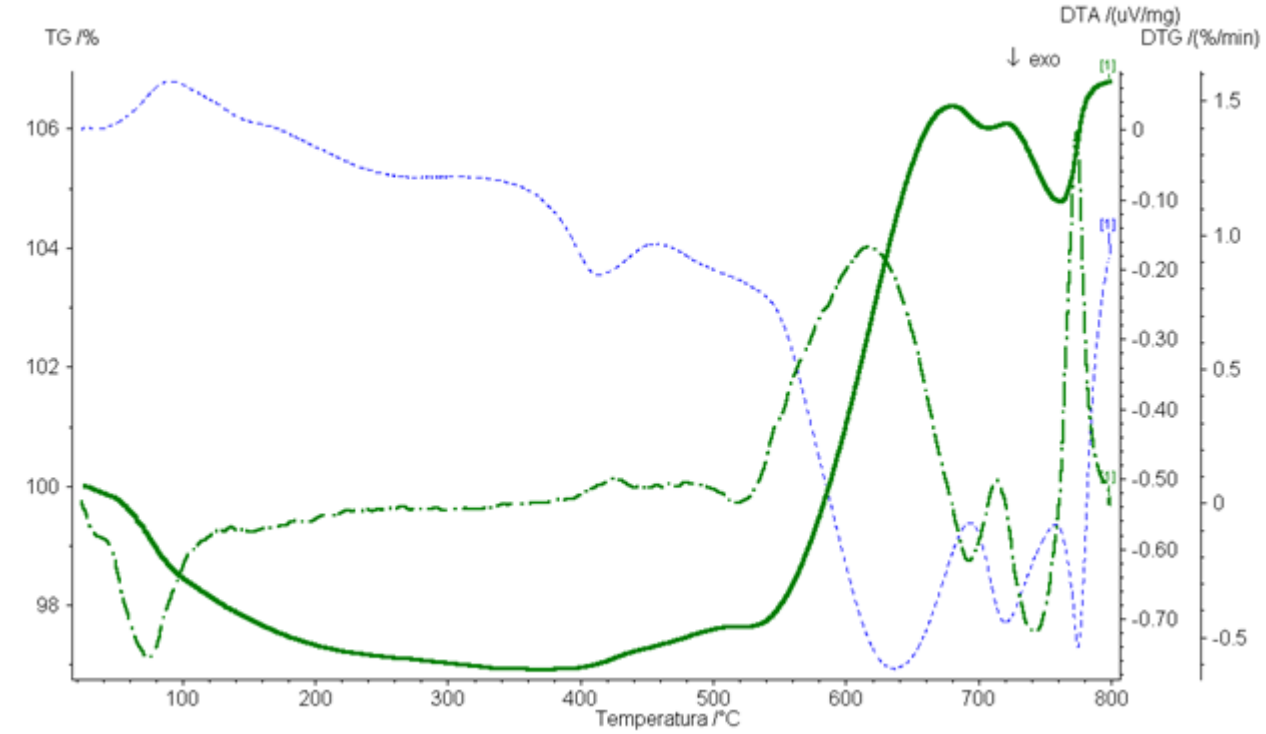

Figure 2.44: TG/DTG/DTA curves measured on the screen-printing paste obtained from the synthesized CdS powder.

To figure out this phenomenon, an XRD analysis was performed after the thermogravimetric measurement. The corresponding XRD pattern is shown in Figure 2.45, where the presence of cadmium oxide sulphate ($Cd_3O_2SO_4$), cadmium sulphate ($CdSO_4$) and cadmium oxide (CdO)

crystalline phases can be observed. The formation of $Cd_3O_2SO_4$ and $CdSO_4$, in particular, explains the weight gain above 550°C.

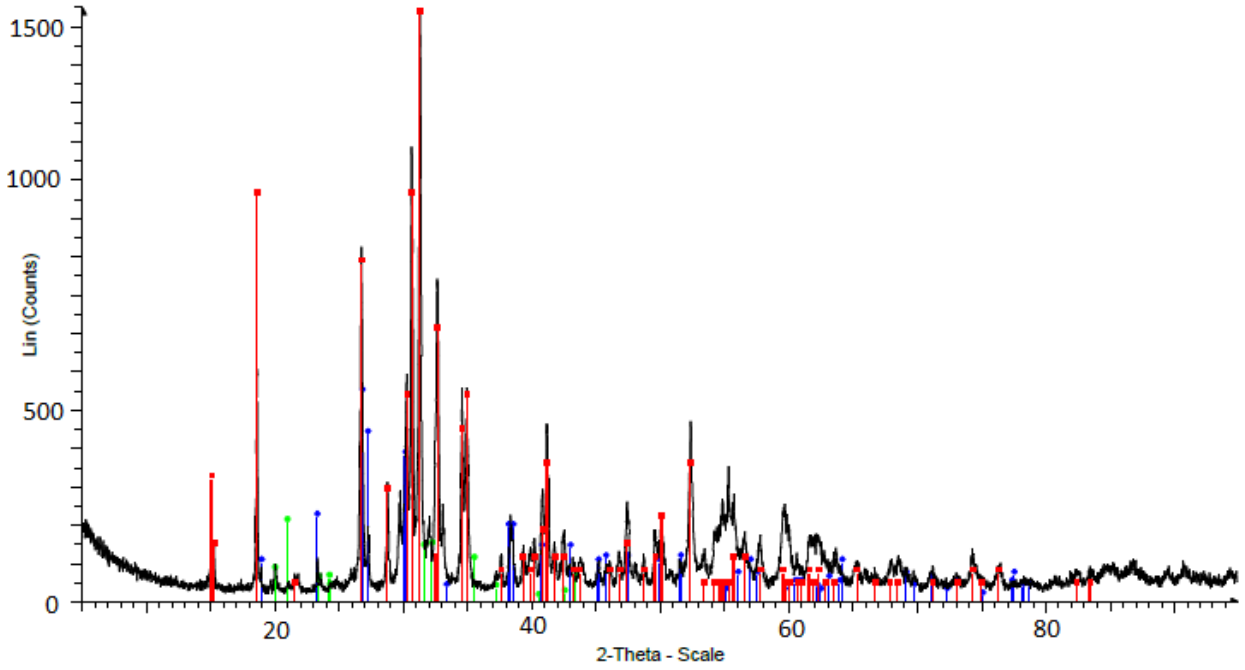

Figure 2.45: XRD pattern of the CdS powder after the thermal analysis. PDF cards of the identified crystalline phases marked as follows: (i) red marks, monoclinic $CdSO_4$ (s.g. Pn21m); (ii) blue marks, orthorhombic $CdSO_4$ (s.g. Cmcm); (iii) green marks, $Cd_3O_2SO_4$ (s.g. Cm2a); (iv) light blue marks, cubic CdO (s.g. Fm − 3m) [adapted from A.4].

2.3.3.3 Electrical Characterization

The powder characterized was then mixed with an organic vehicle (as described in section 2.2.3.1) and deposited onto substrates by means of screen printing technique. The firing of sensors obtained was done at a temperature of 350°C, which was chosen based on thermogravimetric results.

Chemoresistive gas-sensing properties of nanostructured CdS was investigated both in thermo- and in photo-activation mode. With this aim, a series of experiments were carried out, focusing on gases belonging from different chemical classes. The aim was to obtain an overview of a possible selective behaviour of CdS gas sensor.

2.3.3.3.1 Thermo-Activation Mode

In thermo-activation mode, we have chosen to analyze methanol (5 ppm), ethanol (5 ppm) and n-butanol (5 ppm) as alcohols, acetone (10 ppm) as ketone, acetaldehyde (10 ppm) as aldehyde, sulphur dioxide (10 ppm) as anhydride, molecular hydrogen (20 ppm) as low-reactive compound, nitrogen dioxide (1 ppm) as oxidizing agent and methane (2500 ppm) as hydrocarbon. The gas concentrations were chosen by considering their Threshold Limit Values (TLV) [2.126]. The sensors were tested at the following working temperatures: 250, 300 and 350°C. We decided to not exceed 350°C since data obtained from TG analysis.

The sensors showed a very good selectivity to alcohols in comparison to all other gases, at all working temperatures. The dynamic responses of a few representative CdS sensors are shown in Figure 2.46, where two consecutive measurements of ethanol and n-butanol are reported for all working

temperatures. Response to ethanol required only a few minutes to reach a steady state, with a huge response enhancement with respect to methanol (more than one order of magnitude, Figure 2.46 a)). With n-butanol, the behaviour was very similar, but with an even higher response (see Figure 2.46 b)).

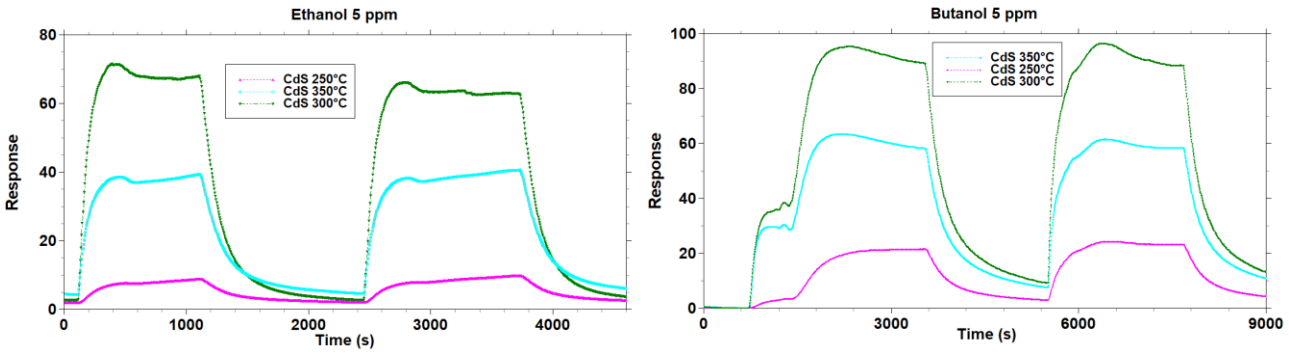

Figure 2.46: Dynamic responses of CdS sensors vs. *a)* 5 ppm of ethanol and *b)* 5 ppm of n-butanol in thermos-activation mode [adapted from A.4].

At 250°C, we observed reducing behaviour in the case of alcohols and oxidizing behaviour in the case of all other gases. At 300°C and 350°C, all gases, except NO_2 at 350°C, resulted in a reducing behaviour. The variation of the response, after the first exposure, can be evaluated within a range of 10%, this being a good indicator of the stability of the response. The response and recovery time of devices can be easily evaluated from the measurements showed in Figure 2.46. The kinetics of the surface reactions is very slow (order of hours) only for the first exposure to methanol at 300°C, whereas the response time for the other compounds, at all temperatures, can be evaluated between 10 and 20 min. The recovery time ranges between two and three times longer than the corresponding response time, which is a well-known property of chemoresistive films. The responses to the specified gas concentrations are shown in the histogram of the Figure 2.47.

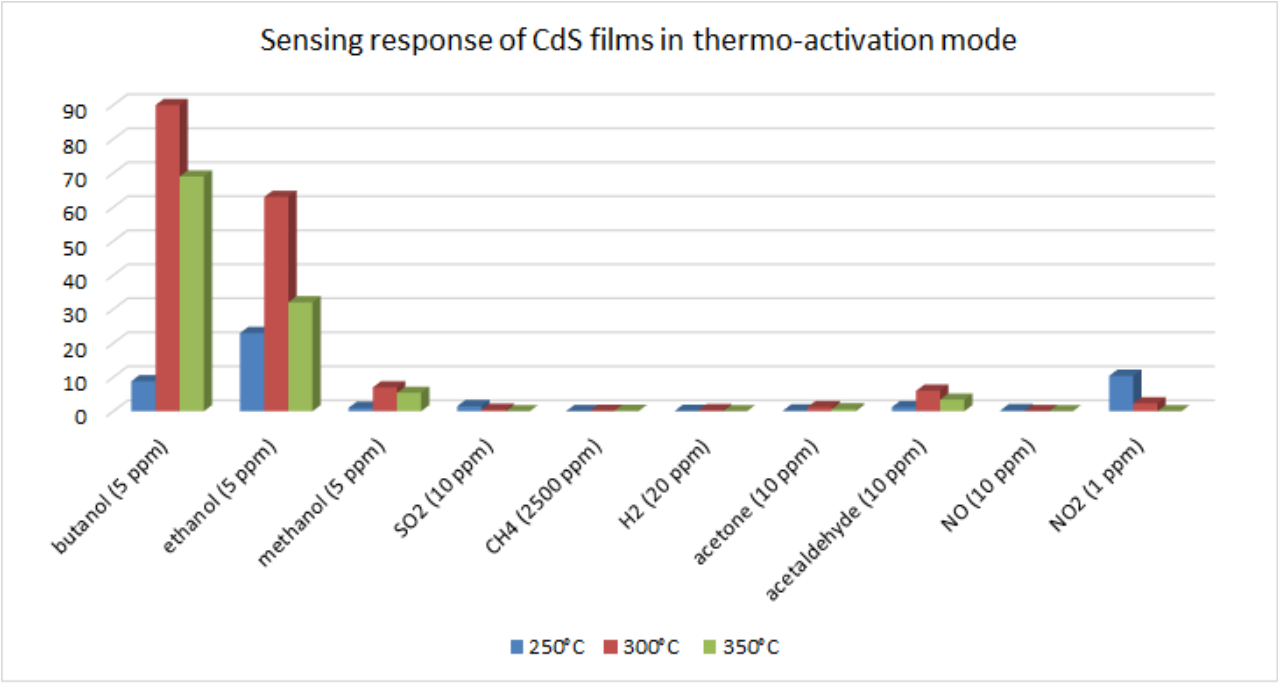

Figure 2.47: Summary histogram of CdS sensor responses in thermo-activation mode [adapted from A.4].

As it can be seen from this Figure, in the case of alcohols there was an increment of sensing responses with the alcoholic carbon chain size increase, for all working temperatures analysed. At 250°C, the

response to alcohols increased from 1 for methanol to 10 for ethanol and 20 for n-butanol, while for all other gases we recorded very low responses (absolute value about lower than 1, except for NO_2, which yielded |R| ~ 10). At 300°C, we observed a reducing behaviour for all gases, with R ~ 7 for methanol, 60 for ethanol and 90 for n-butanol. The other categories of gases produced negligible responses (lower than 1), except for acetaldehyde, for which R ~ 6 was found at this working temperature (nevertheless, one order of magnitude lower than ethanol and n-butanol). At 350°C sensors showed similar general trend obtained at 300°C, but with lower responses. Therefore, the best sensors performance was recorded at 300°C, the temperature at which CdS proved its ability to selectively detect alcohols, probably also in complex gaseous mixtures.
Then, CdS films sensitivity was studied under dry air conditions, by using ethanol with CdS as sample gas. As it can be seen in the Figure 2.48, the trend demonstrated in the calibration curve is in line with the trend of the common metal-oxide gas sensors [2.106, 2.107]. We also analysed the sensor sensitivity in wet air, to investigate the humidity influence on the CdS sensing responses. Like what obtained with SnS_2, CdS sensors highlighted a decrease in the gas sensors' response by more than one order of magnitude in presence of humidity.

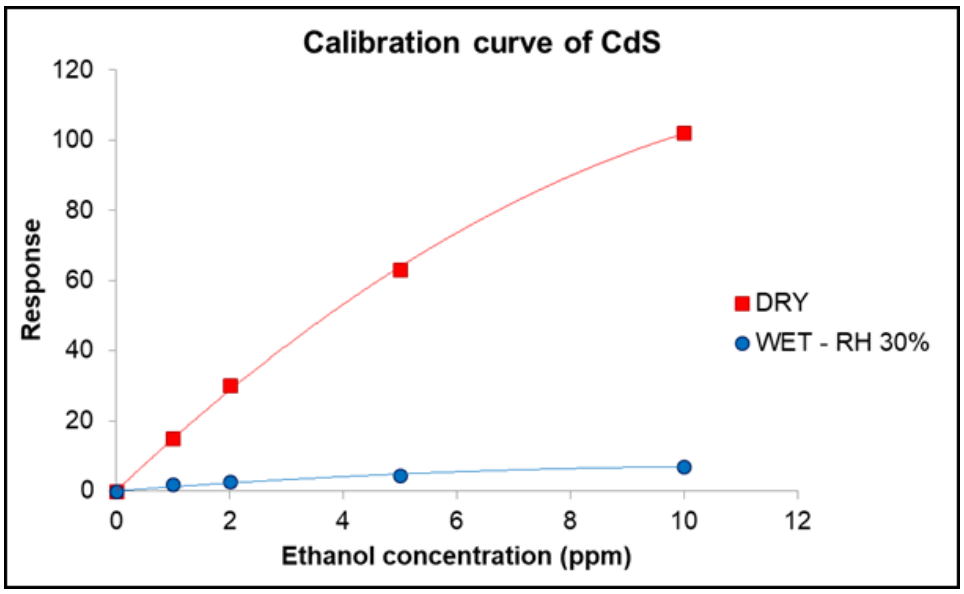

Figure 2.48: Sensitivity of the CdS gas sensor vs 5 ppm of ethanol both in the dry and wet air [adapted from A.2].

It is important to consider that the reduction factor was almost independent of the gas tested, and then the presence of water vapour diminishes the sensitivity but does not alter the selectivity obtained in dry air. Therefore, the humidity influence had no effect on the selective chemoresistive property of the CdS sensor. The effect of humidity, likewise of the SnS_2 case, is probably due to a competitive interaction between the analyte and OH^- group on the sensing films. It was verified that humidity levels greater than RH% = 20%–30% had no significant effects on the conductance of the sample.

To prove the sensor stability, the response of CdS thick films vs. 5 ppm of ethanol was analysed over time, in dry air. The result, reported in Figure 2.49, highlights a reproducible sensing behaviour during a period of six weeks. The main features observed are a very modest response variation and the absence of a definite trend.

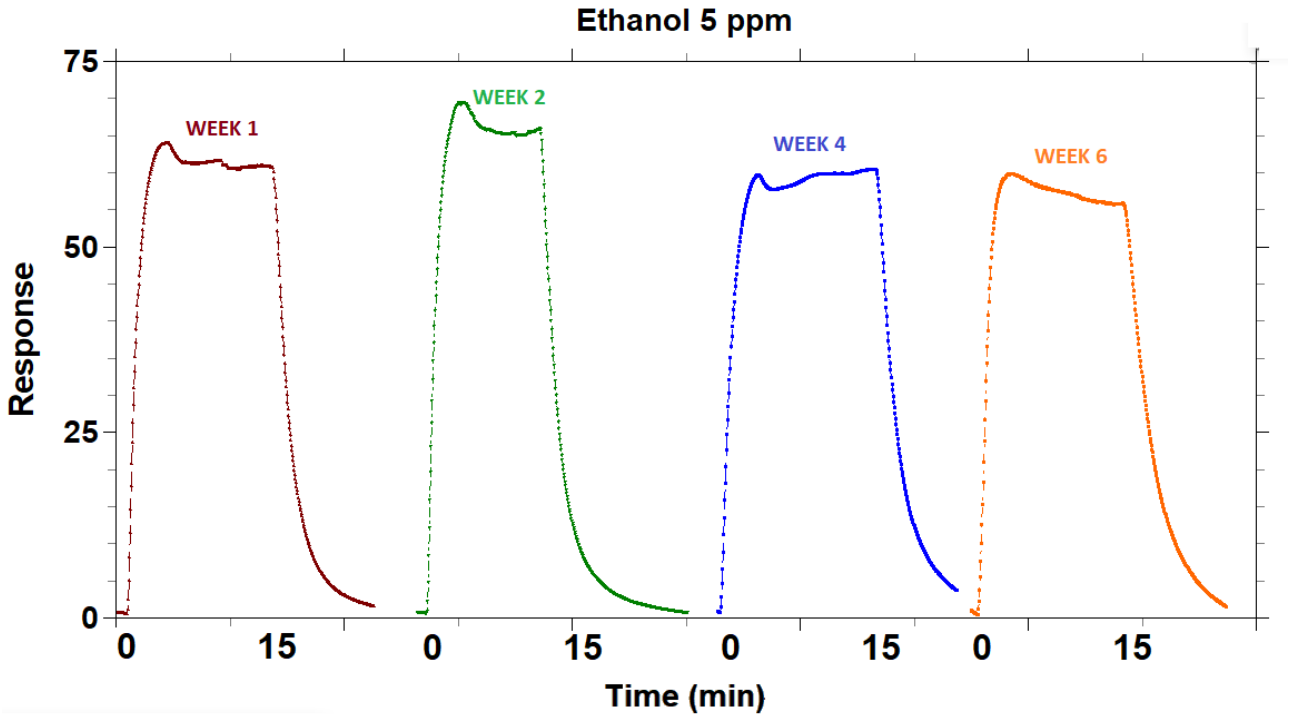

Figure 2.49: Repeatability of the CdS sensor response vs 5 ppm of ethanol over the time [adapted from A.2].

Considering the high selectivity showed by CdS sensors, a possible interpretation of the sensing mechanism is proposed. Indeed, the dehydrogenation of the alcohol by the adsorbed oxygen ions on CdS surface could explain this result. In the case of methanol, as the molecule approaches the CdS oxygen-covered surface, it can lose one H from the CH_3 group and that of the OH-group, due to the attraction with O^- ads, resulting in the formation of a water molecule, which desorbs releasing one electron into the material (Figure 2.50).

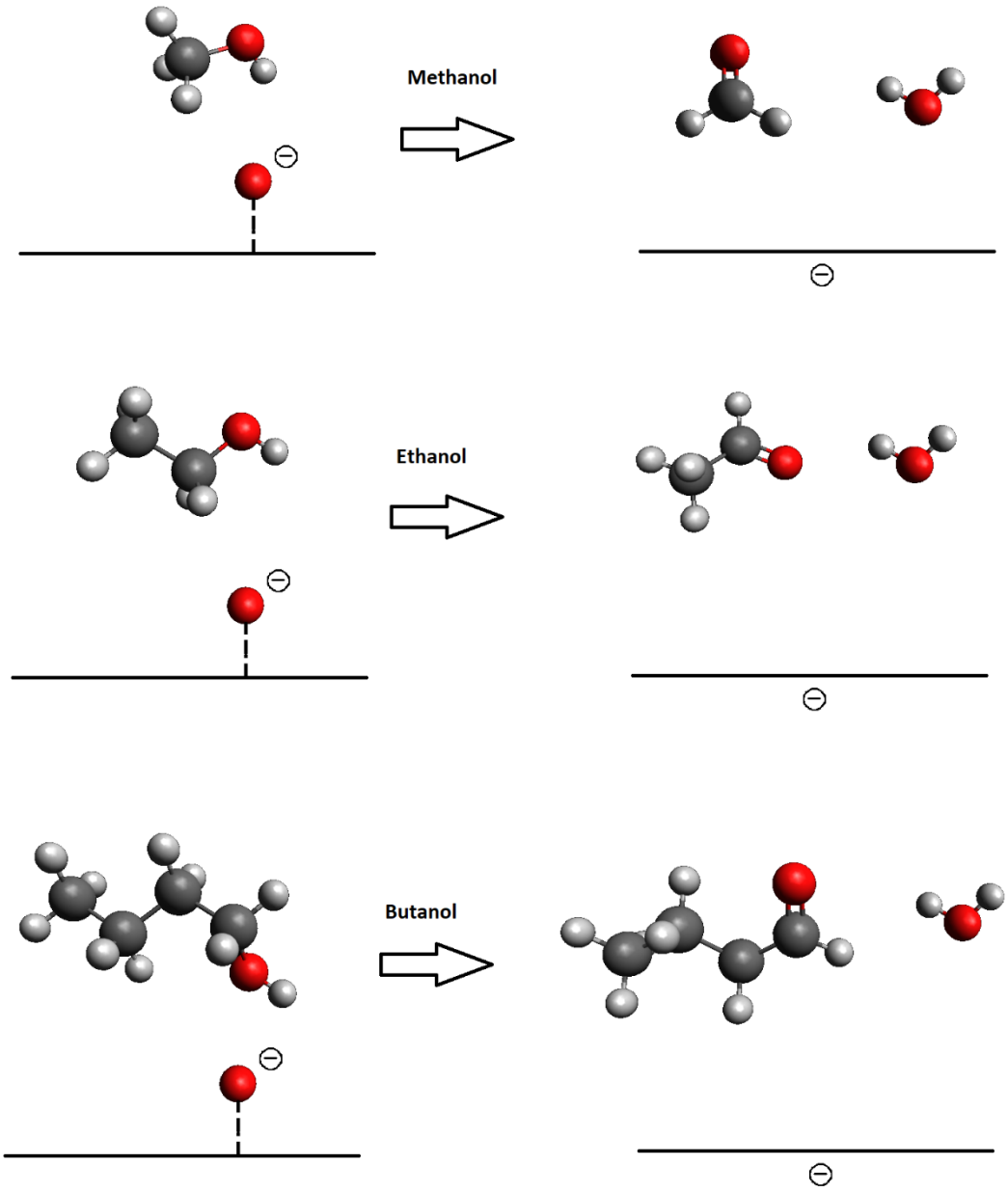

Figure 2.50: Schematic representation of the proposed sensing mechanisms between CdS sensors and alcoholic chains [adapted from A.4].

Thus, the dehydrogenated methanol turns into formaldehyde formation as follows:

$$CH_3OH + O^- \rightarrow CH_2O + H_2O + e^-$$

The reaction could also keep on, with further oxidations, until the formation of CO_2 and release of other electrons in the CdS semiconductor. A similar process could occur in the case of ethanol, which would turn into acetaldehyde, and in the case of n-butanol, which would turn into butyraldehyde, as shown in the following reactions:

$$CH_3CH_2OH + O^- \rightarrow CH_3COH + H_2O + e^-$$

$$CH_3CH_2CH_2CH_2OH + O^- \rightarrow CH_3CH_2CH_2COH + H_2O + e^-$$

The huge increase in response between methanol (CH_3OH) and ethanol (CH_3CH_2OH) is probably due to the different electronegativity of the CH_3 group as substitute compared to H, as it can be seen in Figure 2.50. Indeed, the higher electronegativity of CH_3 than H could attract the shared negative charge more strongly, making the hydrogens of the CH_2 group more acid than those of CH_3.Therefore, they have a higher probability to react, and this is reflected in a higher sensor's response. The situation is similar in the case of n-butanol, where the hydrogens of the CH_2 group closest to the OH group are even more acid (reaction sketched in Figure 2.50). Since the difference in electronegativity between H and CH_3 is much higher than that between CH_3 and $CH_3CH_2CH_2$, the reactivity increases of ethanol compared to methanol is higher than between butanol and ethanol. This agrees with the sensor behaviour observed. In addition to this phenomenon, it is reasonable to think that the efficiency of the reactions increases with the length of the alcoholic chain also because of the stronger attraction between the molecule and the surface, operated by the increasing number of hydrogen bonds that can be established between the surface and the hydrogens of the chain which are not involved in the reaction. Concerning the other gases, we generally observed low responses, which could be an indication of reactions with very low efficiency. An exception is represented by NO_2 at 250°C, which yields a response, in absolute value, of the same order of ethanol, but it strongly decreases with increasing temperature, reaching a very low value at the ideal alcohols detection temperature (300°C). At this point, a comparison of chemoresistive properties between CdS and its metal-oxide counterpart (CdO) was carried out, to individuate possible differences. With this aim, CdO nanoparticles with similar size and shape to CdS ones were synthesized and used as sensing material.
Firstly, an electrical characterization of metal-oxide and metal-sulfide films vs. gases in dry condition was carried out. Figure 2.51 shows the results obtained with 5 ppm of ethanol for CdS and CdO. Several measures were carried out to identify the best working temperature of all films vs. tested gases. The comparison between CdO and CdS (Figure 2.51), carried out at the relative best working temperature (300 °C) for both sensing materials, highlights the negligible response of CdO with respect to CdS.

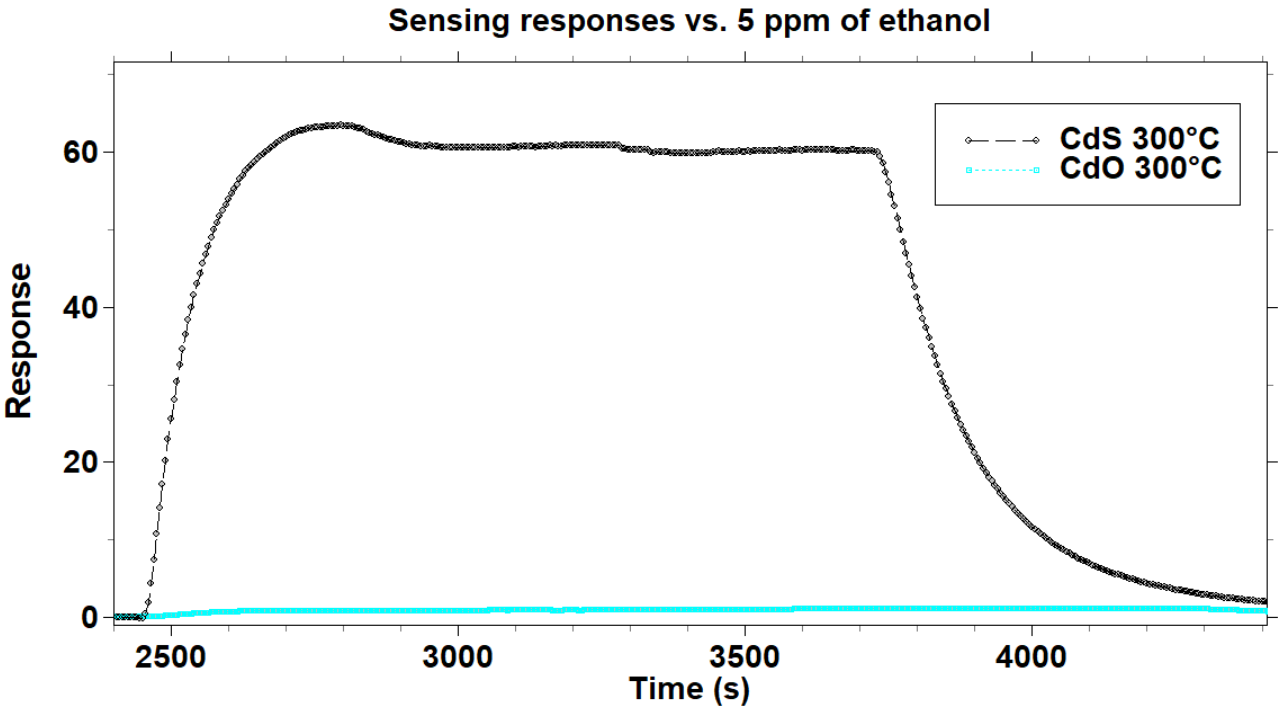

Figure 2.51: Dynamic responses of CdS and CdO sensors vs 5 ppm of ethanol at 300°C [adapted from A.2].

We decided to investigate further only the CdS films, whereas CdO layers exhibited too poor chemoresistive properties with the gas tested. With this aim, Arrhenius plot was obtained as reported in [2.127]. In Figure 2.52, both in Arrhenius plot and in barrier measurement, a drastic change in slope was observed at the temperature of about 750 K. A linear increase of barrier with a temperature increase was recorded above this value. We assumed that the change was mainly attributable to the transition of the CdS to CdO, as confirmed by thermal analysis. The rapid increase in the barrier height, once the transition occurred, reflected the decrease in conductance observed in the graph from 740 K to 900 K. A possible cause for this trend may be the oxygen-chemisorbed species at surface, whose reactivity increases after the material has almost completely turned from CdS to CdO, resulting in larger surface negative charge, responsible for a sharp barrier increase [1.1].

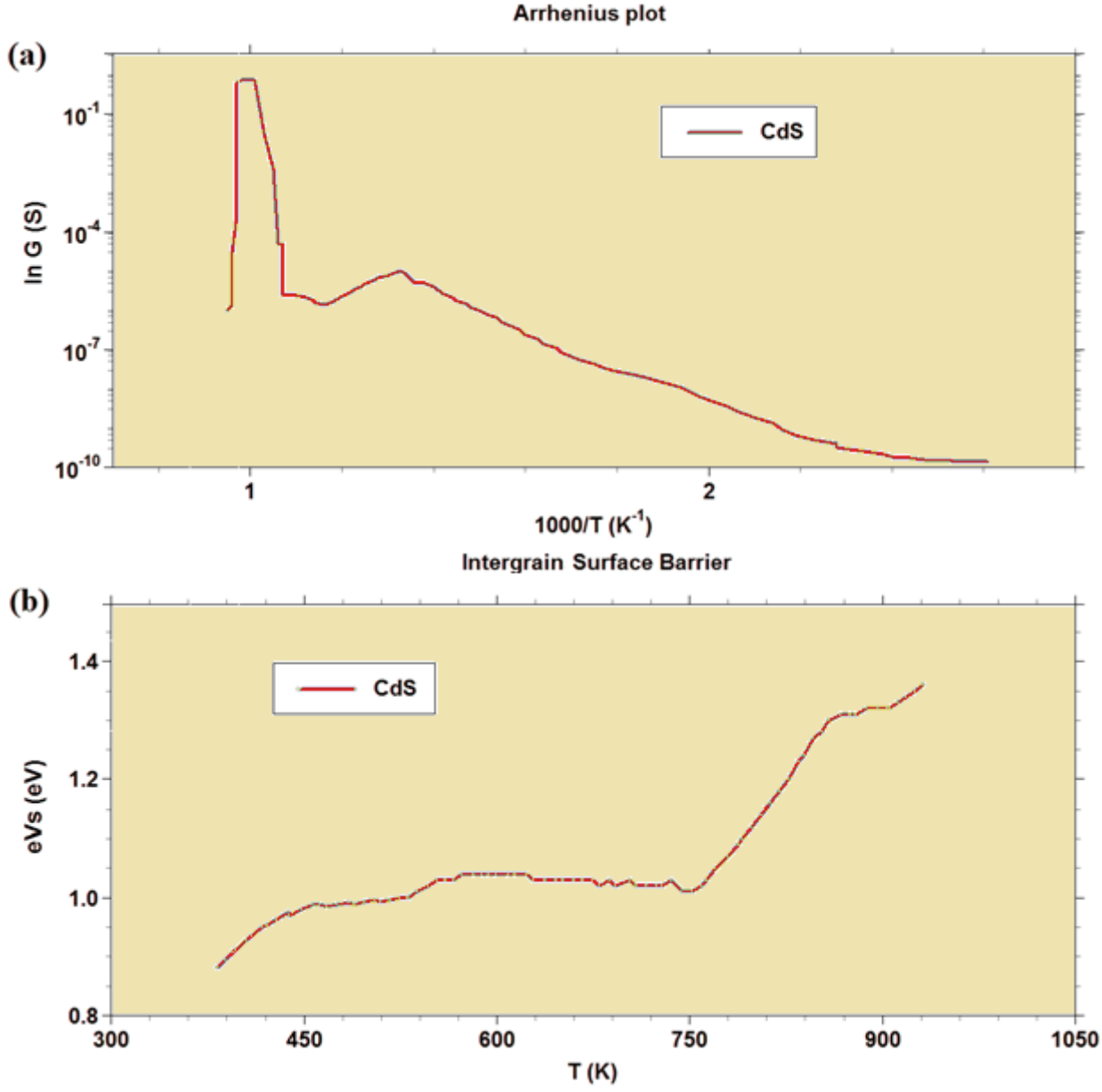

Figure 2.52: a) Arrhenius plot and *b)* intergrain barrier height of the CdS sensor [adapted from A.2].

2.3.3.3.2 Photo-Activation Mode

Several works, in literature, showed how the electrical properties of nanostructured CdS are influenced by visible and near-infrared electromagnetic radiation [2.128-2.130]. Moreover, this semiconductor highlighted a good photo-catalytic behaviour [2.131]. Nevertheless, the literature lacks on studies about the irradiation influence on the adsorption properties of CdS.
It is well-known that irradiation influences the extent of the space charge layer confined at the surface of CdS nanograins, which involves atmospheric oxygen adsorption. This region dominates the electrical resistance of a polycrystalline film because it forms an electrostatic potential barrier at the surface of grains, which charge carriers have to overcome via either thermionic emission or tunnelling to allow electrical conduction [2.132, 2.133]. These properties promote this research on the CdS chemoresistive behaviour in photo-activation mode. With this aim, we analysed the conductance variation of the CdS thick film when exposed, in the gas chamber, of controlled concentrations of CO (10 ppm), H_2S (10 ppm), benzene (2 ppm), ethanol (10 ppm), and methane (2500 ppm). CdS sensors were kept at room temperature during all measurements. The photo-excitation of CdS surface was carried out by means of five commercial LEDs, with radiation wavelengths ranging from 400 to 645 nm.

We show, in Figure 2.53, the electrical response of a CdS thick film vs. the injection of tested gases in the test chamber. As it can be noticed, there is a complete reversibility in the surface reaction between gases analysed and the CdS thick film, which involve in a reversible conductance change between the initial condition of dry air presence and the injection of a gas mixture, with a consequent return to the initial dry air condition. The injection time took into consideration was 500 s, meanwhile, the standard recovery time was of 1300.
The gas sensing characterization highlighted that the response to all gases depends on the wavelength of the impinging radiation while has little dependence on the luminous intensity. The red light (645 nm) induced a very low response, whose signal-to-noise ratio was very poor, but starting from yellow light (592 nm) up to the violet light (400 nm) the responses to all gases were significantly higher

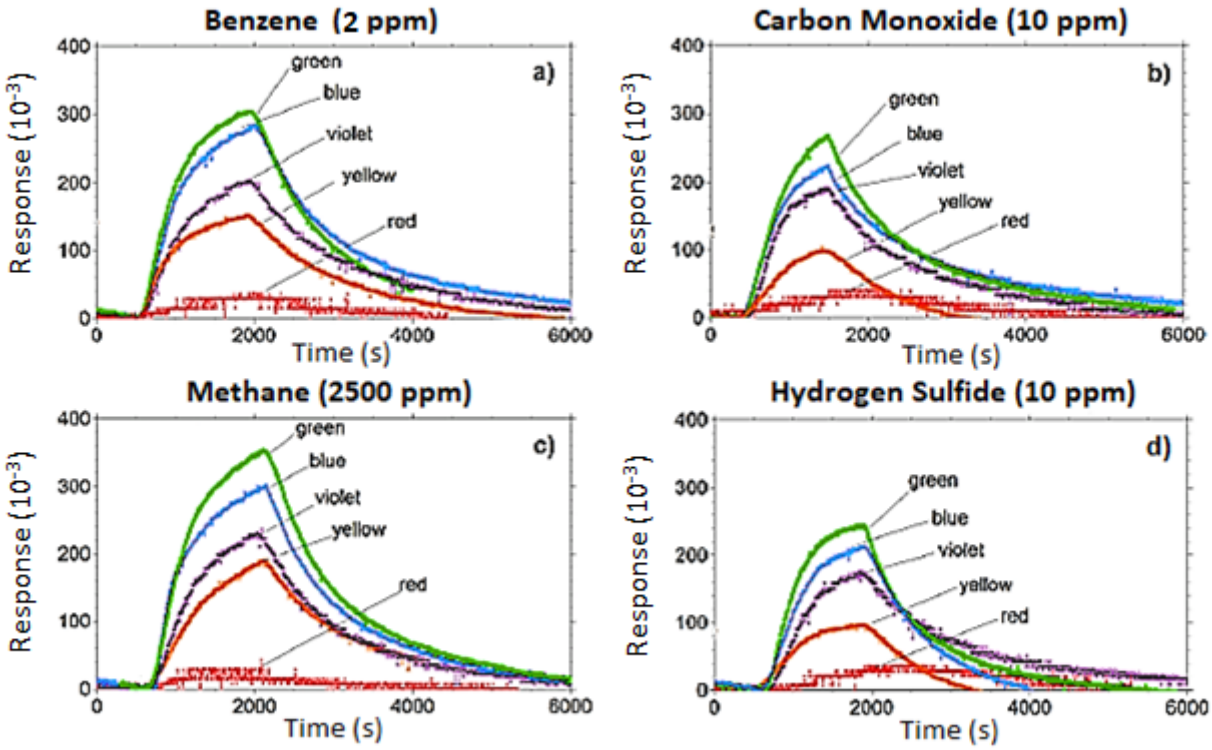

Figure 2.53: Gas-sensing responses of CdS sensors, photo-activated with different radiation wavelengths, vs. *a)* benzene (2 ppm), *b)* CO (10 ppm), *c)* methane (2500 ppm), and *d)* hydrogen sulphide (10 ppm) [adapted from A.5].

The shape of the response curve vs. wavelength of the exciting light is like an asymmetrical bell and is reported in Figure 2.54.

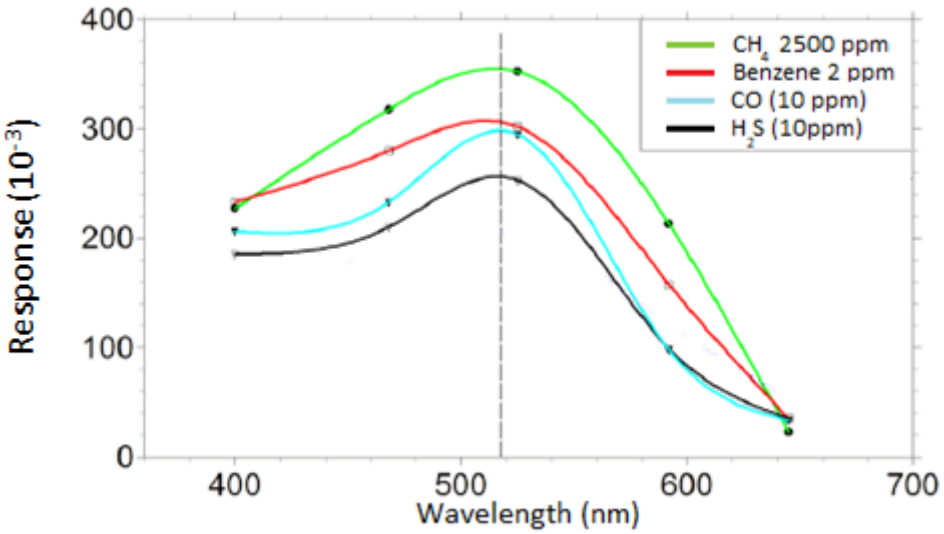

Figure 2.54: Curve of the sensing response values vs. incident radiation wavelengths [adapted from A.5].

For all gases tested, the response peak was found for a green light at 525 nm, which corresponds to photons with energy equal to 2.36 eV. Thus, the light-induced surface chemical reactions are resonant with the energy of impinging radiation tuned on the CdS bandgap. In order to verify the exact band-gap energy of our nanostructured CdS, a UV–visible absorption measurement was carried out. The result, shown in Figure 2.55, highlighted that an absorption band in the ultraviolet-visible range

between 450 and 570 nm, peaked slightly below 500 nm. This absorption peak is blue-shifted compared to the characteristic peak at 515 nm of bulk cubic cadmium sulphide (II), due to the electronic transitions. This phenomenon is known as "quantum size effect" [2.134, 2.135]. However, the value measured confirms that photo-activation and catalysis of chemical reactions over CdS surface increased when the energy of the incident radiation approached the band-gap energy of CdS.

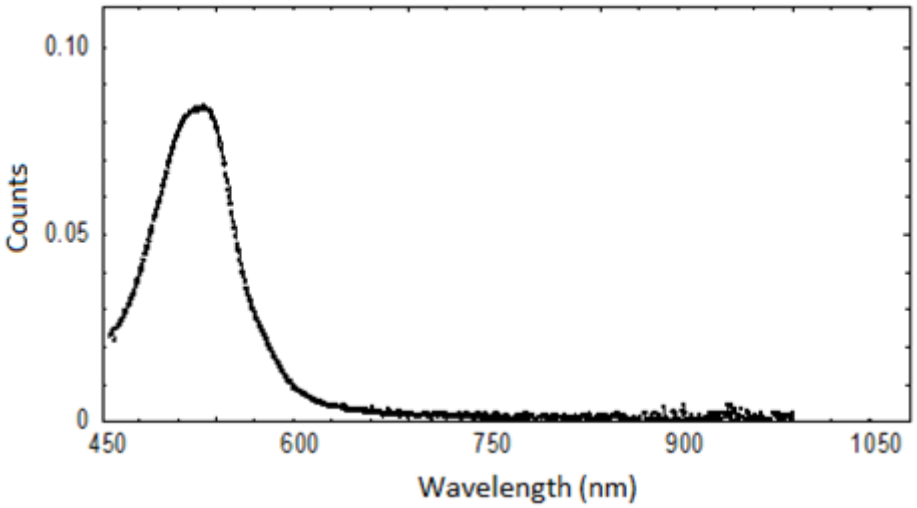

Figure 2.55: Uv-vis. absorption of as-synthesized CdS nanoparticles [adapted from A.4].

The increase of conductance with irradiation is ascribed to many effects. The optical transitions of electrons into the conduction band (CB) are a fast bulk-related effect, responsible for the very first steep part of the transient. Besides this well-known effect, there is an additional contribution, which is specific of polycrystalline semiconductors. A fraction of the photogenerated electron-hole pairs can be separated by the driving electric field, pushing the holes towards the surface, where they can annihilate electrons trapped in surface states, causing oxygen desorption, with subsequent decrease of the barrier height. Electron-hole couples that are generated close to the depletion zone are separated by the much stronger electric field present in the depletion zone. A sketch of this effect, which is a surface-related process, therefore with characteristic time constants much higher than bulk related processes, is shown in Figure 2.56.

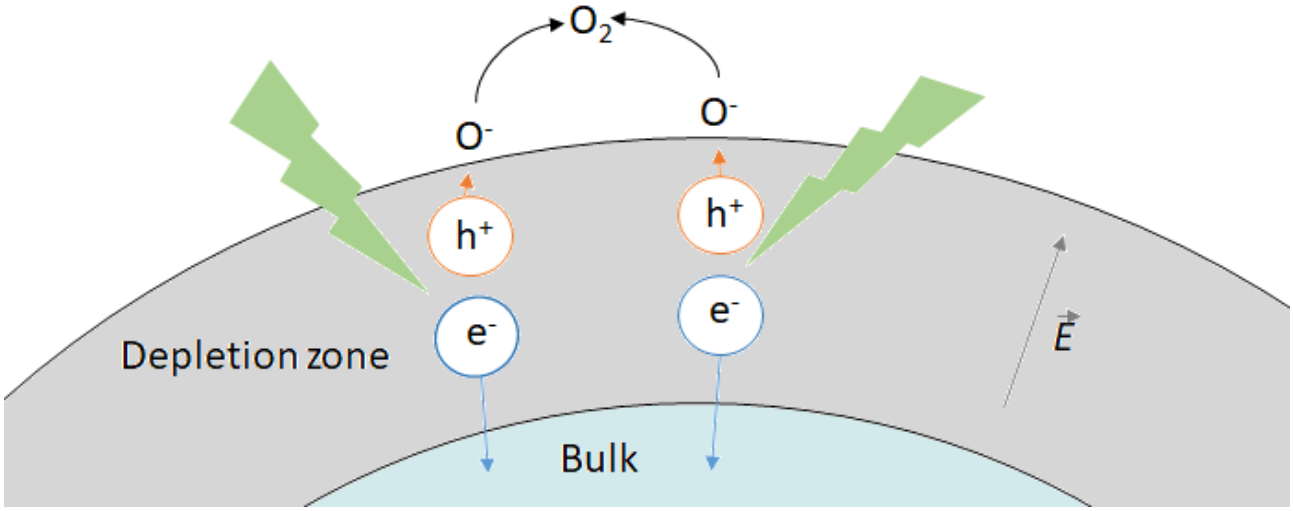

Figure 2.56: Sketch of incident radiation effect on oxygen desorption [adapted from A.5].

It is noteworthy that the optical properties of the investigated polycrystalline CdS turned out to be consistent with those of the single crystal. Indeed, the absorption edge lies at 2.4 eV and the photosensitivity peaks are near the edge [2.136]. The film photo-activated with the green light showed a resistance of about 300 KΩ. The explanation of the enhancement of the surface chemical activity with irradiation lies in the Fermi level shift induced by the radiation. The increase in the number of carriers in the CB (as conductivity reaches a local maximum) results in a shift of the Fermi level to higher energies, thus decreasing the Schottky barrier height, which is, for n-type semiconductors like CdS, the energy difference between the CB at the surface and the Fermi level. The Schottky barrier height depends on the band bending eVs, which, in the simple planar geometry, is described by the following equation:

$$eV_s = \frac{e^2 N_s^2}{2\varepsilon N_d} \qquad Eq.\,2.5$$

where N_s is the density of charged surface states, e the permittivity, and N_d the density of donor states. From Eq. (2.5), the lower is the barrier, the lower is the density of charge trapped in surface states. The gas concentrations were in the ppm range. Then, a very little percentage of surface charge interacts with gas molecules in dark condition, resulting in a negligible effect. Instead, as the density of charged states is lowered by illumination, the variation of conductance because of the surface chemical reactions with gases is larger because a higher percentage of surface charge is involved. The reason behind the resonant behaviour, i.e., the bell shape of the response curve of Figure 2.54, can be interpreted in terms of physics of electronic transitions. The decrease in response at higher wavelengths (lower energies) is very rapidly owing to an increasing number of photons with energy below the bandgap. The decrease at shorter wavelengths (higher energies) is gentler and it can be explained relaying on a fundamental work on CdS [2.137]. Here, a numerical simulation shows that the electron means a free path for inelastic scattering decreases with increasing energy above the threshold of the bandgap. Thus, the higher the energy the larger the fraction of conduction electrons lost for inelastic scattering. Therefore, the excess energy is transferred to the phonon field of the lattice. This results in a perturbative term in the Hamiltonian, which modifies the band structure, thus decreasing the group velocity of electrons in the conduction band. It follows that the excitation near bandgap energy corresponds to a local maximum in photoconductivity, as experimentally highlighted by Bube *et al.* [2.138].

Although the photo-activated CdS sensor did not show a selectivity behaviour among gases tested, the interesting chemoresistive properties highlighted in this work enables the possible use of the nanostructured CdS as a functional material for gas-sensing applications at room temperature.

2.4 Silicon Carbide

Silicon carbide (SiC) is a long-time known material, massively produced since 1890. Since it was discovered by Edward Goodrich Acheson during attempts to prepare artificial diamonds, it shows exceptional mechanical properties. Ceramics obtained by sintering SiC grains are very hard and find application in car brakes, bullet-proof vests and in general in high endurance applications [2.139]. Its thermal strength is also extraordinary, holding stability even above 1000°C, making it possible high-temperature applications (SiC melting point is above 3000 K at 35 atm) [2.140]. Electrically, it is a semiconductor with a mid-high band-gap, in the range 2.3-3.3 eV, depending on the crystal phase [2.141]. This feature allowed the use of SiC for devices based on wide bandgap semiconductors, like silicon or gallium nitride. Electronic applications of SiC are light-emitting diodes and high-

temperature and/or high-voltage devices, as JFETs and MOSFETs rated at 1200 V [2.142]. Furthermore, Oliveros et al. [2.143] reported its possible applications in bioelectronics as an alternative to silicon devices normally used as a substrate in biomedical application, given the cytotoxicity issues of Si highlighted by Kubo et al. [2.144].
So far, silicon carbide has been widely studied as a substrate for sensor devices due to the properties reported above, especially the chemical and mechanical stability at high working temperatures. In particular, SiC-based gas sensors have been widely studied as Schottky diodes, field effect transistors or capacitor systems using SiC as a dielectric material, by measuring the variation of electrical current or capacitance due to the interaction between gases and the surface of an activated material. These SiC sensors have been used to detect various gaseous compounds including hydrogen, hydrocarbons, CO and NOx [2.145-2.148]. Starting from the classic SiO_2/SiC capacitor, different types of metal-oxide semiconductors (MOS) were investigated to improve the sensing properties and stability of the device [2.149-2.152] even if the performance of MOS sensors in SiC is strongly limited by a poor interface quality between the metal oxide and the surface of SiC substrate.
However, silicon carbide is also a material that can be synthesized in form of nanostructured particles [2.153]. Nanostructured semiconductors show electrical properties very different from single crystals, due to the major role that the surface potential plays in the conduction mechanism. Under proper operating conditions (thermo- or photo-activation), a nanostructured material highlights a high surface reactivity that can dominate the resistance of the whole nanostructure [2.154]. Chemoresistive gas sensors exploit this phenomenon, transducing the variations of the chemical composition of the atmosphere into variations of the electrical resistance of a film composed by the nanostructured material [2.155].
Encouraged by the multiple fields in which SiC can be applied and the possibility to have it in form of a nanosized powder, we decided to investigate its possible chemoresistive properties. Indeed, through the combination of the high stability and the surface reactivity, it is possible to obtain a gas sensor device suitable for commercial use.

2.4.1 Powder preparation

Silicon carbide nanopowder was purchased from Tec Star. The datasheet reported high chemical purity of the sample (>99%) and an average grain size of 34 nm.
At the first step, the commercial powder was treated to purify it from possible contaminants: the powder was diluted with distilled water in 10mL vials and was washed an EBA 200 centrifuge at 6000 rpm for 15 minutes. This cycle was repeated four times with distilled water, and other four times with 2-propanol. Afterwards, the powder was heat treated at 650°C for 2 hours in a Lenton oven, in ambient air, in order to remove possible organic contamination.
The purified powder was then treated in a Retsch bull mill (type MM 200), at 1500 rpm for 30 minutes using ceramic balls and vials in order to homogenize nanoparticle sizes.

2.4.2 Chemical, Structural and Morphological Characterization

Results of the XRD measurements of the treated nanopowder are shown in Figure 2.57. The analysis of the phase composition highlighted the presence of three different crystal phases of silicon carbide in the sample, i.e. Moissanite 3C or Zb-type (cubic phase, s.g. F-43m) pdf n. 029-1129, SiC-RS-type (cubic s.g. Fm-3m) pdf n. 049-1623 and Moissanite 21R (trigonal phase, s.g. R3m) pdf n.049-1430. The cubic phase Moissanite 3C was predominant in the sample, with a concentration of 95.55%. The crystallite size, estimated through Rietveld method, resulted to be 21.6 ± 0.14 nm.

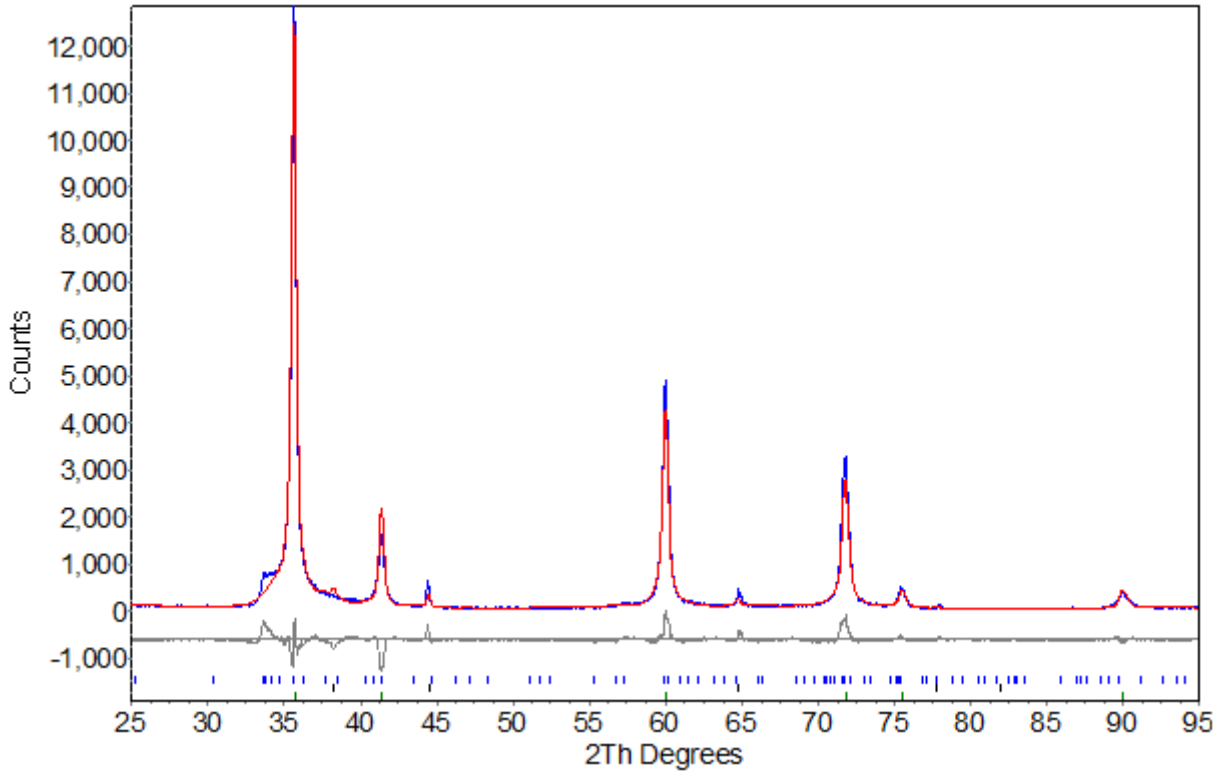

Figure 2.57: The XRD analysis of the SiC nanopowder.

The SEM-EDX characterization is shown in Figure 2.58. The SEM images highlighted that the morphology of SiC grains was spherical-like, with an average size of tens of nanometers. As inset in Figure 2.58, the EDX analysis for the powder is reported, in order to investigate possible chemical contamination. It can be noticed that the SiC sample showed a high chemical purity, in the allowed range of the instrument error.

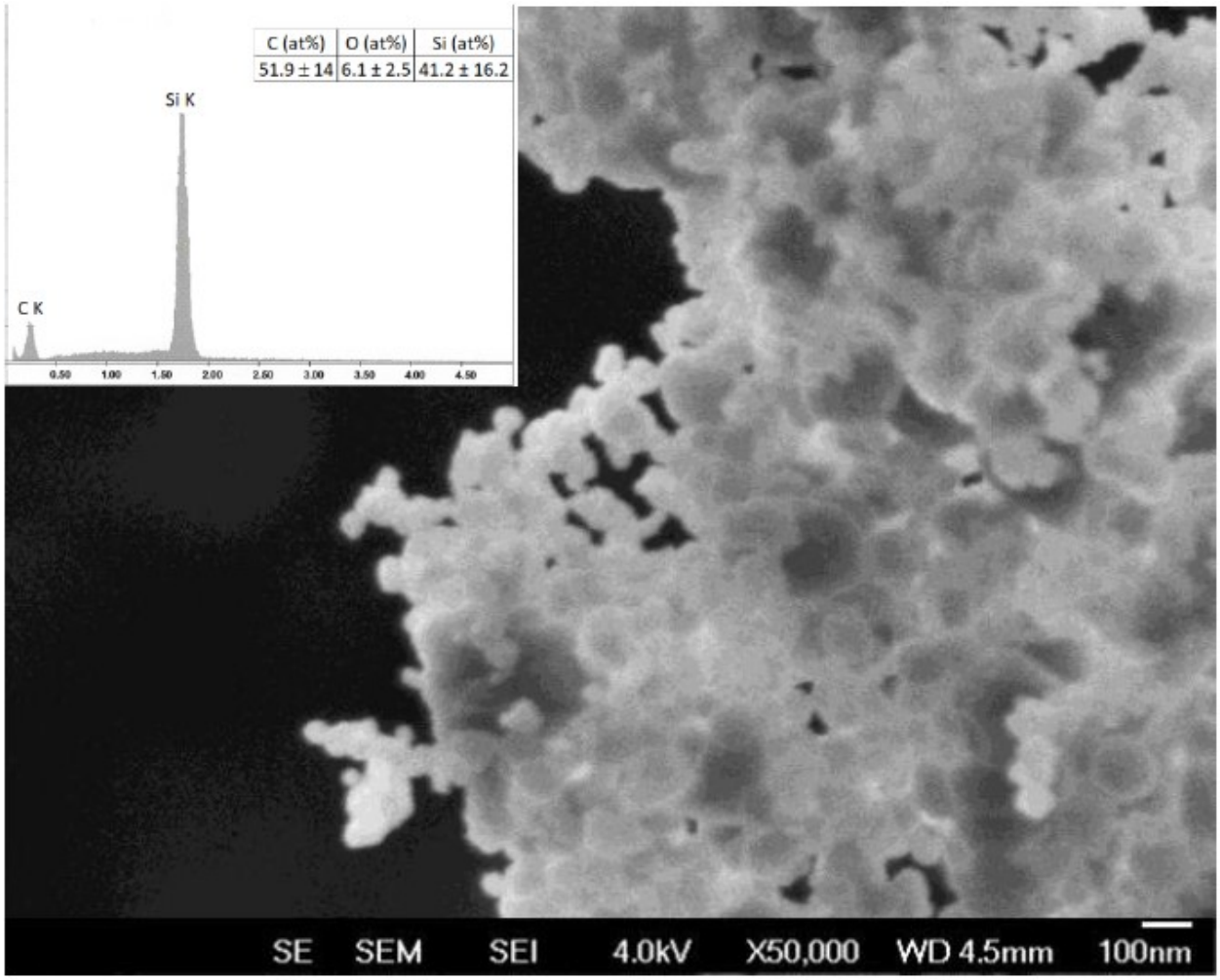

Figure 2.58: SEM image of the SiC nanopowder. The EDX analysis is reported as an inset.

The TEM analysis, reported in Figure 2.59, confirmed that the clusters previously observed with the SEM analysis are composed of structures with spherical-like morphology. The SAED diffraction pattern is shown as an inset in Figure 2.59. The interplanar distances estimated were 2,53, 1,56, and 1,32 Å, which confirmed XRD analysis results regarding the predominant cubic phase.

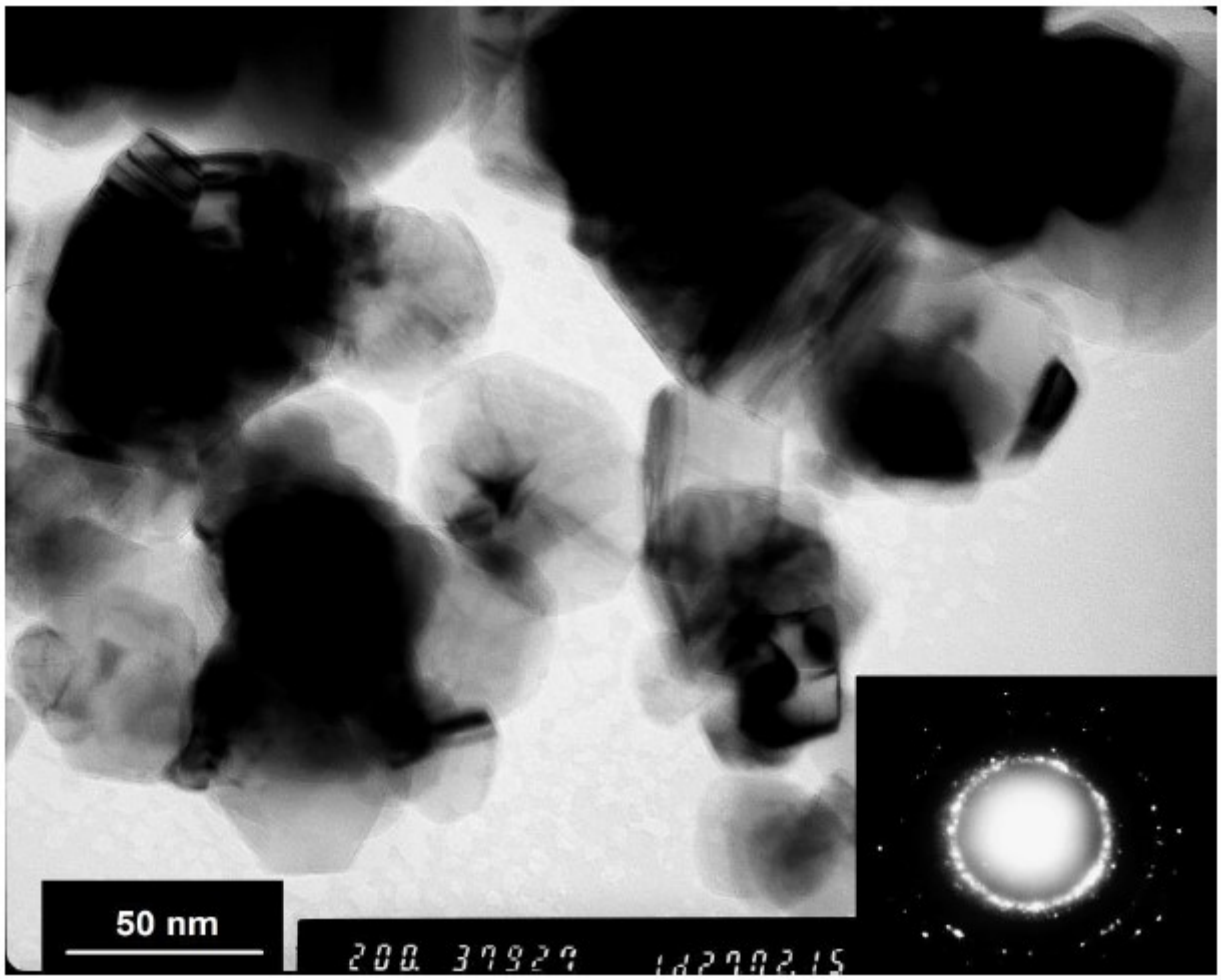

Figure 2.59: TEM image of SiC nanopowder. In the inset of the figure, SAED analysis of the SiC powder.

The TXRF analysis, reported in Figure 2.60, was carried out to investigate possible traces of chemical contamination in the SiC treated sample. The quantification was performed by ab initio simulation of the fluorescence spectrum. The Figure 2.60 shows experimental and simulated spectra in the region of interest including the peaks of the contaminants. As it can be seen, the analysis highlighted the presence of very low concentrations of tungsten, copper, nickel, iron, calcium and chloride, reported in weight percentage. The spectra in the Figure 2.60 showed FeKa and NiKa peaks, mainly due to environmental contamination rather than in the sample, since they are also visible in the blank wafer spectrum. Therefore, spectra highlighted the high chemical purity of the treated SiC powder.

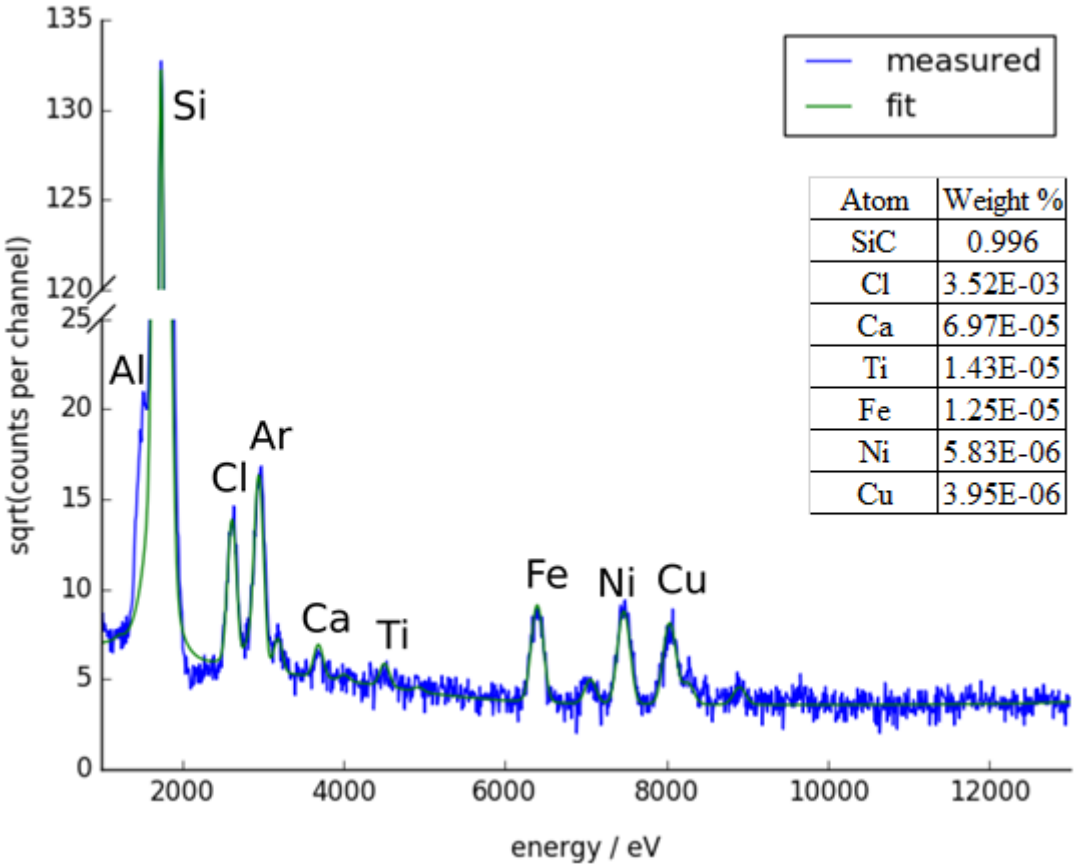

Atom	Weight %
SiC	0.996
Cl	3.52E-03
Ca	6.97E-05
Ti	1.43E-05
Fe	1.25E-05
Ni	5.83E-06
Cu	3.95E-06

Figure 2.60: TXRF analysis of the SiC nanopowder.

Shown in Figure 2.61 is the diffuse reflection spectra obtained for SiC powder. The band-gap energy of the treated SiC powder was determined through Kubelka-Munk method [2.156]. Diffuse reflection spectra were obtained in the wavelength range of 200–1000 nm by means an Ocean Optics Q65000 spectrometer. Measures were carried out through an optical system consisting of the seven-silica UV-grade fibre of 600 microns diameter. The six side fibre provided the incident radiation and the central one collected the reflected radiation. Barium sulphate was used as blank and a black paper as a dark reference. The band gap determined was about of 2.34 eV, very close to the value of the 3C SiC of 2.36 eV reported in the literature [2.157]. The difference of 0.03 eV could be attributable to the imprecision of the method used.

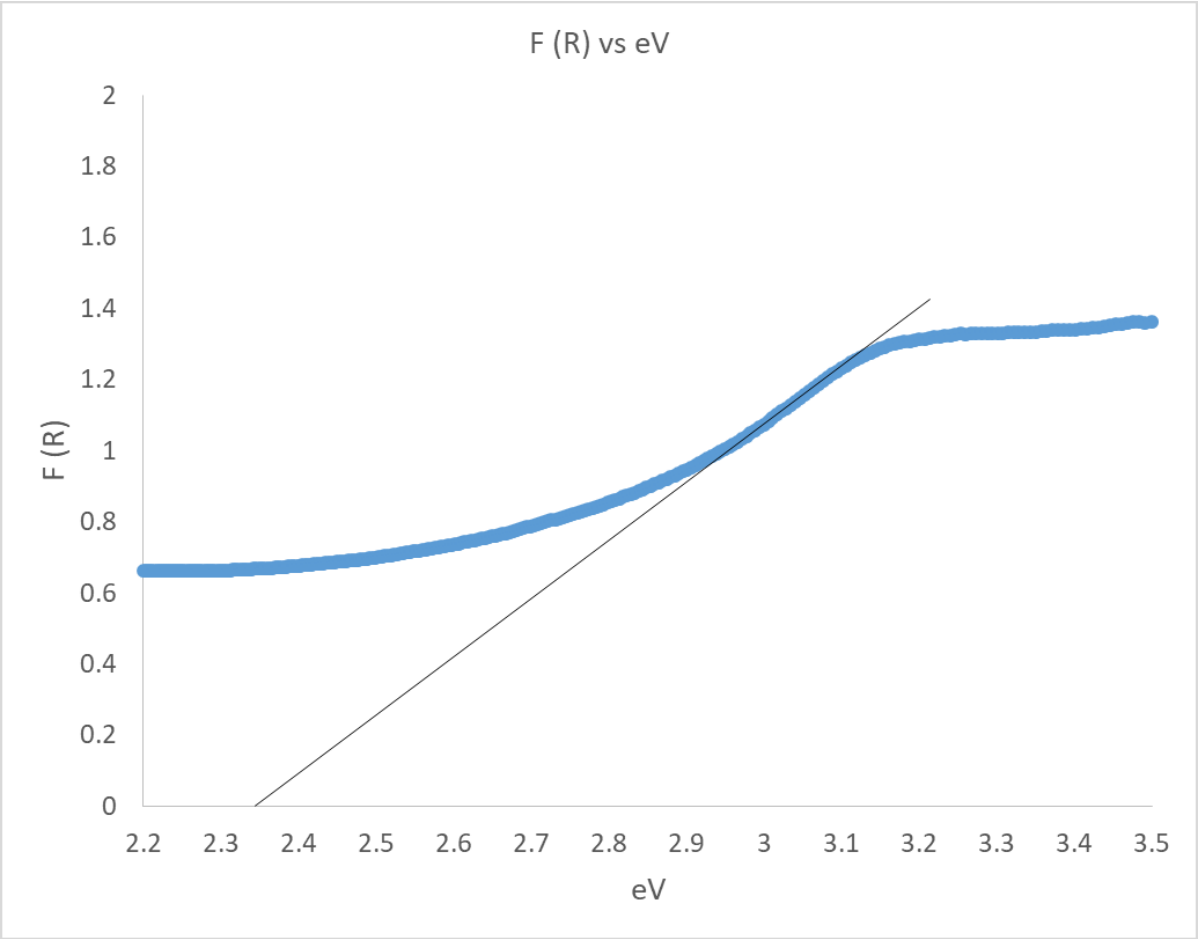

Figure 2.61: Kubelka-Munk function calculated through total reflectance spectra of the SiC nanopowder.

2.4.3 Electrical Characterization

The characterized SiC powder was deposited onto substrates and firing stabilization was carried out at a temperature of 650°C. Then, obtained SiC thick films were tested as a sensitive element of gas sensors by exposing them to 13 gases belonging to different chemical classes, such as alcohols, ketones, aldehydes, NOx and other VOCs. The sensing properties of nanostructured SiC was investigated both in thermo- and photo-activation mode. Since the material did not show any chemoresistive behaviour when photo-excited, we report data obtained in thermo-activation mode only.

Sensor responses were investigated at operating temperatures ranging from 250 °C to 800°C. Temperature above 800°C was not investigated because most of the alumina substrates were broken at this temperature.

2.4.3.1 Thermo-Activation Mode

Firstly, it was investigated the relationship between the resistance of silicon carbide screen-printed layer vs temperature. The Figure 2.62 shows mean data obtained with ten films investigated. SiC thick films showed a very high resistivity at low temperature, with a resistance of 7.9 Gohms at 250°C. The film resistance decreases with an exponential trend when the temperature increase, reaching 500 Mohms at the temperature of 800°C.

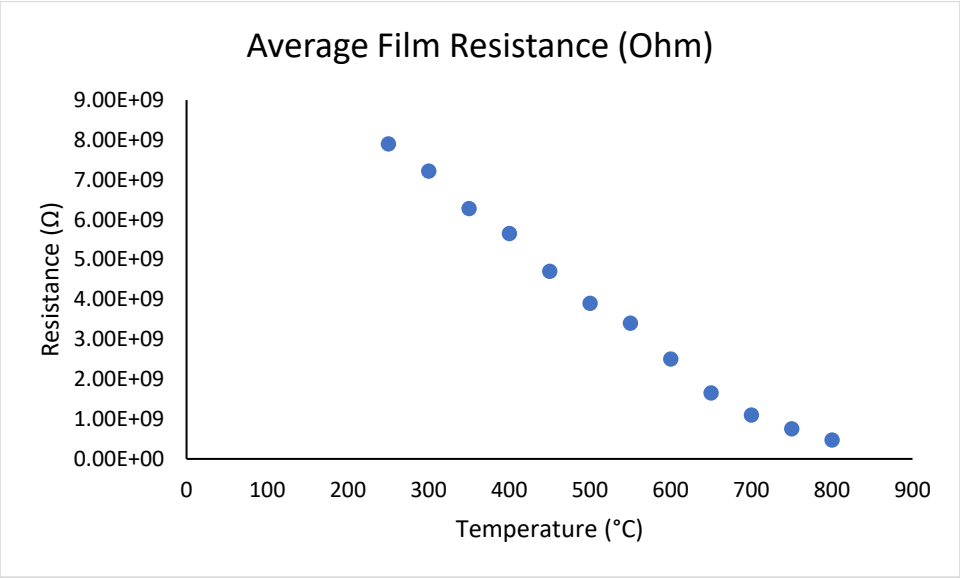

Figure 2.62: Temperature vs. resistance plot of the SiC nanopowder.

The measurements highlighted that SiC layer resulted to be insensitive, from a chemoresistive point of view to all gases tested until working temperature of 550°C in dry air and 500°C in wet air. In Figures 2.63 and 2.64 are reported summary graphs of SiC sensor sensing responses, both in dry air (Figure 2.63) and in presence of 13% of relative humidity (Figure 2.64).

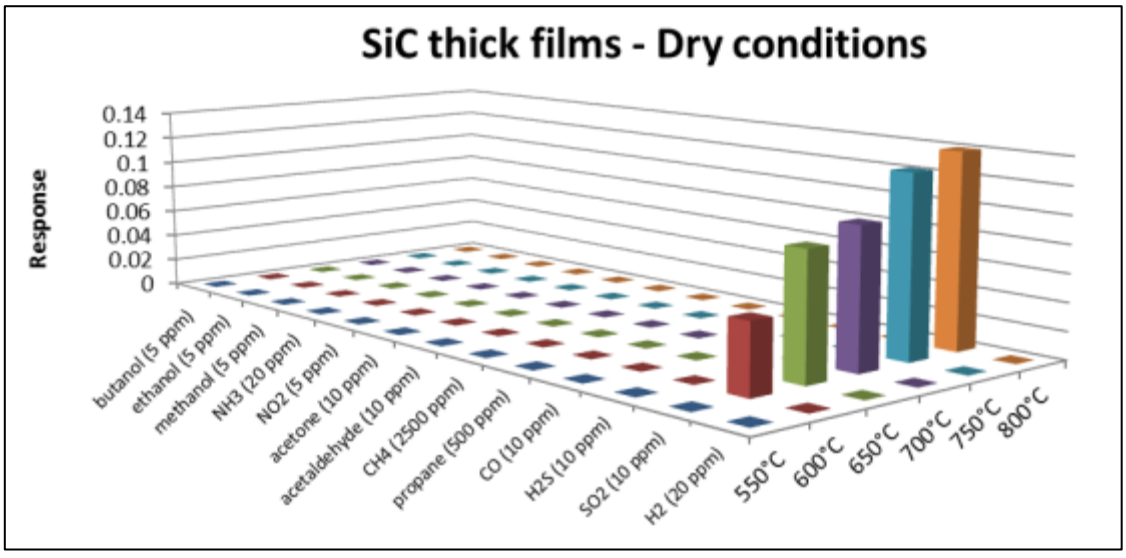

Figure 2.63: Summary histogram of SiC sensor responses vs. gases tested at different working temperatures, in dry air.

As it can be seen from Figure 2.63, the SiC layer did not highlight any change in conductance in presence of almost all gases tested in dry air, except for SO_2, at a concentration of 10 ppm. Indeed, when exposed to this gaseous molecule, silicon carbide-based sensors showed a detectable and reversible change in conductance starting from working temperature of 600°C. The sensing response to 10 ppm of SO_2 increased at higher working temperatures than 600°C, as is shown in Figure 2.63. The sensing behaviour of SiC thick film was also investigated in humidity air, in order to understand the sensing properties of the sensor in environment closest to real sensing applications, where humidity is the most common interfering [2.158]. The summary of results obtained in presence of 13% of relative humidity is reported in Figure 2.64.

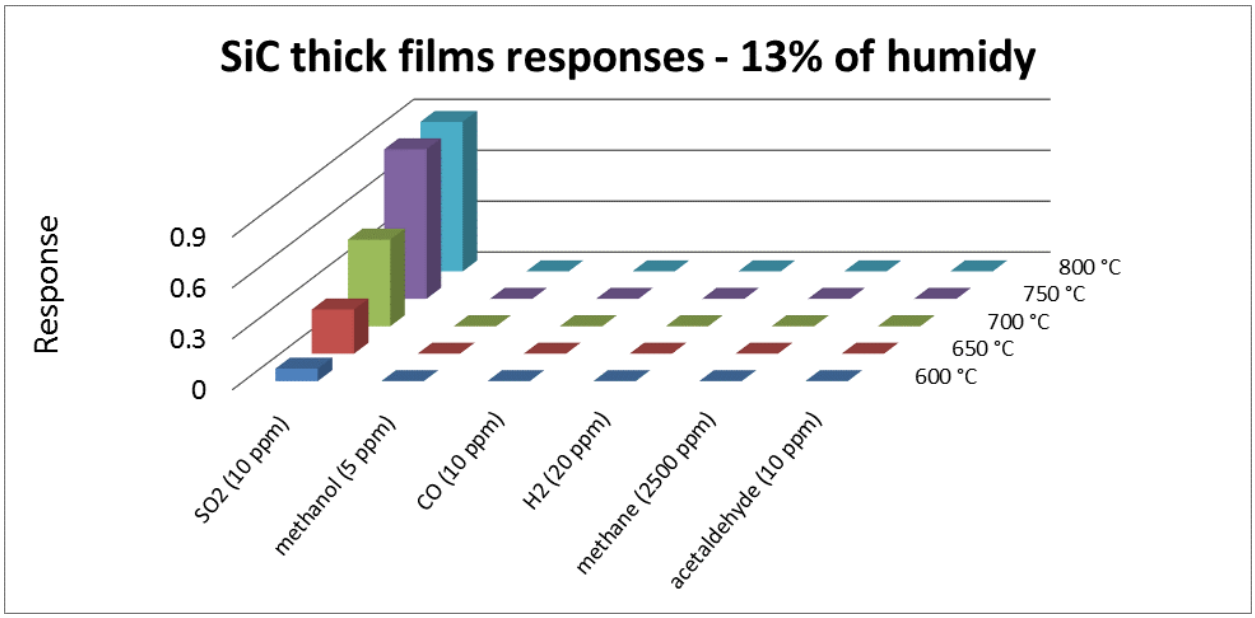

Figure 2.64: Summary histogram of SiC sensor responses vs. gases tested at different working temperatures, in wet air.

As it can be seen from this Figure, the behaviour of the sensing material was the same that in dry air, showing a detectable change in conductance only in presence of 10 ppm of SO_2. However, the minimum working temperature useful to detect 10 ppm of SO_2 was lower in the wet air than in dry air (550°C in wet air vs. 600°C in dry air). Moreover, values of sensing responses vs. SO_2 were higher in the wet air than in dry air for all the working temperatures where a conductance change was recognizable, as it can be seen in Figures 2.63 and 2.64. Thus, contrary to what reported in the literature for metal oxides commonly used as chemoresistive gas sensors, the presence of humidity seemed to improve the sensing performance for silicon carbide films, maintaining the selectivity of responses vs. SO_2 and increasing the response value to this analyte. Based on the data obtained, it was decided to carry out the further sensing characterization at 650°C, that was the temperature that highlighted the best compromise between SiC sensing properties and a reasonable temperature to maintain the stability of the alumina substrate and the electronic system.

To deeply investigate the humidity influence in sensing properties of SiC sensors, the sensing responses of SiC films to 10 ppm of SO_2 vs various percentages of relative humidity was studied. Dynamic responses of these characterizations are reported in Figure 2.65.

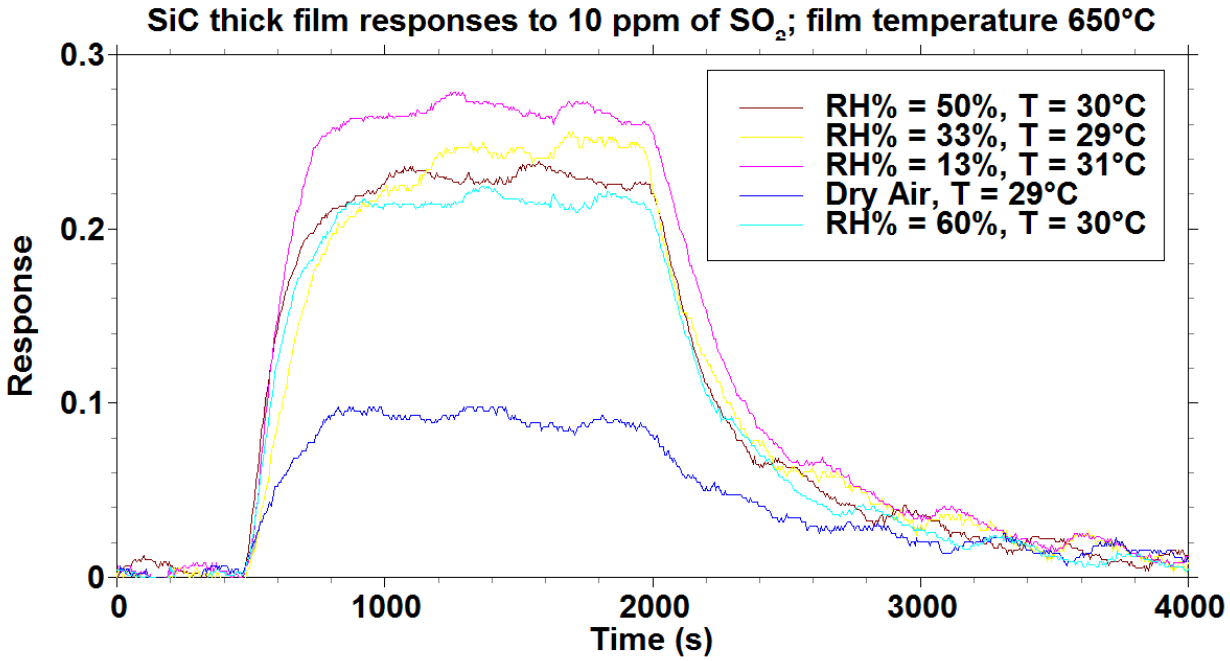

Figure 2.65: Dynamic responses of SiC sensors vs. 10 ppm of SO_2 in presence of a different percentage of relative humidity.

As it can be seen, all responses in the wet air were higher than the response in dry air. The maximum response was recorded with 13% of relative humidity, and with a higher percentage of relative humidity the response slowly decreased, but they were still higher than the response in dry air. This is counter-tendency in respect with the behaviour of metal oxides commonly used in the chemoresistive gas-sensing field, since usually, the humidity reacts with the film surface, occupying and thus decreasing possible reactive sites resulting in decreases of sensing response compared with the response in the dry air [2.103]. The response and recovery times vs. 10 ppm of SO_2 were also investigated since they are useful parameters to understand catalysis and speed of interface reaction. Results obtained are reported in Table 1.

Table 1: Summary table of recovery and response times of SiC sensors vs. 10 ppm of SO_2 in presence of a different percentage of relative humidity.

Relative Humidity %	Response Time (s)	Recovery times (s)
Dry Air	300	590
13%	259	380
33%	435	312
50%	302	336
60%	318	367

In one hand, the response time, calculated as the time that the sensor used to keep the 90% of the response, was independent of the presence of different percentages of the relative humidity. On the other hand, the recovery times, calculated as the time that the sensor used to switch back to 1/e of the response value, it was lower in presence of humidity than in dry air. Therefore, the presence of humidity affected both response value and time of reaction. These data highlighted that the presence of humidity probably modified the reaction kinetic between SO_2 and SiC layer surface.
To investigate the repeatability of the SiC sensor, the device was exposed to SO_2 at a fixed concentration of 10 ppm. The Figure 2.66 shows sensing responses by exposing the sensor to 4 cycles of SO_2 adsorption/desorption, at different relative humidity percentage.

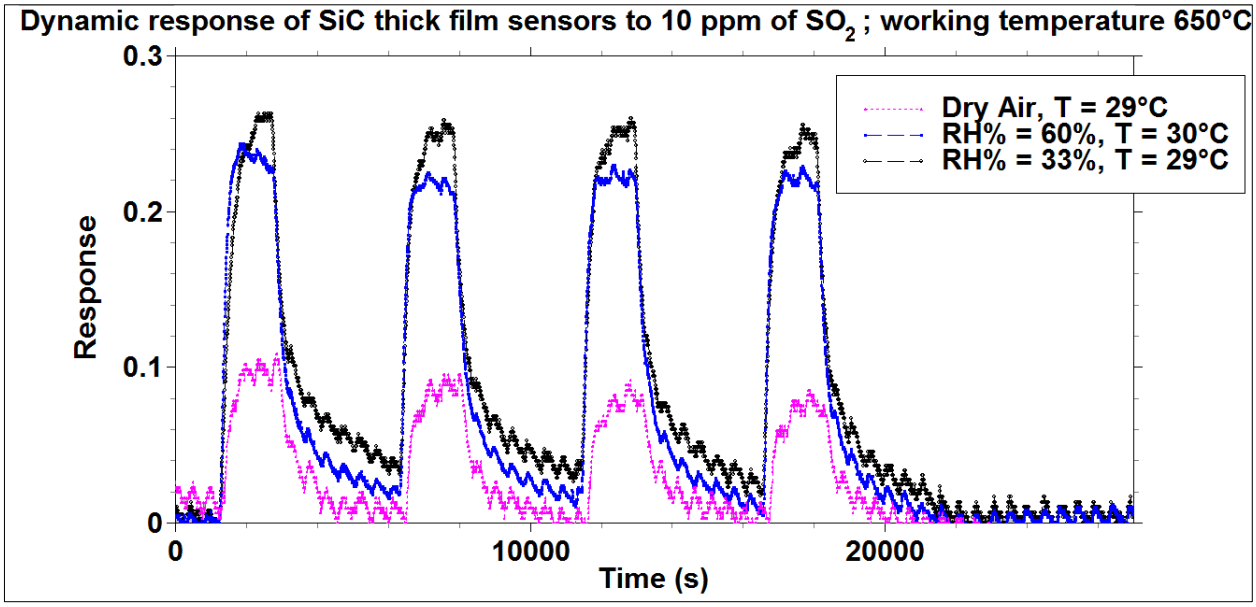

Figure 2.66: Stability of SiC sensors responses vs. 10 ppm of SO_2 at different RH%.

SiC sensors showed a repeatable and stable response in the range of hours, especially in wet condition. The last sensing parameter investigated of SiC device was the sensitivity, in order to study the trend of the SiC sensing response vs various SO_2 concentrations, such as 1, 2, 5, 15 and 25 ppm. The data obtained, illustrated in Figures 2.67 at a relative humidity of 50%, have highlighted that the trend in the calibration curve is in line with the trend of the common metal-oxide gas sensors, with a decreasing of SiC sensor sensitivity increasing the concentration of SO_2.

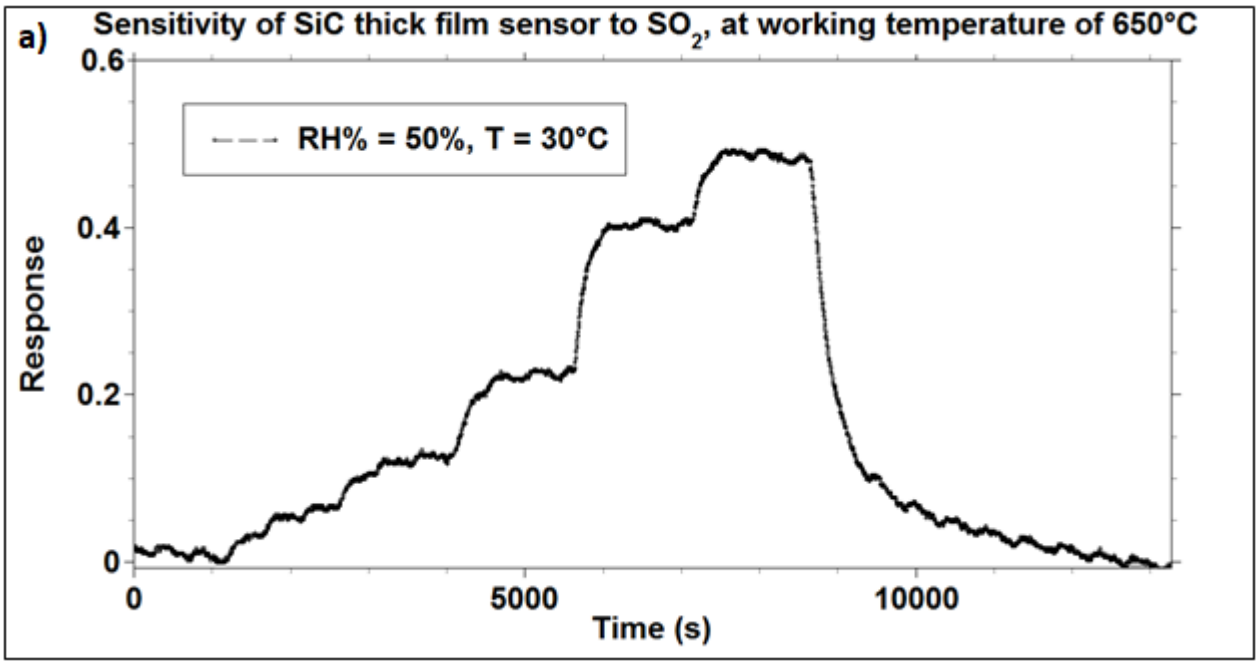

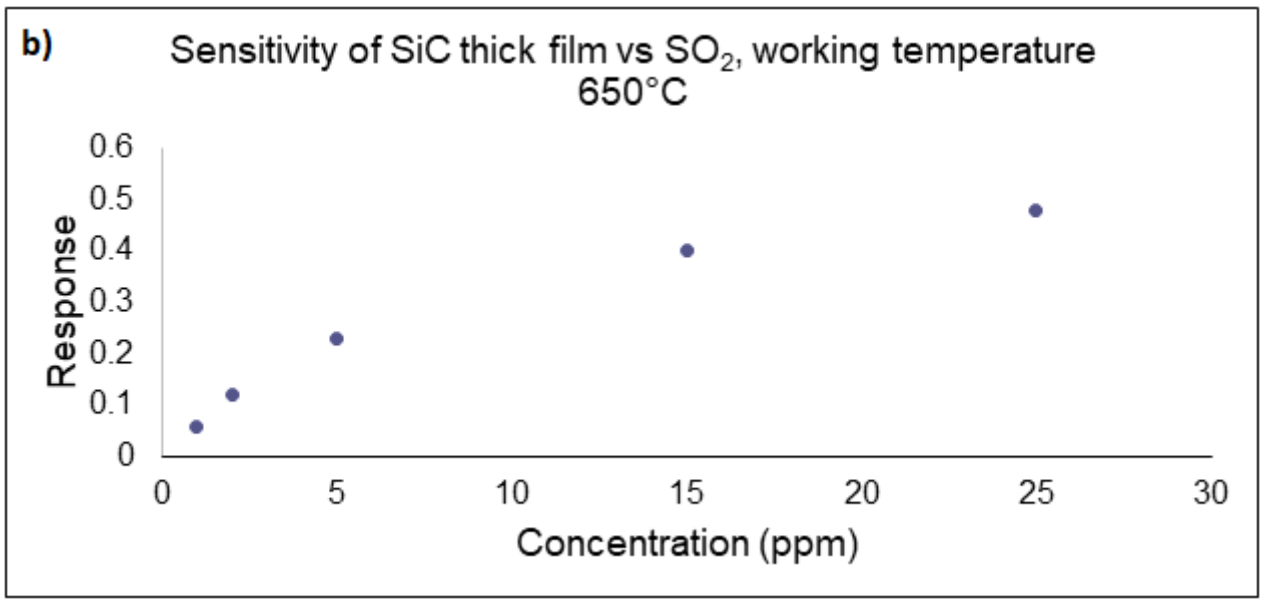

Figure 2.67: a) and *b)* sensitivity of SiC sensor vs. 10 ppm of SO2 at 650°C, in presence of 50% of the relative humidity.

The lower detection limit found at 650°C for SiC sensors was 1 ppm of SO_2, a useful concentration for gas application since is two times lower than the time-weighted average (TWA) exposure limit and 5 times lower than the Short-Time Exposure Limit (STEL) [2.126].
To examine the possible cross-selective property of the SiC thick film, the sensor was exposed to 10 ppm of SO_2 and then in the gas chamber were injected in sequence four different gases, as reported in Figure 2.68.

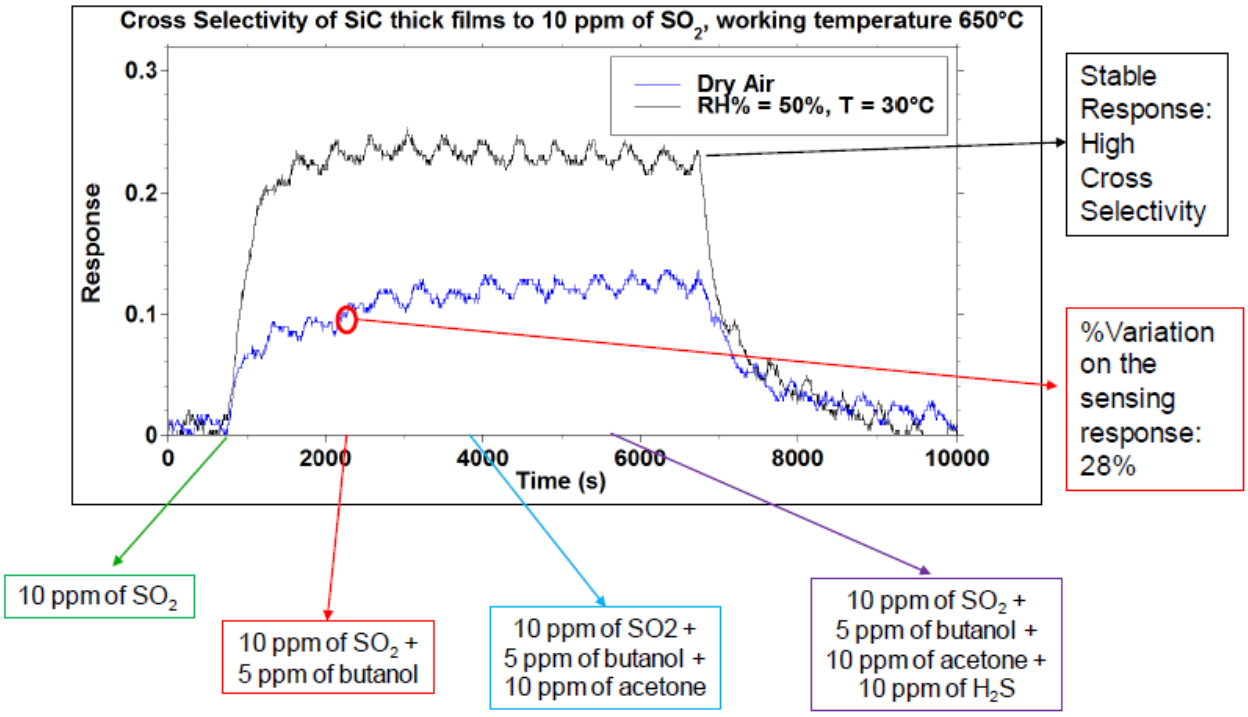

Figure 2.68: Cross selectivity investigation of the SiC sensor vs. SO2 at 650°C in presence of humidity.

As possible interfering species were chosen butanol and acetone, which are usually gases that react strongly with chemoresistive sensors, and H_2S since it is one of the most common interfering in applications where there is the presence of sulphur dioxide [2.159]. This characterization highlighted

a great cross selectivity of SiC sensor in wet condition, meanwhile, an influence of 28% on the sensing response was detected in presence of 5 ppm of butanol in dry air. Since common applications of a gas sensor are in presence of humidity, the high cross selectivity shown by SiC highlights its possible specific use to detect SO_2 in harsh environmental condition.

2.4.3.1.1 SiO_2/SiC core-shell formation and sensing mechanism

To understand the sensing behaviour of SiC thick films, XPS analyses were conducted with the aim to detect possible composition change on the surface of SiC nanoparticles at a temperature higher than 600°C, related to the increase of the SiC sensor reactivity vs SO_2, as reported in the previous paragraph. XPS measurements were performed on three samples, the pristine SiC powder and the SiC powder after a heat treatment at 650°C and 850°C for 5 hours in a furnace, under a constant air flux. It is clear from the data shown in Figure 2.69, after heat treatments, there is a large increase in oxygen content in the SiC powder and a large decrease of the carbon concentration.

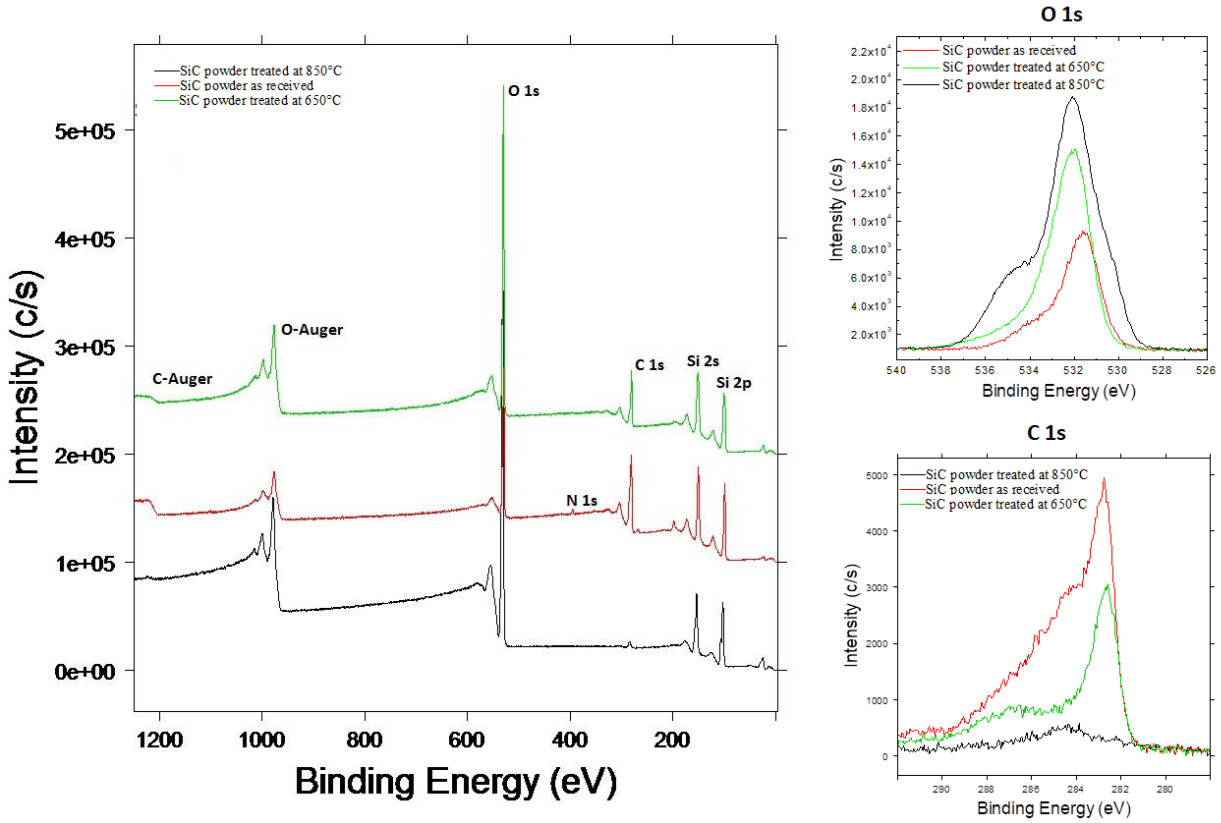

Figure 2.69: XPS analysis of SiC powder no thermal-treated, heated up at 650°C and at 850°C.

This increase in oxygen concentration could be ascribed to the oxidation of the SiC nanoparticle surfaces, that allows the formation of a SiO_2/SiC core shell. Data of atomic percentage in the three samples are reported in the table below.

Table 2: Summary of XPS data obtained for the different SiC samples.

Sample	O (%)	C (%)	Si (%)
SiC not heated	15.2	49.9	34.9
SiC 650°C 2h	51.9	32.3	29.9
SiC 850 2h	64.6	5.6	29.8

Several studies reported theoretical and experimental investigations on SiC nanopowder oxidation at high temperature. Newsome et al. [2.160], proposed a theoretical study about the oxidation of SiC powder exposed to the air, at high temperature, due to the interaction between grain surface and O_2 or H_2O gaseous molecules. Likewise, Roy et al., in their review, cited several experimental works about variables that can affect the oxidation of the SiC powder, such as the role of the SiC grain size and the furnace environment moisture content [2.161].
Therefore, a thermogravimetric analysis was carried out to deeply investigate the oxidation process that occurs in the SiC powder used in this work. In Figure 2.70 are shown the TG/DTG/DTA analysis performed in dry air atmosphere by using the commercial powder after washing cycles, as reported in the paragraph 2.4.1, but without the heat treatment. The initial weight decrease, between 30-120°C, is attributable to the desorption of H_2O molecules adsorbed on the surface of SiC nanopowder, as found for SnS_2 and CdS powders previously. The TG curve shows that no significant changes occurred to the material up to about 400°C, where a small weight increase was detected, till a temperature of 600-650°C. Afterwards, it can be noticed a higher increase of the SiC powder weight starting from 650°C, which continued up to 900°C with an exponential trend. It should be noticed that both last weight increases involved in an endothermic peak in the DTA analysis. On the one hand, these two-weight increase can be explained by the oxidation of the SiC nanoparticle surfaces, which is temperature dependent and the oxidation rate improves when the temperature increases [2.161]. In the other hand, the starting oxidation temperature depends on SiC grain size, and the value of 600-650°C as initial temperature, obtained in our thermogravimetric analysis, is in line with what reported by Ebrahimpour et al. [2.162].

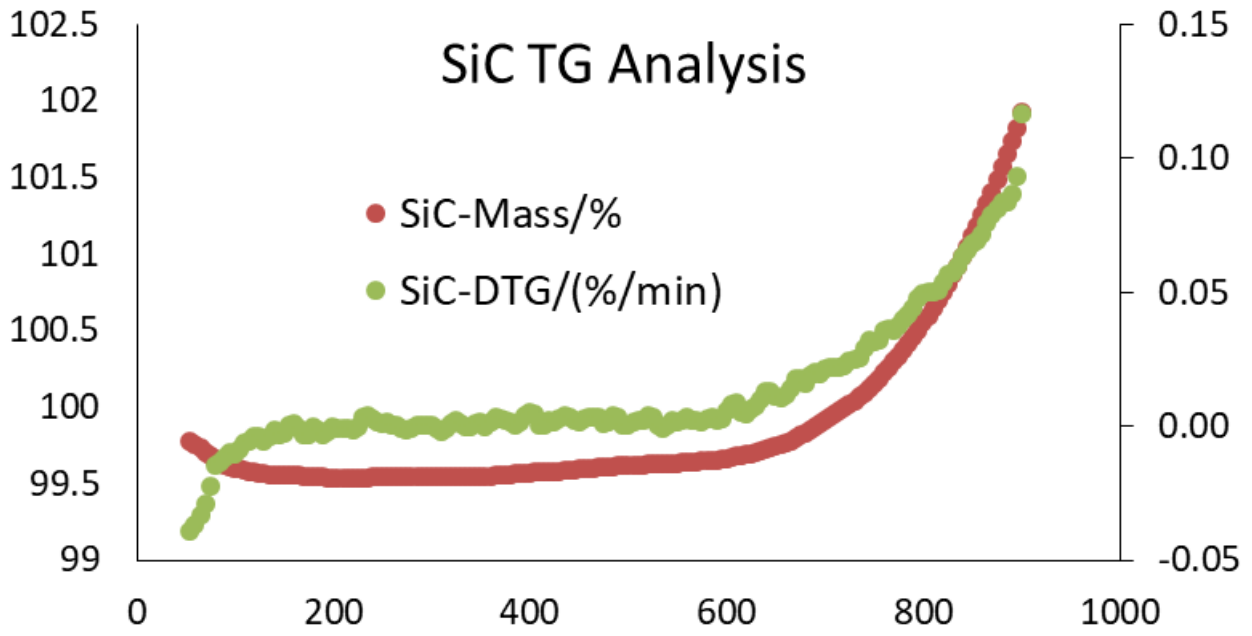

Figure 2.70: TG/DTG SiC powder analysis.

The TG analysis carried out highlights that SiC reactivity vs SO_2, that started at 600-650°C, coincides with the temperature of the oxidation rate increase of the SiC surface. Hence, the surface catalysis could be attributed to the SiO_2 shell that was formed on the SiC nanoparticle surfaces.
A further thermogravimetric analysis, in isothermal mode, was carried out to investigate the formation of a stable SiC/SiO_2 core-shell at 650°C, which was the temperature used for the gas sensing characterization. With this aim, a proper amount of SiC powder, not previously thermally treated, was heated up to 650°C for 15 hours. The thermogravimetric result, reported in Figure 2.71, highlights

that the stabilization of the SiO_2/SiC core shell is achieved after about 10 hours of the powder exposition at 650°C.

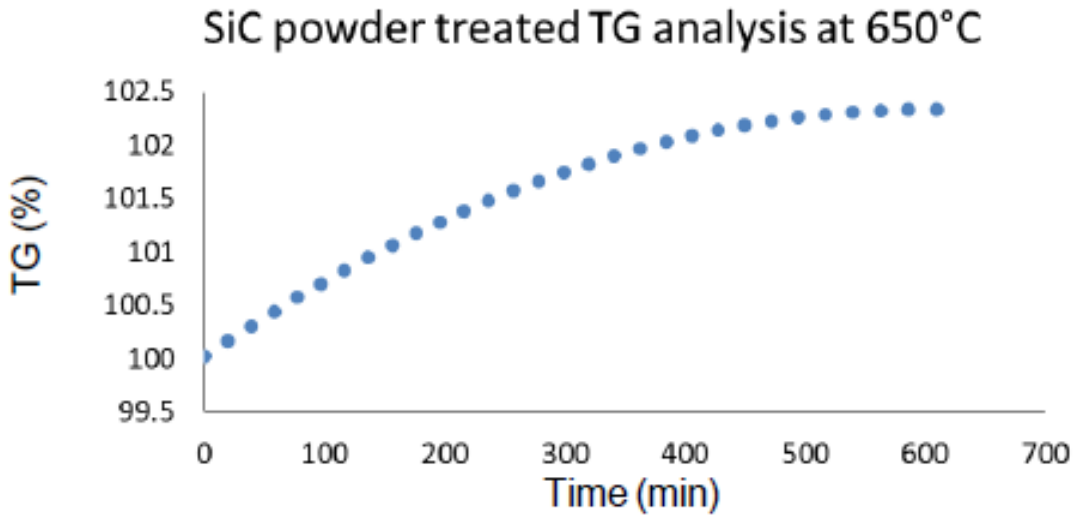

Figure 2.71: TG analysis of the SiC powder, at 650°C, over the time.

This analysis allowed understanding that the sensing measurements, reported in the previous section, were carried out when the SiO_2/SiC core-shell was formed and completely stable. XPS and TGA results highlighted that formation of SiO_2/SiC core-shell promotes, in this study, the high sensor selectivity of the SiC sensor to SO_2.

This high selectivity about SiO_2/SiC core-shell was not found in previous articles, in which authors used SiO_2 especially as support to other sensing material since the low catalytic and chemoresistive properties of pure nanostructured SiO_2 [2.163]. The explanation of the highly selective behaviour could really lie in the core/shell formation. Indeed, many works in literature highlight how core shells of composite materials show better chemical, physical and optical properties than individual materials studied separately [2.164].

To better understand which is the role of the SiO_2/SiC core-shell in the reaction with the gaseous SO_2, the gas sensing mechanism was investigated through the Proton-Transfer-Reaction Mass Spectrometry (PTR-MS), that allows to analyse the product coming out of the gas chamber that allows to analyse the product coming out of the gas chamber after the interaction between SO_2 and sensors. With this aim, suitable bags were used to contain gas mixtures to be analysed. One bag was filled with ten ppm of SO_2, diluted in 80% of N_2 and 20% O_2, directly from certified cylinders. Furthermore, two bags were loaded with the same gaseous mix, but after its passing in the gas chamber containing SiC sensors. PTR-MS analysis of the three bags highlighted the formation of SO as a product of the reaction between SO_2 and SiC surface at 650°C, as it can be seen from the Figure below:

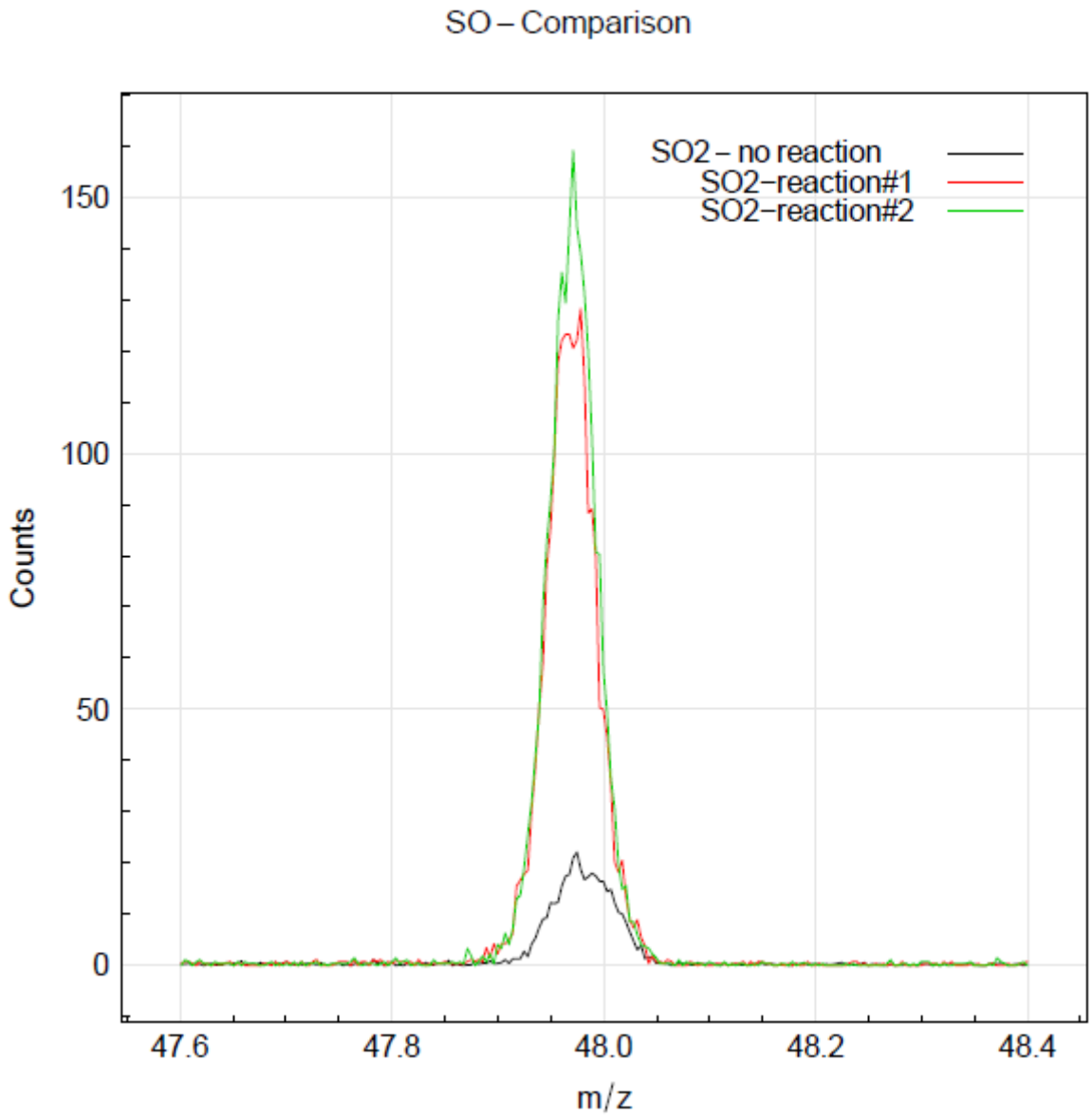

Figure 2.72: PTR-MS analysis of the not reacted SO_2 bag and SO_2 bags after reaction with SiC sensor.

The formation of SO let us suppose the following reactions over SiC nanograin surface:

$$SO_{2(g)}+O^-_{(ads)} \rightarrow SO_{(g)}+O_2+1e^-$$

$$SO_{2(g)}+O^{2-}_{(ads)} \rightarrow SO_{(g)}+O_2+2e^-$$

depending on the charge of oxygen adsorbed on SiO_2/SiC core shell. The electron produced by the reaction can return in the semiconductor, justifying its conductance increase while exposed to SO_2.

A schematic representation of SiC sensors behaviour is reported below:

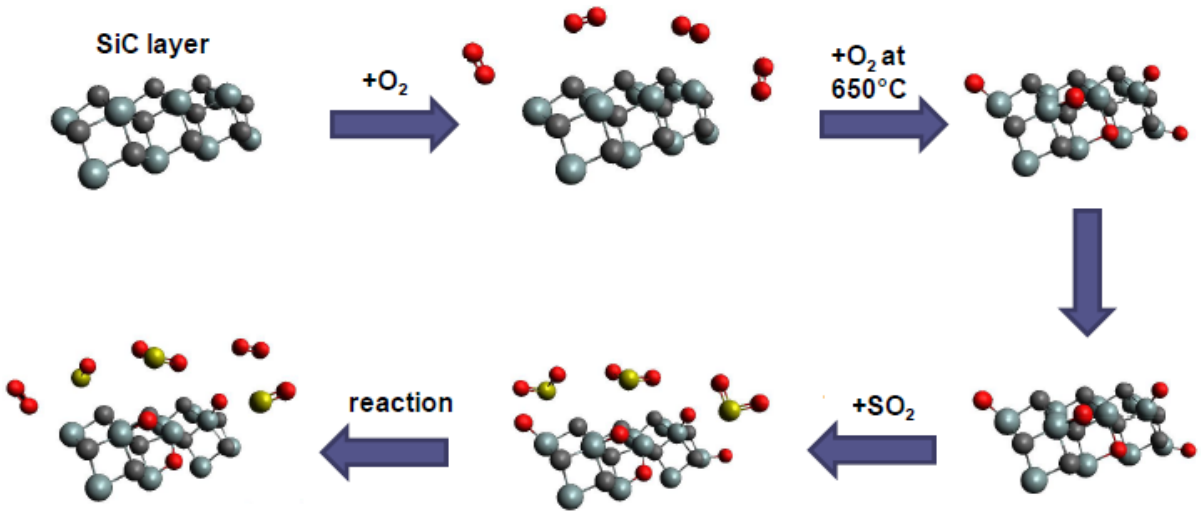

Figure 2.73: Schematic representation of the interaction between SO_2 molecules and SiC layer at 650°C.

2.5 ZnO and Au/ZnO

Parts of this paragraph have been published in [A.1]. In the last years, due to the growing interest in high performing gas sensors, the need of controlling the morphology of metal-oxide nanostructures has been considered for the optimization of synthesis processes. From a gas-sensing point of view, ZnO has shown properties in line with the "3s rule", exhibiting good sensitivity, selectivity and stability over the time [2.165]. Some progress has been achieved, either by using ZnO nanostructures [2.166, 2.167] or a combination of different materials, e.g., noble metal-ZnO [2.168, 2.169] and p–n hetero-contact systems [2.170-2.173]. The ways in which specific functionalization is combined with the ZnO nanostructures significantly affect their sensing properties [2.174]. Then, choosing an appropriate synthesis method, it is possible to control the physical and chemical properties of the product obtained [2.175].

It is well known that through surface functionalization by noble metals such as Pd, Au, and Pt, the sensing performances of semiconductor layers can be significantly enhanced [2.176-2.180]. Among these, Au nanoparticles decoration on ZnO surface was deeply studied for the modification that causes in its electronic [2.181], optical [2.182] and catalytic properties [2.183].

With this aim, researchers identified a class of semiconductor materials, which exhibit both chemoresistive and photoconductive properties. As a matter of fact, the irradiation of the surface with proper wavelengths provides the material with more active sites for gas-surface reactions. Considering, for example, tungsten trioxide (WO_3) and zinc oxide (ZnO), light exposure enables gas sensing at room temperature [2.184]. ZnO is a typical wide-bandgap semiconductor, which has proven to be efficient in various applications such as the realization of gas sensors [2.185], electronic devices [2.186] and electrodes for DSSCs [2.187].

To develop ZnO gas sensors, capable of working at low temperatures, light illumination can be employed to increase carrier concentration in the semiconductor conduction band and to promote photo-desorption mechanisms. As well known, the adsorbed oxygen atoms on n-type semiconductor surfaces (e.g., ZnO) are negatively charged and a built-in-field is originated. Photons, with higher energy than that of the band-gap, promote the separation of the electron-hole pairs produced. As the built-in-field is a result of the oxygen chemisorption, surface gas adsorption/reaction has a significant effect on surface photoconductivity. In addition, the decoration of ZnO nanostructures with gold

nanoclusters could improve the photoconductivity properties of the material and, at the same time, enhance its catalytic behaviour [2.188].
So far, the sensing behaviour of gold-decorated ZnO nanostructures have been extensively studied in thermo-activation mode [2.189], but only a few types of research have investigated the effect of the radiation to improve the chemoresistive properties of Au/ZnO. These works studied the interaction of Au/ZnO with a restrained number of gaseous molecules, and the photo-activation mechanism was investigated with a specific excitation wavelength, usually the UV [2.190]. Recently, Gogurla et al. have shown the sensing performance of an Au-ZnO plasmonic device activated with diverse radiation wavelengths and tested with several gases [2.191].
In a previous work [2.29], we investigated the difference between the chemoresistive properties of thin- and thick-films made of nanostructured pure ZnO in photo-activation mode. This study highlights better sensing features of thin films with respect to those of thick films. Starting from these results, we decided to focus the attention on the sensing properties of thin layers of pure ZnO and of ZnO decorated with gold clusters nanoparticles, in photo-activation mode.

2.5.1 Synthesis

ZnO powder (named pure ZnO) was synthesized by standard sol-gel technique. The ZnO solution was prepared by dissolving 300 mg of zinc acetate dihydrate in 2 mL of ethanol. Then, monoethanolamine was dropwise added under fast stirring, keeping the ratio between the metal ion and the amine equal to 1. The solution was stirred for 60 min.

ZnO decorated with gold nanoclusters (Au/ZnO) was prepared by a precipitation method using Gold(III) Bromide ($AuBr_3$) as a precursor. A molar concentration of 4.2 $mmol^{-1}$ $AuBr_3$ solution was heated at 80°C. The pH was adjusted to 7 by dropwise addition of a NaOH solution. Approximately 1 g of ZnO was dispersed in the solution. This dispersion caused a pH change, so it was re-adjusted to 7 by consequent dropwise addition of an HCl solution. Thus, the suspension was heated at 80°C and stirred for 2 h. The products were washed several times with distilled water to remove bromide ions residual as well as the unreacted Au species. After washing, calcination is needed to allow the decomposition of gold precursors to their metallic state. This procedure was carried out at 450°C for 4 h.

2.5.2 Chemical, Structural and Morphological Characterization

The results of XRD measurements of the synthesized nanopowders are shown in Figure 2.74. All films after annealing at 500°C were crystalline, as confirmed from XRD patterns. Diffraction peaks of wurtzite hexagonal ZnO (ICDD No. 36-1451) and cubic Au (ICDD No. 04-0784) were detected in the samples, according to the relative compositions, confirming that annealing at 450°C is sufficient to promote the oxides crystallization and the Au ions reduction. The Au ions reduction inside sol–gel oxide matrixes has been already investigated by [2.192]. This phenomenon approximately occurred at 200°C, due to the decomposition of gold chloride species and to the oxidation of organic compounds that can donate electrons, thus reducing noble metal ions [2.193]. By analysing the ZnO reflections, the (002) diffraction peak is much more intense than the predicted value; this fact indicates an extensive orientation along the c-axis. Performing a Lorentzian fit on the XRD peaks and measuring the full width at half maximum (FWHM), the mean crystallite diameter of ZnO was estimated to be 29 nm, by means of the Scherrer's relationship, while for Au it was 20 nm.

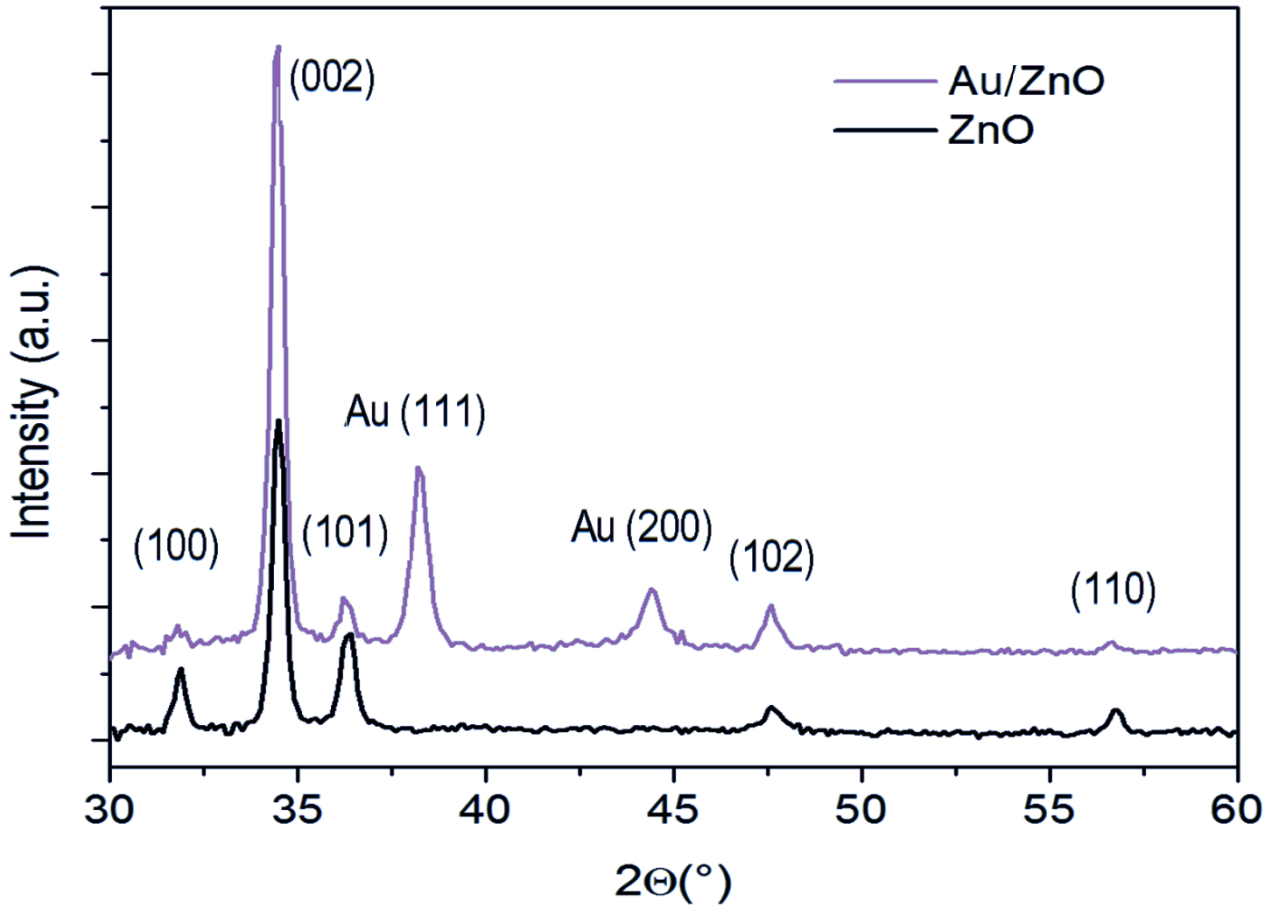

Figure 2.74: XRD analysis of pure ZnO and Au/ZnO [adapted from A.1].

The SEM-EDX characterizations are reported in Figure 2.75. The SEM images in Figure 2.75 *a)* and *b)* highlighted the nanometric size of the grains, which compose the films. The EDX chemical analysis showed a high degree of purity for both pure ZnO and Au/ZnO. Moreover, the weight concentration of Au, detected in the layer of Au/ZnO, was about 5.3%.

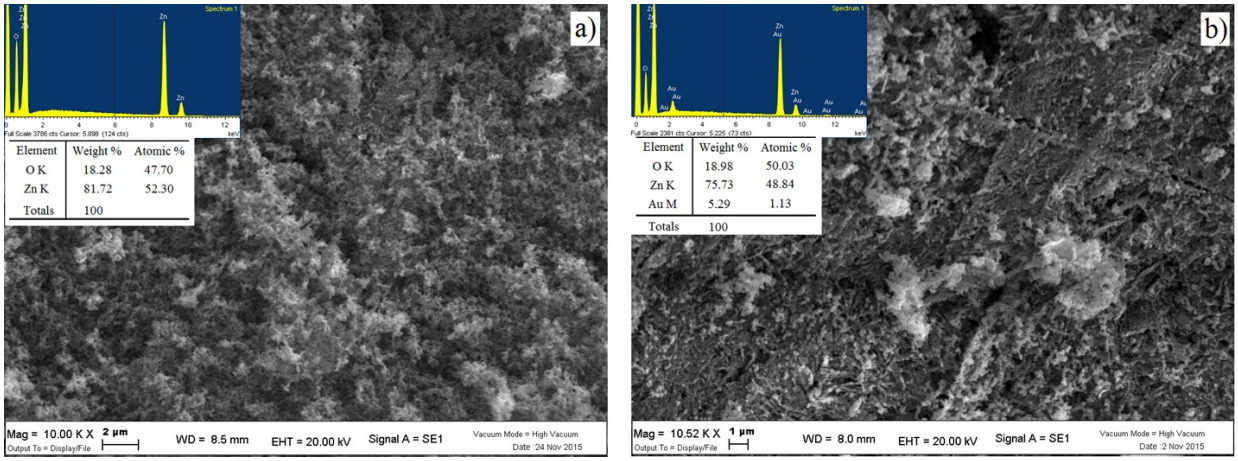

Figure 2.75: SEM images and EDX analysis of *a)* pure ZnO and *b)* Au/ZnO [adapted from A.1].

In the TEM image below is highlighted the presence of the Au clusters over ZnO nanoparticles. It is clearly observable the difference of grain size between ZnO (tens nanometers) and Au (few nanometers).

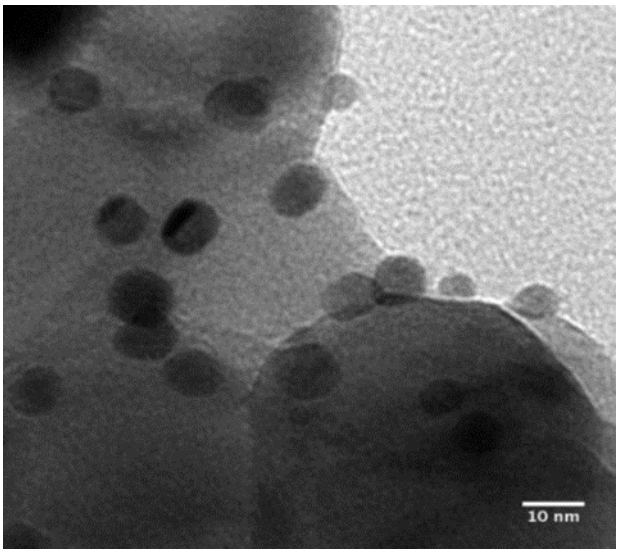

Figure 2.76: TEM image of Au/ZnO nanoparticles.

Optical absorption spectra of the ZnO and Au/ZnO films, deposited on SiO_2 substrates, are shown in Figure 2.77. The absorption spectrum of ZnO film in air follows the typical curve of ZnO, which is transparent in the visible and in near-infrared (NIR) range and presents an absorption onset in the UV, in the range of 350-370 nm, due to the zinc oxide band-gap. In the spectrum of Fig. 3, the exciton peak typical of low dimensional ZnO crystals is also evident [2.194]. For the Au/ZnO film, the presence of Au NPs is clearly confirmed by the localized surface plasmon resonance (LSPR) peak, recorded at ≈ 590 nm, while outside the LSPR range, the absorption of Au/ZnO sample is overlaid to the pure ZnO film.

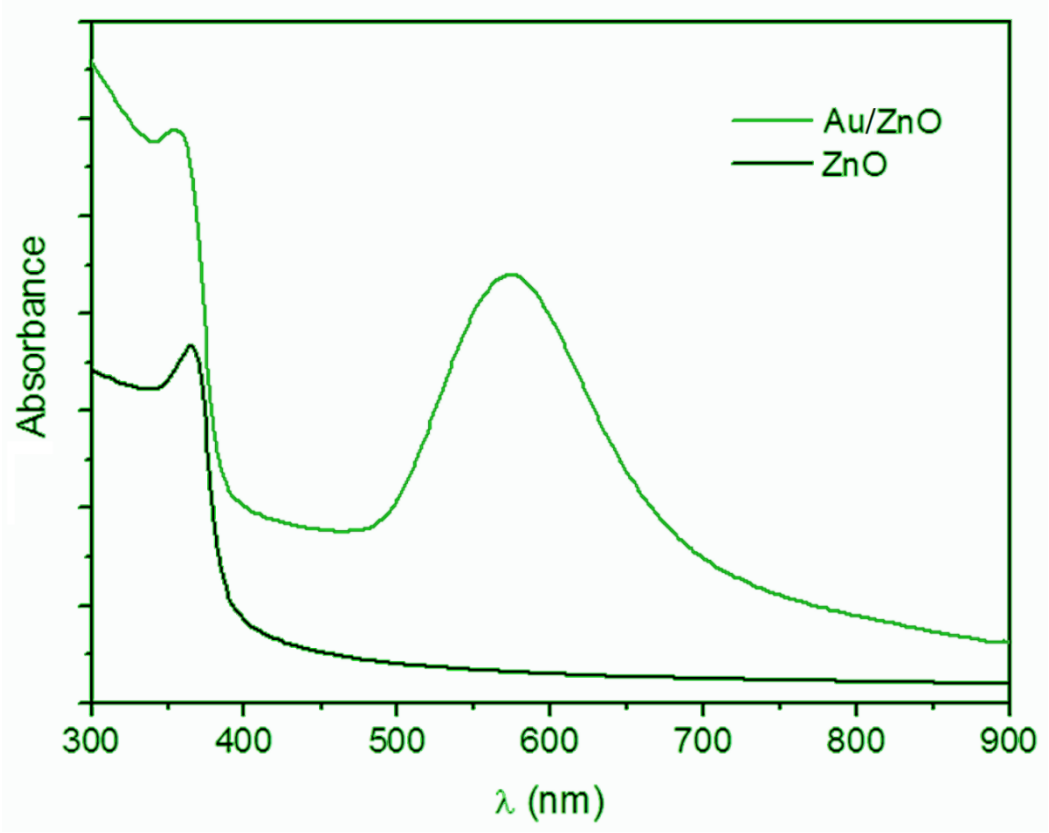

Figure 2.77: Uv-visible spectra of pure ZnO and Au/ZnO samples [adapted from A.1].

Figure 2.78 shows the Total Reflection X-Ray Fluorescence (TXRF) analysis of pure ZnO and Au/ZnO nanopowders. The quantification was performed by ab initio simulation of the fluorescence spectrum. The estimated atomic gold-to-zinc ratio was of 0.0193 (corresponding to 0.045 weight fraction of Au in a ZnO matrix). To fit properly the region containing the Au and Zn peaks, bromine was added to the model sample with a concentration of 0.0014 weight fraction. The spectra in Figure 2.78 showed Fe Kα and Ni Kα peaks, mainly due to environmental contamination rather than in the sample, since they are also visible in the blank wafer spectrum. The analysis highlighted the high purity of the obtained ZnO and detected a very little contamination of bromine in the Au/ZnO sample (0.14 atomic%).

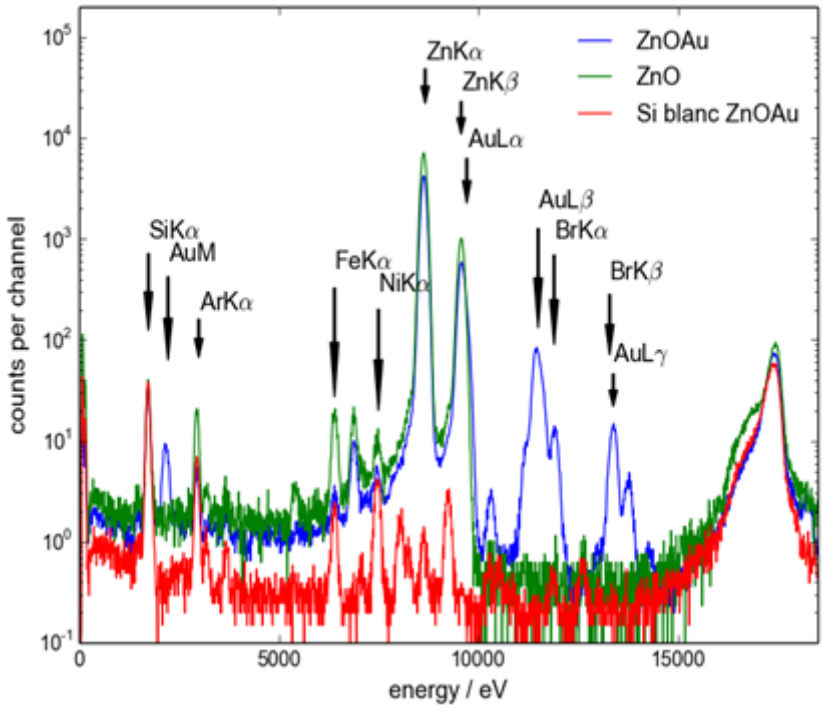

Figure 2.78: TXRF analysis of ZnO and Au/ZnO samples [adapted from A.1].

2.5.3 Electrical Characterization

Obtained powders were mixed with an ethanol solution and thus deposited by spin-coating technique at 2000 rpm for 30 seconds on two substrate types of, a transparent glass for the optical absorption measurements and an alumina substrate with interdigitated electrodes for the electrical measurements. Thin films were thermally stabilized at 100°C for 10 minutes in an air atmosphere. The process of spinning/stabilization was repeated up to 4 times. Films thickness, measured by ellipsometry, resulted to be 250 nm. A final annealing at 500°C for 1 hour in the air was performed.
To investigate the sensing behaviour of the nanostructured materials and to highlight the differences between pure ZnO and Au/ZnO layers, several gaseous compounds were tested.
The gas concentrations were chosen in according to the Threshold Limit Values (TLV) [2.126], i.e. CO (10 ppm), methane (2500 ppm), acetaldehyde (10 ppm), acetone (10 ppm), butanol (5 ppm), methanol (5 ppm), NO_2 (5 ppm), and SO_2 (10 ppm). In the case of methanol, we focused on concentrations far below its TLV. For the other compounds, we injected concentrations of the same order of TLV, except for the case of acetone, whose odour threshold is 50 times lower than TLV, therefore we used a half concentration value with respect to odour threshold.

LEDs used to photo-activate layers were four: green (525 nm), blue (468 nm), violet (400 nm), and UV (385 nm) light.

2.5.3.1 Photo-Activation Mode

The sensors were first stabilized in dry air, under continuous illumination of diverse radiations wavelengths. For each radiation energy, several gases were tested. We chose to limit the exposure time at 25 minutes since usually, within this range time, thin-film sensors tested in photo-activation mode reach the 90% of the maximum response value, by using our experimental setup. The Figure 2.79 summarizes the responses obtained with the two sensing materials, tested in presence of selected gases in the dry air.

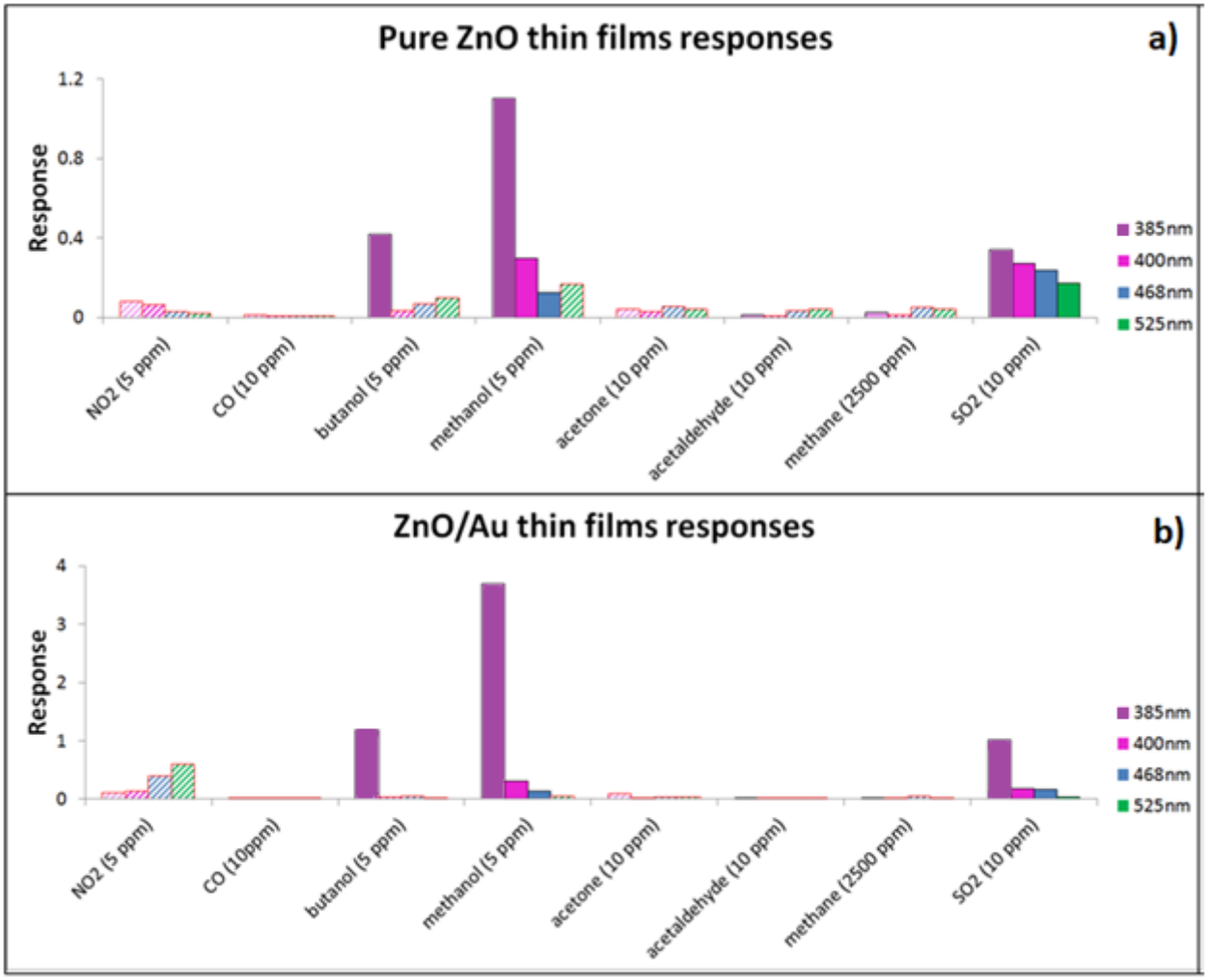

Figure 2.79: Summary of *a)* ZnO and *b)* Au/ZnO gas-sensing responses vs. gases analysed, photo-activated with four different LEDs [adapted from A.1].

It can be observed that, for both pure ZnO and Au/ZnO films, the highest responses were obtained with butanol, methanol and sulphur dioxide. At the same time, the conductance variations of the films recorded in presence of CO, acetone, acetaldehyde and methane were negligible. Conversely, the measurements performed with 5 ppm of NO_2 resulted in a significant signal for almost all radiation wavelengths we tested. However, the case of NO_2 deserves deeper considerations, and it will be discussed last.

The above mentioned highest responses, achieved with butanol, methanol and SO_2, were obtained by illuminating both the sensing films with a radiation wavelength of 385 nm. This behaviour has already been observed in previous works [2.29], in which it was demonstrated that a more effective chemoresistive interaction occurs between analytes and ZnO nanoparticles as the energy of the incident radiation approaches the ZnO band gap (3.37 eV). The responses of Au/ZnO films, excited with a radiation wavelength of 385 nm, to butanol, methanol and SO_2, were significantly higher than those obtained with pure ZnO layers, as it can be seen in Figure 2.78. With this excitation wavelength, the ratio between the responses of Au/ZnO and pure ZnO films remains constant ($R_{Au/ZnO}/R_{ZnO} \approx 3$) for the three gases. Moreover, it can be noticed that the ratio between the responses obtained at 385 nm of radiation and those obtained at different radiation wavelengths was significantly higher in the case of Au/ZnO films (e.g. for methanol R385/R400 ≈ 12) than pure the ZnO ones (e.g. for methanol R385/R400 ≈ 3.7). It is also interesting to highlight that, for butanol and methanol, pure ZnO films showed a different behaviour (oxidizing/reducing) in the interaction between their surface and chemical compounds. This anomalous phenomenon occurs for all the four radiation wavelengths used in the sensors electrical characterization, and it could be ascribed to an induced conductivity switching in ZnO thin film, as reported in the literature for nitrogen dioxide [2.195]. Here, two competing mechanisms were suggested to occur: a change in charge carrier density and a participation of oxygen vacancies.
Figure 2.79 shows the dynamic response to 5 ppm of methanol of pure ZnO and Au/ZnO films in dry air.

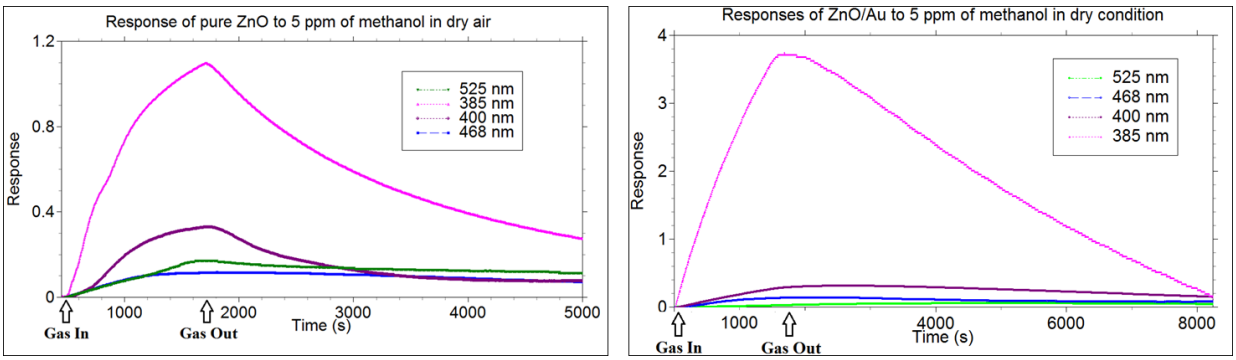

Figure 2.80: Dynamic responses of *a)* ZnO and *b)* Au/ZnO sensors vs. 5 ppm of methanol, photo-activated with four different LEDs [adapted from A.1].

One can observe, for both the films, that a better kinetics of the reaction occurred when the layers were photo-activated with the wavelength of 385 nm, with respect to the other three wavelengths. This behaviour was also obtained with almost all the other tested gases and could be a consequence of the low-radiation energy, which allows the formation of only a few hole-electron pairs. The last could be dragged by the electric field toward the surface, where they would be annihilated by electrons trapped in the surface states, resulting in desorption process and restoration of conductance level. Instead, when the energy of the excitation wavelength is significantly lower than the energy of the semiconductor band-gap, no efficient photo-activation occurs to create enough electron-hole pairs. Indeed, in presence of oxygen, the density of charged surface states (O^-/O_2^-), remains sufficiently high to cause the pinning of Fermi level [2.196], resulting in a great decrease of the semiconductor surface reactivity in presence of few ppm of chemical compounds.
Moreover, Figure 2.79 highlights a faster response and recovery time (calculated as 1/e of the response value) of Au/ZnO than pure ZnO when photo-activated with UV LED (385 nm). This behaviour was also confirmed with the other gases analysed, in particular with SO_2 (Figure 2.80) and butanol.

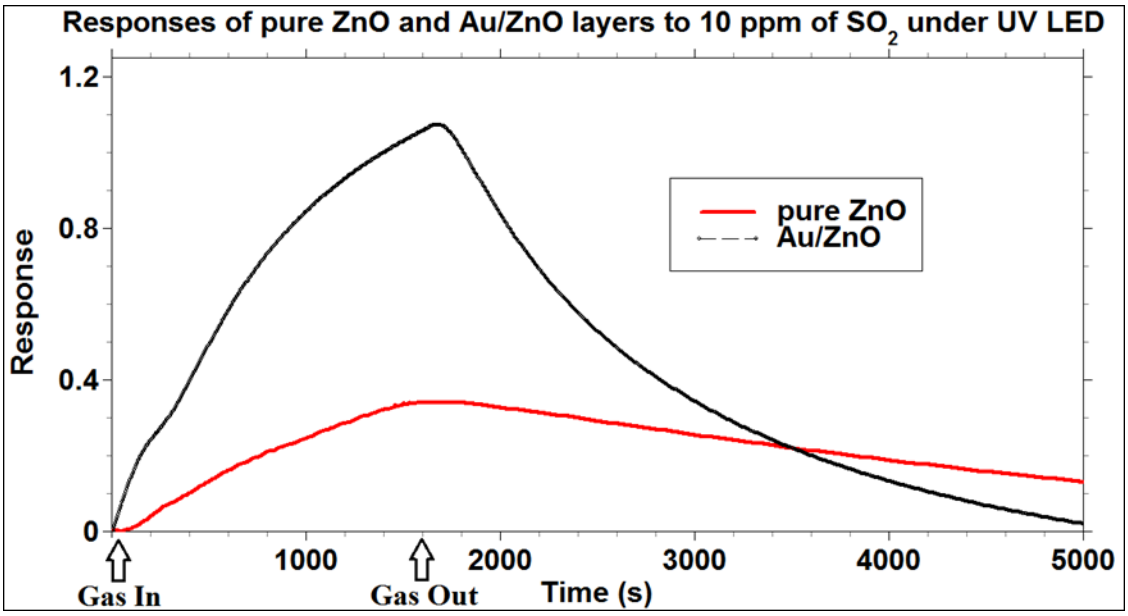

Figure 2.81: Dynamic responses of *a)* pure ZnO and *b)* Au/ZnO sensors vs. 10 ppm of SO_2 illuminated with a UV LED [adapted from A.1].

The influence of humidity on the gas sensing properties of ZnO and Au/ZnO sensors was also investigated. The characterization was performed for those analytes that gave the better chemoresistive properties in dry air for the ZnO and Au/ZnO layers. We tested butanol, methanol, SO_2 and NO_2 by using the incident radiation wavelength of 385 nm, and NO_2 with the green LED. Gas concentrations were the same used for the sensing characterization in dry air. The measures were carried out with a relative humidity of 20%, 40%, 60%, and 80%.

The sensing responses to 5 ppm of methanol and butanol decreased drastically already at 20% RH for both materials, vanishing at 40% RH. This trend is probably due to the interaction between the OH^- groups of water with the sensing layers, which hindered interaction of hydroxyl groups contained in the alcohols.

The SO_2 sensing characterization in wet air highlighted interesting features of the sensing layers. The recorded temperatures were 23.2°C (RH% = 20%), 23.1°C (RH% = 40%), 23.4°C (RH% = 60%) and 23.7 (RH% = 80%). Considering pure ZnO, the response to SO_2 quickly decreased when relative humidity was increased. At the same time, the recovery times became much longer than the one in dry air, resulting in incomplete recovery at relative humidity higher than 60%. On the contrary, Au/ZnO sensors showed a gradual response decrease to 5 ppm of SO_2 when humidity was increased, but the response remained significant even at 80% of relative humidity, as shown in Figure 2.81. Furthermore, the recovery times in wet air were like each other as compared to the measurement carried out under dry air.

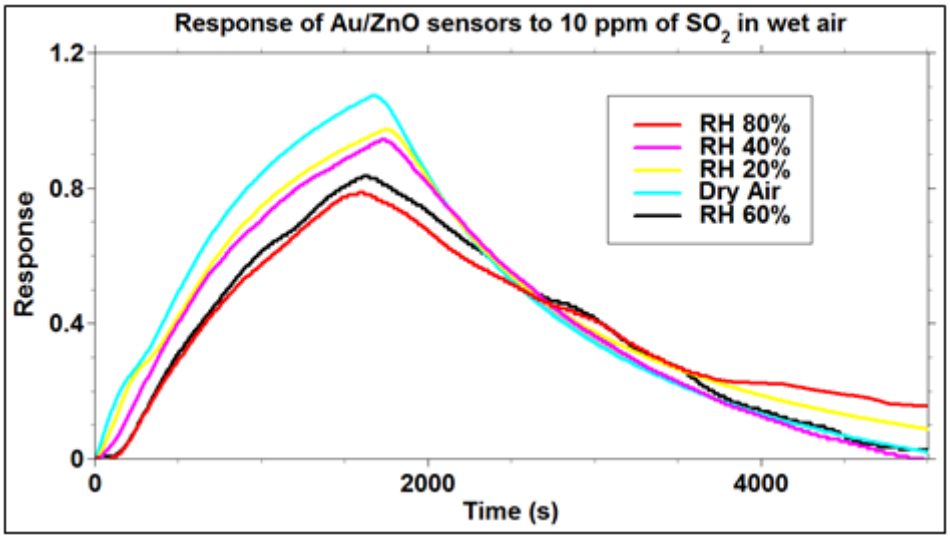

Figure 2.82: Dynamic responses of Au/ZnO sensors vs. 10 ppm of SO_2, illuminated with a UV LED, at different percentage of relative humidity [adapted from A.1].

The better chemoresistive properties of Au/ZnO than pure ZnO, which arose in Figure 2.78, 2.79 and 2.80 especially at 385 nm of excitation wavelengths, were clearly due to the gold nanoclusters and they can be explained by means of two main reasons. First, the limiting factor that controls the efficiency of light-excited single oxide semiconductor photocatalysts is the high-rate recombination of the photo-generated charge carriers [2.197]. In Au/ZnO layers, the presence of gold nanoclusters leads to an efficient charge separation of the photogenerated electron-hole pairs in Au, which modifies the photocatalysts properties on the ZnO surface and, consequently, increases the lifetime of the photo-generated pairs. This condition allows longer time for the charge carriers diffusion and for their migration on the catalysts surface, which promote redox processes in the valence and in the conduction bands of the semiconductor [2.198]. Hence, this enhancement can be explained through an "electronic mechanism" as well as a "chemical mechanism". In the "electronic mechanism", the Au nanoclusters act as electron acceptors on the ZnO surface, contributing to the increase of the depletion layer by a compensation effect [2.199]. Therefore, with respect to the pure oxide case, the change in the resistance results larger, leading to the increase in response. In the "chemical mechanism", Au catalytically activates the dissociation of molecular oxygen, whose ionic products diffuse to the ZnO nanograins [2.200].

As far as the second reason, it concerns the high activity, as heterogeneous and homogeneous catalysts, of unsupported Au nanoparticles in the process of oxidation and reduction of several VOC types, as reported in previous works [2.201, 2.202]. The role of the catalyst is under continuous discussion and different mechanisms have been proposed [2.203]. Based on the above considerations, the better chemoresistive properties of Au/ZnO than pure ZnO are addressed.

Regarding NO_2, its strange behaviour vs Au/ZnO is commented below. The oxidizing character of NO_2 in the interaction with semiconductor catalysts surface is well known, both under thermo- and photo-activation modes [2.29, 2.168]. The responses of ZnO and Au/ZnO films to NO_2, reported in Figure 2.78, confirmed this behaviour for all the four radiation wavelengths. The reaction most probably occurring between this chemical compound and the sensing layers of ZnO and Au/ZnO is [2.168]:

$$NO_2 + e^- \rightarrow NO^-_{2(ads)}$$

The above reaction causes a decrease in electron density at the surface of the semiconductor layer, which undergoes an increase in resistance, this being observed in our sensing measurements. Others type of VOCs, which show this behaviour with activated catalysts, are CO_2 and O_3.
Although the responses in Figure 2.78 confirmed the better ability of Au/ZnO and ZnO sensors to detect gaseous compound at 385 nm, they showed a peculiar characteristic of the two sensing materials in the case of NO_2. NO_2 measurements with pure ZnO sensors showed the same trend of the other gases tested, i.e., a higher response as the wavelength radiation approaches the energy of the ZnO band gap, whereas Au/ZnO films highlighted a clearly different behaviour. In fact, the latter presented an increase of the response to NO_2 as the energy of the incident radiation decreased, and it showed a major chemoresistive interaction under green-light irradiation (525 nm) with respect to the other three wavelengths tested. This feature is also highlighted in Figure 2.82, which shows the dynamic responses of the two sensing films to 5 ppm of nitrogen dioxide as a function of the incident radiation wavelength.

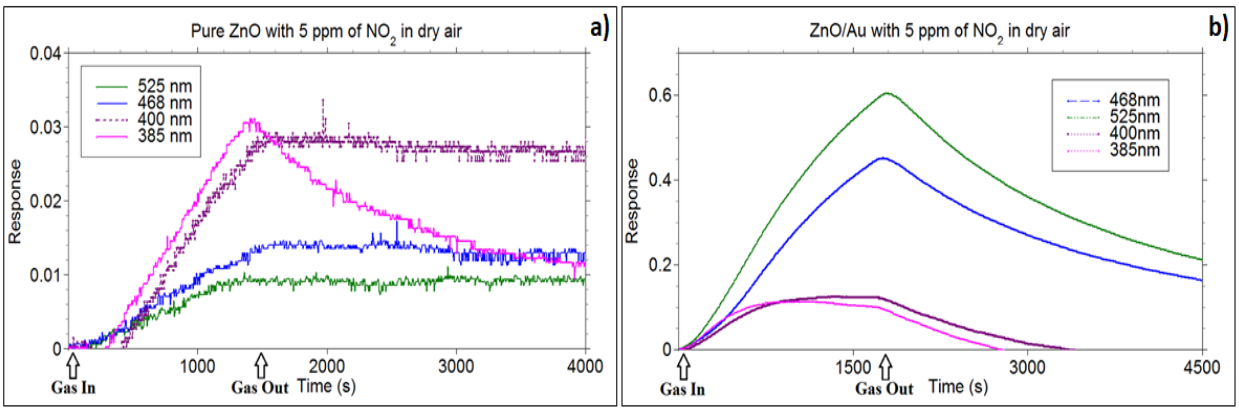

Figure 2.83: Dynamic responses of *a)* pure ZnO and *b)* Au/ZnO sensors, vs. 5 ppm of NO_2, photo-activated with four different LEDs [adapted from A.1].

The kinetics of the interaction between this chemical compound and pure ZnO layers appears to be slower than that showed by Au/ZnO films, and it is coupled with a lack of reversibility of the former (except for 385 nm), as extensively discussed in Ref. [2.29]. Instead, for Au/ZnO films, the responses to NO_2 resulted reversible for all radiation wavelengths used.
As introduced before, the behaviour of Au/ZnO layers with NO_2 is different from both pure ZnO tested with the same gas and from Au/ZnO tested with the other gaseous compounds Au/ZnO. Indeed, with nitrogen dioxide, the reversible and highest response for Au/ZnO sensors was obtained with green light (525 nm), and not at 385 nm as for pure ZnO films. At the same time, the responses achieved for the other chemical compounds tested with Au/ZnO at 525 nm of excitation were negligible. From the sensing point of view, the behaviour of Au/ZnO tested with NO_2 under green light radiation is quite interesting for a possible use of this sensor in the selective detection of nitrogen dioxide at room temperature in dry air. Furthermore, sensing tests carried out in wet air showed that the responses of ZnO and Au/ZnO layers to 5 ppm of NO_2 decreased quickly with 385 nm as incident radiation, and they became negligible at 60% RH. On the contrary, the sensing response of Au/ZnO to NO_2 was still interesting even in the wet air, when the layers were photo-activated with the green LED (525 nm). It is worth noting that the conductance variation of the sensors remained measurable up to 80% RH, although the recovery times became longer compared to the one measured in dry air. The sensing response to NO_2 of Au/ZnO in the wet air is reported in the Figure 2.83.

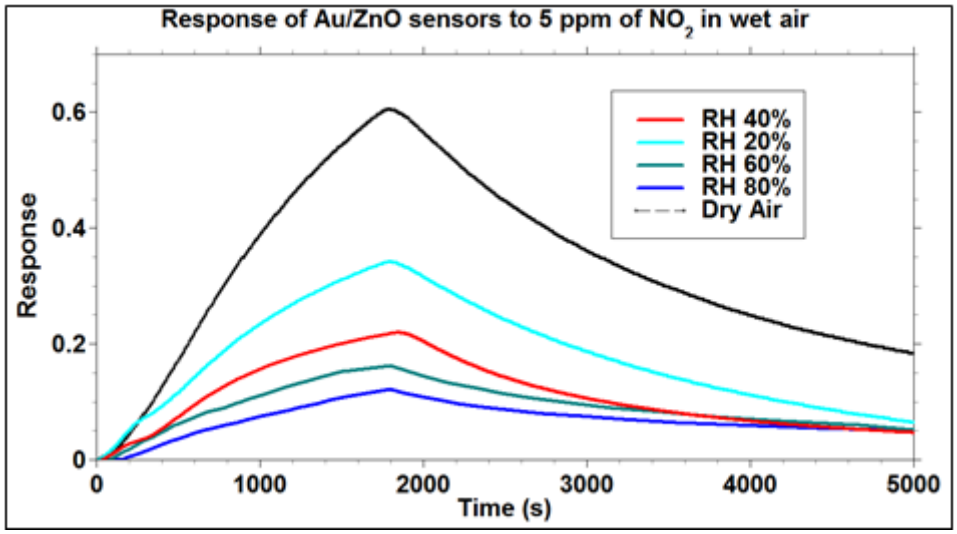

Figure 2.84: Dynamic responses of Au/ZnO sensors vs. 5 ppm of NO_2, photoactivated with green light LED, in wet condition [adapted from A.1].

Testing temperatures in the test chamber were 23.0°C (RH% = 20%), 23.7°C (RH% = 40%), 24.2°C (RH% = 60%) and 23.9°C (RH% = 80%). A possible interpretation of the NO_2 reactivity on Au/ZnO layers under green light could lie in an accentuated photo-catalysis property of gold nanoclusters due to its surface plasmon resonance, which is near to 525 nm, and this could play a fundamental role. Sarina et al. [2.204] and Mukherjee et al. [2.205] demonstrated that, when gold nanoparticles are illuminated with a suitable radiation energy, the conduction electrons in the 6sp band of gold nanoparticle surface can gain energy from absorption of light via the localized surface plasmon resonance (LSPR) effect, and then migrate to the higher energy levels of 6sp band through an intraband migration. These "hot electrons", which shift to the higher energy levels, can be captured by oxidizing molecules such as oxygen or, as is our case, NO_2. Then, in the case of the interaction between Au/ZnO films and NO_2, this gold feature leads to a greater change in layers conductance and to an improvement of chemoresistive properties. To understand the mechanism that occurs at the surface between the nanostructured material and NO_2, which is out of the scope of this work, it would be necessary to follow the reactions by using a proper technique, such as XANES, and to test other oxidizing gases at different radiation wavelengths.

Bibliography

[2.1] V. E. Bochenkov and G. B. Sergeev, “Sensitivity, selectivity, and stability of gas-sensitive metal-oxide nanostructures,” Metal Oxide Nanostruct. Their Appl., vol. 3, pp. 31–52, 2010.
[2.2] Das, S., Jayaraman, V. SnO_2: A comprehensive review of structures and gas sensors. Prog. Mater Sci. 2014, 66, 112–255.
[2.3] Scanning Electron Microscopy, Ludwig Reimer, Springer-Verlag Berlin Heidelberg, 1998, ISBN: 978-3-642-08372-3.
[2.4] https://minalab.fbk.eu/scanning-electron-microscopy-sem.
[2.5] http://www.unife.it/centri/centro/microscopia-elettronica/servizi/strumenti-1-
[2.6] Williams, David; Carter, C. (2009). Transmission Electron Microscopy: A Textbook For Materials Science. New York, USA: Springer. p. 35. ISBN 978-0-387-76500-6.
[2.7] https://www.bo.imm.cnr.it/unit/articles/characterization-bologna-unit.
[2.8] X-ray Powder Diffractometry. An Introduction. (Serie: Chemical Analysis, Vol. 138.) Von R. Jenkins und R. L. Snyder. John Wiley & Sons, New York, 1996.
[2.9] I. Jiménez, J. Arbiol, G. Dezanneau, A. Cornet, J.R. Morante, Crystalline structure, defects and gas sensor response to NO_2 and H2S of tungsten trioxide nanopowders, In Sensors and Actuators B: Chemical, Volume 93, Issues 1–3, 2003, Pages 475-485.
[2.10] Bruker AXS: TOPAS V4: General profile and structure analysis software for powder diffraction data. - User's Manual, Bruker AXS, Karlsruhe, Germany, 2008.
[2.11] R.W. Cheary, A.A. Coelho, A fundamental parameters approach to X-ray line-profile fitting, J. Appl. Crystallogr. 25 (1992) 109-121;
[2.12] R. W. Cheary, A.A. Coelho, J.P. Cline, Fundamental Parameters LineProfile Fitting in Laboratory Diffractometers, J. Res. Natl. Inst. Stand. Technol. 109 (2004) 1-25.
[2.13] A. Kern, A.A. Coelho, R.W. Cheary, Convolution based profile fitting. Diffraction Analysis of the Microstructure of Materials, edited by Mittemeijer, E.J. & Scardi, P. Materials Science, Springer, Germany, 2004.
[2.14] D. Balzar, Voigt-function model in diffraction line-broadening analysis. - Microstructure Analysis from Diffraction, edited by R. L. Snyder, H. J. Bunge, and J. Fiala, International Union of Crystallography, 1999.
[2.15] C Garzella, E Comini, E Tempesti, C Frigeri, G Sberveglieri, TiO_2 thin films by a novel sol–gel processing for gas sensor applications, In Sensors and Actuators B: Chemical, Volume 68, Issues 1–3, 2000, Pages 189-196.
[2.16] Liu, J., Wang, X., Peng, Q. and Li, Y. (2005), Vanadium Pentoxide Nanobelts: Highly Selective and Stable Ethanol Sensor Materials. Adv. Mater., 17: 764–767.
[2.17] Coats, A. W., Redfern, J. P. (1963). "Thermogravimetric Analysis: A Review". Analyst. 88 (1053): 906–924.
[2.18] Bhadeshia H.K.D.H. “Thermal analyses techniques. Differential thermal analysis”. University of Cambridge, Material Science and Metallurgy, 2002.
[2.19] Knop-Gericke, A. (2012), X-ray Photoelectron Spectroscopy. An Introduction to Principles and Practices. By Paul van der Heide. Angew. Chem. Int. Ed., 51: 9218. doi:10.1002/anie.201205395.
[2.20] Cabot, A., Diéguez, A., Romano-Rodríguez, A., Morante, J.R., Bârsan, N. Influence of the catalytic introduction procedure on the nano-SnO2 gas sensor performances: Where and how stay the catalytic atoms? (2001) Sensors and Actuators, B: Chemical, 79 (2-3), pp. 98-106.
[2.21] https://fmps.fbk.eu/x-ray-photoelectron-spectroscopy-xps.

[2.22] Klockenkämper, R. and von Bohlen, A. (eds) (2014) Fundamentals of X-Ray Fluorescence, in Total-Reflection X-Ray Fluorescence Analysis and Related Methods, John Wiley & Sons, Inc., Hoboken, New Jersey. doi: 10.1002/9781118985953.ch01.
[2.23] Alessandri, I., Comini, E., Bontempi, E., Faglia, G., Depero, L.E., Sberveglieri, G.Cr-inserted TiO2 thin films for chemical gas sensors (2007) Sensors and Actuators, B: Chemical, 128 (1), pp. 312-319.
[2.24] https://minalab.fbk.eu/proton-transfer-mass-spectrometry-ptrms.
[2.25] Hanaor, D; Triani G.; Sorrell C.C.; (2011). Morphology and photocatalytic activity of highly oriented mixed phase titanium dioxide thin films. Surface and Coatings Technology, 205(12): 3658–3664. doi:10.1016/j.surfcoat.2011.01.007.
[2.26] M. Faustini, G. L. Drisko, C. Boissiere, D. Grosso, Liquid deposition approaches to self-assembled periodic nanomasks, Scripta Materiala 2014.
[2.27] Choy, K.L. Chemical vapour deposition of coatings (2003) Progress in Materials Science, 48 (2), pp. 57-170.
[2.28] Comini, E., Faglia, G., Sberveglieri, G., Pan, Z., Wang, Z.L.Stable and highly sensitive gas sensors based on semiconducting oxide nanobelts(2002) Applied Physics Letters, 81 (10), pp. 1869-1871.
[2.29] B. Fabbri, A. Gaiardo, A. Giberti, V. Guidi, C. Malagù, A. Martucci, M. Sturaro, G. Zonta, S. Gherardi, P. Bernardoni, Chemoresistive properties of photo-activated thin and thick ZnO films, In Sensors and Actuators B: Chemical, Volume 222, 2016, Pages 1251-1256.
[2.30] Kidd, J. Conventional Techniques for the production of High Density Interconnects (1987) Microelectronics International: An International Journal, 4 (3), pp. 34-37.
[2.31] Honoré, M., Lenaerts, S., Desmet, J., Huyberechts, G., Roggen, J. Synthesis and characterization of tin dioxide powders for the realization of thick-film gas sensors (1994) Sensors and Actuators: B. Chemical, 19 (1-3), pp. 621-624.
[2.32] Choe, J., Calata, J.N., Lu, G.-Q. Constrained-film sintering of a gold circuit paste (1995) Journal of Materials Research, 10 (4), pp. 986-994.
[2.33] Guidi V., Malagù C., Carotta M.C., Vendemiati, "Printed films: Materials science and applications in sensors, electronics and photonics" B. in WOODHEAD PUBLISHING SERIES IN ELECTRONIC AND OPTICAL MATERIALS (2012) pp. 278-334.
[2.34] H. Gleiter, Nanostructured materials: state of the art and perspectives, Nanostructured Materials, 6, 3-14, 1995.
[2.35] S. Pavasupree, S. Ngamsinlapasathian, Y. Suzuki, and S. Yoshikawa, J. Nanosci. Nanotechnol., 2006, 6(12), 3685.
[2.36] P. Jiang, J. F. Bertone, and V. L. Colvin, Science, 2001, 291, 453.
[2.37] S. D. Evans, S. R. Johnson, Y. L. L. Cheng, and T. H. Shen, J. Mater. Chem., 2000, 10, 183.
[2.38] S. Sun, C. B. Murray, D. Weller, L. Folks, and A. Moser, Science, 2000, 287, 1989.
[2.39] M. Haruta, Cattech, 2002, 6, 102.
[2.40] K.R. Jayadevan, T.Y. Tseng, Oxide nanoparticles, Encyclopedia of Nanoscience and Nanotechnology, 8 (2004), 333-376.
[2.41] Corriu, R.J.P.Ceramics and nanostructures from molecular precursors (2000) Angewandte Chemie - International Edition, 39 (8), pp. 1376-1398.
[2.42] Kuchibhatla, S.V.N.T., Karakoti, A.S., Bera, D., Seal, S. One dimensional nanostructured materials (2007) Progress in Materials Science, 52 (5), pp. 699-913.
[2.43] Jiang, J., Oberdörster, G., Biswas, P. Characterization of size, surface charge, and agglomeration state of nanoparticle dispersions for toxicological studies (2009) Journal of Nanoparticle Research, 11 (1), pp. 77-89

[2.44] Keller, A.A., Wang, H., Zhou, D., Lenihan, H.S., Cherr, G., Cardinale, B.J., Miller, R., Zhaoxia, J.I. Stability and aggregation of metal oxide nanoparticles in natural aqueous matrices (2010) Environmental Science and Technology, 44 (6), pp. 1962-1967.
[2.45] Hulteen, J.C. A general template-based method for the preparation of nanomaterials (1997) Journal of Materials Chemistry, 7 (7), pp. 1075-1087.
[2.46] Caruntu, G., Caruntu, D. and O'Connor, C. J. 2009. Liquid-Phase Synthesis of Inorganic Nanoparticles. Encyclopedia of Inorganic Chemistry.
[2.47] Cushing, B.L., Kolesnichenko, V.L., O'Connor, C.J. Recent advances in the liquid-phase syntheses of inorganic nanoparticles (2004) Chemical Reviews, 104 (9), pp. 3893-3946.
[2.48] S. Sahni, S. B. Reddy, B.S. Murty, Influence of process parameters on the synthesis of nano-titania by sol–gel route. Materials Science and Engineering A, 452–453, 758–762, 2007.
[2.49] M. Shojaie-Bahaabad, E. Taheri-Nassaj ,Economical synthesis of nano alumina powder using an aqueous sol–gel method. Materials Letters 62, 3364–3366, 2008.
[2.50] N. Lecerf, S. Mathur, H. Shen, M. Veith, S. Hufner, Chemical vapour and sol-gel synthesis of nanocomposite and ceramics using metal organic precursor. Scripta mater. 44, 2157–2160, 2001.
[2.51] N.N Ghosh and P. Pramanik, Synthesis of nano-sized ceramic powders using precipitated silica in aqueous sol-gel method, Nanostructured materials, 8 (8), 1041- 1045, 1997.
[2.52] M. Cernea, O. Monnereau, P. Llewellyn, L. Tortet and C. Galassi, Sol-gel synthesis and characterization of Ce doped-BaTiO3, J. Eur. Ceram. Soc., 26, 3241-3246, 2006.
[2.53] D. Sarkar, D. Mohapatra, S. Ray, S. Bhattacharyya, S. Adak and N. Mitra, Synthesis and characterization of sol-gel derived ZrO2 doped Al2O3 nanopowder, Ceram. Int., 33, 1275-1282, 2007.
[2.54] C. J. Brinker, G. W. Scherer, Sol-Gel Science. The Physics and Chemistry of Sol-Gel Processing. Processing Academic Press, San Diego, 1990.
[2.55] http://www.wikiwand.com/it/Processo_sol-gel.
[2.56] Burton, W.K., Cabrera, N. Crystal growth and surface structure. Part I (1949) Discussions of the Faraday Society, 5, pp. 33-39.
[2.57] Cabrera, N., Burton, W.K. Crystal growth and surface structure. Part II (1949) Discussions of the Faraday Society, 5, pp. 40-48.
[2.58] Alivisatos, A.P. Semiconductor Clusters, Nanocrystals, and Quantum Dots. Science 1996, 271, 933–937.
[2.59] Ma, D.D.D.; Lee, C.S.; Au, F.C.K.; Tong, S.Y.; Lee, S.T. Small-diameter silicon nanowire surfaces. Science 2003, 299, 1874–1877.
[2.60] Wang, Z.L.; Song, J.H. Piezoelectric Nanogenerators Based on Zinc Oxide Nanowire Arrays. Science 2006, 312, 242–246.
[2.61] Fang, X.S.; Bando, Y.; Gautam, U.K.; Zhai, T.; Gradecak, S.; Golberg, D. Heterostructures and superlattices in one-dimensional nanoscale semiconductors. J. Mater. Chem. 2009, 19, 5683–5689.
[2.62] Chen, K.C.; Wu, W.W.; Liao, C.N.; Chen, L.J.; Tu, K.N. Observation of Atomic Diffusion at Twin-Modified Grain Boundaries in Copper. Science 2008, 321, 1066–1069.
[2.63] Law, M.; Greene, L.E.; Johnson, J.C.; Saykally, R.; Yang, P.D. Nanowire dye-sensitized solar cells. Nat. Mater. 2005, 4, 455–459.
[2.64] Yang, P.; Yan, H.; Mao, S.; Russo, R.; Johnson, J.; Saykally, R.; Morris, N.; Pham, J.; He, R.; Choi, H.-J. Controlled growth of ZnO nanowires and their optical properties. Adv. Funct. Mater. 2002, 12, 323–331.
[2.65] Lai, C.H.; Huang, K.W.; Cheng, J.H.; Lee, C.Y.; Hwang, B.J.; Chen, L.J. Direct growth of high-rate capability and high capacity copper sulfide nanowire array cathodes for lithium-ion batteries. J. Mater. Chem. 2010, 20, 6638–6645.

[2.66] Chen, L.J. Metal silicides: An integral part of microelectronics. JOM 2005, 57, 24–30.
[2.67] Huang, K.W.; Wang, J.H.; Chen, H.C.; Hsu, H.C.; Chang, Y.C.; Lu, M.Y.; Lee, C.Y.; Chen, L.J. Supramolecular nanotubes with high thermal stability: A rigidity enhanced structure transformation induced by electron-beam irradiation and heat. J. Mater. Chem. 2007, 17, 2307–2312.
[2.68] Wen, Z.H.; Li, J.H. Hierarchically structured carbon nanocomposites as electrode materials for electrochemical energy storage, conversion and biosensor systems. J. Mater. Chem. 2009, 19, 8707–8713.
[2.69] Lu, M.Y.; Lu, M.P.; Chung, Y.A.; Chen, M.J.; Wang, Z.L.; Chen, L.J. Intercrossed sheet-like Ga-doped ZnS nanostructures with superb photocatalytic actvitiy and photoresponse. J. Phys. Chem. C 2009, 113, 12878–12882.
[2.70] Rogach, A.L.; Talapin, D.V.; Shevchenko, E.V.; Kornowski, A.; Haase, M.; Weller, H. Organization of Matter on Different Size Scales: Monodisperse Nanocrystals and Their Superstructures. Adv. Funct. Mater. 2002, 12, 653–664.
[2.71] Sun, S.; Murray, C.B.; Weller, D.; Folks, L.; Moser, A. Monodisperse FePt nanoparticles and ferromagnetic FePt nanocrystal superlattices. Science 2000, 287, 1989–1992.
[2.72] Murray, C.B.; Kagan, C.R.; Bawendi, M.G. Synthesis and characterization of monodisperse nanocrystals and close-packed nanocrystal assemblies. Annu. Rev. Mater. Sci. 2000, 30, 545–610.
[2.73] Sundar, V.C.; Eisler, H.-J.; Bawendi, M.G. Room-Temperature, Tunable Gain Media from Novel II–VI Nanocrystal–Titania Composite Matrices. Adv. Mater. 2002, 14, 739–743.
[2.74] Wu, Y.; Wadia, C.; Ma, W.L.; Sadtler, B.; Alivisatos, A.P. Synthesis and Photovoltaic Application of Copper(I) Sulfide Nanocrystals. Nano Lett. 2008, 8, 2551–2555.
[2.75] Li, T.L.; Lee, Y.L.; Teng, H. $CuInS_2$ Quantum Dots Coated with CdS as High-Performance Sensitizers for TiO2 Electrodes in Photoelectrochemical Cells. J. Mater. Chem. 2011, 21, 5089–5098.
[2.76] Bierman, M.J.; Jin, S. Potential applications of hierarchical branching nanowires in solar energy conversion. Energy Environ. Sci. 2009, 2, 1050–1059.
[2.77] Zou, Z.; Qiu, Y.; Xie, C.; Xu, J.; Luo, Y.; Wang, C.; Yan, H. CdS/TiO_2 nanocomposite film and its enhanced photoelectric responses to dry air and formaldehyde induced by visible light at room temperature. J. Alloys Compd. 2015, 645, 17–23.
[2.78] Xu, K.; Li, N.; Zeng, D.; Tian, S.; Zhang, S.; Hu, D.; Xie, C. Interface bonds determined gas-sensing of SnO_2-SnS_2hybrids to ammonia at room temperature. ACS Appl. Mater. Interfaces 2015, 7, 11359–11368.
[2.79] Shi, W.; Huo, L.; Wang, H.; Zhang, H.; Yang, J.; Wei, P. Hydrothermal growth and gas sensing property of flower-shaped SnS_2 nanostructures. Nanotechnology 2006, 17, 2918–2924.
[2.80] Fu, X.; Liu, J.; Wan, Y.; Zhang, X.; Meng, F.; Liu, J. Preparation of a leaf-like CdS micro-/nanostructure and its enhanced gas-sensing properties for detecting volatile organic compounds. J. Mater. Chem. 2012, 22, 17782–17791.
[2.81] Kim, H.R.; Haensch, A.H.; Kim, I.D.; Barsan, N.; Weimar, U.; Lee, J.H. The role of NiO doping in reducing the impact of humidity on the performance of SnO_2-based gas sensors: Synthesis, strategies, and phenomenological and spectroscopy studies. Adv. Funct. Mater. 2011, 21, 4456–4463.
[2.82] Yamazoe, N. Toward innovation of gas sensor technology. Sens. Actuators B 2005, 108, 2–14.
[2.83] Barsan, N.; Koziej, D.; Weimar, U. Metal oxide-based gas sensor research: How to? Sens. Actuators B 2007, 121, 18–35.
[2.84] D. Ma, W. Zhang, Q. Tang, R. Zhang, W. Yu, Y. Qian, Large-scale hydrothermal synthesis of SnS2 nanobelts, J. Nanosci. Nanotechno. 5 (2005) 806-809.

[2.85] H. Chang, E. In, K.-J. Kong, J.-O. Lee, Y. Choi, B.-H. Ryu, First-principles studies of SnS_2 nanotubes: A potential semiconductor nanowire, J. Phys. Chem. B 109 (2005) 30-32.
[2.86] H. Sun, M. Ahmad, J. Luo, Y. Shi, W. Shen, J. Zhu, SnS_2 nanoflakes decorated multiwalled carbon nanotubes as high performance anode materials for lithium-ion batteries, Mater. Res. Bull. 49 (2014) 319-324.
[2.87] B. Yang, X. Zuo, H. Xiao, SnS_2 as low-cost counter-electrode materials for dye-sensitized solar cells, Mater. Lett. 133 (2014) 197-199.
[2.88] W. Deng, X. Chen, Z. Liu, A. Hu, Q. Tang, Z. Li, Y. Xiong, Three-dimensional structure-based tin disulfide/vertically aligned carbon nanotube arrays composites as high-performance anode materials for lithium ion batteries, J. Power Sources 277 (2015) 131-138.
[2.89] L. Wang, L. Gao, H. Song, High-performance top-gated monolayer SnS_2 field-effect transistors, Advanced Optoelectronics for Energy and Environment, AOEE 2013, Wuhan (China) 25-26 May 2013.
[2.90] X. Liu, H. Bai, Hydrothermal synthesis of visible light active zinc-doped tin disulphide photocatalyst for the reduction of aqueous Cr(VI), Powder Technol. 237 (2013) 610-615.
[2.91] Barsan, N., Schweizer-Berberich, M. & Göpel†, W. Fresenius J Anal Chem (1999) 365: 287.
[2.92] C. Malagù, A. Giberti, S. Morandi, C.M. Aldao, Electrical and spectroscopic analysis in nanostructured SnO_2: "long-term" resistance drift is due to in-diffusion, J. Appl. Phys. 110 (2011) 093711.
[2.93] C.M. Aldao, D.A. Mirabella, M.A. Ponce, A. Giberti, C. Malagù, Role of intragrain oxygen diffusion in polycrystalline tin oxide conductivity, J. Appl. Phys. 109 (2011) 063723.
[2.94] Ou, J.Z.; Ge, W.; Carey, B.; Daeneke, T.; Rotbart, A.; Shan, W.; Wang, Y.; Fu, Z.; Chrimes, A.F.; Wlodarski, W.; et al. Physisorption-Based Charge Transfer in Two-Dimensional SnS_2 for Selective and Reversible NO_2 Gas Sensing. ACS Nano 2015, 9, 10313–10323.
[2.95] Li Y, Xie H, Tu J (2009) Nanostructured SnS/carbon composite for supercapacitor. Mater Lett 63:1785–1787.
[2.96] Rao MM, Jayalakshmi M, Reddy RS (2004) Time-selective hydrothermal synthesis of SnS nanorods and nanoparticles by thiourea hydrolysis. Chem Lett 33:1044.
[2.97] Gaponendo SV (1998) Optical properties of semiconductors nanocrystals. Cambridge University Press, Cambridge.
[2.98] Sunil H. Chaki, M. P. Deshpande, Devangini P. Trivedi, Jiten P. Tailor, Mahesh D. Chaudhary, Kanchan Mahato. Wet chemical synthesis and characterization of SnS_2 nanoparticles. Appl Nanosci (2013) 3:189–195.
[2.99] Dumbrava, A.; Badea, C.; Prodan, G.; Popovici, I.; Ciupina, V. Zinc sulfide fine particles obtained at low temperature. Chalcogenide Lett. 2009, 6, 437–443.
[2.100] Zhang, Y.C.; Du, Z.N.; Li, K.W.; Zhang, M. Size-controlled hydrothermal synthesis of SnS_2 nanoparticles with high performance in visible light-driven photocatalytic degradation of aqueous methyl orange. Sep. Purif. Technol. 2011, 81, 101–107.
[2.101] M. Yang, Y.C. Zhang, W.M. Dai, K. Hang, Y.Q. Pan, Synthesis of SnS_2/SnO_2 nanocomposite for visible light-driven photocatalytic reduction of aqueous Cr(VI), Key Eng. Mat. 538 (2013) 46-49.
[2.102] J. Madarász, P. Bombiczb, M. Okuyaa, S. Kanekoa, Thermal decomposition of thiourea complexes of Cu(I), Zn(II), and Sn(II) chlorides as precursors for the spray pyrolysis deposition of sulfide thin films, Solid State Ionics 141–142 (2001) 439–446.
[2.103] D. Haridas, V. Gupta, Enhanced response characteristics of SnO2 thin film based sensors loaded with Pd clusters for methane detection, Sens. Actuators B 166 (2012) 156-164. doi:10.1016/j.snb.2012.02.026
[2.104] A. Giberti, M.C. Carotta, B. Fabbri, S. Gherardi, V. Guidi, C. Malagù, High-sensitivity detection of acetaldehyde, Sens. Actuators B 174 (2012) 402-405.

[2.105] V. Guidi, M.C. Carotta, B. Fabbri, S. Gherardi, A. Giberti, C. Malagù, Array of sensors for detection of gaseous malodors in organic decomposition products, Sens. Actua. B, (2012) 349-354.
[2.106] Kim, S.; Park, S.; Park, S.; Lee, C. Acetone sensing of Au and Pd-decorated WO_3 nanorod sensors. Sens. Actuators B 2015, 209, 180–185.
[2.107] Koziej, D.; Thomas, K.; Barsan, N.; Thibault-Starzyk, F.; Weimar, U. Influence of annealing temperature on the CO sensing mechanism for tin dioxide based sensors-Operando studies. Catal. Today 2007, 126, 211–218.
[2.108] R. R. Chianelli, G. Berhault, B. Torres, Unsupported transition metal sulfide catalysts: 100 years of science and application, Catalysis Today 147 (2009) 275-286.
[2.109] S. J. Tauster, T. A. Pecoraro, R. R. Chianelli, Structure and properties of molybdenum sulfide: correlation of O_2 chemisorption with hydride sulfurization activity, Journal of Catalysis 63 (1980) 515-519.
[2.110] L.P. Chikhale, J.Y.Patil, A.V.Rajgure, F.I.Shaikh, I.S.Mulla, S.S.Suryavanshi, Structural, morphological and gas sensing properties of undoped and Lanthanum doped nanocrystalline SnO_2, Ceramics International 40 (2014) 2179–2186.
[2.111] Tomchenko, A.A.; Harmer, G.P.; Marquis, B.T.; Allen, J.W. Semiconducting metal oxide sensor array for the selective detection of combustion gases. Sens. Actuators B 2003, 93, 126–134.
[2.112] Malagù, C.; Fabbri, B.; Gherardi, S.; Giberti, A.; Guidi, V.; Landini, N.; Zonta, G. Chemoresistive gas sensors for detection of colorectal cancer biomarkers. Sensors 2014, 14, 18982–18992.
[2.113] D. Shvydka, J. Drayton, A.D. Compaan, V.G. Karpov, Piezo-effect and physics of CdS-based thin film photovoltaics, Appl. Phys. Lett. 87 (2005) 123505.
[2.114] S.-L. Fu, T.-S. Wu, M.-P. Houng, The photoconduction mechanisms of screen-printed CdS films, Sol. Energ. Mater. 12 (1985) 309–317.
[2.115] I.J. Ferrer, P. Salvador, Photoluminescence and electroluminescence mechanisms at polycrystalline CdS in air and in contact with aqueous electrolytes, J. Appl. Phys. 66 (1989) 2568.
[2.116] R.R. Arya, P.M. Sarro, J.J. Loferski, Efficient cadmium sulfide on silicon solar cells, Appl. Phys. Lett. 41 (1982) 355.
[2.117] X. Jiao, L. Zhang, Y. Lv, Y. Su, A new alcohols sensor based on catoluminescence on nano-CdS, Sens. Actuators B 186 (2013) 750–754.
[2.118] Fu, X.; Liu, J.; Wan, Y.; Zhang, X.; Meng, F.; Liu, J. Preparation of a leaf-like CdS micro-/nanostructure and its enhanced gas-sensing properties for detecting volatile organic compounds. J. Mater. Chem. 2012, 22, 17782–17791.
[2.119] Jiao, X.; Zhang, L.; Lv, Y.; Su, Y. A new alcohols sensor based on cataluminescence on nano-CdS. Sens. Actuators B: Chem. 2013, 186, 750–754.
[2.120] Du, L.; Zhang, Y.; Lei, Y.; Zhao, H. Synthesis of high-quality CdS nanowires and their application as humidity sensors. Mater. Lett. 2014, 129, 46–49.
[2.121] Wang, P.; Deng, P.; Nie, Y.; Zhao, Y.; Zhang, Y.; Xing, L.; Xue, X. Synthesis of CdS nanorod arrays and their applications in flexible piezo-driven active H_2S sensors. Nanotechnology 2014, 25.
[2.122] Winter, J.; Gomez, N.; Gatzert, S.; Schmidt, C.; Korgel, B. Variation of cadmium sulfide nanoparticle size and photoluminescence intensity with altered aqueous synthesis conditions. Colloids Surf. A 2005, 254, 147–157.
[2.123] Kundu, M.; Khosravi, A.A.; Kulkarni, S.K. Synthesis and study of organically capped ultra-small clusters of cadmium sulphide. J. Mater. Sci. 1997, 32, 245–258.
[2.124] Dumbrava, A.; Badea, C.; Prodan, G.; Ciupina, V. Synthesis and characterization of cadmium sulfide obtained at room temperature. Chalcogenide Lett. 2010, 7, 111–118.
[2.125] Nie, Q.; Yuan, Q.; Chen, W.; Xu, Z. Effects of coordination agents on the morphology of CdS nanocrystallites synthesized by the hydrothermal method. J. Cryst. Growth 2004, 265, 420–424.

[2.126] https://www.cdc.gov/niosh/.
[2.127] Clifford, P.K.; Tuma, D.T. Characteristics of semiconductor gas sensors II. transient response to temperature change. Sens. Actuators 1982–1983, 3, 255–281.
[2.128] S. G. Hickey, D. J. Riley, and E. J. Tull, J. Phys. Chem. B 104, 7623 (2000).
[2.129] P. Vasa, P. Taneja, P. Ayyub, B. P. Singh, and R. Banerjee, J. Phys.: Condens. Matter 14, 281 (2002).
[2.130] L. Xi, W. X. W. Tan, K. S. Chua, C. Boothroyd, and Y. M. Lam, Thin Solid Films 517, 6430 (2009).
[2.131] Zhang, Y., Zhang, N., Tang, Z.-R., Xu, Y.-J. Transforming CdS into an efficient visible light photocatalyst for selective oxidation of saturated primary C-H bonds under ambient conditions (2012) Chemical Science, 3 (9), pp. 2812-2822.
[2.132] C. Malagù, M. C. Carotta, A. Giberti, V. Guidi, G. Martinelli, M. A. Ponce, M. S. Castro, and C. M. Aldao, Sens. Actuators, B 136, 230 (2009).
[2.133] A. Giberti and C. Malagu, Thin Solid Films 548, 683 (2013).
[2.134]] A.I. Ekimov, Al.L. Efros, A.A. Onushchenko, Quantum size effect in semiconductor microcrystals, Solid State Commun. 56 (1985) 921–924.
[2.135] Y. Wang, N. Herron, Nanometer-sized semiconductor clusters: materials synthesis, quantum size effects, and photophysical properties, J. Phys. Chem. 95 (1991) 525–532.
[2.136] G. Kuwabara, J. Phys. Soc. Jpn. 9, 97 (1954).
[2.137] N. B. Kindig and W. E. Spicer, Phys. Rev. 138, A.561 (1965).
[2.138] R. H. Bube, J. Chem. Phys. 21, 1409 (1953).
[2.139] Z. Li et al., International Journal of Applied Ceramic Technology, article in press, doi: 10.1111/ijac.12514.
[2.140] S. Cao et al., Journal of Materials Science, 51, pp. 1-10 (2016); doi: 10.1007/s10853-016-9780-3.
[2.141] N. Alaal et al., Journal of Physics D: Applied Physics, vol. 49, issue 8 (2016); doi: 10.1088/0022-3727/49/10/105306.
[2.142] R. Elpelt et al., Materials Science Forum, ICSCRM 2015, Volume 858, 2016, Pages 817-820, doi: 10.4028/www.scientific.net/MSF.858.817.
[2.143] Oliveros, A., Guiseppi-Elie, A. & Saddow, S.E. Biomed Microdevices (2013) 15: 353.
[2.144] K. Kubo, N. Tsukasa, M. Uehara, Y. Izumi, M. Ogino, M. Kitano et al.,Calcium and silicon from bioactive glass concerned with formation of nodules in periodontal-ligament fibroblasts in vitro. J. OralRehabil. 24, 70–5 (1997).
[2.145] P. Tobias, B. Golding, R. Ghosh, Interface states in high temperature gas sensors based on SiC, IEEE Sens. J. 3 (2003) 543–547.
[2.146] J. Schalwig, P. Kreisl, S. Ahlers, G. M¨uller, Response mechanism of SiC based MOS field-effect gas sensors, IEEE Sens. J. 2 (2002) 394–402.
[2.147] S. Nakagomi, A.L. Spetz, I. Lundström, P. Tobias, Electrical characterization of carbon monoxide sensitive high temperature sensor diode based on catalytic metal gate–insulator–silicon carbide structure, IEEE Sens. J. 2 (2002) 379–386.
[2.148] S. Kanadasamy, A. Trinchi, W. Wlodarski, E. Comini, G. Sberveglieri, Hydrogen and hydrocarbon gas sensing performance of Pt/WO_3/SiC MROSIC devices, Sens. Actuator B 111 (2005) 111–116.
[2.149] S. Kim, J. Choi, M. Jung, S. Joo, S. Kim, Silicon carbide-based hydrogen gas sensors for high-temperature applications, Sensors 13 (2013) 13575–13583.
[2.150] K.M. Bothe, P.A. von Hauff, A. Afshar, A. Foroughi-Abari, K.C. Cadien, D.W.Barlage, Electrical comparison of HfO_2 and ZrO_2 gate dielectrics on GaN, IEEE Trans. Electron Devices 60 (2013) 4119–4124.

[2.151] Y.C. Chang, M.L. Huang, Y.H. Chang, Y.J. Lee, H.C. Chiu, J. Kwo, M. Hong,Atomic-layer-deposited Al_2O_3 and HfO_2 on GaN: a comparative study on interfaces and electrical characteristics, Microelectron. Eng. 88 (2011)1207–1210.
[2.152] C.-M. Hsu, J.-G. Hwu, Improvement of electrical performance of HfO_2/SiO_2/4H-SiC structure with thin SiO_2, ECS J. Solid State Sci. Technol. 2(2013) 3072–3078.
[2.153] C. Su et al., Journal of Macromolecular Science, Part B: Physics, Volume 55, Issue 6, 2 June 2016, Pages 627-641, doi: 10.1080/00222348.2016.1179248.
[2.154] Guidi et al., Materials Science and Applications in Sensors, Electronics and Photonics, ISBN: 978-1-84569-988-8.
[2.155] M. Kachniarz et al., Advances in Intelligent Systems and Computing, Volume 352, 2015, Pages 111-120, doi: 10.1007/978-3-319-15835- 8_13.
[2.156] Nobbs, J. H. (1985), Kubelka—Munk Theory and the Prediction of Reflectance. Review of Progress in Coloration and Related Topics, 15: 66–75. doi:10.1111/j.1478-4408.1985.tb03737.x.
[2.157] Goldberg Yu., Levinshtein M.E., Rumyantsev S.L. in *Properties of Advanced SemiconductorMaterials GaN, AlN, SiC, BN, SiC, SiGe* . Eds. Levinshtein M.E., Rumyantsev S.L., Shur M.S., John Wiley & Sons, Inc., New York, 2001, 93-148.
[2.158] Vezzoli, M., Ponzoni, A., Pardo, M., Falasconi, M., Faglia, G., Sberveglieri, G. Exploratory data analysis for industrial safety application (2008) Sensors and Actuators, B: Chemical, 131 (1), pp. 100-109.
[2.159] Henley et al., Journal of Volcanology and Geothermal Research, Volume 324, 15 September 2016, Pages 190-199, doi: 10.1016/j.jvolgeores.2016.04.024.
[2.160] Newsome, D.A., Sengupta, D., Foroutan, H., Russo, M.F., Van Duin, A.C.T. Oxidation of silicon carbide by O2 and H2O: A ReaxFF reactive molecular dynamics study, part I (2012) Journal of Physical Chemistry C, 116 (30), pp. 16111-16121.
[2.161] Roy, J., Chandra, S., Das, S., Maitra, S. Oxidation behaviour of silicon carbide - A review (2014) Reviews on Advanced Materials Science, 38 (1), pp. 29-39.
[2.162] Ebrahimpour, O., Chaouki, J., Dubois, C. Diffusional effects for the oxidation of SiC powders in thermogravimetric analysis experiments (2013) Journal of Materials Science, 48 (12), pp. 4396-4407.
[2.163] Hu, J., Wang, L., Cai, W., Li, Y., Zeng, H., Zhao, L., Liu, P. Smart and reversible surface plasmon resonance responses to various atmospheres for silver nanoparticles loaded in mesoporous SiO_2 (2009) Journal of Physical Chemistry C, 113 (44), pp. 19039-19045.
[2.164] Boyadjiev, S.I., Kéri, O., Bárdos, P., Firkala, T., Gáber, F., Nagy, Z.K., Baji, Z., Takács, M., Szilágyi, I.M. TiO_2/ZnO and ZnO/TiO_2 core/shell nanofibers prepared by electrospinning and atomic layer deposition for photocatalysis and gas sensing (2017) Applied Surface Science, 424, pp. 190-197.
[2.165] Wang, L., Wang, S., Zhang, H., Wang, Y., Yang, J., Huang, W. Au-functionalized porous ZnO microsheets and their enhanced gas sensing properties, (2014) New Journal of Chemistry, 38 (6), pp. 2530-2537.
[2.166] Sahu, D., Panda, N.R., Acharya, B.S., Panda, A.K. Enhanced UV absorbance and photoluminescence properties of ultrasound assisted synthesized gold doped ZnO nanorods, Optical Materials, (2014), 36 (8), pp. 1402-1407.
[2.167] J. Hyung, J. Yun, K. Cho, I. Hwang, J. Lee, S. Kim, Necked ZnO nanoparticle-based NO_2 sensors with high and fast response, Sens. Actuators B: Chem. 140 (2009) 412–417.
[2.168] M.C. Carotta, A. Cervi, V. Natale, S. Gherardi, A. Giberti, V. Guidi, et al., ZnO gas sensors: a comparison between nanoparticles and nano tetrapods-based thick films, Sens. Actuators B: Chem. 137 (2009) 164–169.

[2.169] P. Rai, Y.-S. Kim, H.-M. Song, M.-K. Song, Y.-T. Yu, The role of gold catalyst on the sensing behaviour of ZnO nanorods for CO and NO_2 gases, Sens. Actuators B: Chem. 165 (2012) 133–142.
[2.170] P. Singh, V.N. Singh, K. Jain, T.D. Senguttuvan, Pulse-like highly selective gas sensors based on ZnO nanostructures synthesized by a chemical route: effect of in doping and Pd loading, Sens. Actuators B: Chem. 166–167 (2012) 678–684.
[2.171] S.-J. Jung, H. Yanagida, The characterization of a CuO/ZnO hetero contact-type gas sensor having selectivity for CO gas, Sens. Actuators B: Chem. 37 (1996) 55–60.
[2.172] J. Choi, G. Choi, Electrical and CO gas sensing properties of layered ZnO–CuO sensor, Sens. Actuators B: Chem. 69 (2000) 120–126.
[2.173] C.S. Dandeneau, Y. Jeon, C.T. Shelton, T.K. Plant, D.P. Cann, B.J. Gibbons, Thin film chemical sensors based on p-CuO/n-ZnO hetero contacts, Thin Solid Films, 517 (2009), 4448–4454.
[2.174] S. Ayg, D. Cann, Hydrogen sensitivity of doped CuO/ZnO hetero contact sensors, Sens. Actuators B: Chem. 106 (2005) 837–842.
[2.175] X.H. Liu, J. Zhang, X.Z. Guo, S.H. Wu, S.R. Wang Amino acid-assisted one-pot assembly of Au, Pt nanoparticles onto one dimensional ZnO microrods. Nanoscale, 2 (2010), pp. 1178–1184.
[2.176] Y. Zhang, Q. Xiang, J.Q. Xu, P.C. Xu, Q.Y. Pan, F. Li Self-assemblies of Pd nanoparticles on the surfaces of single crystal ZnO nanowires for chemical sensors with enhanced performances. Journal of Materials Chemistry, 19 (2009), pp. 4701–470.
[2.177] A. Kolmakov, D.O. Klenov, Y. Lilach, S. Stemmer, M. Moskovits Enhanced gas sensing by individual SnO_2 nanowires and nanobelts functionalized with Pd catalyst particles. Nano Letters, 5 (2005), pp. 667–673.
[2.178] Q. Xiang, G.F. Meng, H.B. Zhao, Y. Zhang, H. Li, W.J. Ma, J.Q. Xu Au nanoparticle modified WO_3 nanorods with their enhanced properties for photocatalysis and gas sensing. Journal of Physical Chemistry C, 114 (2010), pp. 2049–2055.
[2.179] J. Zhang, X.H. Liu, X.Z. Guo, S.H. Wu, S.R. Wang A general approach to fabricate diverse noble-metal (Au, Pt, Ag, Pt/Au)/Fe_2O_3 hybrid nanomaterials. Chemistry- A European Journal, 16 (2010), pp. 8108–8116.
[2.180] Jia, C., Zhong, W., Deng, M., Jiang, J. Microscopic Insight into the Activation of O2 by Au Nanoparticles on ZnO (101) Support, (2016) Journal of Physical Chemistry C, 120 (8), pp. 4322-4328.
[2.181] Li, F., Zhang, L., Wu, S., Li, Z., Wang, Y., Liu, X. Au nanoparticles decorated ZnO nanoarrays with enhanced electron field emission and optical absorption properties, Materials Letters, 145, (2015), pp. 209-211.
[2.182] Georgiev, P., Kaneva, N., Bojinova, A., Papazova, K., Mircheva, K., Balashev, K. Effect of gold nanoparticles on the photocatalytic efficiency of ZnO films Colloids and Surfaces A: Physicochemical and Engineering Aspects, 460, (2014), pp. 240-247.
[2.183] Shinde S.D., Patil G.E., Kajale D.D., Gaikwad V.B., Jain G.H. Synthesis of ZnO nanorods by spray pyrolysis for H 2S gas sensor Journal of Alloys and Compounds, 528, (2012), pp. 109-114.
[2.184] Monakhov, E.V., Kuznetsov, A.Yu., Svensson, B.G. Zinc oxide: Bulk growth, role of hydrogen and Schottky diodes, Journal of Physics D: Applied Physics, 42 (15), (2009).
[2.185] C. Zhang, M. Debliquy, H. Liao, Deposition and microstructure characterization of atmospheric plasma-sprayed ZnO coatings for NO_2 detection, Appl. Surf. Sci. 256 (2010) 5905–5910.
[2.186] S.-Y. Tsai, M.-H. Hon, Y.-M. Lu, Fabrication of transparent p-NiO/n-ZnO hetero-junction devices for ultraviolet photodetectors, Solid-State Electron. 63 (2011) 37–41.
[2.187] K. Hara, T. Horiguchi, T. Kinoshita, Highly efficient photon-to-electron conversion with mercurochrome-sensitized nano porous oxide semiconductor solar cells, Solar Energy Mater. Solar Cells 64 (2000) 115–134.

[2.188] Bora, T., Myint, M.T.Z., Al-Harthi, S.H., Dutta, J. Role of surface defects on visible light enabled plasmonic photocatalysis in Au-ZnO nanocatalysts, RSC Advances, 5 (117), (2015), pp. 96670-96680.
[2.189] Li, C., Lin, Y., Li, F., Zhu, L., Meng, F., Sun, D., Zhou, J., Ruan, S. Synthesis and highly enhanced acetylene sensing properties of Au nanoparticle decorated hexagonal ZnO nanorings, RSC Advances, 5 (106), (2015), pp. 87132-87138
[2.190] Mun, Y., Park, S., An, S., Lee, C., Kim, H.W. NO_2 gas sensing properties of Au-functionalized porous ZnO nanosheets enhanced by UV irradiation, Ceramics International, 39 (8), (2013), pp. 8615-8622.
[2.191] Gogurla, N., Sinha, A.K., Santra, S., Manna, S., Ray, S.K. Multifunctional Au-ZnO plasmonic nanostructures for enhanced UV photodetector and room temperature NO sensing devices, Scientific Reports, 4, (2014), art. no. 6483.
[2.192] S. Sakka, H. Kozuka, Sol-gel preparation of coating films containing noble metal colloids. J. Sol–Gel Sci. Technol. 13, 701 (1998).
[2.193] B.F.G. Johnson, R. Davis, in: J.C. Bailer Jr., H.J. Emeleus, R.Nyholm, A.F. Trotman-Dickenzon, "Comprehensive Inorganic Chemistry", vol. 3, (Pergamon, New York, 1973) p. 129.
[2.194] A.J. Morfa, G. Beane, B. Mashford, B. Singh, E. Della Gaspera, A. Martucci, P. Mulvaney. Fabrication of ZnO Thin Films from Nanocrystal Inks J. Phys. Chem. C, 114, (2010), 19815-19821.
[2.195] Rishi Vyas, Sarla Sharma, Parul Gupta, Arun K. Prasad, S.K. Dhara, A.K. Tyagi, K. Sachdev, S.K. Sharma, Nitrogen dioxide induced conductivity switching in ZnO thin film Journal of Alloys and Compounds 571 (2013) 6–11.
[2.196] Hao Chen, Yuan Liu, Changsheng Xie, Jun Wu, Dawen Zeng, Yichuan Liao, A comparative study on UV light activated porous TiO_2 and ZnO film sensors for gas sensing at room temperature, Ceramics International, 38, (2012), Pages 503-509.
[2.197] P.K. Chen, G.J. Lee, S.H. Davies, S.J. Masten, R. Amutha, J.J. Wu, Hydrothermal synthesis of coral-like Au/ZnO catalyst and photocatalytic degradation of OrangeII dye, Mater. Res. Bull. 48 (2013), pp. 2375–2382.
[2.198] V. Iliev, D. Tomova, L. Bilyarska, A. Eliyas, Influence of the size of gold nanoparticles deposited on TiO_2 upon the photocatalytic destruction of oxalic acid, J. Mol. Catal. A: Chem. 263 (2007), pp. 32–38.
[2.199] S. Matsushima, Y. Teraoka, N. Miura, N. Yamazoe, Electronic interaction between metal additives and tin dioxide in tin dioxide-based gas sensors, Jpn. J. Appl. Phys. 27 (1988), pp. 1798–1802.
[2.200] T.A. Baker, X. Liua, C.M. Friend, The mystery of gold's chemical activity: local bonding, morphology and reactivity of atomic oxygen, Phys. Chem. Chem. Phys. 13 (2011), pp. 34–46.
[2.201] Maxwell, I., Driving forces for innovation in applied catalysis, Stud. Surf. Sci. Catal. 101, (1996), pp. 1-9.
[2.202] Wickham, D. T., Parker, D. H., Kastanas, G. N., Lazaga, M. A., Koel, B. E., Reactivity of oxygen ad atoms on the Au (111) surface, Prepr. – Am. Chem. Soc., Div. Pet. Chem. 37, (1992), pp. 1034-1037.
[2.203] Haruta, M., Tsubota, S., Kobayashi, T., Kageyama, H., Genet, M.J., Delmon, B. Low-Temperature Oxidation of CO over Gold Supported on TiO_2, α-Fe_2O_3, and Co_3O_4, J. Catal. 144, (1993), pp. 175-192.
[2.204] Sarina, S., Waclawik, E.R., Zhu, H. Photocatalysis on supported gold and silver nanoparticles under ultraviolet and visible light irradiation, Green Chemistry, 15 (7), (2013), pp. 1814-1833.
[2.205] Mukherjee, S., Libisch, F., Large, N., Neumann, O., Brown, L.V., Cheng, J., Lasiter, J.B., Carter, E.A., Nordlander, P., Halas, N.J. Hot electrons do the impossible: Plasmon-induced dissociation of H_2 on Au, Nano Letters, 13 (1), (2013), pp. 240-247.

3 Micro-Electro-Mechanical System devices

3.1 Overview of MEMS devices

The technological development of suitable MEMS substrates plays a key role in producing sensors with optimal characteristics. Indeed, its function of the transducer of the sensing material signal allows the complete operation of a chemoresistive gas sensor. In detail, a substrate performs a threefold effect:

- mechanical support to the sensing paste;

- to supply the input voltage to the sensing material and extract the output signal;

- it must be able to heat up the sensing material for its thermo-activation, and having, at the same time, good insulating properties.

These functions can only be carried out by materials possessing certain peculiar characteristics, including:

- high mechanical stability and robustness. This feature is not only required to support sensing material during sensor operation but also to withstand mechanical stress due to its deposition. In our case, for example, the deposition types for obtaining the thick film (i.e. screen-printing technique) provide a working pressure on the substrate of about 2 kilograms, while in the thin film deposition (for spin coating) the substrate must able to support an angular velocity of 314 rad / s (3000 rpm) for 30 seconds for different cycles. Furthermore, the mechanical stability is also required for the final packaging processes, to obtain the final integration of the sensor with the electronic elaborator system.
- The substrate must be easily workable in the process, which allows the deposition of at least two metal circuitries (heater and interdigitated electrodes) on it. One relative to the heater, and the other one that is needed to provide electric current and tension to the sensitive material. In many cases, these processes must also include the deposition of electrical insulators, so that they do not permit current passages between the two separate circuits. Indeed, the cross-talking between the heater and the sensing film, due to the passage of parasitic current, can lead to instability and modify responses of the gas sensor.
- The material used for the substrate must possess a high thermal stability, as the sensitive materials are usually thermo-activated at temperatures ranging from 200°C to 600°C. For this reason, it is preferable to use materials that highlighted a low thermal expansion coefficient. Furthermore, they must show a low thermal conductivity to not disperse the heat on the surface part not affected by the sensing material, which would result in high energy consumption. Among the basic properties required for a material used as a substrate is also important the high electrical resistivity and a high dielectric constant is also important, which limit electric dispersions of currents circulating in metal electrodes.
- The high chemical stability of the substrate is mandatory. This characteristic is important both for substrates stability over the time and for the chemical equilibrium of gaseous species detected. Indeed, catalytic effects or chemical interactions of the substrate vs. gaseous compounds in the air can change the concentration of these gases and produce new chemical species, thus altering the interaction between the sensing material with the real initial gaseous environment.

It is really important that a substrate possess the features listed above to ensure optimal sensor operation. Traditionally, little attention has been paid to the substrate but, conversely, its characteristics affect both the deposition process and the final characteristics of the sensor. Indeed, many device problems still present on commercial sensors are due not only to sensing material drawbacks but also to the technological limits of platforms used as substrates.
Over the last years, the technological development focused mainly on 4 types of materials used as MEMS substrates, i.e. alumina, silicon, polymers and paper [1-4]. However, as the aim of this work was to produce substrates equipped with heaters to thermo-activate nanostructured semiconductors at high temperatures, polymers and paper were not considered, because of their low thermal stability.

In the next two sections, will be presented first the commercial alumina substrates commonly used in most research centres, including the SSL of the University of Ferrara. Then will be introduced the purpose of this last part of the thesis, i.e. the development, in these three years of PhD, at the Bruno Kessler Foundation, of a low cost, high performance, and low-energy consumption silicon and quartz microheaters, suitable for chemoresistive gas-sensing applications.

3.1.1 Alumina substrates

Alumina is the ceramic material most used in past as substrate for the chemoresistive gas sensor. Indeed, the firsts commercial Taguchi sensors, as reported in the patent [3.5], were provided with alumina substrate. Nowadays, it is still widely adopted, particularly in academic research [3.6, 3.7]. The great attention attracted to the alumina is due to the characteristics of this material, which make it one of the most suitable materials for performing the role of the transducer in a chemoresistive gas sensor.
Commonly alumina used to construct substrate is that one at a concentration range between 94% and 96% [3.8]. In this material, pure alumina powder is obtained from Bauxite (the principal font of aluminium existent in nature). Then it is ground together with other oxides (SiO_2, NaO, MgO) in order to obtain a substrate with the desired chemical-physical characteristics. Grinding is effected in a mill with blades to ensure a good mixing level. Then, the obtained compound undergoes two treatments at different pressures depending on the desired thickness (later or less than 1 mm). Then, after imposing a form to the substrate, it is exposed to firing for 12-24 hours; this thermal treatment is composed of two principal steps, i.e. pre-treatment and sintering. The first step is done at 300-600°C and is necessary to eliminate organic additives, used for grinding. The second step, the sintering, is done at 1500-1700°C and is needed to promote the adhesion between powder particles through events named "densification" and "growth of grains". Densification is a process that reduces the porosity of the sample, making it denser; the growth of grains, instead, is a process which increases the average dimension of the particles constituting the material. While densification needs high temperatures, the growth of grains occurs naturally during the process itself. The modulation of temperatures and of total firing times is the key to optimize physical-chemical characteristics of materials. Then, substrates must be characterized by a smooth and uniform surface and from the lowest number possible of visible surface defects.
Alumina substrates, thus realized, show high mechanical strength (1100 $Kgmm^{-2}$), high thermal stability (up to 2000°C) and a relatively low thermal conductivity (18 $Wm^{-1}K^{-1}$). Furthermore, alumina substrates can be easily integrated into processes that allow the low-cost deposition of electrical circuits.
Substrates of Alumina 96% used so far in the SSL laboratories of the University of Ferrara are provided with two electronic circuits:
- a heater of platinum (Pt 100) on the substrate backside;

- interdigitated electrodes in gold on the substrate frontside, on which the sensing material will be deposited.

Size of devices is 2.54x2.54 mm^2, with a thickness of 250 μm. The alumina bulk and a layer of dielectric material allow to electrically insulate the heater and the interdigitated electrode (Figure 3.1).

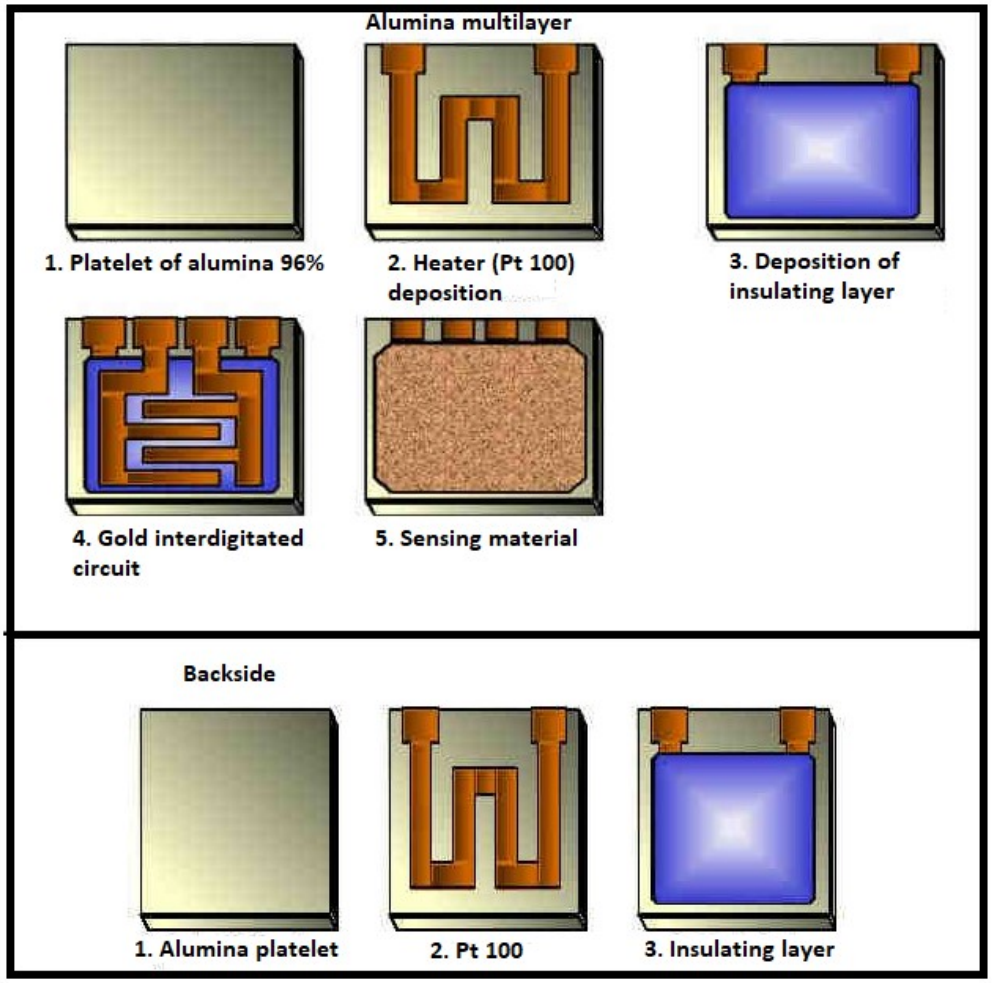

Figure 3.1: Multilayer sensor configuration. On the upper side, the sensitive layer is deposited over the gold interdigitated contacts and electrically contact this circuit. On the lower side, is highlighted the temperature self-regulating system that consists of a variable resistance (Pt 100).

Despite the great qualities of alumina as a substrate, three main drawbacks arose in the sensor operation mode. The first regards the high-power consumption of the heater to heat up the sensing material: as it can be seen in Figure 3.2, alumina substrates used at the SSL laboratories need high-power values to heat sensors up to suitable temperature to thermo-activate common MOX semiconductors. For example, to reach a temperature of 500°C it is necessary a power of about 1 W.

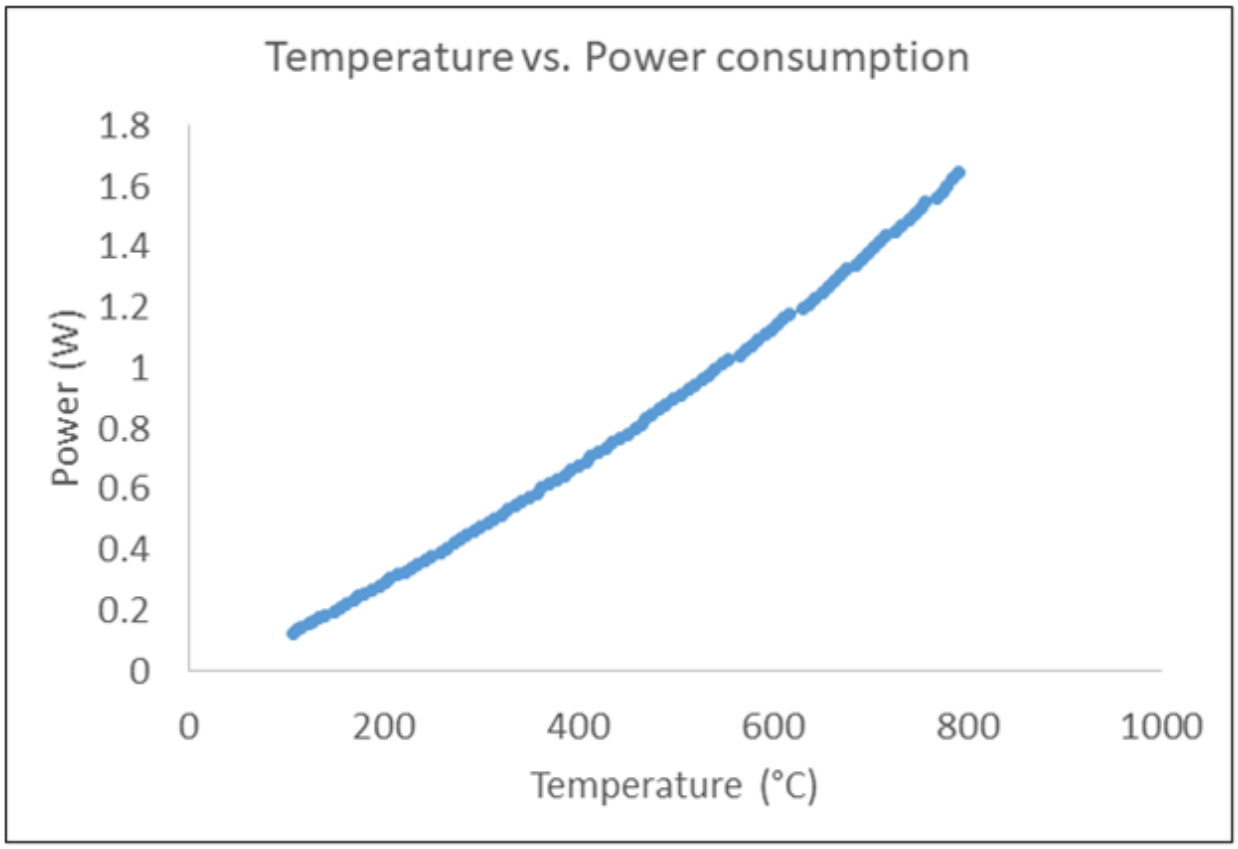

Figure 3.2: Power consumption vs. temperature of alumina substrates used in the SSL laboratories of the University of Ferrara.

This high-power consumption is due to a not so low thermal conductivity of alumina substrate, that involves a quite great thermal-energy dispersion of the sensor.
The second problem concerns reactivity of alumina substrates vs. gases at the sensor working temperatures. In fact, alumina highlighted in previous works a not negligible chemical activity, that allows interaction with gaseous compounds such as O_2, H_2 and CO_2 [3.9] These reactions can thus affect the operation of the sensor, by changing the concentration of the gases that would be present in the initial reaction mixture and by limiting the sensing response reliability of the sensing material.
The third shortcoming of alumina substrates regards the scarce reproducibility of the single device. Indeed, methods usually adopt to deposit circuits and dielectric material (such as screen-printing technique) show an unsatisfactory reliability, which implies differences in terms of characteristics between each substrate [3.10]. Moreover, these differences bring to a characterization of every single substrate, with a great loss of time.
Given drawbacks are shown by alumina substrate, in this work, it was decided to explore other technological materials for developing more suitable MEMS substrate.

3.1.2 Silicon and quartz MEMS

The advancements in microelectronics over the last 35 years have been due to the progress made in silicon technology, suitable also in the last period for quartz [3.11, 3.12]. Higher integration, faster devices and lower power consumption have been realised by the miniaturisation of planar devices using silicon microtechnology. Extremely high device performance for a very low unit cost is now possible using well-defined batch-fabrication procedures. Moreover, the material properties, interfaces and surfaces can be well controlled. The potential benefits of silicon technology also satisfy the physical sensor requirements for a portable gas monitoring instrument, which are low power,

miniaturisation, low weight and low unit fabrication costs [3.13]. The application of silicon technology also enables electronic circuits to be integrated onto the sensor chip, so allowing miniaturisation of the modifier, noise reduction and on-chip compensation. Sensors with this type of integrated circuitries are referred to as intelligent sensors [3.10, 3.14]. With the costs of microprocessor technology reducing each year, it is a real possibility to have a low-cost miniature hazardous gas monitor with an improved accuracy and reliability. The suitability of silicon and quartz technology for the design of microsensors in portable instrument applications led to its selection as the enabling technology for this part of the research.
From the state of the art point of view, silicon microheaters produced using MEMS technology have been pioneered since the early '90 and derive from the so-called micro-hotplate devices [3.15]. These sensors operate at high temperatures (350-450°C). This thermal load is of major concern in the design of the sensor and affects the materials choice [3.16].
Analysing the microheater gas sensor market one can see that commercially available devices invariably adopt high temperature compliant (>600°C) layers [3.17]: tungsten (W), platinum (Pt) or poly-silicon (Poly-Si) conductive layers, separated by Chemical Vapor Deposited (CVD) silicon oxide and/or nitride dielectric layers. This material choice is to grant stability during high-temperature curing and operation. Key examples of these fabrication processes are reported in the literature: the double platinum process by Kang et al. [3.18], the polysilicon process by Zhou et al. [3.19], and tungsten heater proposed by Santra et al. [3.20]. Moreover, all fabrication processes used in commercial products require a custom MEMS fabrication line, with the sole exception of Cambridge CMOS CCS09F, now discontinued, which used the CMOS-SOI (complementary metal-oxide semiconductor-silicon on insulator) process reported by Ali et al. [3.21]. Therefore, and to the best of our knowledge, no fabless approach to microheater fabrication has been adopted, because of the lack of a cheap, CMOS compatible process. Indeed, fabrication of MEMS usually requires a dedicated fabrication line for each device technology, lacking the standardization level of IC fabrication. Only a few examples exist of MEMS processing based on standard CMOS-BEOL (back-end-of-line) technology: devices like Texas Instruments Digital Mirror [3.22] and Akustica microphone [3.23] are fabricated using BEOL metal layers and inter-metal dielectrics. The clear advantage of moving towards a more standardized process is the possibility to leverage on a mature and widespread technology, eventually enabling fabless production.

Therefore, the goal of this part of the work was to develop silicon (named SMHP) and quartz (named QMHP) Micro HotPlates through a simple and reliable process suitable for a not dedicated fabrication line. Despite the great thermal conductivity and low resistivity of silicon, it was the ideal candidate for this topic, since the possibility of its micromachining allows the creation of adapt thin membranes.

It was also decided to produce quartz microheaters because of its compatibility with the silicon micromachining process. Furthermore, quartz has quite interesting properties, suitable for the chemoresistive gas sensor, such as:

- great thermal and mechanical stability;

- high electrical resistivity;

- lower thermal conductivity (3 $Wm^{-1}K^{-1}$) than alumina (18 $Wm^{-1}K^{-1}$).

A further attractive feature of quartz is its "transparency" to UV-visible radiation in a certain wavelengths range, that can lead to the development of sensors in which it is possible to exploit both chemoresistive and optical properties of the sensing material [3.24]. In literature, there are not present

studies about quartz micro-hotplate. The high cost of pure wafers could be the major limitation of deep investigation of quartz microdevices.

Design, realization process and characterizations of substrates were entirely carried out at the Micro-Nano Facility of the Bruno Kessler Foundation.

3.2 Design of silicon and quartz MEMS devices

MEMS technology has been employed because it allows miniaturisation, reduced fabrication unit costs and better reproducibility. It also makes possible the integration of the device with its associated signal conditioning circuitry. However, at this stage of the study, only sensor elements, i.e. interdigitate electrode, heater and inter-metals passivation have been integrated into the design to minimise cost and process complexity.
The design of the device is of fundamental importance in the development of MEMS device. To realize a suitable process flow and to optimize the necessary steps for the preparation of a device adapted for our needs, it is necessary to fully understand the operational features required to the device that we want to accomplish.
The fundamental parts that must compose our micro-heater are:

- a metallic electrode that acts as a heater, to thermo-activate the sensing film at high and stable temperatures;
- an open metal circuitry (interdigitated electrodes), which provides electrical current to the sensing film and, at the same time, plays the role of the transducer of the chemical interaction between gases and receptor;
- these two metal levels must be electrically isolated, but not thermally isolated;
- it is preferable to deposit a further electrode on the substrate surface, with the purpose of further checking the actual temperature of the device.

Furthermore, it is important to specify that the technology available to develop silicon and quartz micro-heaters, in the FBK, was the planar microtechnology, coupled with thin film processing technique [3.11, 3.12]. With this technique, it is possible to deposit thin layers over silicon and quartz wafers, which can be defined by means of lithography.
Taking into account these considerations, it was decided to explore two layout types (namely L1.1 and L2) and two alternative processes (namely P1 and P2) for each material substrate (quartz and silicon).
Considering the design from the top view of the sensor, the two layouts selected are shown in Figure 3.3:

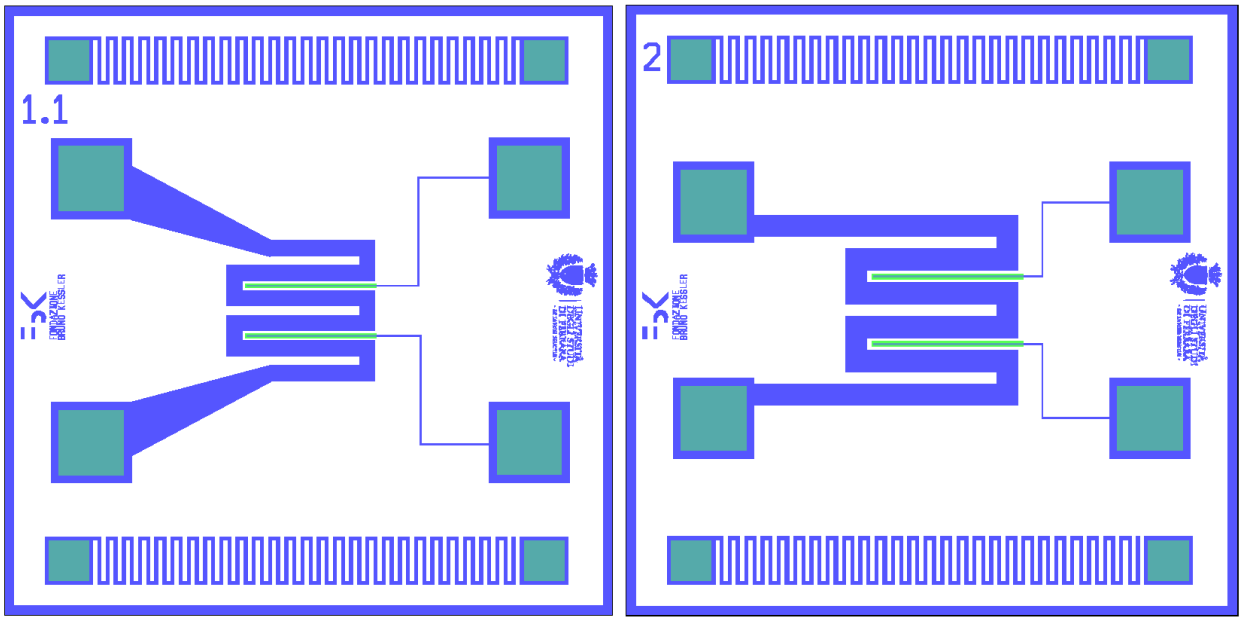

Figure 3.3: Top view geometry of L1.1 (left) and L2 (right) layouts.

The lateral size of all devices was chosen of 3x3 mm, at this first stage of research. This arbitrary choice was taken to concentrate initially our attention on the development of a robust process. Once the appropriate process has been identified and its repeatability is verified, the size of the device can be reduced to decrease the power consumption and increase the number of the device for each silicon and quartz wafer, thus decreasing the process cost for every single device.

Regarding the two processes (P1 and P2), our attention was mainly dedicated to the electrical inter-metals passivation and the positioning level of these electronic circuits. In the process called P1, both for SMHP and QMHP, it was decided to deposit the two metal circuitries on the same level, thus with a single deposition (horizontal approach). In a subsequent step, it was deposited and defined the insulating layer to electrically isolate the open circuit and the heater (Figure 3.4).

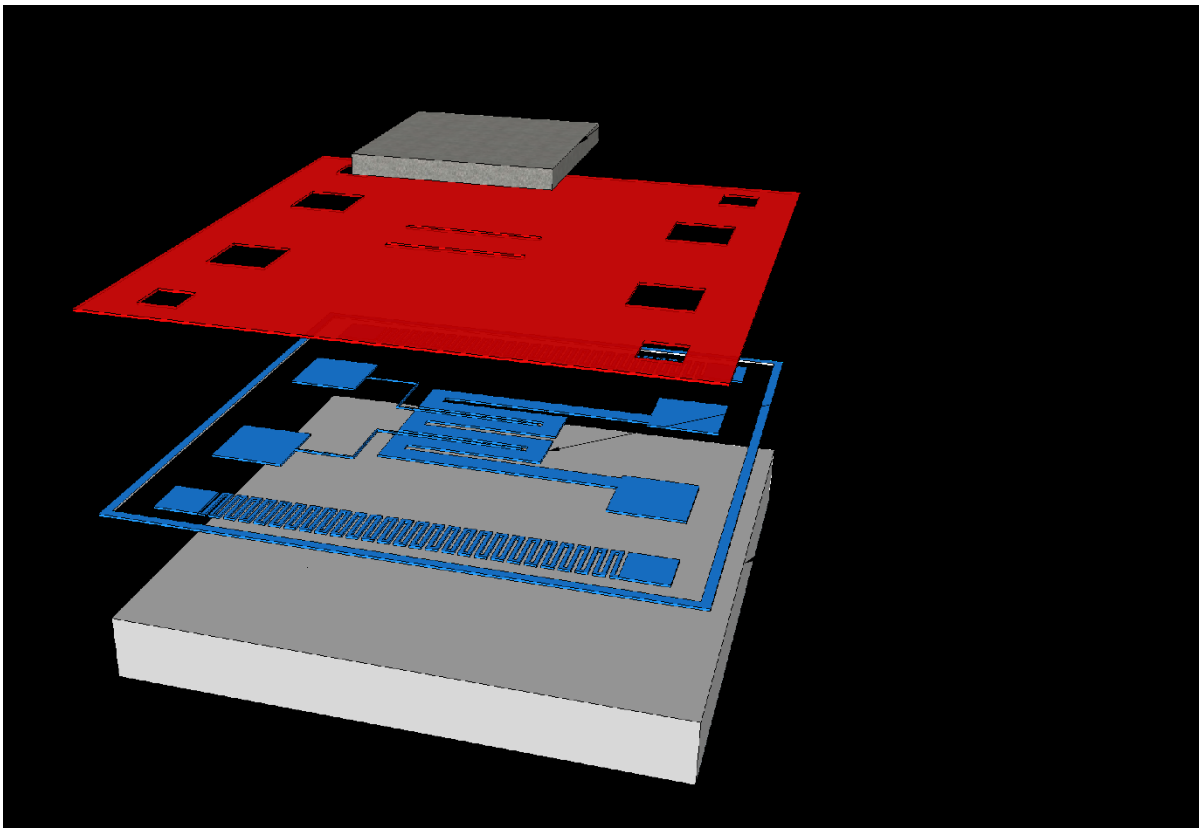

Figure 3.4: Representation of the sensor structure P1, designed at the FBK. As it can be seen, the two metal circuits are on the same level. In a second step, they will be electrically insulated through a suitable dielectric material.

The process P2 shows a substantial difference over P1. Indeed, the heater and interdigitated electrodes placed on two different levels with respect to P2 (vertical approach). The heater was deposited as the first layer and then covered in the second step by an inter-metal passivation. Finally, the open circuit has been deposited over the insulating material, as shown in Figure 3.5.

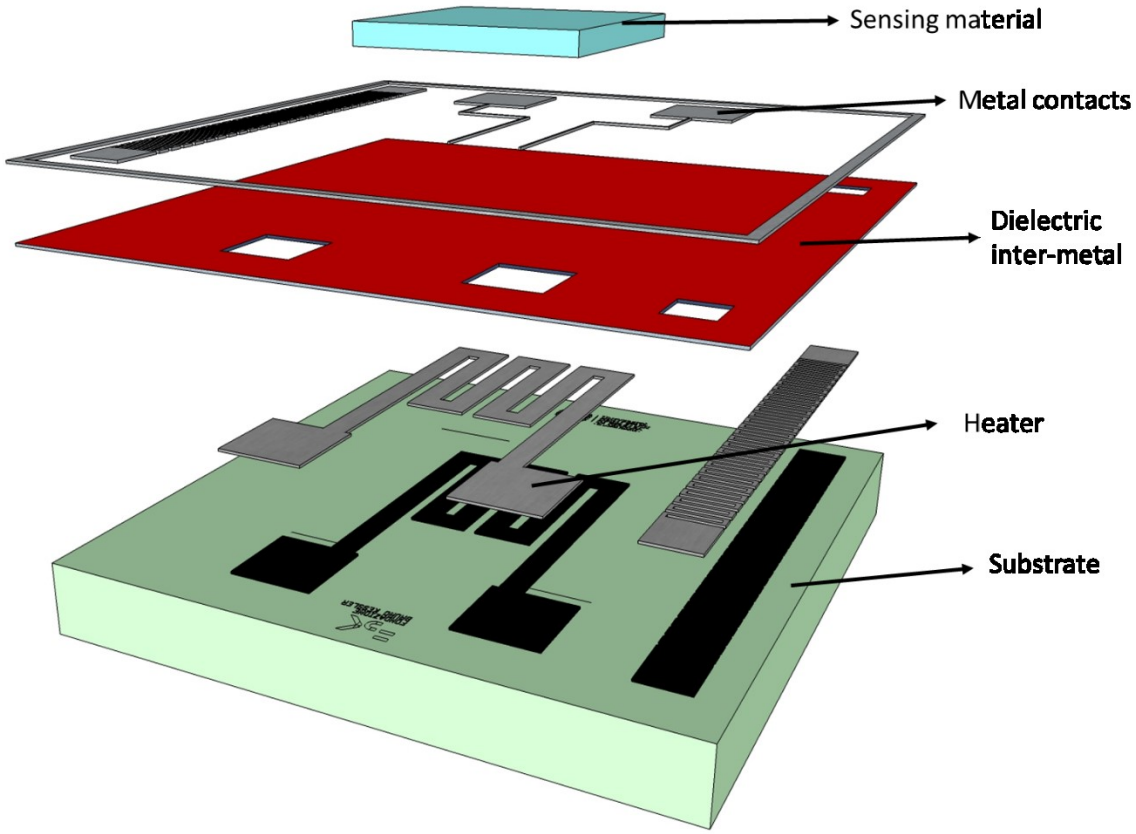

Figure 3.5: Representation of the sensor structure P2, designed at the FBK. As it can be seen, the two metal circuits are on two different levels, separated by a layer of the dielectric material.

In the paragraphs 3.2.1 and 3.2.2, we reported in detail the different design projects employed for silicon and quartz, respectively, due to their divergent characteristics in terms of micro-fabrication, which lead to exploring different development possibilities.

3.2.1 Design of silicon microheaters

The great drawback of silicon as material to produce micro-heaters, as reported in section 3.1.2, lies in its low resistivity. However, the possibility to easily process silicon wafers in micromachining processes allows to use it as "support" for membranes or free-standing structures. Many works in literature showed the development of these silicon structures by means of micromachining technique, which allows micro-heaters development with ultra-low power consumption [3.25, 3.26]. The performance of a wide variety of other microsensor types has benefited from the application of this process method [3.27]. Micromachining describes the processing techniques that together can accurately define three-dimensional structures. Micromachining fabrication techniques originate from microelectronic planar processing techniques, and so provide the same benefits of accuracy and batch processing. Generally, micromachining technology can be classified as either bulk or surface micromachining. Bulk micromachining technology is based on the anisotropic etching of the Single Crystal Silicon (SCS) substrate used for the sensors. The well-defined etch rates of different SCS planes [3.28] allow for a high degree of control over three-dimensional structures etched in the bulk. Surface micromachining employs deposition and selective etching of sacrificial layers and thin films to produce free-standing surface microstructures. Bulk micromachining techniques were employed here to produce thermally insulated ultra-thin membrane structures. This micromachined structure is

named micro-hotplate (MHP). The heater can be placed in either plane with the chemoresistor or embedded within the membrane, so allowing the chemoresistor to be superimposed above the microheater [3.10].
Since the possibility to use micromachining, the silicon design process must first be considered a deposition of a stable layer composed of a dielectric material. This insulating layer will play the role of mechanical support for the micro-heater, once the silicon has been etched in the last step. It should also possess a high thermal stability, having to withstand the high firing and operative temperatures of the sensing material (up to 650°C).
The two process flows designed for silicon (P1S and P2S) were developed taking into consideration the formation of a suspended membrane of insulating dielectric material (through the bulk micromachining technique), containing the electrodes, the inter-metal passivation and finally the sensing material.

In Figure 3.6 is reported a simplified version of the design process P1S.

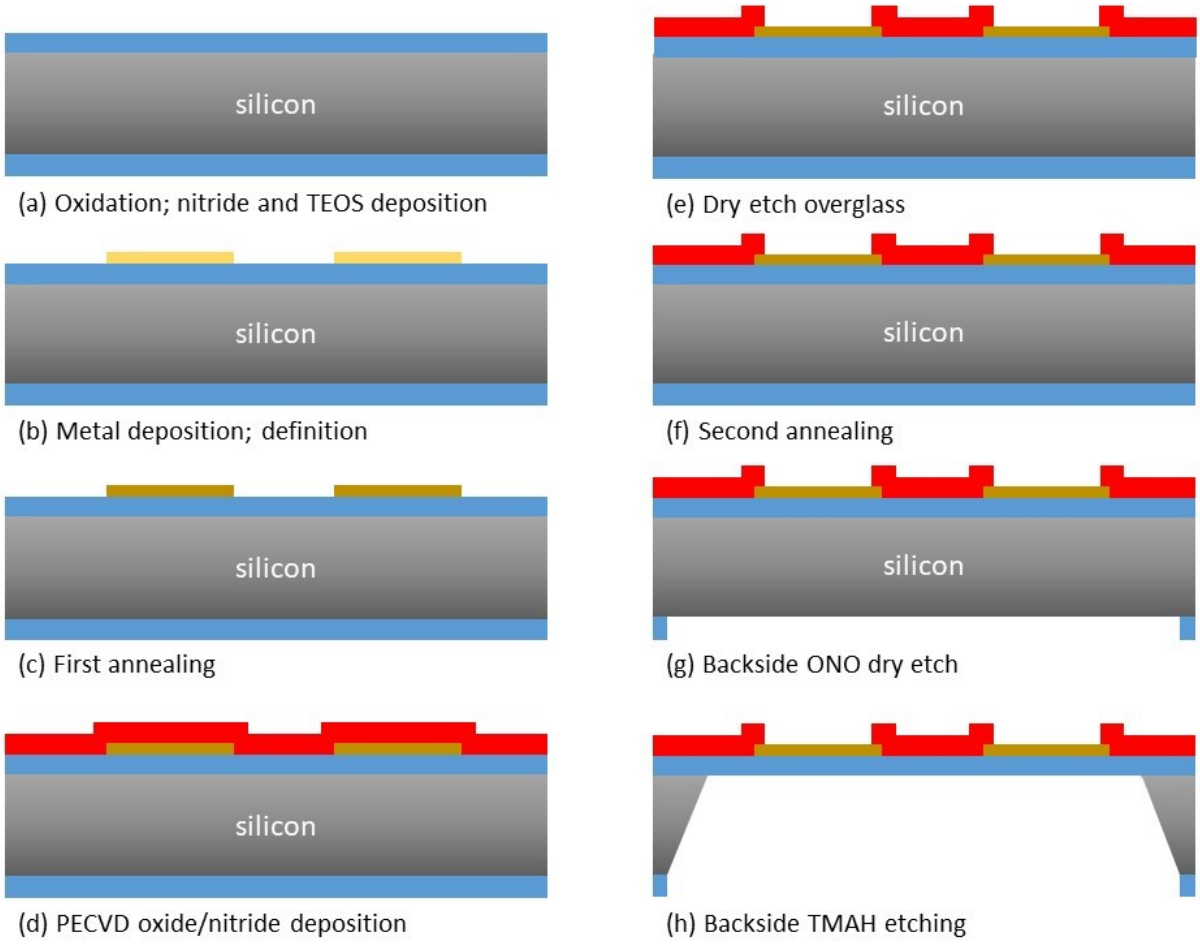

Figure 3.6: The schematic representation of P1S process steps.

As it can be seen, the first step *(a)* regarded the deposition of a silicon oxide/silicon nitride/silicon oxide ($SiO_2/Si_3N_4/SiO_2$, named ONO) insulating layer, by means of thermal oxidation and Low-Pressure Chemical Vapour Deposition (LPCVD) techniques, in the double side of the silicon wafer. In the second step *(b)*, the deposition of a suitable metal was carried out, to obtain the micro-heater and interdigitated electrodes. Metals were defined through lithography and metal lift-off techniques, and then circuits were thermally stabilized with an annealing treatment *(c)*. Afterwards, a layer of Si_3N_4/SiO_2 (over glass layer) was deposited via Plasma-Enhanced Chemical Vapour Deposition (PECVD), to electrically insulate circuits each other *(d)*. In step *(e)*, the overglass was defined to

create openings over the open circuit (where sensing material can contact it) and, at the same time, over the metal pads, for final packaging of the device through ball bonding. Then, the overglass was thermally stabilized *(f)*. Lastly, the membranes were realized by etching the ONO layer and the silicon from the backside, by using a suitable silicon etcher.
In detail, P1S required a quite short process, with five blocks of fabrication steps and three masks. Regarding process P2S, a fast representation is reported in the Figure below.

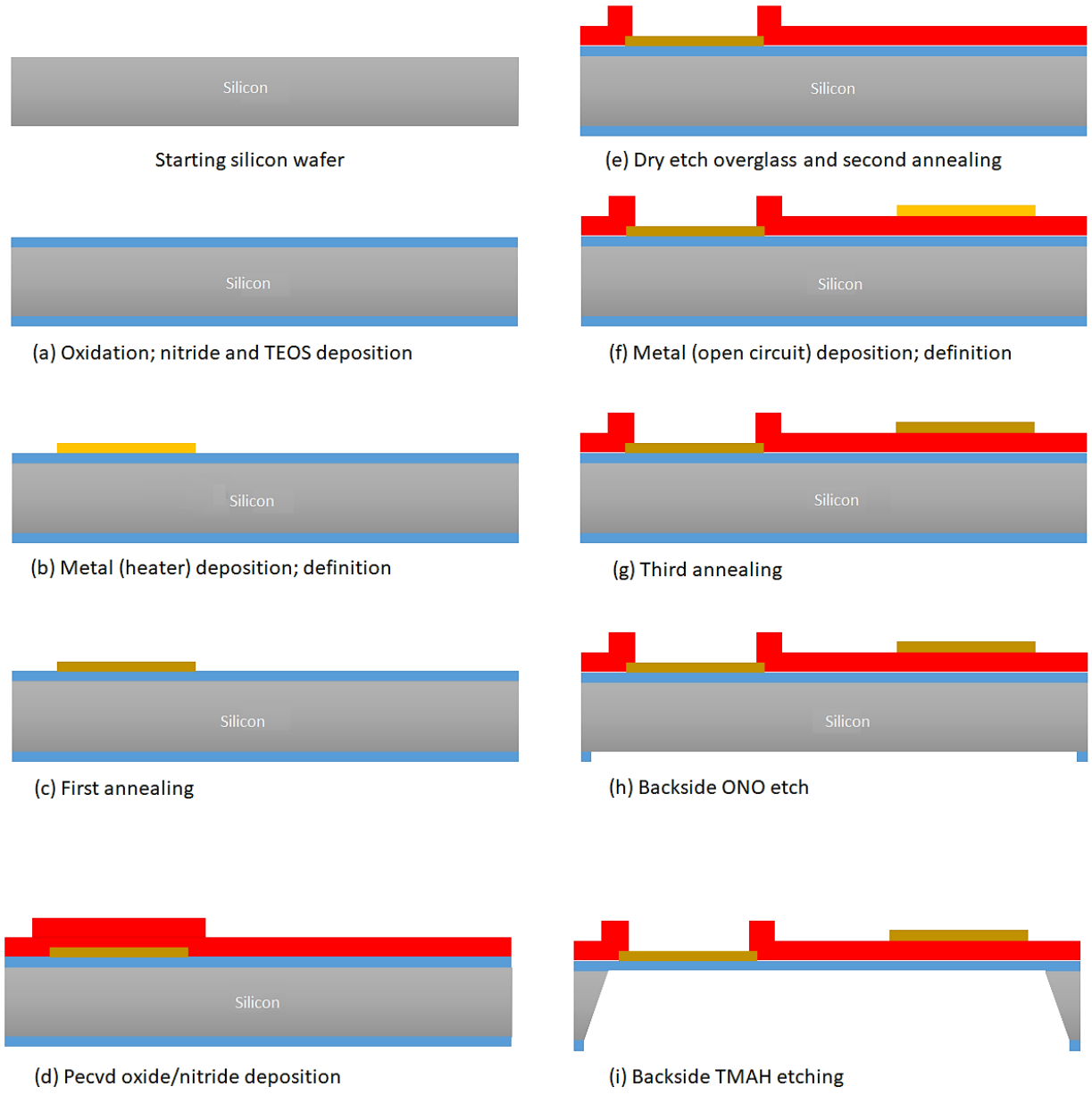

Figure 3.7: The schematic representation of P2S process steps.

As can be clearly seen from figures 3.6 and 3.7, and as claimed in section 3.2, the major difference in the design of the P1S and P2S process is in the deposition of the two metal circuitries. While in P1S they are defined during the same steps and located at the same fabrication level (over the first ONO layer), in PS2 it was decided to separate them from a layer of continuous insulating material. In the one hand, the steps involved in P2S are basically the same that in P1S, with an initial deposition of an insulating layer (a), depositions of metal layers, their definition and thermal stabilization (steps b, c, f, and g), deposition and definition of a PECVD inter-metal passivation and final etching of ONO

layer and silicon on the wafer backside to obtain a membrane. In the other hand, in the process P2S, the separation of the heater and open circuit depositions into two processes leads to an increase in practical steps and in the number of masks for microheater development compared to the P1S process. The P2S requires six blocks of fabrication steps four masks.
The P2S process is therefore at a disadvantage compared to P1S in terms of cost and time-consuming. Nevertheless, we decided to test the P2S process in order to test its solidity and verify the characteristics of the devices thus obtained. In fact, the separation of the electrodes and heater on two levels, by means of a continuous layer of an insulating material, can result in a better electrical insulation than microheater proposed in P1S. Indeed, it is important to point out that in silicon microheaters proposed so far in the literature, greatest limits found were precisely that of poor isolation between the two metal circuits and the membrane stress, which led to a poor stability of the sensor itself over time [3.29].

3.2.2 Design of quartz microheaters

So far, surely silicon was the material most used in micro-machining technology. Nevertheless, the concepts of micromachining and micromechanics are not restricted to this material and other materials can be interesting for the conception and realization of specific microdevices [3.30]. Indeed, in the last years, in many devices such as micro-balance, piezoelectric and pressure sensors, were used monocrystalline quartz as substrate material [3.31-3.33]. These researchers have led to the development of quartz micromachining process. Furthermore, a further improvement of this technique was reached when industry adopted large production of quartz device, especially for digital watch devices. The wet chemical etching process for quartz wafer is well established. Despite this, contrarily to silicon, no etch stop material is known for quartz requiring etching through the quartz wafer. This restriction puts a limitation on quartz micromachining to yield various geometrical shapes that are possible with silicon, e.g. free-standing structures or ultra-thin membrane. However, monocrystalline quartz has shown excellent electrical resistivity and low thermal conductivity in many works [3.34] (see section 3.1.2). These characteristics allow ideally to deposit a microheater directly on the surface of the monocrystalline quartz, without the need for interlayer to act as an insulating material. Furthermore, the development of quartz MHP have a strong high robustness compared to silicon MHP, in which it is necessary to create a thin membrane and fragile for the microheater.
Therefore, we decided to take advantage of this opportunity to develop microheaters in quartz, by using simple processes and less working steps than silicon. As in the case of silicon, they were designed two different processes for silicon microheaters, named P1Q and P2Q. A fast schematic representation of P1Q is reported in the Figure below:

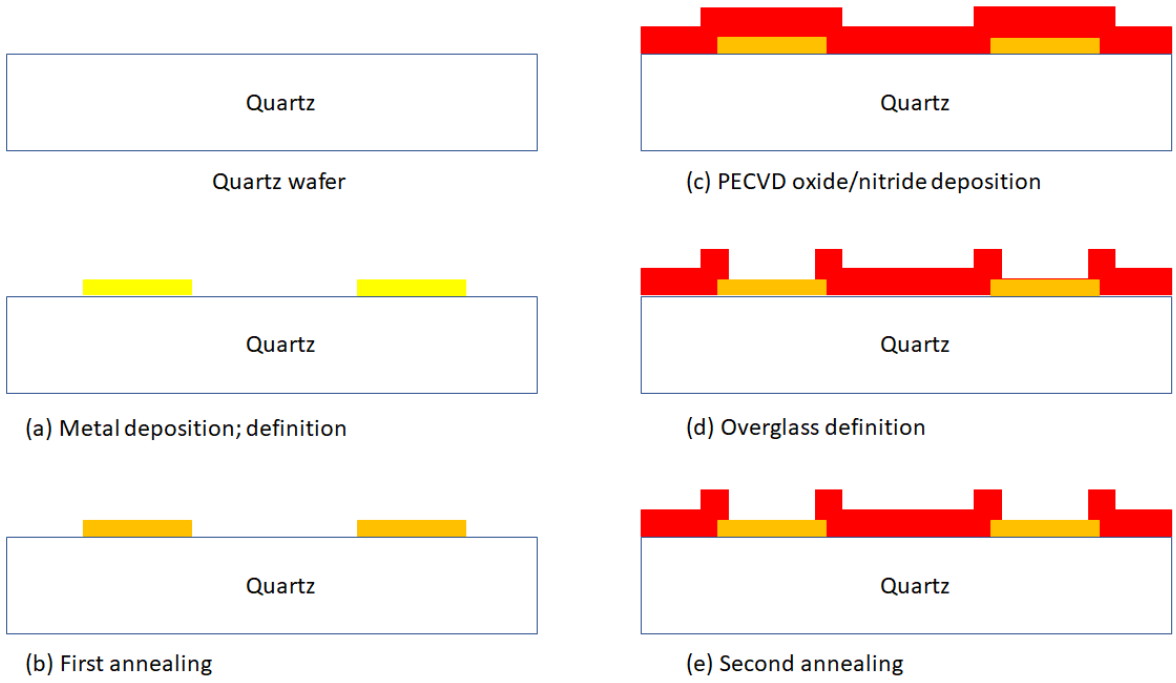

Figure 3.8: The schematic representation of P1Q process steps.

The P1Q is a very fast process. First, heater and interdigitated electrodes were deposited, defined and thermally stabilized. Then, electrodes were electrically insulated from each other with a Si_3N_4/SiO_2 layer, deposited by means of PECVD technique and defined through a lithography process. Eventually, a second annealing was carried out to thermal stabilized the inter-metal passivation.
The P1Q process has been completed through three blocks of fabrication steps, and the use of two masks.
Also, in this case, the process P2 for quartz involved two different depositions of the heater and interdigitated electrodes, as it can be seen in Figure 3.9.

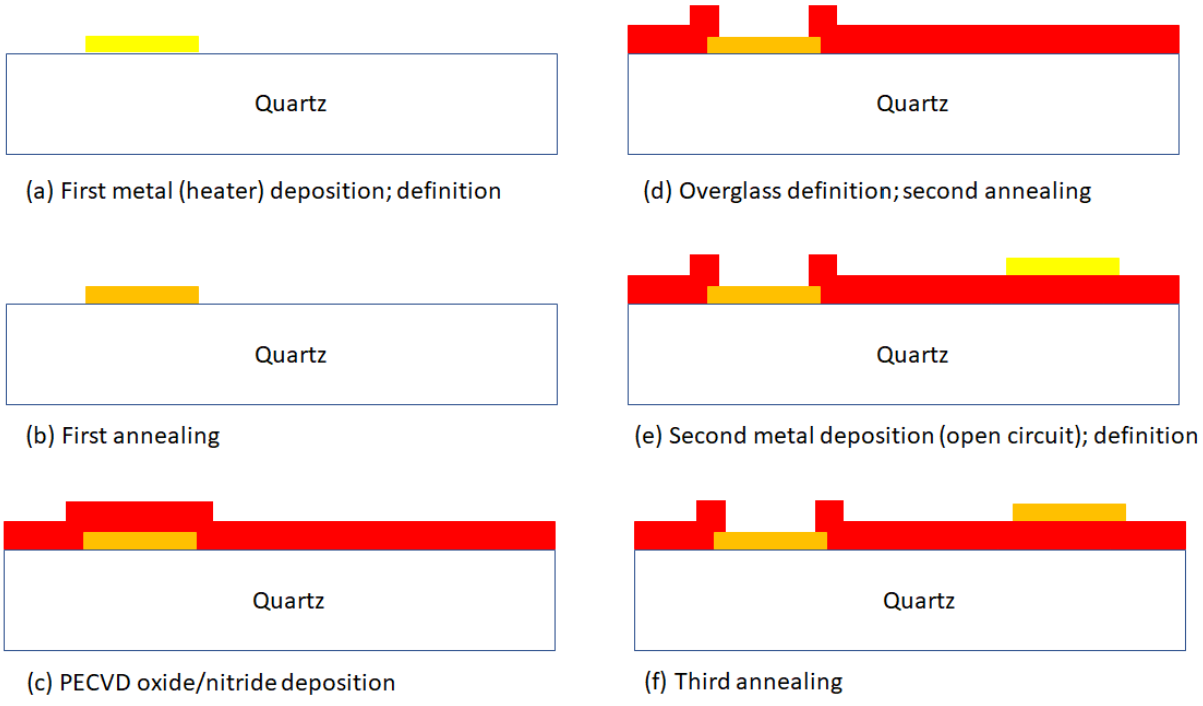

Figure 3.9: The schematic representation of P2Q process steps.

This process, compared to P1Q, required three more steps regarding second metal circuit (interdigitated electrodes) deposition, i.e. metal deposition, its definition and thermal stabilization. Nevertheless, the study of such a microheater layout is useful to verify whether the configuration of the dielectric layer shows better performs with the P1Q or P2Q design.
The P2Q process requires four blocks of fabrication steps and three masks.

3.3 Process instrumentation

The previous section introduces the types of process designs chosen for the development of silicon and quartz microheaters. At this stage, it is necessary to explain the type of instrumentation present in the clean rooms of FBK, giving a brief explanation of their functionality and their role in the development of the MEMS devices described in this work.
The Micro-Nano characterization & fabrication Facility (MNF) group of FBK is organized in three distinct areas:

- fabrication;
- testing;
- packaging.

The presence of all three types of fundamental laboratories, allows the complete production of a device, starting from quartz and silicon wafers up to obtain the finished product. The Microfabrication Area runs two separate clean rooms, the Detector Cleanroom (class 10-100), dedicated to the development of radiation sensors, and the MEMS Cleanroom (class 100-1000), where microdevices and sensors for different applications are developed [3.35]. In both clean rooms, the standard microfabrication utilizes 6” wafers of silicon or quartz. Quality of clean rooms and processes are certified ISO 9001:2015.
Below are reported the instrumentation used to develop the quartz and silicon micro-hotplates.

3.3.1 Thermal oxidation and Low-Pressure Chemical Vapour Deposition

Thermal oxidation and LPCVD are technologies that allow growing/depositing layers of materials with controlled thickness, and with good surface homogeneity. Both techniques take advantage of high temperatures and they are carried out on horizontal tubes, usually in quartz. The fundamental difference between these two techniques is that thermal oxidation is forced growth of SiO_2 on native silicon, while LPCVD is used to deposit layers on the surface of wafers.
Thermal oxidation of silicon is usually performed at a temperature between 800 and 1200°C. O_2, H_2O or a mixed of O_2/H_2O are fluxed into the tube, depending on whether dry or wet thermal oxidation is required. Therefore, this technique forces an oxidizing agent to diffuse into the silicon wafer at high temperature and react with it, in order to grow SiO_2 [3.36].
LPCVD technique uses heat to initiate a reaction of a precursor gas on the solid substrate. Low pressure (LP) is used to decrease any unwanted gas phase reactions and increases the deposition uniformity [3.37]. The LPCVD process can be done in a cold or hot walled quartz tube reactor. In LPCVD, the tube is evacuated to low pressures. Once the tube is under vacuum, the tube is then heated up to the deposition temperature, which corresponds to the temperature at which the precursor gas decomposes. The working temperature can range from 425-900°C, depending on the process and the reactive gases being used. Gas is injected into the tube, where it diffuses and reacts with the

surface of the substrate creating the solid phase material. Any excess gas is then pumped out of the tube and goes through an abatement system. LPCVD films are typically more uniform, lower in defects, and exhibit better step coverage that films produced by PECVD and Physical Vapour Deposition (PVD) techniques. The disadvantage of LPCVD is that it requires higher temperatures, which puts limitations on the types of substrate and other materials that can be present in the samples. Nevertheless, its properties yield LPCVD a fundamental instrument in a microfabrication facility. Polysilicon, silicon nitride, silicon oxynitride, and silicon dioxide are material most deposited using LPCVD. These films can offer sidewall protection for structures that require electrical isolation. The sidewall coverage amount depends on the temperature and type of LPCVD deposition being performed and in the case of a trench feature, the aspect ratio of the feature. In general, the higher the process temperature, the better the conformity.
In this work, we used thermal growth LPCVD to deposit the first insulating layer (ONO) over both sides of silicon wafers. The instrument used was a Centrotherm E 1200 HT 260-4 4 Diffusion and LPCVD Furnaces (Figure 3.10):

Figure 3.10: Horizontal tubes used in FBK for thermal oxidation and LPCVD processes.

This instrument allows growing/depositing of various types of SiO_2 and Si_3N_4 layers, both in wet and dry condition, with a deposition thickness ranging from 20 nm to 2μm (±3%).

3.3.2 Photolithography and etching processes

Photolithography is a very simple and cheap method, deeply used in microfabrication to pattern the multiple layers deposited onto substrates. Optical lithography is basically a photographic process by which a light-sensitive polymer, called a photoresist, is exposed and developed to form three-dimensional relief images on the substrate. In general, the ideal photoresist image has the exact shape of the designed or intended pattern in the plane of the substrate, with vertical walls through the thickness of the resist. Thus, the final resist pattern is binary: parts of the substrate are covered with resist while other parts are completely uncovered. This binary pattern is needed for pattern transfer since the parts of the substrate covered with resist will be protected from etching, ion implantation, or other pattern transfer mechanism [3.38, 3.39].

Photolithography technique was used at the first time in the 1820s, when Nicephore Niepce invented a photographic process that used Bitumen of Judea, a natural asphalt, as the first photoresist. Bytheway, the light-sensitivity of bitumen was very poor and very long exposures were required. In 1940, Oskar Süß introduced the first “positive” photoresist by using diazonaphthoquinone [3.40]. In 1954, Louis Plambeck Jr. developed the Dycryl polymeric letterpress plate, which made the plate making the process faster.
The general sequence of processing steps for a typical photolithography process is as follows: substrate preparation, photoresist spin coat, pre-bake, exposure, post-exposure bake, development, and post-bake. A resist strip is the final operation in the lithographic process after the resist pattern has been transferred into the underlying layer.
There two different kinds of the photosensitive polymer. The most common photoresist, called "positive", becomes soluble in the developer when exposed; differently, in the "negative" photoresist, unexposed regions are soluble in the developer. The standard resolution of photolithography process is 2 μm, although with the latest techniques you can get up to tens nanometer [3.41, 3.42].
In our work, photolithography technique was used to define all pattern of layers deposited over silicon and quartz wafers. They have used both the positive or positive/LOR photoresist, depending on the definition type chosen. We utilized two track types for coating and developing of photoresists over silicon and quartz wafers (Figure 3.11).

Figure 3.11: SVG 8600 Photoresist Coat Tracks available in FBK for photoresist coating and developing.

To create the pattern by means of photoresist exposition, in this work were used two different mask aligners, reported in Figure 3.12.

Figure 3.12: Mask aligners available in FBK to expose photoresist: *(left)* the Karl Suess automatic mask aligner, model MA150BSA and *(right)* the Karl Suess manual mask aligner, model MA6.

Bake operations were carried out in a standard oven.
Regarding the etching, in our processes, we considered both wet and dry etchings. For metal circuitries definition, we employed wet etching, by using organic/inorganic solutions.

Figure 3.13: One FBK station for wet etching in photolithography processes.

The dry method was used for final etch concerning the definition of the insulation layer and for the definition, on the wafer backside, of silicon membrane excavation. The instrument employed was a reactive ion etcher of OEM, model Tegal 903 ACS.

Figure 3.14: The reactive ion etcher OEM Tegal 903 ACS, available in FBK.

This apparatus is focused on the anisotropic etching of SiO_2 and Si_3N_4 layers, with the 5% of uniformity.

The final stripping of the photoresist was obtained, in all photolithography processes employed in our MHP microfabrication, by means of a plasma dry stripper (Figure 3.15).

Figure 3.15: The dry stripper Asher, type Matrix System One, available in FBK.

3.3.3 Physical Vapour Deposition

Physical vapour deposition (PVD) is a technique that allows obtaining layers by means of a variety of vacuum deposition methods. It is mostly used to form thin films and coatings. A process in which a reference material goes from a condensed phase to a vapour phase and then back to a thin film condensed phase characterizes PVD. PVD is used in the manufacture of items, which require thin films for mechanical, optical, chemical or electronic functions. Examples include semiconductor devices such as thin film solar panels, aluminized PET film for food packaging and balloons and MOX deposition for gas sensor [3.43-3.46].

Among the different vacuum deposition methods, most used are the cathodic arc deposition, the electron beam physical vapour deposition, the evaporative deposition and the sputter deposition [3.47-3.49].

The PVD technique allows deposition of practically any type of inorganic material and different organic materials, and the possibility of using different types of evaporation allows obtaining, from the same starting material, films with completely different properties. Moreover, the deposited layers result in high strength. Thanks to these advantages and its ductility, the PVD technique is widely used in microfabrication processes.

The PVD instrument used at the FBK laboratories is an Ulvac, model EBX-16C, provided with e-gun Ferrotec EV S-6.

Figure 3.16: The PVD Ulvac, model EBX-16C, with e-gun Ferrotec EV S-6, available at the FBK.

In this Ulvac model, the technique used to lay down the sample is the electron beam physical vapour deposition, with a vacuum of 1.0 x 10^{-5} Pa. This instrument provides deposition of various metals (such as gold, titanium, chromium, platinum and silver) and insulating layers as a SiO_2 layer. The minimum deposition thickness of a continuous layer is 3 nm. The film thickness is monitored during deposition by means of a quartz crystal MAXTEK Film Deposition Controller (Maxtek MDC-360). The purpose of this instrument in our work has been to deposit the necessary metals to obtain electrodes on the substrate.

3.3.4 Furnace

Thermal treatments are of high importance in the development of an MHP device. Indeed, they stabilize the layers deposited in the various process steps. This thermal stabilization becomes fundamental in the case of devices that must be used under constant high-temperature conditions, as in the case of MHPs. As far as our procedure is concerned, we have decided to carry out a firing step after the deposition of each of the basic layers that compose our MHP, i.e. the two metallic circuitries and the inter-metal passivation. The heat treatment in many cases also serves to stabilise chemically and morphologically the materials deposited on silicon or quartz wafers. The morphological and chemical stabilization of the deposited metals, due to an increase in their roughness, is highlighted in many works [3.21]. About insulating materials such as silicon oxides and silicon nitrides, many processes involving their deposition produce a large quantity of gas, which remains trapped inside the deposited layer. An adapt heat treatment stabilises both morphologically and chemically the material, releasing excess gas. Therefore, the parameters of thermal treatments should not be underestimated for the success of the entire development process of microheaters.

The instrument used at the FBK is an Expertech Oxidation/Annealing Furnaces.

Figure 3.17: The Expertech Furnace for heat treatments at the FBK.

This furnace, equipped with three temperature controls, allows both oxidation and reduction treatments, until a working temperature of 1200°C.

3.3.5 Plasma-Enhanced Chemical Vapour Deposition

Plasma-enhanced chemical vapour deposition (PECVD) is a chemical vapour deposition process used to deposit thin films from a gas state (vapour) to a solid state on a substrate. Chemical reactions are involved in the process, which occur after creation of a plasma of the reacting gases. The plasma is generally created by radio frequency, frequency or direct current (DC) discharge between two electrodes, space between which is filled with the reacting gases [3.50]. This provides an advantage of lower temperature processing compared with purely thermal processing methods like LPCVD. PECVD processing temperatures range between 200-400°C, meanwhile, the working temperature of LPCVD processes is in the range between 425-900°C [3.51]. However, this lower temperature highlighted the drawbacks of a high concentration of gases produced during the film deposition. These gases remain embedded inside the layer of the deposited material. Accordingly, the materials deposited with this technique result in less thermal and mechanical stability than materials deposited with alternative techniques such as LPCVD.
In MHP production processes presented in this work, we utilized the PECVD method to deposit the inter-metal passivation. The instrument used was an STS-MPS PECVD (Figure 3.18).

Figure 3.18: STS-MPS PECVD instrument available at the FBK.

This equipment allows the deposition of silicon oxide and silicon nitride layer, with different properties depending on parameters used (generator frequency, temperature and pressure). Furthermore, it is equipped with a time checked deposition rate on a reference.
The choice of the PECVD to deposit the upper insulating layer was forced. In fact, this step takes place after the deposition of metal circuitries. Since the presence of metals such as platinum, titanium, gold and so on, can compromise the good realization of other types of devices produced in FBK, the processing procedure imposed prohibits the introduction of "contaminated" wafers with metals in the instrument used for LPCVD. Furthermore, the high temperature of LPCVD technique can compromise the metal stability deposited. Consequently, it was decided to use PECVD technique to lay the overglass (SiO_2/Si_3N_4) layer.

3.4 Micro-fabrication process description

In this section, the various steps of the microheaters fabrication will be presented in detail. The characterizations carried out on the individual steps will be reported in order to select, among the various machining alternatives, the best alternative for finally having an optimized process to develop IC microheater suitable for gas sensing application. The fabrication of the MOS devices investigated in the present work was performed on 6 inches quartz and the silicon wafer. Silicon wafer used were p-type Si <100> double side polished, with a resistivity of 12-18 Ωcm. Quartz wafers used had a thickness of 600 μm, were double polished and produced by means of electric flame.

3.4.1 Initial Insulating layer

As mentioned in paragraph 3.3.1, the initial deposition of the insulating layer was carried out only for the processes concerning silicon, since quartz, having a high intrinsic resistivity, can come directly into contact with the metal circuits that will be integrated on the device without giving significant problems of electric dispersion. Furthermore, the low thermal conductivity of quartz allows for low heat dissipation.

The initial deposition of insulating material, consisting of silicon oxide and silicon nitride layers, is of fundamental importance because this thin film will be, eventually, the base of the membrane that will support the metal levels and sensing material of the final device. This membrane must have a high thermal and mechanical resistance, as well as a very low thermal expansion and an almost void residual stress value (section 3.2.1) [3.52]. In particular, residual stress plays a key role in the membrane stability [3.53]. Indeed, if the membrane has residual stress values, which can be compressive or tensile, it will not be perfectly planar, thus reducing its robustness. Moreover, if additional heating stress were to be summed up to the residual stress, due to thermal expansion of the membrane materials, the membrane stability would be definitely compromised. In literature, many works show characterizations of different combinations of silicon oxides and silicon nitride layers, deposited through LPCVD or growth by means of thermal growth, to obtain high established films [3.54, 3.55].
For this purpose, here in FBK, a thorough characterization over the years has allowed the development of a high-quality standard recipe [3.56, 3.57]. This recipe provides a triple layer deposition, called ONO (paragraph 3.3.1), by thermal growth and LPCVD. First, a SiO_2 layer is formed on silicon wafers by means of thermal oxidation at a temperature of 975°C. This technique exploits the high temperature forced oxidation of silicon by means of an oxidizing agent, which can be vapour water or oxygen. The rate of oxide growth is often predicted by the Deal-Grove model [3.58]. The reaction that formed the SiO_2 layer over a silicon wafer is the following:

$$Si + H_2O_{(g)} \rightarrow SiO_2 + H_{2(g)}$$

$$Si + O_{2(g)} \rightarrow SiO_2$$

In our case, we used a wet thermal oxidation. SiO_2 thus deposited showed a compressive stress of 352 MPa. The deposition time was 40 min, to obtain a layer thickness of 200 nm.
Afterwards, a layer of silicon nitride was deposited over SiO_2. Instead of the thermal oxidation, where the formation of SiO_2 is due to the interaction between oxidant agent and the silicon wafer, the Si_3N_4 is deposited on the wafer surface by means of a gaseous reaction. In our process, the reaction occurred to deposit silicon nitride gases is:

$$3SiCl_2H_2 + 4\ NH_3 \rightarrow Si_3N_4 + 6\ HCl + 6\ H_2$$

Silicon nitride deposited by LPCVD contains up to 8% hydrogen. Si3N4 thus deposited highlighted a tensile stress of 1207 MPa. The grown time was 42 min, in order to obtain a Si_3N_4 thickness of 100 nm.
Finally, a further layer of silicon oxide was raised above the previous two. Differently to the first SiO_2 layer, in this case, the oxide layer has been deposited and not directly grown on the surface of the wafers. The SiO_2 deposition was obtained by flowing gaseous tetraethyl orthosilicate (TEOS) inside quartz tubes containing silicon wafers at 720°C. The degradation reaction of TEOS to produce SiO_2 is:

$$Si(OC_2H_5)_4 \rightarrow SiO_2 + \text{byproducts}$$

where possible byproduct is CO_2, H_2, alkanes and so on. The residual stress of the SiO_2 layers was compressive, of about 104 MPa. The deposition thickness was 600 nm.
Since the two SiO_2 layers are compressive and Si_3N_4 is quite tensile, the final layer obtained is balanced, with a low residual stress of 121 MPa. Furthermore, ONO has a high thermal stability, higher than 650°C, which is the maximum temperature reached for some sensing materials in the firing step. The resistivity of the triple layer was about 10^{14} Ωcm.

3.4.2 Micro-heater and interdigitated electrodes

Metal circuitries, whose function in the device has been explained in paragraph 3.1, have been deposited through PVD (section 3.3.3) technique both in silicon and quartz wafers. In the one hand, for many metals, including gold and platinum, direct deposition on the SiO_2 surface is not recommended due to very poor adhesion between the two surfaces [3.59]. This low adhesion strength is probably mainly due to a lacking stable form of those metals with oxygen, which involves a high surface energy in the interface between the SiO_2 surface and the metal layer, causing the low adhesion [3.59]. On the other hand, there is a class of metal that shows a very strong adhesion with SiO_2, such as titanium, chromium, nickel and so on [3.60]. Therefore, it is recommended to consider this premise for proper deposition of metals in an IC. The choice of the most suitable metal was mainly based on the purpose of the electrode that was going to be deposited. Starting from the heater, one should bear in mind that the heating method for microheaters involves the conversion of electrical work to high-density heat. The electrical power applied to the microheater element is dissipated thermally through the structure according to Joule heating [3.10]. Consequently, the material used as a heater must have certain electrical characteristics, i.e. tuneable resistivity and high resistance to electromigration. So far, heater materials most commonly used, as reported in the literature, have been poly-silicon, tungsten and platinum, due to their high thermal stability and their compatibility with micromachining [3.21, 3.61, 3.62]. In this work, we decided to use Pt, given its higher deposition quality than polysilicon through the PVD technique. Furthermore, the Pt element is also used as a resistance thermometer, because its temperature coefficient of resistivity (α) is relatively high and near to linear over the operating temperature range (up to 700°C). The relationship between resistance and temperature for Pt is expressed as [3.10]:

$$R_{(T)} = R_{(0°C)}(1 + \alpha T)$$

where R_T is the element resistance at the temperature T, $R_{(0°C)}$ is the resistance at 0°C. The α for Pt is taken as $38 \cdot 10^{-4}$, but it depends on deposition parameters, and we have measured it in the finished microheaters. The material that we used as an adhesion layer, both on quartz and silicon wafers, was the titanium, a material that shows a strong surface interaction with both platinum and SiO_2 [3.63].
Considering the interdigitated electrodes, relative to the sensing material, the most commonly used choices so far refer to materials that allow a passage of current with low thermal dispersion. Among these, the best candidate was gold, by using chromium as an adhesion layer (Au/Cr) [3.64]. However, this solution is unfortunately unattractive for our application. In fact, Au/Cr has shown, in many research works, poor thermal stability due to a migration of the chromium layer through the gold film at relatively low temperatures [3.65]. This migration results in a drastic weakening of the adhesion between the substrate and the metal layer, which become unusable. Thus, it was decided to use Pt/Ti deposition also for the interdigitated electrode. This choice brings a great advantage especially for P1 processes since the deposition of both heater and interdigitated electrodes can be done with a single deposition, saving time and costs.
The first step of Pt/Ti deposition was the definition, by means of a positive photoresist for lift-off, of the electronic circuit layouts for both silicon and quartz devices. With this aim, wafers were coated with two different polymers: 1.2 μm of a positive photoresist (FUJIFILM HIPR6512), and 500 nm of a sacrificial layer (named LOR). Then, it was carried out a bake of the coated photoresist at a temperature of 120°C for 1 hours. Afterwards, wafers were exposed to suitable wavelength by using a mask aligner to define electrodes, and the development of photoresist was obtained with a HIPR6517HC commercial solution. Then, the post-bake treatment was performed. Images, obtained after photolithography definition steps by means of an optical microscope, are reported below.

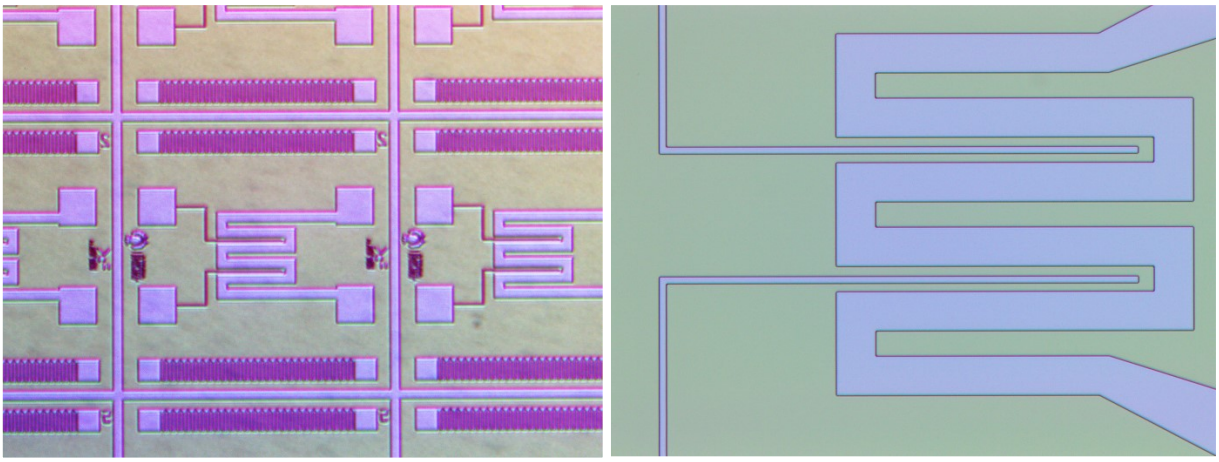

Figure 3.19: Images of developed photoresist in P1S *left)* L2, 2.5x and *right)* L1.1, 10x.

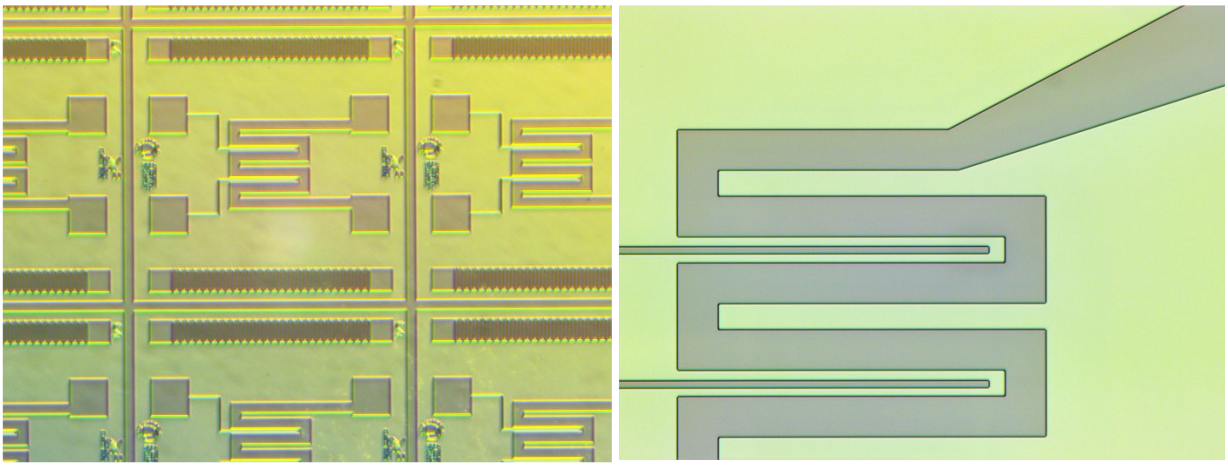

Figure 3.20: Images of developed photoresist in Q1S *left)* L2, 2.5 x and *right)* L1.1, 10x

The role of the sacrificial layer is to create precise and reproducible undercut, useful for metal deposition (Figure 3.21).

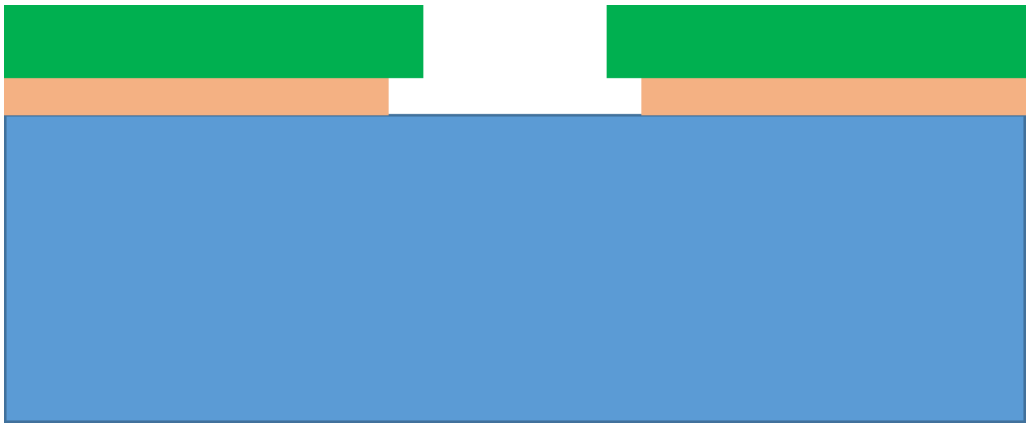

Figure 3.21: Schematic representation of the photoresist/LOR develop (substrate in blue, LOR in pink and positive photoresist in green)

At this stage, 10 nm of Ti was deposited by electron beam evaporation (paragraph 3.3.3). The background pressure in the vacuum chamber was in the 10^{-5} Pa range and the deposition rate was 1 Å/s. 120 nm of Pt was deposited over the titanium layer.

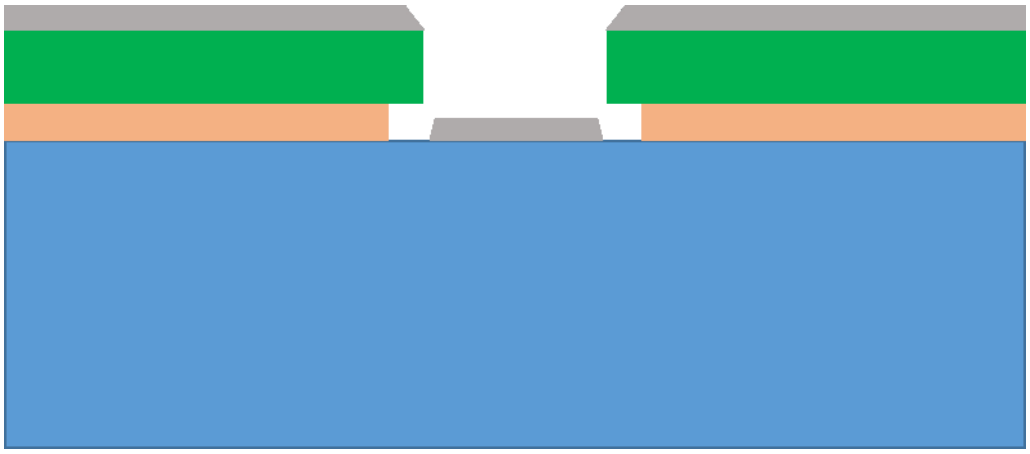

Figure 3.22: Schematic representation of the metal deposition over developed photoresist/LOR (substrate in blue, LOR in pink, positive photoresist in green and metal in grey)

The metal gate was defined by removing the photoresist (lift-off technique) by using dimethyl sulfoxide at 60°C, assisted by ultrasonic treatment. Finally, wafers were heat-treated at 650°C in the oven, under a constant flux of nitrogen, to thermal stabilize metal layers at the maximum temperature that a common final sensor will keep, i.e. the firing temperature. Images of integrated metal circuits at the end of the metal deposition process on silicon and quartz wafers are shown below.

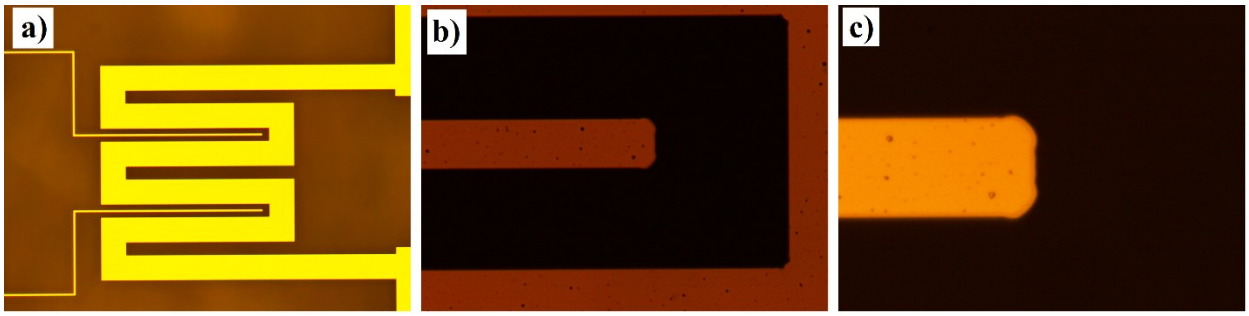

Figure 3.23: Metal interdigitate electrode over quartz wafers, process P1Q, with a magnification of *a) 5x, b) 50x, and c) 100x.*

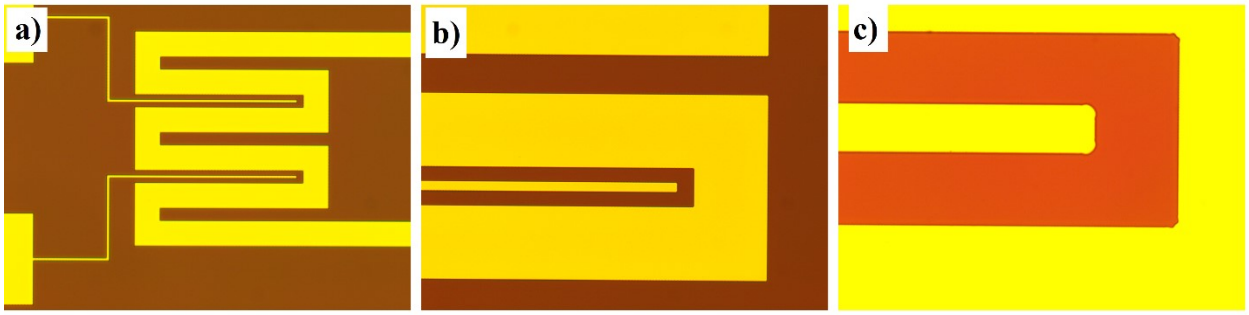

Figure 3.24: Metal interdigitate electrode over silicon wafers, process P1S, with a magnification of *a)5x, b) 10x* and *c) 50x*

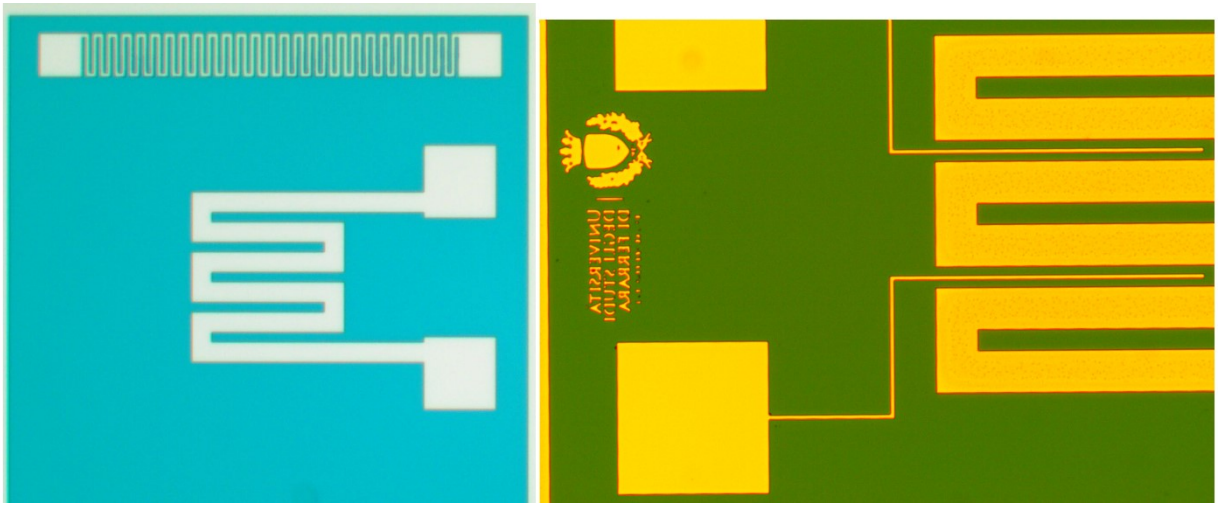

Figure 3.25: Metal interdigitate electrode over silicon wafers, process P2S. *Left)* deposition of the heater (magnification 2.5x), *right)* deposition of the upper circuit (magnification 5x)

Since microheater in processes is subjected to two (process P1) or three (process P2) thermal treatments at 650°C, the effect of heating processes on metals was characterized both from a morphological and electrical point of view. As can be seen from Figure 3.24, the increase in the heating time led to an increase in the roughness of the metal surface, as reported in the literature [3.66]. This increase in roughness is due to the tendency of metals, deposited through our technique, to cluster during aggressive heat treatments. This behaviour can be detrimental to the final bonding of the device on the support to be interfaced to the signal reading electronics. An increase in the surface roughness of platinum can decrease the adhesion between platinum and another surface. To verify the effectiveness of the adhesion between the metal contacts and the bonding wire used for bonding, in the section 3.5.1 are reported data of pull test obtained on the finished devices.

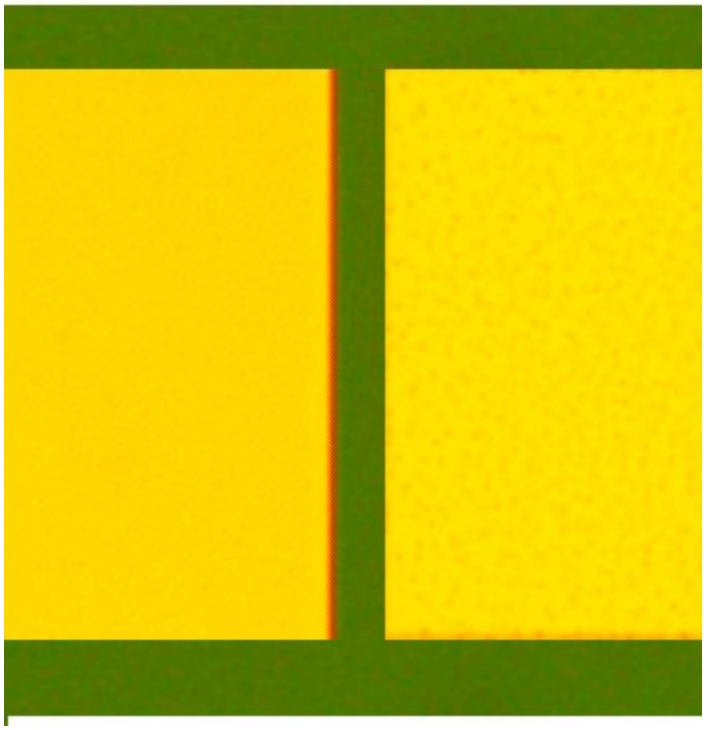

Figure 3.26: Image of metals roughness after *left)* two heating treatments at 650°C for 2 hours and *right)* after three heating treatments at 650°C for two hours.

Along with roughness, other parameters of the metal layer also change with the thermal treatment. Among these, resistivity is one of the elements that has the greatest impact on final properties of the substrate. In the table 3.1 are shown metal resistivity parameters (ohms-per-square) vs. exposition time at 650°C. Measurements were performed with the four-point probe technique, by means of a Napson Four Point Probes instrument.

Table 3.1: Resistivity value of the Pt/Ti metal combination vs. time of the heating treatment, at 22°C.

	120/10 nm Pt/ti	
	Resistivity (Ω/square)	St. Dev. (%)
as deposited	1.92	3.88
2 hours at 650°C	1.45	3.3
6 hours at 650°C	1.41	2.5

Data obtained highlighted that the first thermal treatment strongly affected resistivity of metal elements. However, further cycles of heating did not provide an essential change in Pt/Ti electrical properties.

3.4.3 Insulating PECVD layer

PECVD deposition of inter-metal passivation was the developmental step of the microheater that needed the most in-depth characterization. Indeed, for microheater devices though, PECVD layers are limited because of their high hydrogen content, which makes them change mechanical properties upon heating, due to chemical bonds cleavage, outgassing and condensation [3.67, 3.68].
Despite a deep knowledge of PECVD layer mechanical properties and thermal effects, there is no record in the literature of a fully functional high-temperature multilayer microheater with PECVD passivation. Two devices near the required performance: Lv et al. report a PECVD microheater with curing at 500°C [3.69]. Belmonte et al. developed a PECVD Silicon Nitride-based microheater working at 700°C, but had severe stress related fragility problems and very poor yield [3.4]. Therefore, we decided to investigate optimal PECVD parameters to deposit an insulating material with high thermal stability, up to 650°C.

3.4.3.1 Pre-process tests

The investigation started with a complete characterization of PECVD films at high temperature, both silicon oxides and silicon nitrides. Based on the obtained data, a subset of materials is selected and tested in the fabrication processes of microheater devices, both for quartz and silicon.
PECVD silicon oxides and nitrides were examined, deposited using both the standard high frequency (13.56MHz) plasma and the low frequency (308kHz) plasma generation. The set of candidate materials is reported in Table 3.2.

Table 3.2: Candidate materials and deposition parameters.

	N_2	N_2O	SiH_4	NH_3	pressure	power
	sccm	sccm	sccm	sccm	mTorr	W
HF SiO_2	392	1420	10	0	900	30 HF
LF SiO_2	392	1420	12	0	550	60 LF
HR SiO_2	0	3200	100	0	550	200 LF
HF Si_3N_4	1960	0	40	55	900	20 HF
LF Si_3N_4	1960	0	40	40	550	60 LF
MF Si_3N_4	1960	-	40	40	900	25HF-25LF

Layers were tuned to be used as low-stress BEOL passivation. Both high-frequency layers and their low-frequency variants were tested, together with two more materials: a low-stress silicon nitride obtained by mixing high and low frequency (labeled MF) which was developed by Bagolini et al. [3.70, 3.71], and a high deposition rate variant of the low frequency generated silicon oxide (labeled HR in Table 2). A first set was deposited with a thickness in the range 170-230 nm, this being the target fabrication range, while a second set was deposited with a higher thickness, in the range 690-740nm, to assess the influence of thickness on the mechanical properties, and to provide more suitable samples for the nanoindentation measurements [3.72-3.74].
To tested PECVD materials stability, all layers were deposited onto polished standard single crystal silicon wafer substrates. After the deposition, all samples were annealed in nitrogen atmosphere at increasing temperatures, for a fixed time of 2 hours. Annealing temperatures ranged from 400°C to 900°C with steps of 100°C. All ramps were performed at a rate of 5°C/minute. After each annealing the samples curvature profile was acquired, to measure residual stress. Refractive index was measured at the initial state and after the final anneal with a variable angle spectra ellipsometer (632.8nm He-Ne laser light).
The layers suffered cracking and peeling at different temperatures, that will be considered as damage temperatures. Table 3.3 reports the temperatures that caused damage to each film, together with the as-deposited film thickness.

Table 3.3: Damage temperatures for both films thicknesses.

	thickness	*damage temp.*	*thickness*	*damage temp.*
	nm	°C	nm	°C
HF SiO_2	199	800	689	-
LF SiO_2	230	600	710	700
HR SiO_2	209	800	735	-
HF Si_3N_4	195	700	691	700
LF Si_3N_4	176	500	700	600
MF Si_3N_4	216	600	670	700

As one can see, the damage temperatures are affected by the layer thickness: by increasing the thickness, all layers exhibit a higher resistance to elevated temperatures. Missing temperature data for thick silicon oxides indicate that we did not damage the layers during annealing.
Images of 200 nm films damages, obtained by means an optical microscope, are shown below.

Figure 3.27: Image of surface peeling of 200 nm SiO_2 HF at 800°C (magnification 100x).

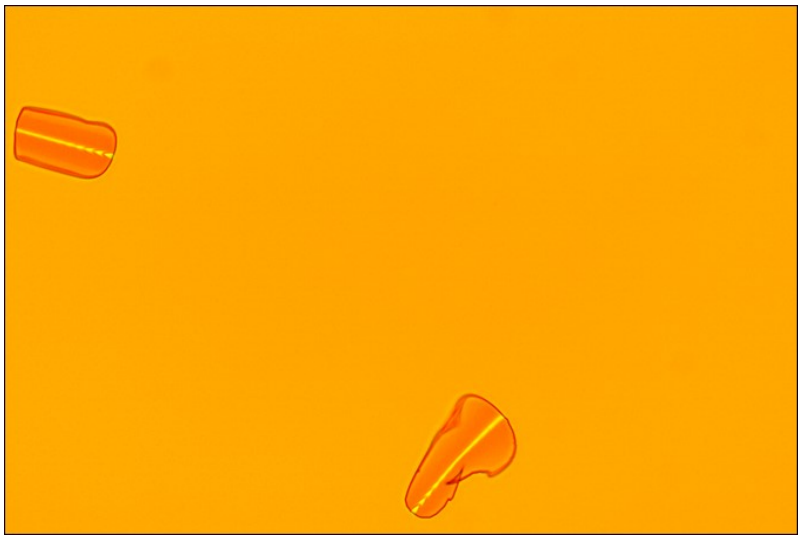

Figure 3.28: The surface peeling image of 200 nm SiO_2 LF at 600°C (magnification 100x).

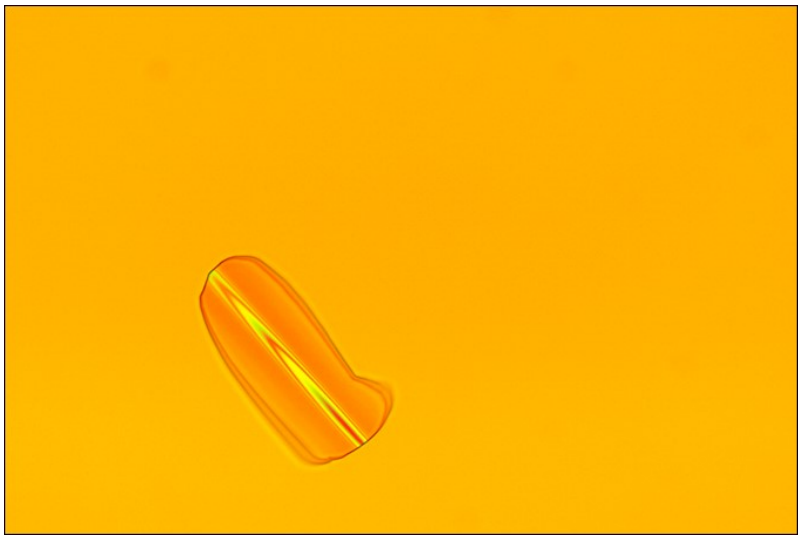

Figure 3.29: The Surface peeling image 200 nm SiO_2 HRF at 800°C (magnification 100x).

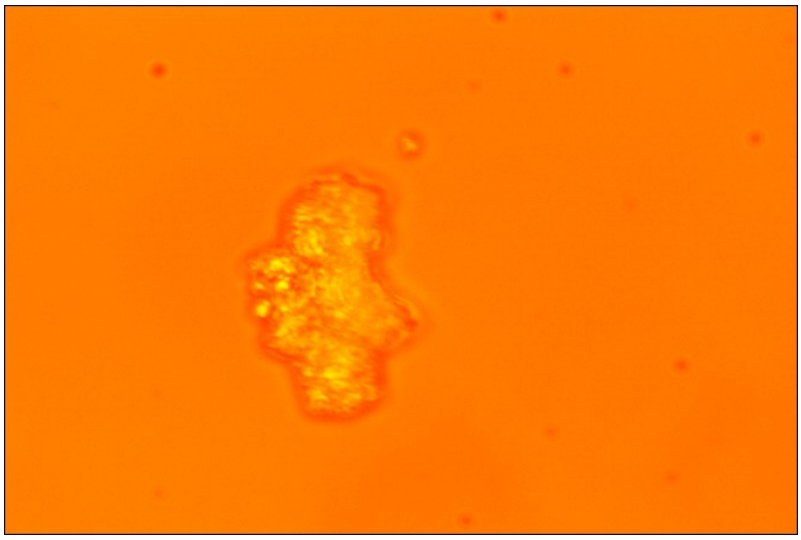

Figure 3.30: A typical cracking of the 200 nm Si_3N_4 HF at 700°C (magnification 100x).

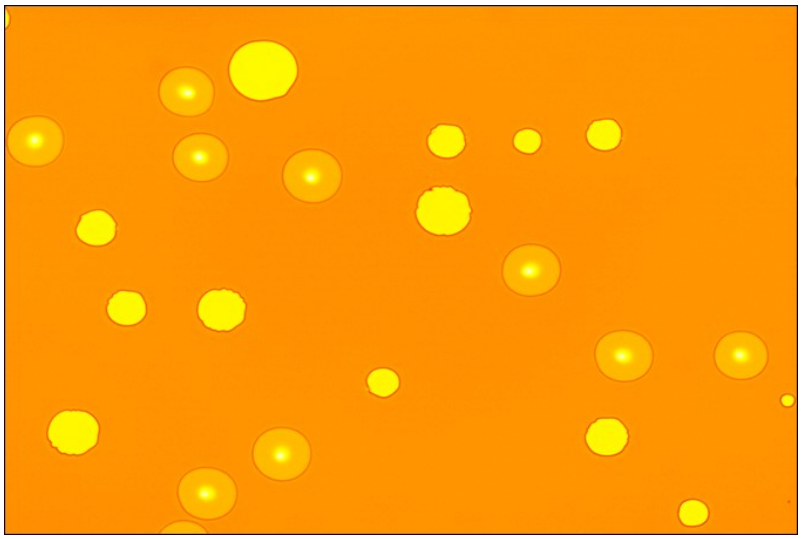

Figure 3.31: Typical cracking of 200 nm Si_3N_4 LF at 500°C (magnification 50x).

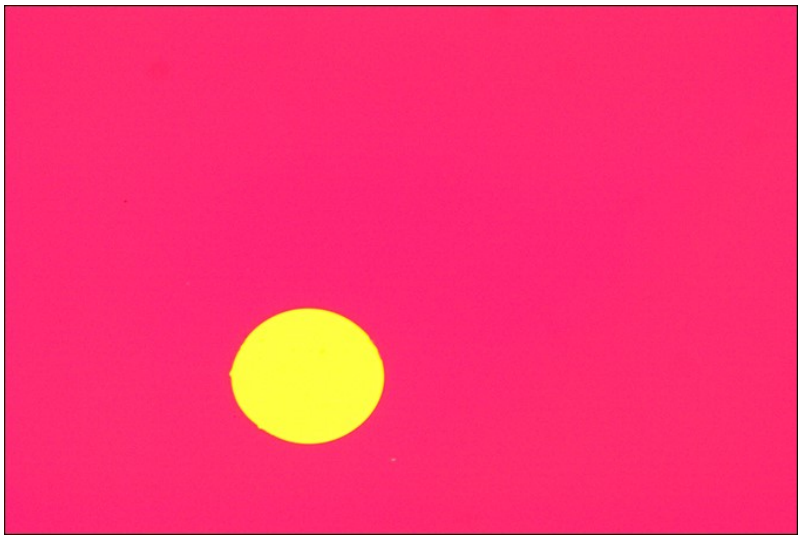

Figure 3.32: The typical cracking of 200 nm Si_3N_4 MF at 600°C (magnification 100x).

At damage temperature, all layers suffered peeling, making wafer curvature measurements impossible, with the sole exception of thin LF and MF nitrides, which suffered minor cracking of the film.

Measurements of the residual stress were performed by wafer curvature method, using Stoney model [3.75]. Measurements were carried out with a Kla-Tencor mechanical profilometer before and after the deposition, as well as after each annealing step. Three profiles were measured for each sample along its diameter separated by an offset of 5 mm; the resulting stress data showed a standard deviation better than 3%. This standard deviation is valid for all stress data reported. The stress measurements for silicon oxide samples are reported in Figure 3.33 and silicon nitride film stresses are reported in Figure 3.34.

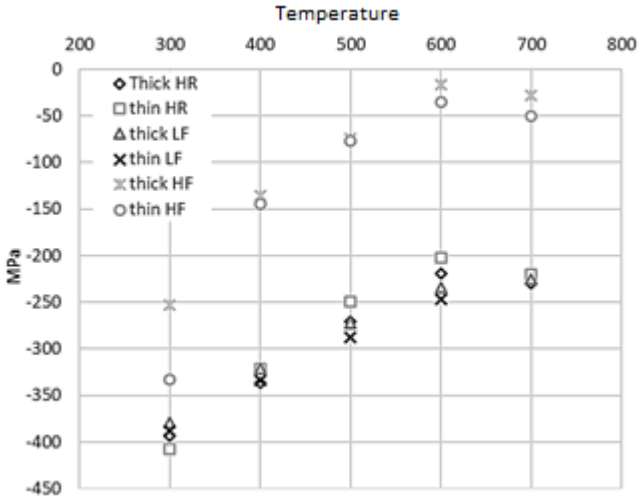

Figure 3.33: Stress values vs. heating temperatures for SiO_2 layers.

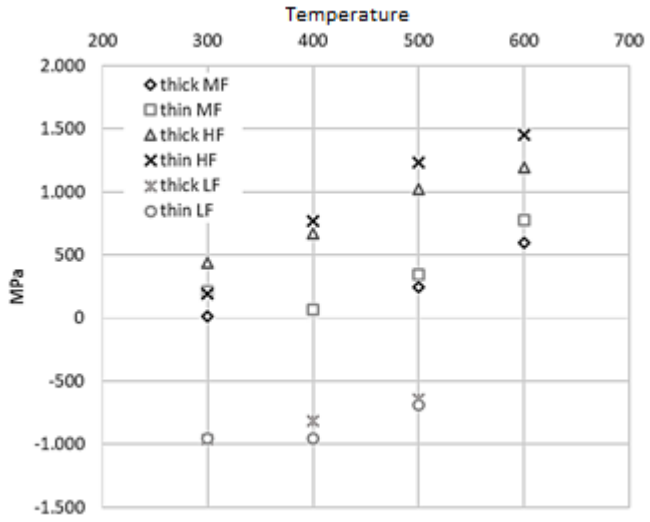

Figure 3.34: Stress values vs. heating temperatures for Si_3N_4 layers.

Measurements show only minor stress differences between thin and thick samples deposited using low-frequency plasma. On the contrary, high-frequency plasma samples show thickness related stress values (Table 3.4). As deposited films have a shift towards tensile regime when the thickness is increased.

Table 3.4: stress vs thickness for HF samples.

		thickness	*stress*	*thickness*	*stress*
	anneal	nm	MPa	nm	MPa
HF SiO_2	none	199	-333	689	-253
HF SiO_2	700°C	196	-50	681	-28
HF Si_3N_4	none	195	195	691	439
HF Si_3N_4	600°C	176	1451	669	1196

Upon annealing, silicon oxide samples stress converges, while silicon nitride becomes less tensile in thick samples with respect to the thin ones. Both silicon nitride and silicon oxide overall stress variation upon annealing are reduced in thick samples compared to the thin ones. Hydrogen being recognized as the major source of compressive residual stress in amorphous silicon and oxide PECVD films [3.76], this result indicates that hydrogen outgassing is inhibited in thick films, leading to a reduced stress variation.

In all silicon oxide samples, the outgassing induced stress variation is dominant up to 600°C (Figure 3.33). The same stress behaviour is reported in the literature [3.77, 3.78].

The thermal expansion coefficient of silicon oxide films decreases upon annealing [3.79] and this increases the mismatch between the silicon substrate and silicon oxide film expansion, inducing a more compressive thermal stress. This effect becomes dominant above 600°C annealing, generating a trend inversion towards compressive (Figure 3.33). Moreover, by FT-IR spectrometry it was observed that at temperatures above 600°C hydrogen cleaves from nitrogen and silicon, and nitrogen condensates with silicon [3.67]. Indeed, temperatures above 600°C are needed for hydrogen cleavage from nitrogen and silicon, as reported in the literature [3.80, 3.81].

HF silicon oxide has the lowest stress values, and stress further reduces upon annealing, approaching zero at 600°C. This makes it the ideal candidate for device passivation. On the other side, silicon

nitrides have high tensile values upon annealing at 600°C, except LF silicon nitride which is initially compressive and does not withstand annealing above 500°C.
All layers steadily reduce their thickness upon annealing, with thickness variation being more pronounced in silicon nitrides than silicon oxides. Thickness values as a function of annealing temperature are reported in Figure 3.35.

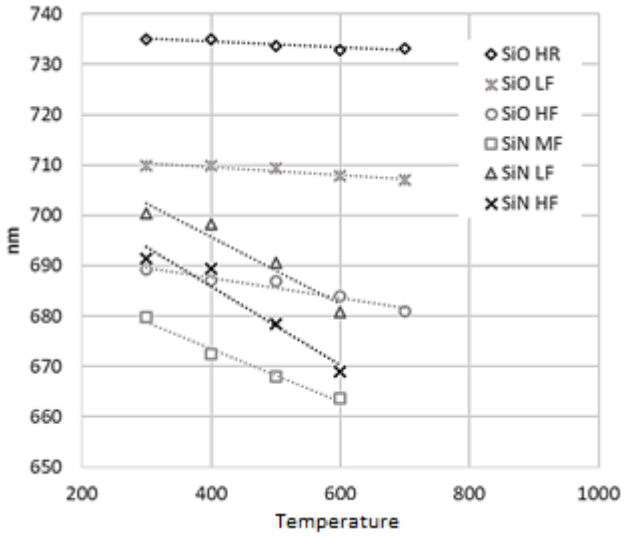

Figure 3.35: The trend of layer thicknesses vs annealing temperatures.

Silicon nitrides thickness variation is much higher than that of silicon oxides, up to 3.2% for HF Si_3N_4, while oxides range from 0,3 (HR) to 0,8 (HF) thickness variation.
Refractive index values are reported in Table 3.5.

Table 3.5: Refractive index of layers as deposited and after annealing at 700°C.

	RI		*RI variation*
	as dep.	*700°C*	*%*
HF SiO_2	1.51	1.463	-3.1
LF SiO_2	1.5	1.465	-2.3
HR SiO_2	1.472	1.465	-0.5
HF Si_3N_4	2.04	2.1	2.9
LF Si_3N_4	1.92	-	-
MF Si_3N_4	2.06	2.11	2.4

Data for the annealed Si_3N_4 LF are missing because the sample was too degraded after annealing at 600°C.
All oxides tend to move towards the stoichiometric index value upon annealing. HR silicon oxide has the lowest index variation, as its as-deposited value is already quite near to the stoichiometric one of 1.46 [3.82]. Instead, silicon nitrides do not move towards the stoichiometric RI value of 2.023, but rather increase further. This effect is related to film densification [3.68] which is evident from thickness data (Figure 3.35). Two models can be used to assess the stoichiometry of PECVD silicon nitrides: Bustarret et.al propose a theoretical approach [3.83] while Dauwe proposes an empirical equation based on experimental data from Rutherford backscattering and elastic recoil detection measurements [3.84].

Table 3.6 reports the values obtained using Bustarret analytical model (labelled A) and Dauwe empirical equation (labelled E).

Table 3.6: Stoichiometric Si_3N_4 values obtained by means of Bustarret and Dauwe model

	RI	*Si/N*		*RI*	*Si/N*	
	(as dep.)	*A*	*E*	*(700°C)*	*A*	*E*
MF	2,06	0,84	0,96	2,11	0,97	1,03
HF	2,04	0,79	0,93	2,1	0,94	1,01
LF	1,92	0,55	0,77	-		

The ratio variation between as-deposited and annealed films is a measure of nitrogen outgassing. It should be noted that, unlike Bustarret equation, the Dauwe linear model does not correctly fit the Si/N ratio of stoichiometric silicon nitride (RI=2.023, Si/N=0.75), overestimating the ratio to 0.91. Both models document an increase in the Si/N ratio, indicating a reduction of nitride content.
The increase in refractive index upon annealing agrees with the literature [3.68] and is a consequence of hydrogen and nitrogen outgassing, combined with the formation of Si-Si bonds.

At this stage, all annealed samples were measured with a CSM nanoindenter equipped with a diamond tip with Berkovich shape, and the elastic modulus was estimated using Oliver Pharr method [3.74]. The characterization of the thin films was obtained using a series of indentations performed at various depths, from 7% to about 100% of the thickness of the film (for "thin" film only from 18% to 100%). The final elastic modulus was estimated using the linear fit of the data acquired at an indentation depth less of 40 % of film thickness.
Elastic modulus estimate from nanoindentation measurements are reported in Table 3.7.

Table 3.7: Comparison of Young modulus obtained with literature values ((*) samples damaged by annealing)

	Literature	*Thin sample*		*Thick sample*	
	GPa	GPa	St.dev.	GPa	St.dev.
HF SiO_2	81 [3.86]	88	5	85	4
LF SiO_2	-	109	5	83	2
HR SiO_2	-	154	11	83	3
HF Si_3N_4	198 [3.87]	184	5	198	9
LF Si_3N_4	-	187	5	241*	10
MF Si_3N_4	276 [3.88]	240	5	204*	3

Each value is an average over 9 measures, the error is estimated as standard deviation. We reported the values of thin layers to have an estimation of the elastic modulus of the layer to be actually used in micro-device fabrication. Moreover, we reported the elastic modulus of thick layers, to minimize the influence of the substrate on the nanoindentation curve. For this reason, in the case of oxides, results obtained on thick films are generally more accurate. Silicon nitrides are less affected by the substrate, as their elastic modulus is not far from that of silicon (179 GPa [3.85]). MF silicon nitride thick sample severe cracking after the last annealing at 700°C makes the value of 204 GPa less reliable than that of the thin sample (240 GPa). Small variations between the value reported in the literature and measured values can be observed in Table 3.7.

This is also because the deposition parameters are different, and values from literature refer to as-deposited samples, without annealing. The values reported in references 3.86 and 3.87 are measured on PECVD silicon oxides and nitrides deposited at the same temperature and using same HF plasma generator frequency as in present work, but with different gas ratios. The value from reference 3.89 is measured on the same MF silicon nitride as the one used in present work.
To the best of our knowledge, data is missing in the literature on LF PECVD silicon nitrides and oxides. The measured data indicate that LF oxides have a very similar elastic modulus to that of HF oxides. Moreover, the annealed silicon oxide elastic modulus is almost identical to that of stoichiometric silicon oxides [3.89]. In the case of nitrides, it is not easy to compare HF with LF as the measured modulus of LF samples is very different between thin and thick film. Nevertheless, as the thick sample was slightly cracked after annealing at 600°C, the thin sample value of 187GPa is more accurate and would confirm the similarity between high and low-frequency Young modulus, as in the case of oxides.
Finally, the samples that survived the above nitrogen annealing tests were further heated at 650°C for 30 minutes in an oxygen atmosphere, as the curing of the sensing paste requires oxygen. Thickness variation was measured after this treatment, to see oxidation effects on the film: as one would expect, all silicon oxides were almost unchanged (differences <1%), while MF nitride had 7% variation and HF nitride had 6% variation, indicating a reaction with the oxygen atmosphere, and the formation of a thicker oxy-nitride layer than the native one already present at room temperature on the exposed surface of the film [3.90].
In general, comparing the performance of oxides with that of nitrides one can see that:

- *residual stress* of oxides decreases upon annealing, while nitrides stress increases, except that of the LF sample.
- *thickness change* upon annealing is more pronounced in nitrides (Figure 3.35).
- *the refractive index* and Si/N ratio of nitrides move away from stoichiometric values upon annealing, indicating that the material is undergoing major structural change, rather than simple outgassing. The refractive index of oxides tends towards the stoichiometric value upon annealing.
- *the elastic modulus* of annealed oxides is almost identical to that of stoichiometric films.
- *Reaction with oxygen atmosphere* during annealing is relevant only in the case of nitrides.

All the above considerations suggest that PECVD silicon oxides, in general, are more capable of withstanding high-temperature annealing than silicon nitrides both in nitrogen and oxygen atmosphere.

3.4.3.2 Deposition onto the process wafers and thermal stability

The selected candidates to be used as an inter-metal dielectric in the fabrication of the gas sensor were HF silicon oxide and HR silicon oxide, since results obtained by previously characterizations. LF and MF silicon nitride were rejected because of structural damage at temperatures above 600°C, while HF silicon nitride builds a very high thermal stress upon annealing (above 1GPa) which is unsuitable for any mechanical structure. LF oxide was discarded for its low thermal stability. HF and HR silicon oxide were both tested separately in quartz and silicon processes.,
Microfabrication steps for deposition and definition of inter-metals passivation were performed for both quartz and silicon processes. Onto silicon and quartz wafers were deposited, over the layers previously described, HF and HR PECVD silicon oxide films, by using parameters reported in Table 3.2. They have deposited two different thicknesses of each insulating layers (300 nm and 600 nm), to investigate the correlation between deposition thickness and electrical insulation between the heater

and interdigitated electrodes in the final MHP (paragraph 3.5.3). After the deposition, SiO_2 layers were defined by using projection lithography. With this aim, 1.2 µm of positive photoresist (FUJIFILM HIPR6512) was deposited onto wafers, and then exposed and developed.

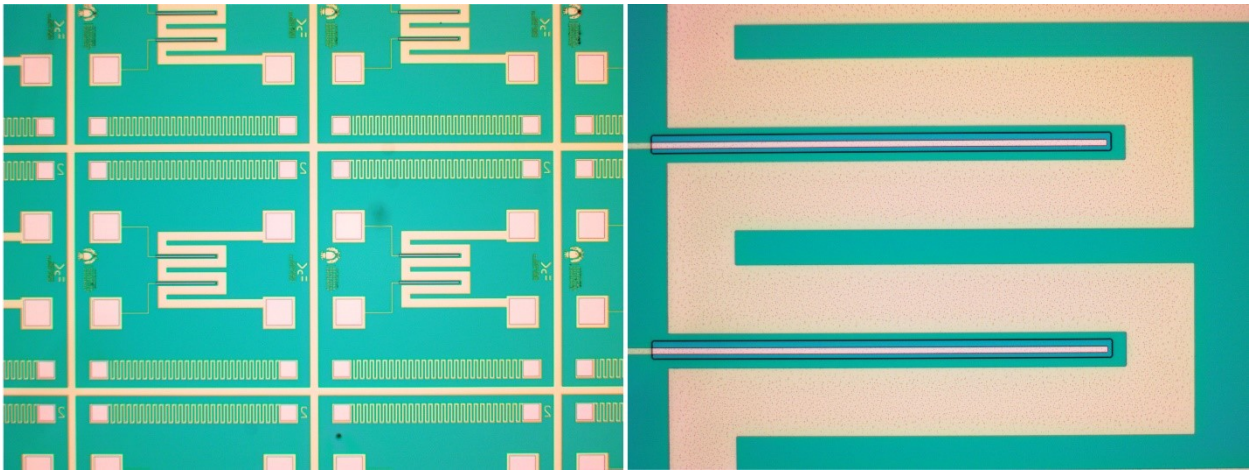

Figure 3.36: Images obtained with an optical microscope of photoresist development for P1S (L2) with a magnification of (*left*) 2.5x and (*right*) 10x.

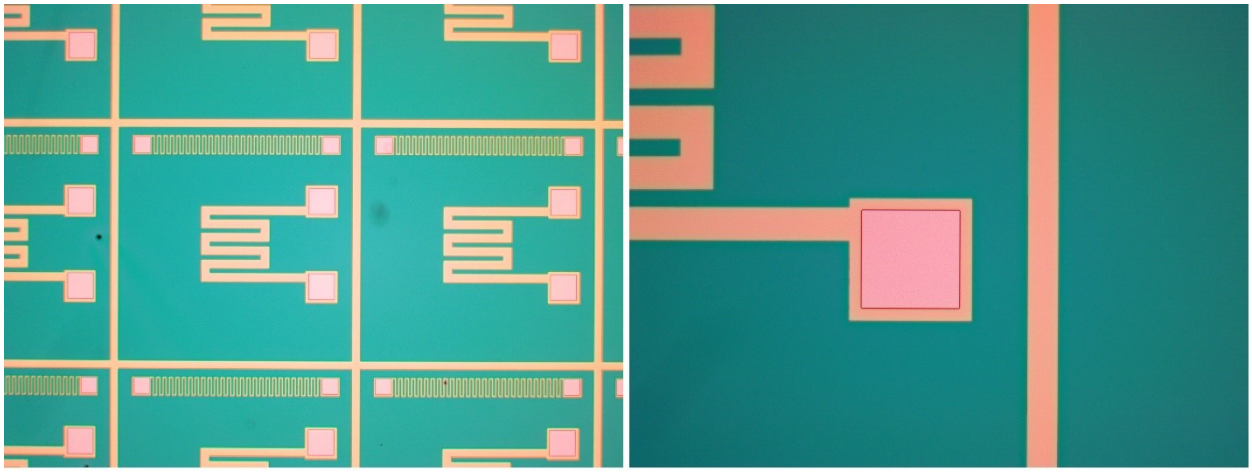

Figure 3.37: Images obtained with an optical microscope of photoresist development for P2S (L2) with a magnification of (*left*) 2.5x, (*right*) 10x.

Afterwards, the insulating layer was etched by standard reactive ion etching, by using TEGAL 903 instrument. Finally, the rest of photoresist was removed.

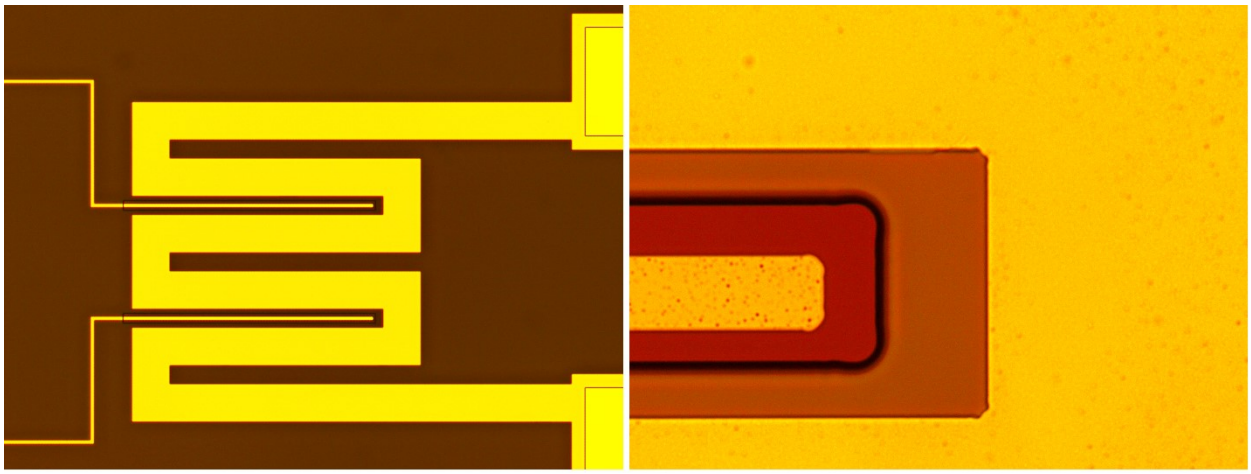

Figure 3.39: Images obtained with an optical microscope of defined inter-metal passivation for P1Q (L2), with a magnification of (*left*) 5x, (*right*) 50x.

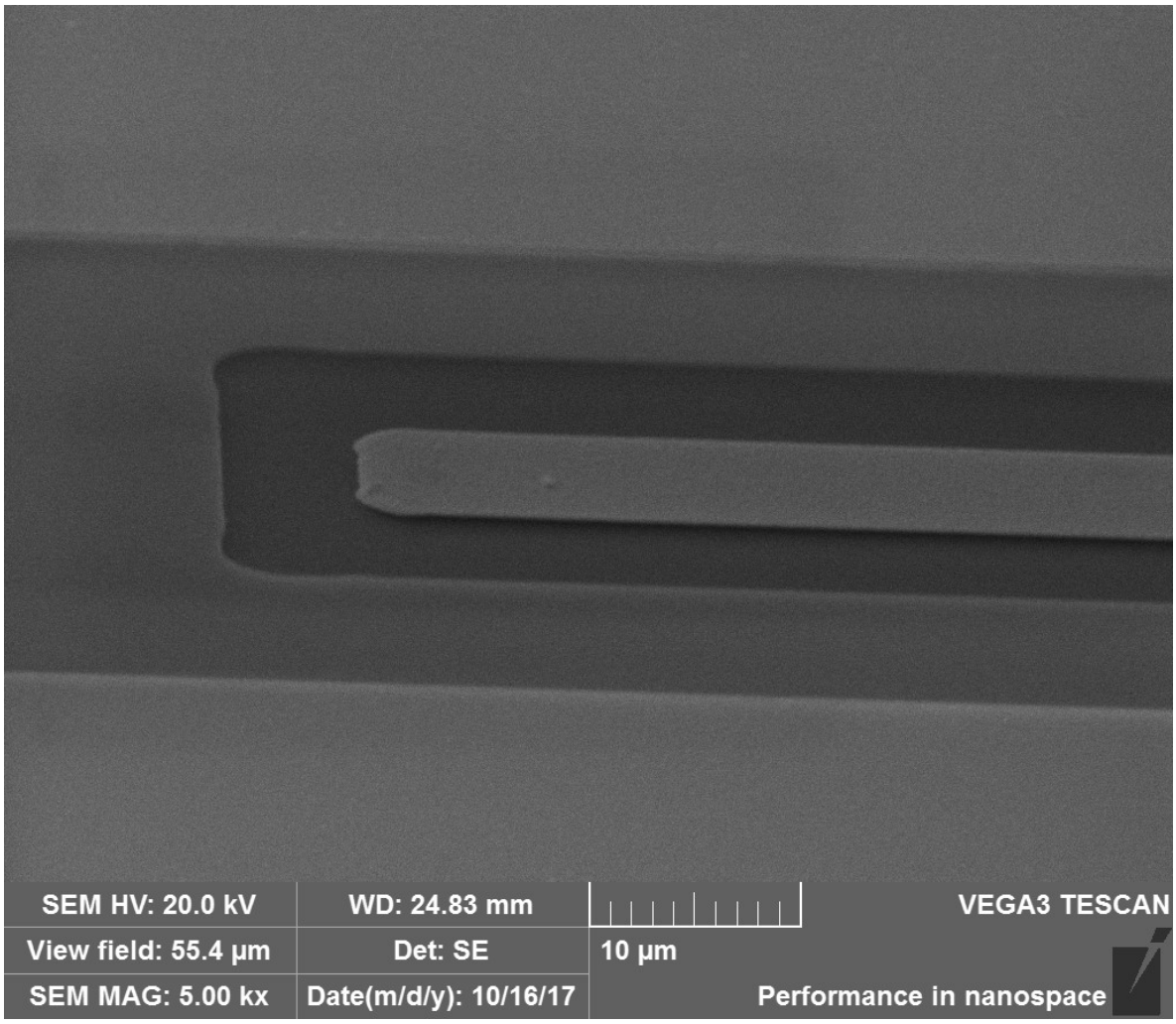

Figure 3.40: SEM image of a detail related to defined inter-metal passivation for P1S (L2)

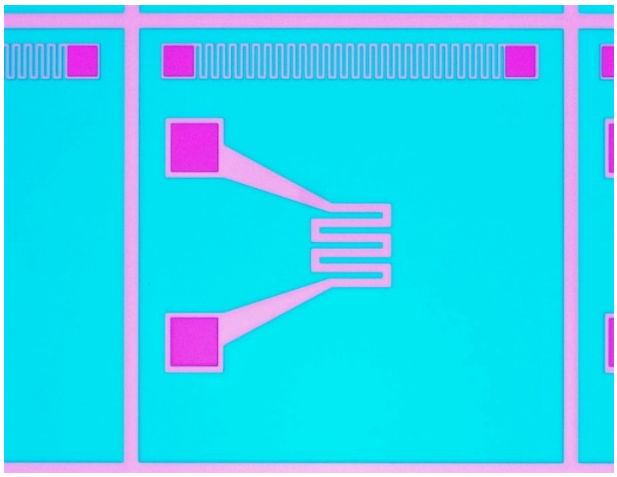

Figure 3.41: Images obtained with an optical microscope of defined inter-metal passivation for P2S (L1.1).

The heat treatment of insulating materials was carried out at 650°C for 2 hours, under N_2 flux. Optical inspection of the slices after heat treatment revealed interesting details. For quartz processes, both HF and HR SiO_2 showed no damage or substantial changes, highlighting good thermal stability

(Figure 3.42). As far as silicon processes are concerned, HF SiO_2 showed good stability, while HR SiO_2 exhibited circular cracking at the interface with metal, as it can be seen in Figure 3.43.

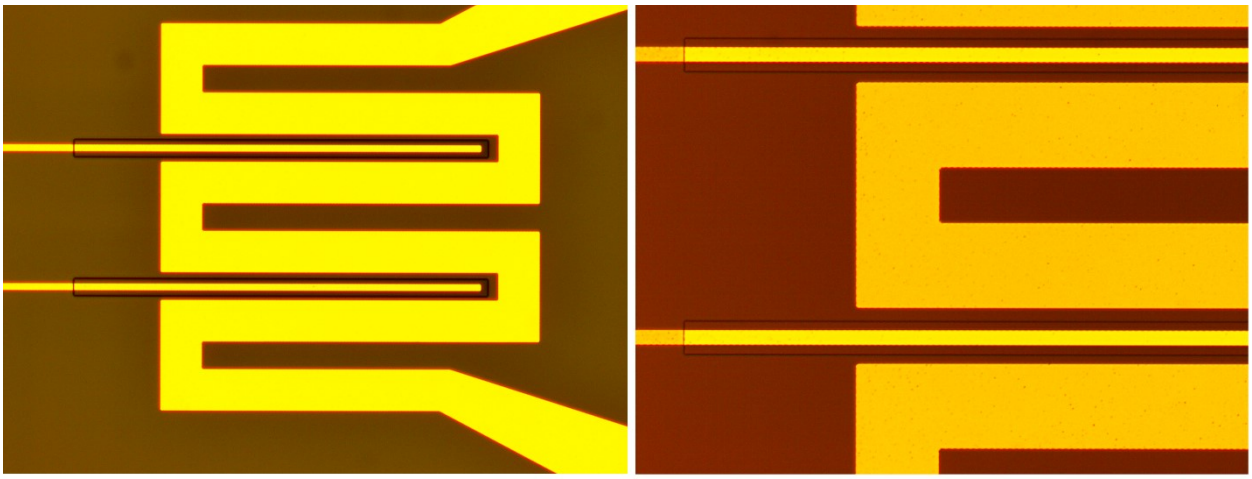

Figure 3.42: Images obtained with optical microscope thermal treated inter-metal passivation for P1Q (L1.1), (*left*) HF SiO_2, the magnification of 5x, (*right*) HR SiO_2, the magnification of 10x.

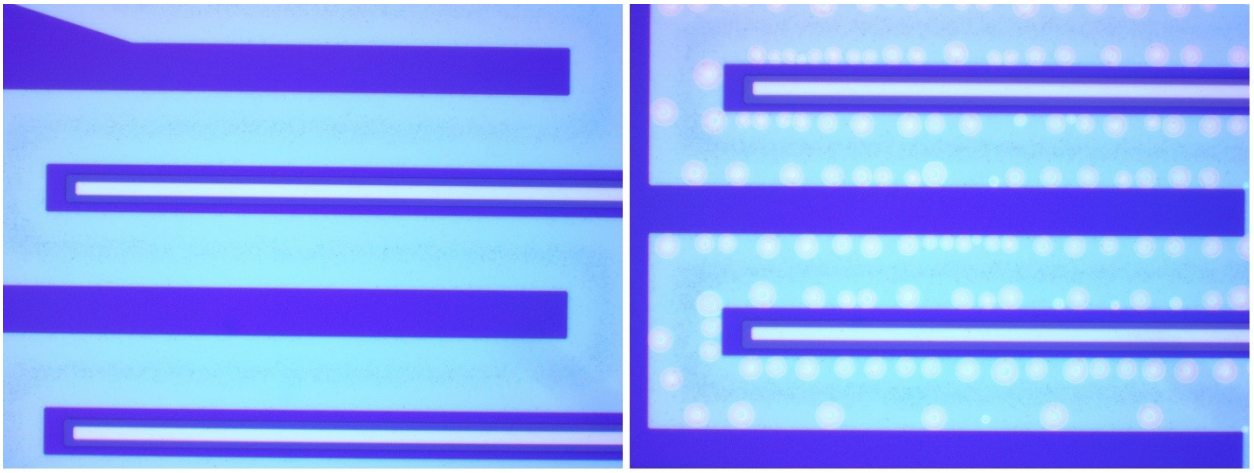

Figure 3.43: Images obtained with optical microscope thermal treated inter-metal passivation for P1S (L1.1), (*left*) HF SiO_2, the magnification of 10x, (*right*) HR SiO_2, the magnification of 10x.

These damages on the HR SiO_2 layer can be formed because of the different thermal stress that is present on the three diverse interfaces on which inter-metal passivation is deposited, i.e. the heater, ONO membrane and the interdigitated electrode. Since HR SiO_2 has a slightly higher compressive stress than HF SiO_2 at 650°C (Figure 3.33), this difference may be the cause of the different stability of HF SiO_2 compared to HR SiO_2 on silicon wafers.
Since results obtained, it was decided to define HF SiO_2 as the best candidate for PECVD MHP production both for silicon and quartz, even if, concerning quartz, HR SiO_2 resulted to be a promising material. Bytheway, it is important to standardize the process, so it is better to choose a single type of insulation that is suitable for both substrate types.
In the section 3.5.3, will be discussed characterizations carried out to investigate the best solution between 300 nm and 600 nm of HF SiO_2 thickness in term of electrical insulation.

3.4.4 Bulk etching of silicon for membrane microstructure

The last process step of silicon MHP microfabrication involved bulk etching of silicon to obtain the final thin ONO membrane. In order to carry out the wet etching of silicon with a suitable solution, it was first necessary to remove, in a selective and defined way, the triple ONO layer deposited on the backside of silicon wafers. The last process step of silicon MHP microfabrication involved bulk etching of silicon to obtain the final thin ONO membrane. The definition of ONO structure was carried out by means of photolithography. Wafer backsides were coated with 1.2 µm of positive photoresist (FUJIFILM HIPR6512) and then exposed and developed with a HIPR6517HC solution. The ONO structure layer was dry etched using TEGAL 903 instrument, and then the rest of photoresist was removed.

At this stage, wafers were ready for wet silicon etching. The silicon anisotropic wet etching is usually performed with a basic solution. Among these, the most used in microfabrication facilities are potassium hydroxide (KOH) and tetra-methyl ammonium hydroxide (TMAH) [3.91]. In our case, we decided to use TMAH.

Silicon <100> wafer etching with TMAH solution has a precise 54.7° angle. We, therefore, took this information into account when calculating the size of the silicon spots on the wafer backsides, so that we could obtain a membrane with dimensions of 1x1 mm^2 on the front side. Since the thickness of wafers was 300 µm and the etch angle was 54.7°, the backside spots should be of 1.424x1.424 mm^2 (Figure 3.44).

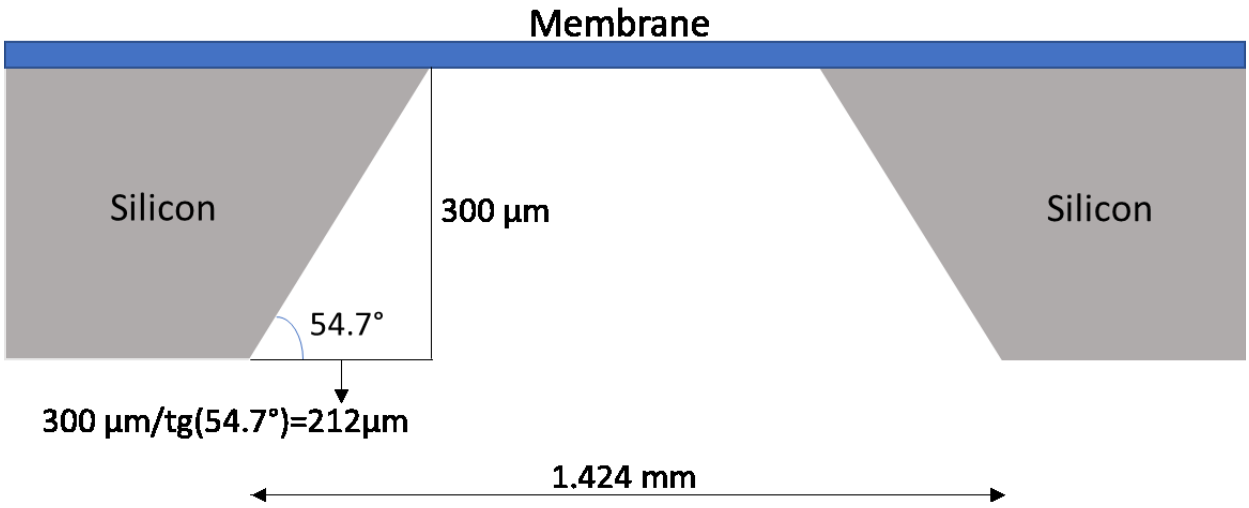

Figure 3.44: Schematic representation of the silicon etching.

The rate of silicon etching depends on TMAH solution concentration and temperature [3.92]. In our case, we used a solution at a concentration of 25% (in water), at a temperature of 90°. The etch rate in this condition was of 42 µm/h, hence for the complete silicon to ONO membrane silicon wafers were dipped in TMAH solution for about 430 minutes. Images of the membrane obtained are reported below.

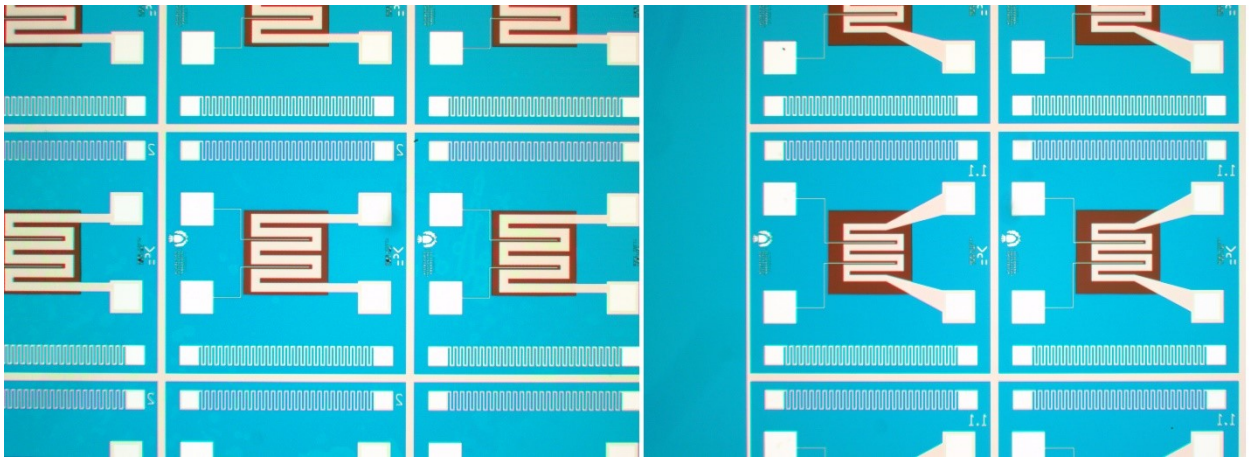

Figure 3.45: Images of devices after TMAH etching for P1S, (*left*) L2 and (*right*) L1.1.

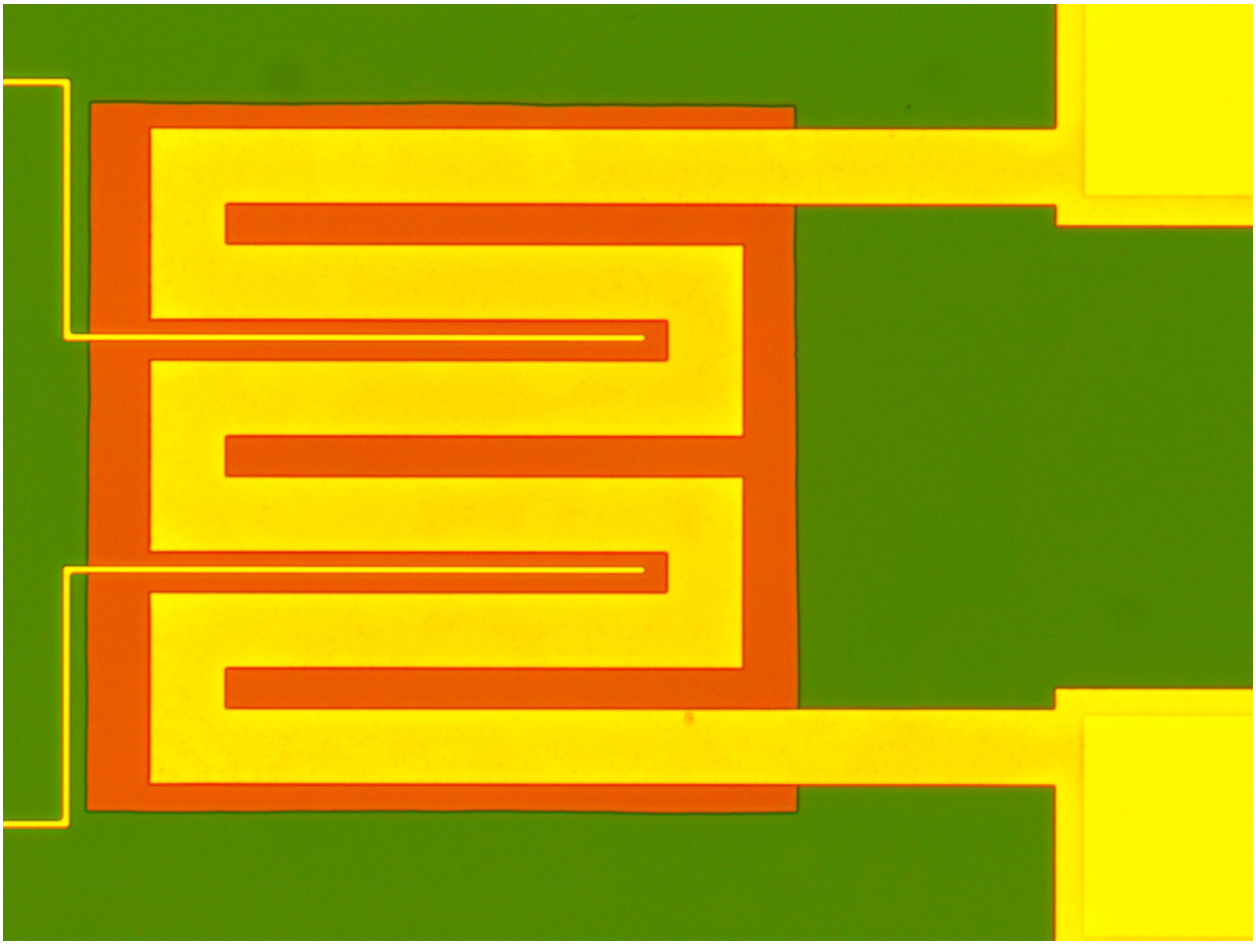

Figure 3.46: Image of devices after TMAH etching for P1S, L2, obtained by means of optical microscope (5x)

3.4.5 Brief process consideration

There were 1271 devices on each silicon and quartz wafer. The development of steps leading to an optimized yield of the sensor microfabrication process has been investigated during all three years of doctoral studies. The first processes revealed several errors in the manufacturing process. The first one, for example, had led to a 5% yield of silicon devices (results turned out to be unusable anyway) for a wrong choice of inter-metal passivation, entrusted to MF Si_3N_4 obtained through PECVD that, given its low stress, was thought giving good results in thermal stability. From this error, the choice

to make an in-depth study of the PECVD insulation type suitable for our purpose. The same applies to all the other steps of the process, which have therefore been optimised on previous errors.

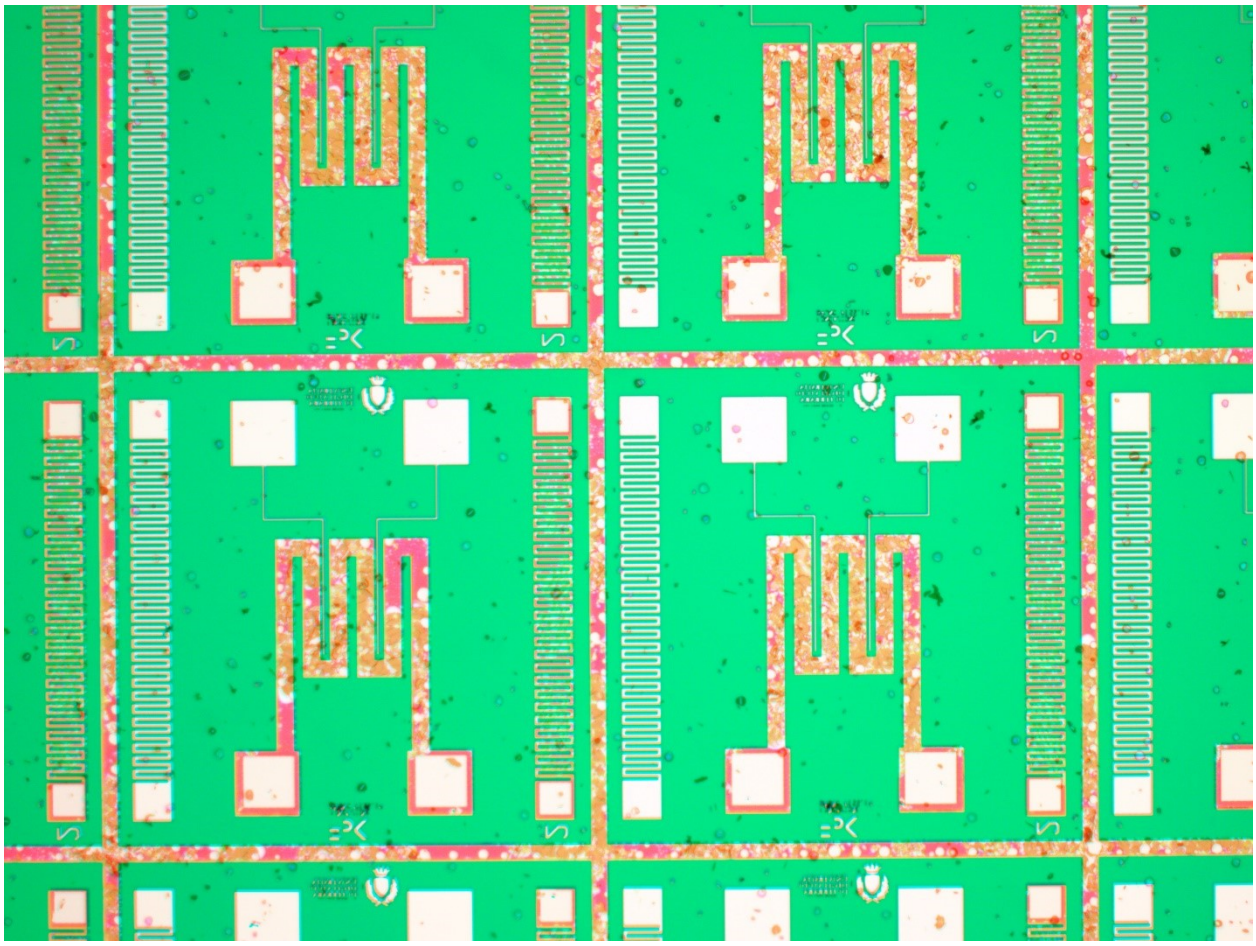

Figure 3.47: Image of silicon devices (L2, P2S) after annealing at 650°C of the upper metal layer. It can be seen the thermal damage on MF Si_3N_4, used as inter-metal passivation.

Having said that, the latest manufacturing process has led to a yield rate of >99% for quartz devices. As far as silicon devices are concerned, the yield was about 97%.

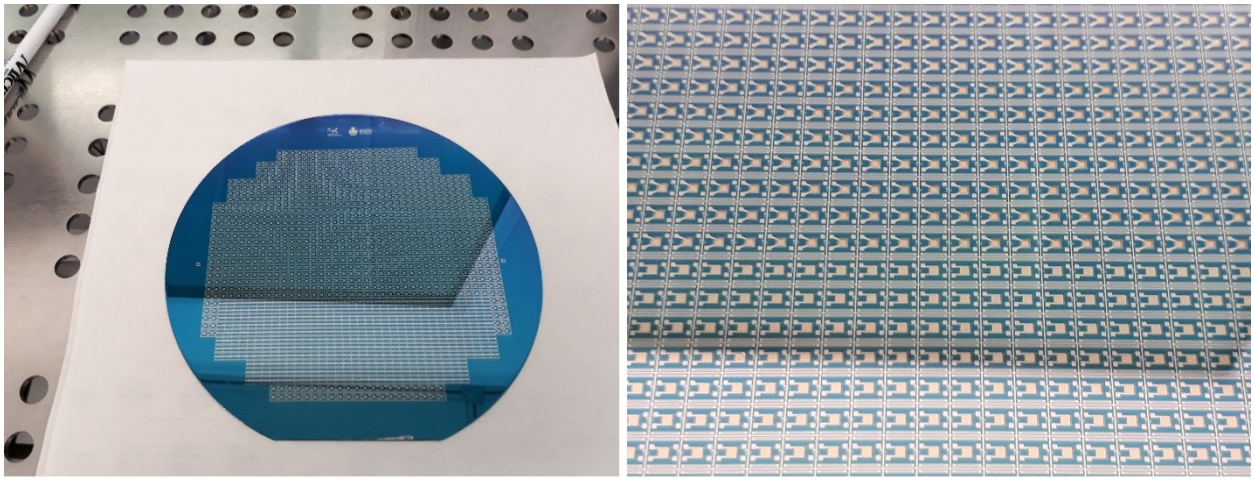

Figure 3.48: Images of a silicon wafer of the last process P1, after TMAH silicon etching (five broken MHPs out of 1271 available).

The yield of silicon membrane slightly decreased, up to 95%, in the remaining production steps of the sensor device, due to the cutting of wafers in single devices and screen printing deposition of the sensing material.

3.5 Characterization of silicon and quartz MHPs

The characterization of the obtained devices was carried out at the end of the microfabrication process. First, we verified that the finished devices could really be used as substrates for chemoresistive gas sensors. In this sense, it was, therefore, important to carry out bonding tests on the electrode pads to check the adhesion necessary to the stability of the finished device, respecting the current regulations on bonding quality. Then, electrical properties of the device were tested. For this purpose, the Temperature Coefficient of Resistance (TCR) of the different heaters was measured and the correlation between the temperature of the microheater and the power consumption of the MHP was subsequently found. Finally, the insulating capacity of inter-metallic passivation in the devices was verified, measuring the amount of electrical current passing from the heater to the electrode interdigitated through the insulating PECVD layer.

3.5.1 Bonding tests

Bonding is of crucial importance in the packaging of a sensor, as described in section 2.2.6. Indeed, this step allows interfacing the sensor with the rest of the electronic equipment, and therefore it is useful for reading the signal that coming out from the transducer. As far as silicon and quartz devices are concerned, the instrument used for the bonding step was a semi-automatic K&S Ball Analog Bonder Model 4014, present at the FBK (see section 2.2.6). In this instrument, we used a gold wire with a diameter of 18 μm. The ball bonding process is a particular wedge bonding type that allows creating a gold ball, thanks to the high-voltage electric charge applied to the wire by means of a needle-like capillary. Then, this ball is pushed down and attached to the sample through a mix of temperature, pressure and ultrasonic energy [3.93]. Next, the wire is passed out through the capillary and the machine moves over the location that the chip needs to be wired up to. The machine again descends to the surface and the wire is crushed (without the ball) between the pad and the tip of the capillary, forming the second bonding.
With this technique, ten silicon and quartz devices for each process type (P1 and P2) were bonded, by using optimal instrument parameters, set after experimental tests. Therefore, 20 quartz samples (P1Q and P2Q processes) and 20 silicon samples (P1S and P2S processes) were prepared. The loop length chosen for all tests was about 2.5 mm, as it can be seen in Figure 3.48.

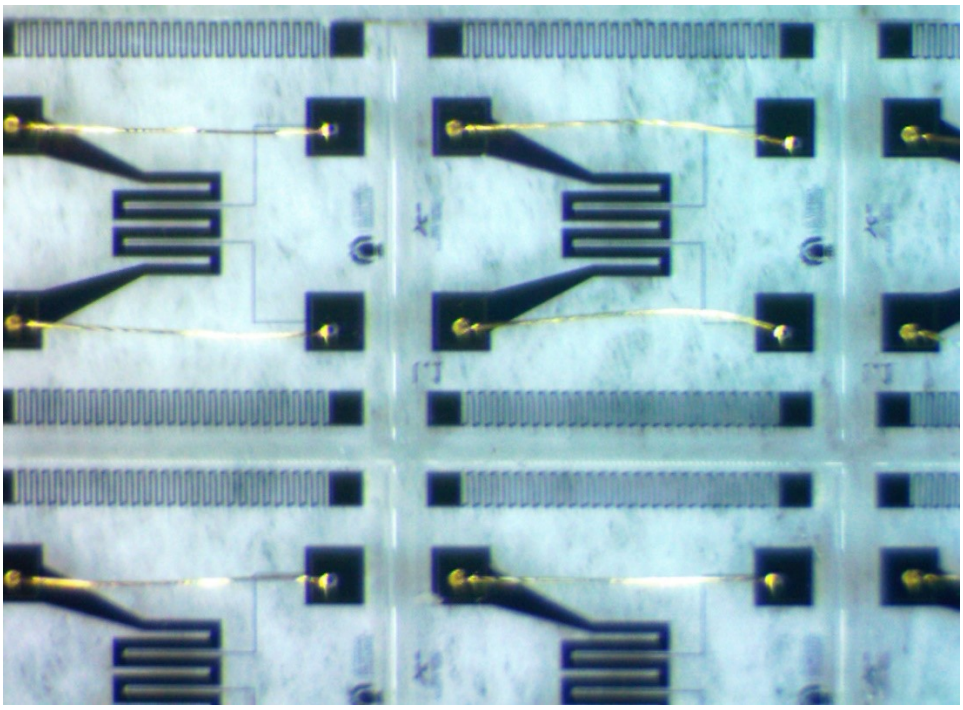

Figure 3.49: Image of ball bonding test with gold wire for quartz substrate (P1Q, L1.1).

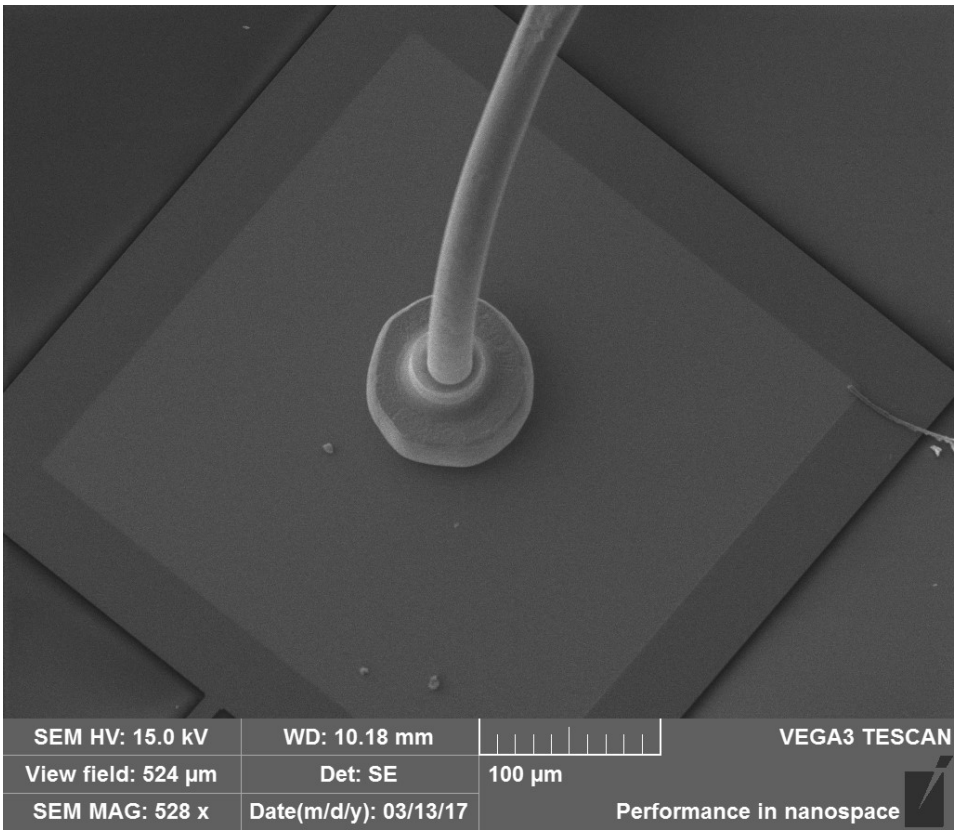

Figure 3.50: SEM image of the ball bonding between the gold wire and Pt/Ti pad of the heater (L2, P1S).

Two types of tests were carried out to verify the bonding quality, i.e. pull and shear tests. The experimental measurements were realized by means of an XYZTEST Condor Ez Bond Tester (figure 3.49). The guidelines for the standards bonding quality are defined by European Standards, namely IEC 62137-1-1 for pull test and IEC 62137-1-2 shear test.

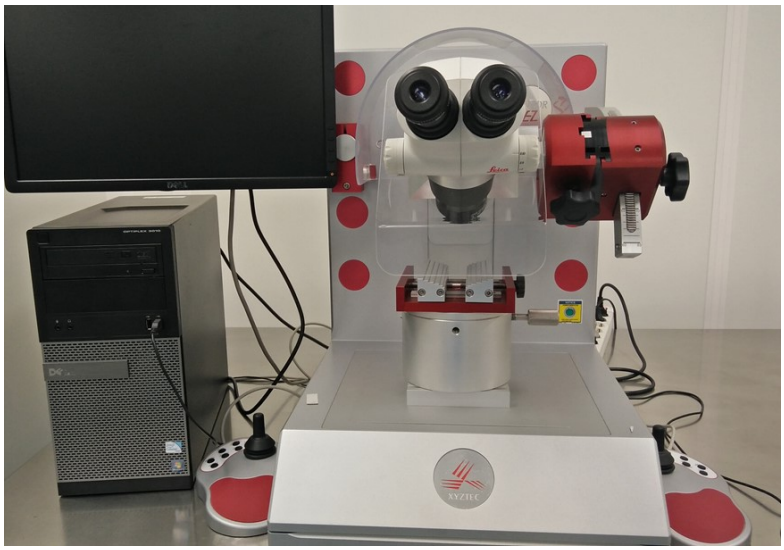

Figure 3.51: XYZTEST Condor Ez Bond Tester, present in the FBK, used for shear and pull tests.

Considering the wire diameter, the ball size and the loop length chosen, pull and shear values required to define tests passed for the standard quality was 1.5 cN and 15 cN, respectively [3.94].

The average values obtained, together with the standard deviations, are shown in the following table.

Table 3.8: Pull and shear test results about the bonding of our devices.

Substate	Process	Shear value (N)	St. dev. %	Pull value (N)	St. dev. %
Quartz	P1	0.37	7.5	0.036	12
	P2	0.5	5.8	0.044	5.7
Silicon	P1	0.55	8.3	0.033	9.8
	P2	0.47	9.3	0.042	7.8

As it can be seen, for both silicon and quartz processes, the adhesion between pads and gold wire have produced satisfactory data, exceeding the required limits. Moreover, data obtained highlighted that, in almost all measurements carried out, the values obtained from P2 processes gave better results than those obtained from P1 ones. The reason for this trend could be lied to the increased roughness of the heater pads in P2 processes, due to a higher heating time compared to process P1 (section 3.4.2). This increased roughness can result in greater adhesion between the pad and the gold wire (ball or "second bond").

3.5.2 Temperature Coefficient of Resistance of microheaters

The operating temperature is determined by the electrical power dissipated thermally to the environment. For a gas-monitoring instrument employing an array of commercial MOS gas sensors, the power consumed by the sensor heaters would be an appreciable fraction of the overall system power consumption (e.g. each alumina gas sensors require ~ 1 W). Reducing the power consumption is vital for applications involving battery-powered portable instruments, as is the case for in-situ measurements. MHP structures have been employed where the heating elements are either embedded or in a planar arrangement in a thin thermally-resistive membrane to reduce thermal power losses.

There are three different mechanisms by which thermal power can be lost; namely thermal conduction, convection and radiation.
The aim of this section is to experimentally calculate the power consumption of silicon and quartz MHP produced. However, in order to calculate this value, it is first essential to investigate the TCR of microheaters, which gives us a correlation between the resistance of the heater and the temperature reached by the MHP.
Therefore, the steady-state calibration of the microheater resistance versus temperature is described first. From TCR and base-line resistance of the heater are computed, so that the element can be used as a resistive temperature sensor. The steady-state I/V characteristics of the heater define both the power dissipated (i.e. $P_H=VI$, where P_H is the Heater Power) and the resistance (i.e. $R_H=V/I$). The known TCR and base-line resistance allow the measured heater resistance to be accurately converted to temperature. Hence, the heater temperature also provides the opportunity for closed-loop temperature control. The MHP performance was primarily assessed by measuring the heater power consumption against temperature statically. Furthermore, to verify the reliability of the MHP process, it was investigated the devices uniformity along the wafers, through the heater I/V curves.
I/V curves for substrates had two purposes in this work. On the one hand, to verify the homogeneity of the deposition process and definition of heaters in silicon and quartz wafers. On the other hand, to obtain data useful for calculating the power consumption of the microheaters. I/V curves were attained through manual electrical testing by means of Manual Probe Station PM8 with Agilent Instrumentation (Figure 3.50). This instrument allows, by means of tungsten tips, to provide constant tension/current into a circuit, and reading the corresponding current/tension value.

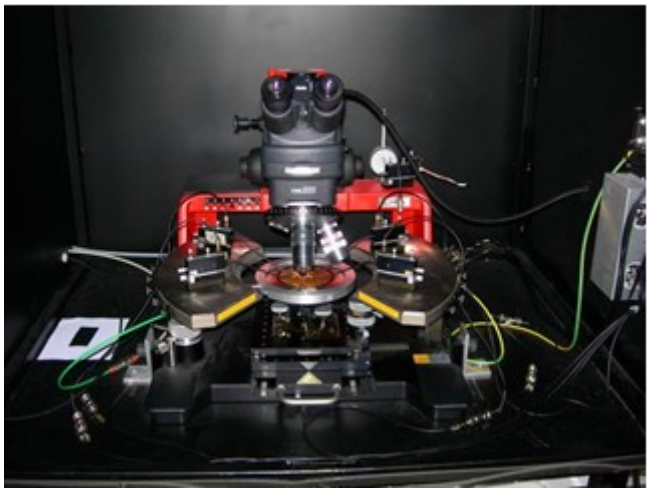

Figure 3.52: The Manual Probe Station PM8 present at the FBK.

Essentially, in our case, the procedure consisted in placing two tungsten tips on the pads of the resistor: one of the two tips was grounding, while on the second one a known potential is applied: measuring the current circulating in the resistor, the resistance is calculated immediately.
To verify the uniformity of the heaters along the wafer surface, it was decided to measure the resistance of a representative number of sensors at room temperature of 22°C. The device was supplied with very low voltages (to not create self-heating phenomena) and the current circulating on the heater was read. Through the slope of the generated curve, it was possible to obtain the heater resistance (Ohm's law, Eq. 2.1). Below is reported one representative I/V curve obtained, which highlighted for the microheater measured an R_H of 73.2 Ω.

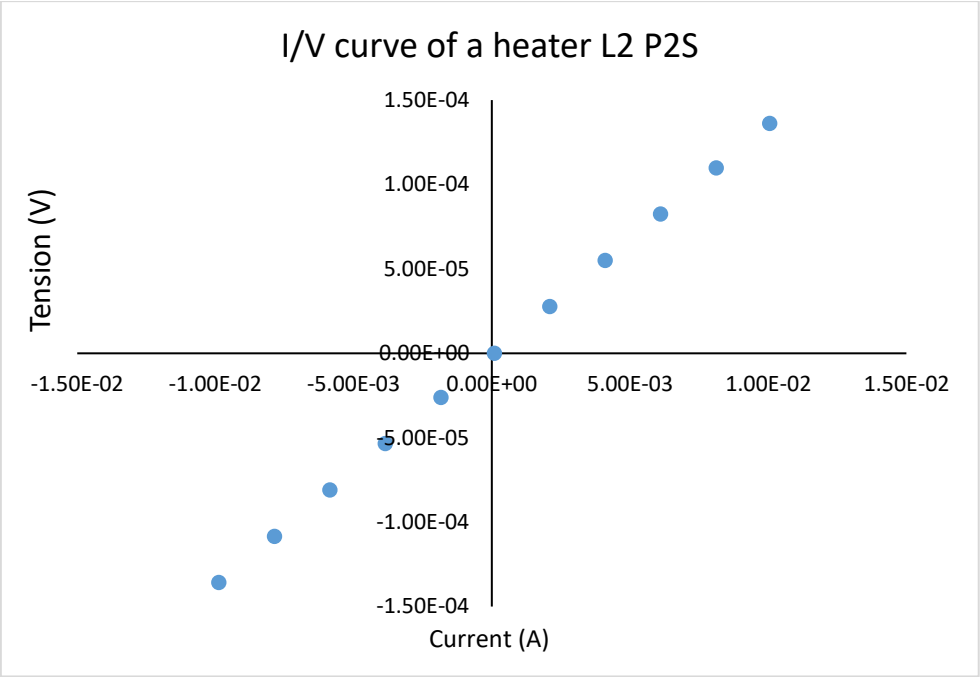

Figure 3.53: The I/V curve obtained for a heater of the L2 layout, P2S.

Measurements of devices along wafers highlighted a slight sectoral unevenness in the resistance of microheaters, as reported in Figure 3.52.

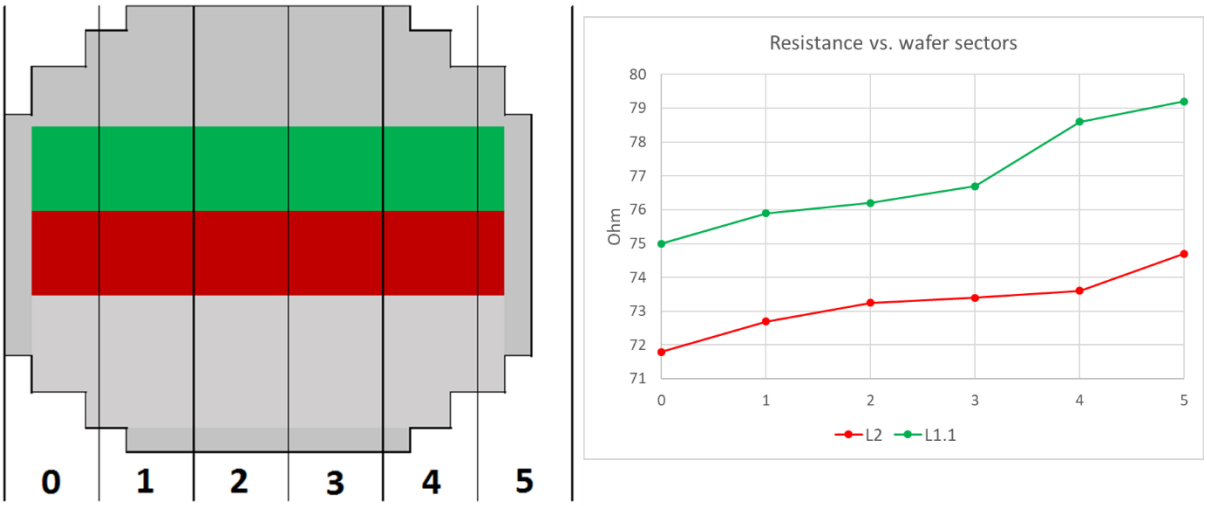

Figure 3.54: left Schematic representation of a wafer (flat downwards), right trend of heater resistances along wafer sectors for L2 and L1.1 (P1Q)

As it can be seen, resistances increased going from left to right on the wafer. A similar trend was also obtained for the other quartz and silicon process wafers. This result could be explained by a lack of thickness homogeneity in metal deposition, or to an uneven in the photolithographic process used to define the heater. However, the difference between the maximum and minimum resistance value was lower than 5% for both layouts in all processes, therefore respecting the value limit given by instrumental characteristics. In Table 3.9 are shown experimental average values for all samples and theory values, obtained by using ohm/squares shown in Table 3.1 and L1.1-L2 heaters sizes.

Table 3.9: Experimental and theoretical values of L1.1 and L2 resistances at 22°C.

		Experimental value (Ω)	Theoretical value (Ω)	% error
L 1.1	P1S	77,12 ± 1.61	79.93	3.52
	P1Q	77,81 ± 1.73		2.65
	P2S	74.8 ± 1.81	77.54	3.53
	P2Q	75.5 ± 1.63		2.63
L 2	P1S	73.24 ± 1.4	75.80	3.38
	P1Q	73.68 ± 1.31		2.80
	P2S	71.36± 1.30	73.65	3.11
	P2Q	71.21± 1.39		3.31

The discrepancy between the theoretical and the measured value is always lower than the declared thickness error value for the instrument used, which is 5%.
These measurements highlighted a good uniformity of substrates along wafers for all processes realized.

At this stage, the trend of the heater I/V curve at higher voltage values was verified. With this aim, the current was measured during voltage variations from 0 to 6 V for the heaters placed on the membranes and from 0 to 9 V for the heaters placed on quartz, with increments of 0.2 V every 50 ms to avoid voltage changes such as to create thermal shocks that could have compromised the stability of substrates. The trend of these curves did not show a big difference between the P1 and P2 processes, rather between quartz and silicon. Hence, they are shown below the measurements carried out with the two types of substrate, regardless of the process.

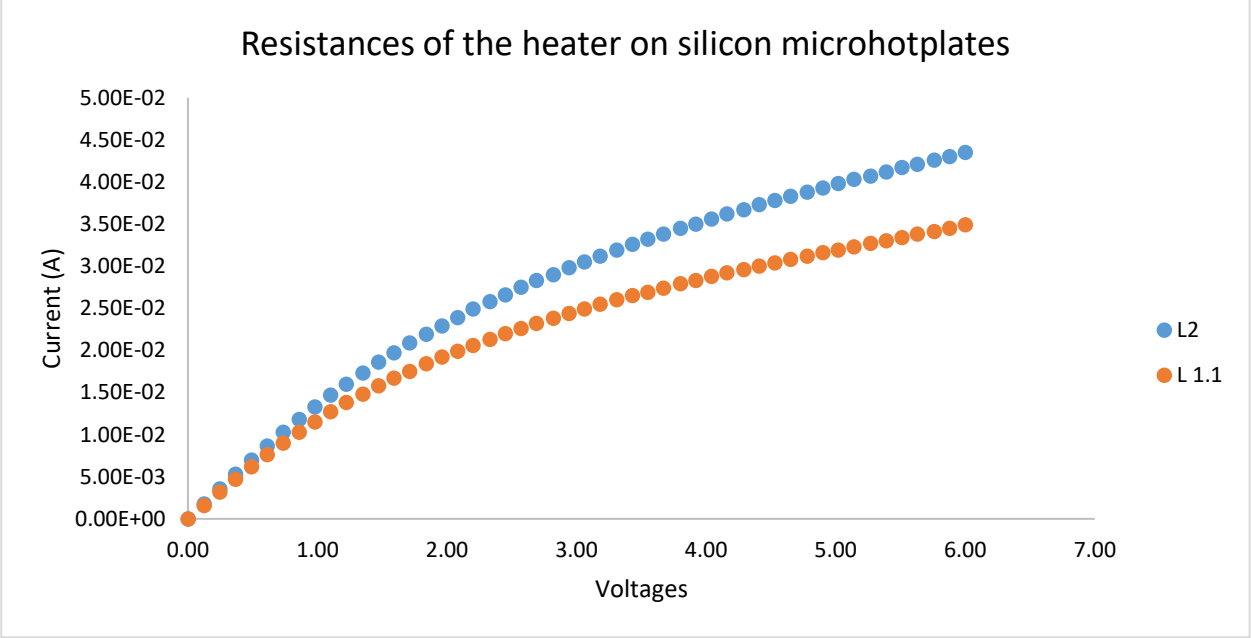

Figure 3.55: I/V curve for microheaters, layout L1.1 and L2.

Once the microheater I/V curves were investigated, the calculation of the TCR was carried out, thus correlating the resistance of the heater to the temperature of the area affected by the resistor. The MHPs were then inserted in a special climatic chamber (Binder, model MKF 115), and the resistance of microheaters was read by a specially constructed analogic system and the aid of a multimeter

(Keithley multimeter 2000). The range of temperature analysed ranging from 0°C to 140°C (Figure 3.56).

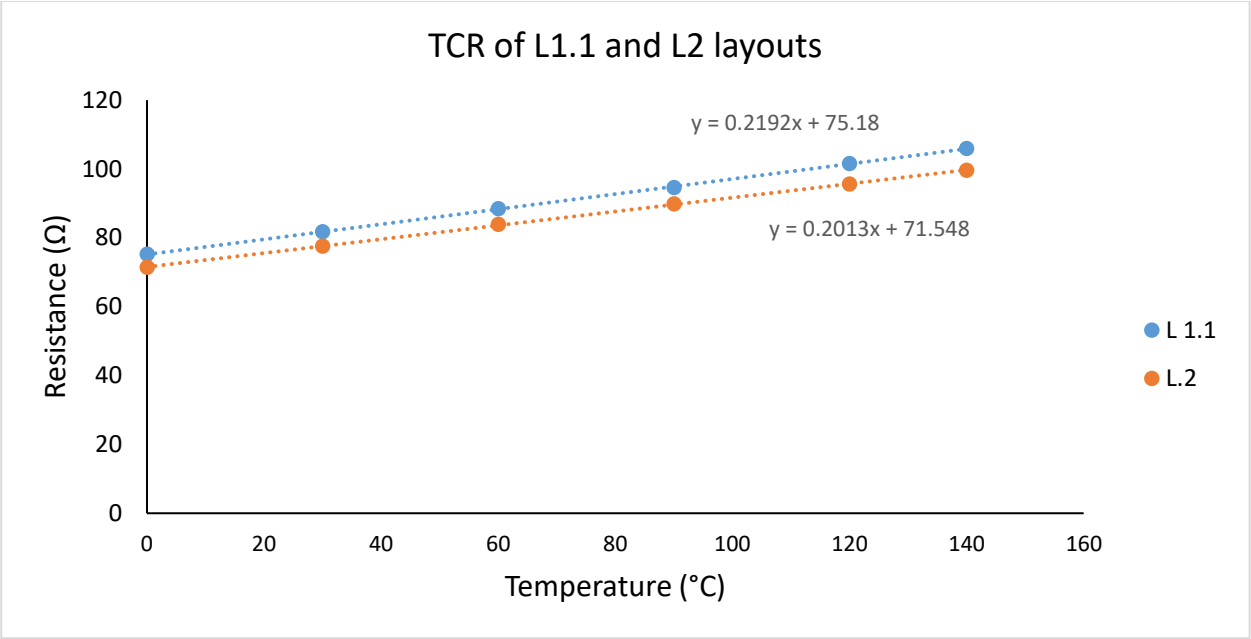

Figure 3.56: Correlation between temperatures and resistance of microheaters, layouts L1 and L2. Temperature range 0-140°C

The mathematical relationship that allows obtaining the TCR of a microheater is given by:

$$TCR = \frac{R_i - R_j}{R_j(T_i - T_j)} \qquad (ppm/°C)$$

It is an accurate equation for linear relationships, with i; j any pair of points of experimental measurement. TCR values calculated for L2 and L1.1 were, in the temperature range of 60-140°C, 2350 and 2470 (ppm/°C), respectively.
However, in our case would be necessary achieve a more precise relationship at high temperatures. Therefore, the quadratic term takes on significant values and the equation can be rewritten as follow:

$$R(T) = R_0[1 + \alpha(T - T_0) + \beta(T - T_0)^2]$$

where α is the TCR term of the previous equation (see section 2.2.7.3). In order to better investigate the β term, the same experiment was repeated at a higher temperature, by means of a hotplate and the previous analogic system.

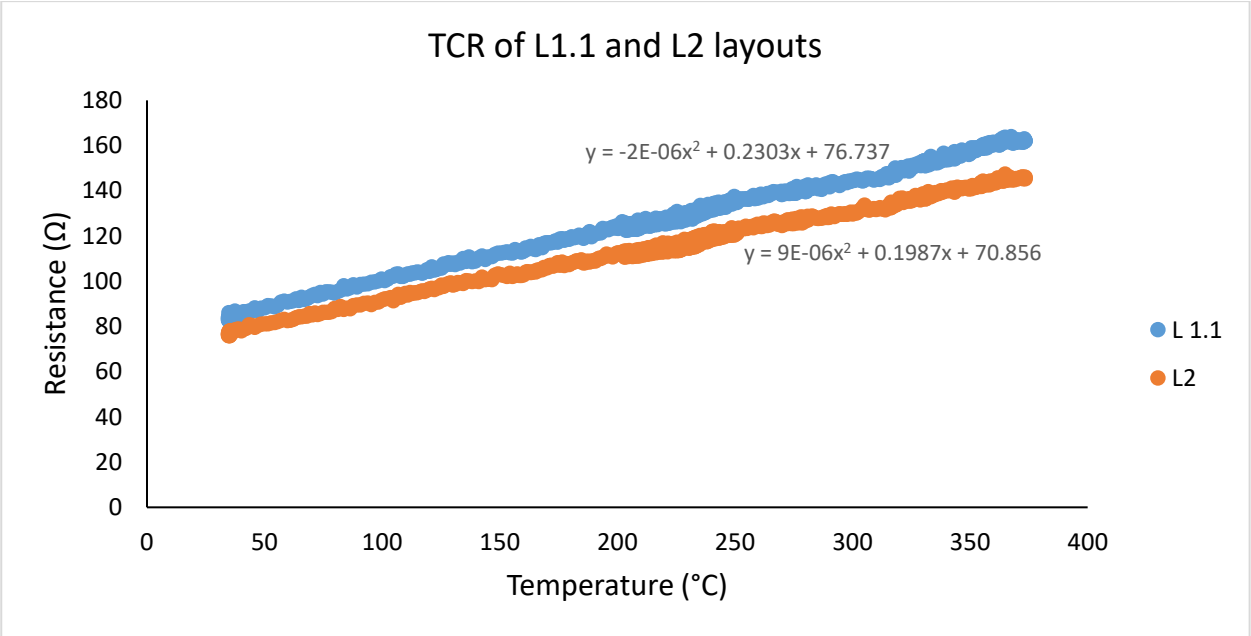

Figure 3.57: Correlation between temperatures and resistance of microheaters, layouts L1 and L2. Temperature range 33-370°C.

The experimental lines are marked because it was decided to repeat more temperature ramps, to verify that there was a repeatability in the correlation between temperature and the heater resistance.
The microheaters have been calibrated by calculating the TCR and baseline resistance from this data. The different resistance between L1.1 and L2 can be attributed to the slight differences in the heater geometry.
At this stage, it is, therefore, possible to establish the temperature-resistance-power dissipated correlation concerning silicon and quartz microheaters, layouts L1.1 and L2. To calculate the power dissipated by heaters, we applied a voltage to the resistor circuit in order to reach a certain resistance, correlated with the previous TCR to the temperature. At this voltage value, we measured the current circulating in the circuit, and through the relationship $P_H=VI$ we calculated the power consumption. This characterization was repeated on 10 samples for each layout and type of substrate (silicon or quartz) to obtain a reliable statistic. Power consumptions obtained were resumed in Table 3.10, together with the relative temperature of microheaters.

Table 3.10: Power consumption of silicon and quartz microheaters.

T(°C)	P_H L2 Silicon (W)	St. dev. %	P_H L1.1 Silicon (W)	St. dev. %	P_H L2 Quartz (W)	St. dev. %	P_H L1.1 Quartz (W)	St. dev. %
100	0.03	2.8	0.031	2.1	0.04	3.9	0.038	3.8
200	0.086	3.6	0.076	3.7	0.182	3.2	0.162	3.3
300	0.139	3.3	0.126	3.2	0.328	4.1	0.296	4.2
400	0.196	3.7	0.175	3.3	0.58	3.8	0.486	3.7
500	0.265	3.6	0.231	3.7	0.715	4.3	0.62	4

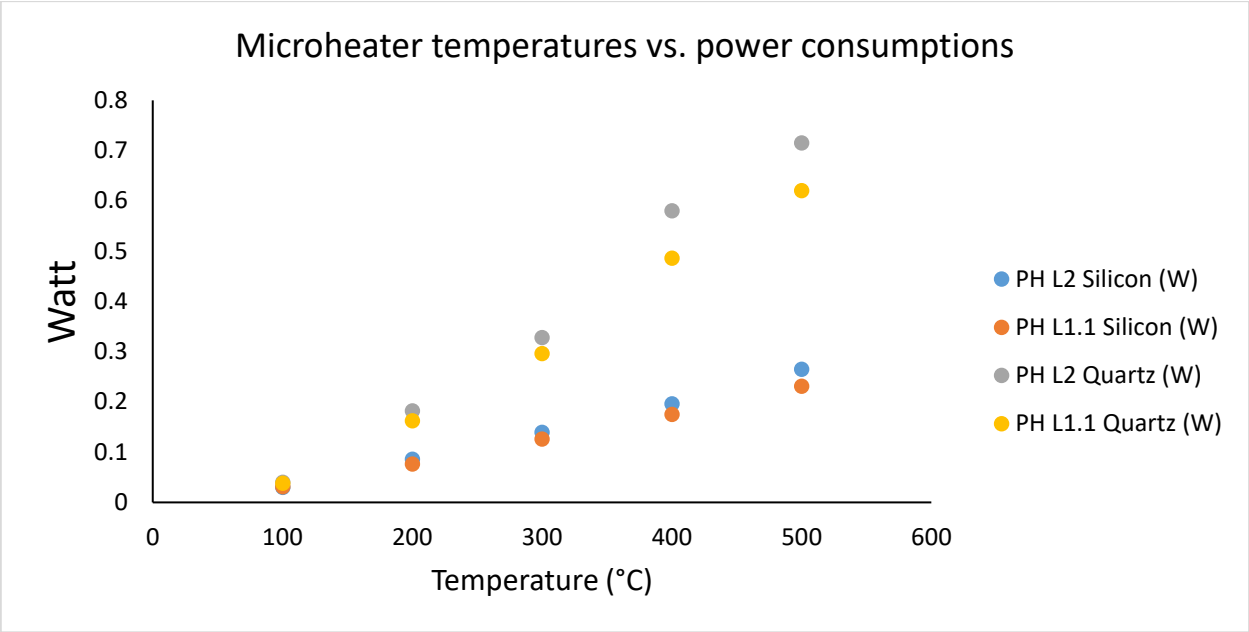

Figure 3.58: Trend of heater power consumptions (average values) vs. temperatures of MHPs.

Figure 3.58 shows very important information. For both types of materials, you can see lower energy consumption for the L1.1 layout compared to the L2 layout. This difference can be given by the different surface extension of the heaters. The L1.1 microheater has a smaller surface area than the L2 layout, which can cause less heat loss through convection, radiation and conduction. In addition, the layouts shown in Figure 3.3 clearly highlight that there is a different thermal distribution between the two heater configurations. In fact, the higher space along the heater coil for L2 layout allows for less heat concentration than in the L1.1 configuration. However, it should also be noted that L1.1 will have a more concentrated heat distribution in the centre of the device than the L2 layout. This may result in less thermal uniformity in a sensitive material lying on the device with a larger deposition area than the heater of the L1.1 layout.

Another important information deductible from the Figure 3.58 is the dissimilar energy consumption in quartz microheaters compared to silicon. This difference is given by the different thermal dispersion of the two devices. In fact, while for silicon MHPs most of the surface of the heater is on the membrane, where the thermal dispersion occurs mainly by convection and radiation, in the quartz MHPs much heat is dissipated by thermal conduction through the substrate itself [3.10, 3.95]. Despite the high consumption of the quartz device, it is worth noting that, at the same temperature of the microheater, it has a consumption that is 35% less than alumina, even though quartz wafers used was more than double thicker than alumina substrates (section 3.1.1). Therefore, by using thinner quartz wafers, devices with even lower power consumption can be obtained while maintaining the robustness of the substrate.

The power consumption in silicon microheaters was not very satisfactory. Indeed, many works can be found in the literature that highlight the production of MHPs in silicon with lower power consumptions [3.96, 3.97]. Therefore, once the optimal process parameters were experimentally established (reported in the previous paragraphs), new configurations were tested, still in the testing phase. Among these, one of the most promising in terms of energy consumption was the one where the surface of the membrane was modified in the layout, increasing its size.

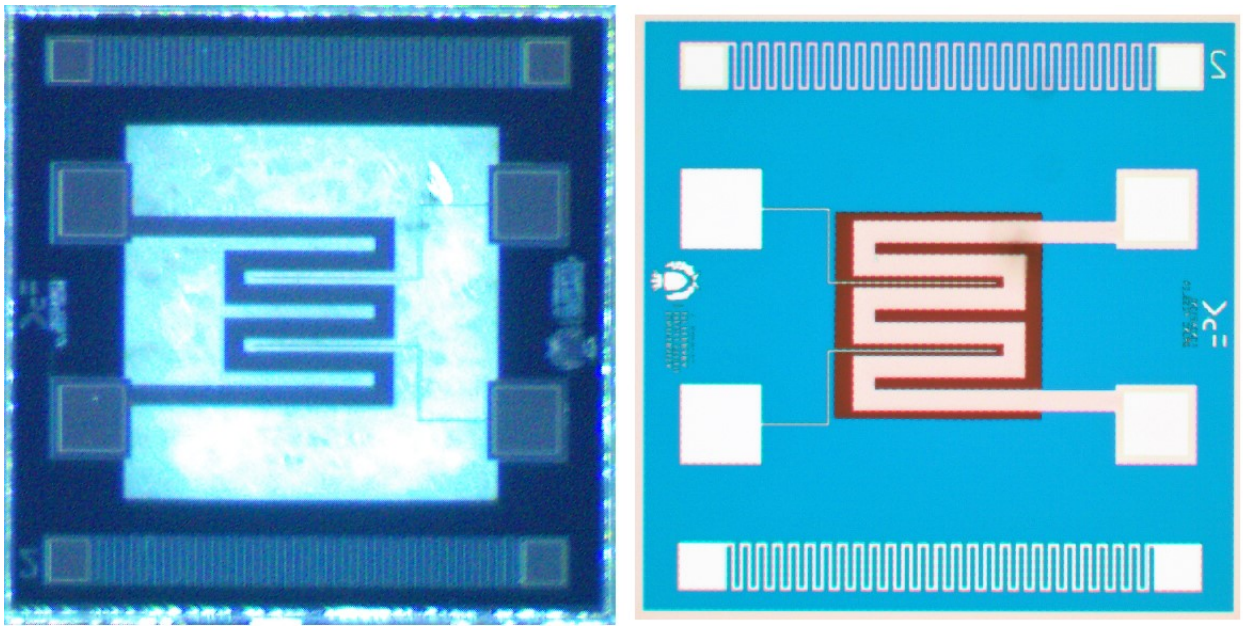

Figure 3.59: (left) new and *(right)* old version of layout L2, process P1S.

Lateral dimensions of membranes were enlarged from 1x1 mm^2 to 1.8x1.8 mm^2. The purpose of this modification was to arrange the entire coil of the heater on the membrane, to decrease as far as possible the thermal dissipation for conduction in the silicon. The only parts of the metal circuitries still present on the device were pads (Figure 3.59). The TCR curves for L1.1 and L2 layouts were also studied for this new device version, resulting to be quite similar to the previous ones.

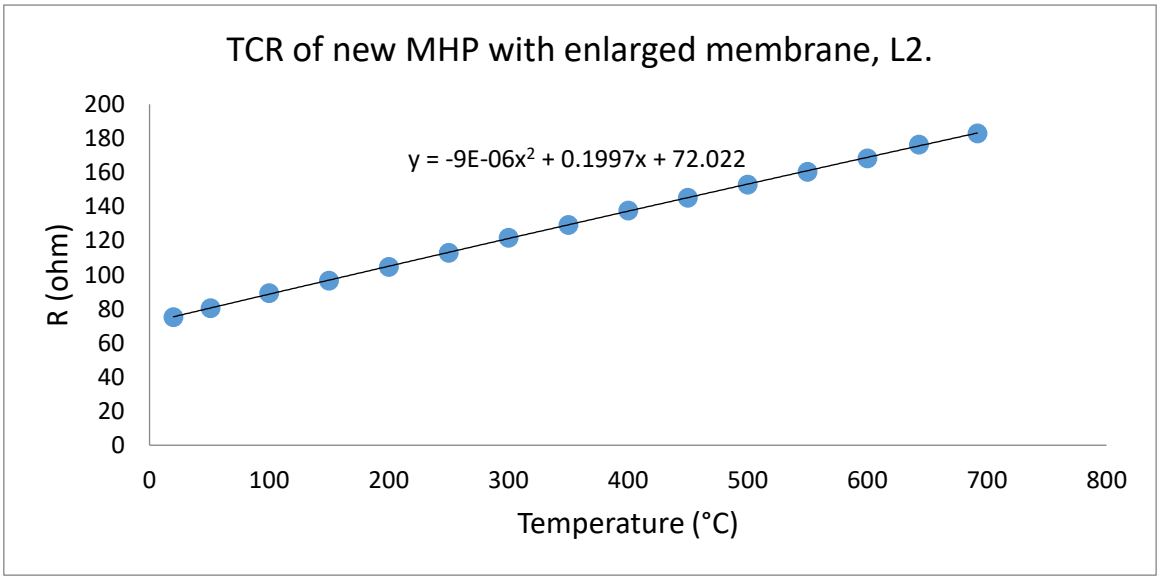

Figure 3.60: TCR of new MHP design (enlarged membrane), L2.

The slight difference with respect to the previous TCR can be given by a different thickness of the metal due to the instrumental error in the deposition reproducibility since this new process has been done with a temporal distance of some months compared to the previous one. Then, we investigated the power consumption of these MHPs, by means of the same method used previously. The curve of power consumption of enlarged membrane microheaters for L2 is reported in the figure below, compared to data obtained with L2 on the smaller silicon membrane.

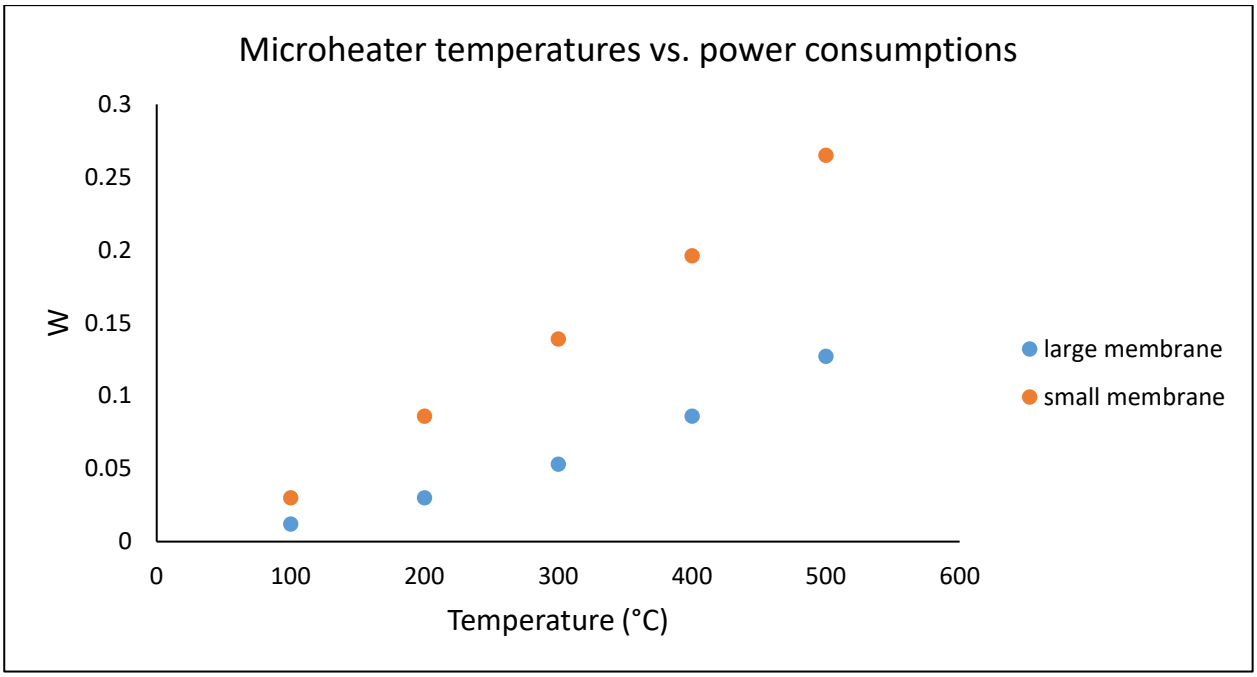

Figure 3.61: Comparison between heater power consumption of silicon small and large membranes (L2).

From Figure 3.61, it can be observed that the largest microheater membrane showed an energy consumption that is strong lower than that of the small membrane (about twice lower at 400°C). This difference is certainly due to the lower thermal conduction dissipation in the new configuration. This device, with a power consumption of about 80mW at 400°C, can consume less than 10mW if used in the pulsing operation. Despite the good result achieved in terms of power consumption of this device, the downside in the process was a relatively low yield (about 60%). The increase of membrane sizes, in fact, has caused a decrease in the mechanical stability of the device, leading to the breakage of several MHPs among process, wafer dicing and deposition of the sensing material. The development of new layouts is still in progress at FBK-MNF laboratories, for both wafer types. More attention is however focused on silicon, in particular, to further decrease power consumption while maintaining the high mechanical stability of the device.

3.5.3 Electrical insulation of HF SiO_2 passivation

The study of the actual electrical insulation between heater and electrodes at high temperature is a very important step in testing the quality of an MHP. Indeed, the presence of a current between the heater and sensing paste would lead to a change in the resistance of the semiconductor, modifying thus sensing responses due to interaction with analytes. The investigation presented in paragraph 3.4.3 highlighted that best PECVD passivation for our goal was the one named HF SiO_2. Two different thicknesses of HF SiO_2 have been deposited in processes, to study the influence of thickness on electrical insulation between heater and electrodes. To measure the possible current transmitted by the heater to the sensing material, it was decided to apply an increasing voltage to the heater, while, at the same time, measuring the current detected in the interdigitated electrodes. To render the analysis as similar as possible to the real operating conditions of the sensor, measurements were carried out on microheaters provided with the SnO_2 sensing material. The instrument used to achieve these data was The Manual Probe Station PM8, the same instrument used to obtain the I/V curves of heaters (section 3.5.3). Collected results are reported in figures below, in which current detected is plotted vs. temperatures of the microheater, due to the tension provided to heater pads.

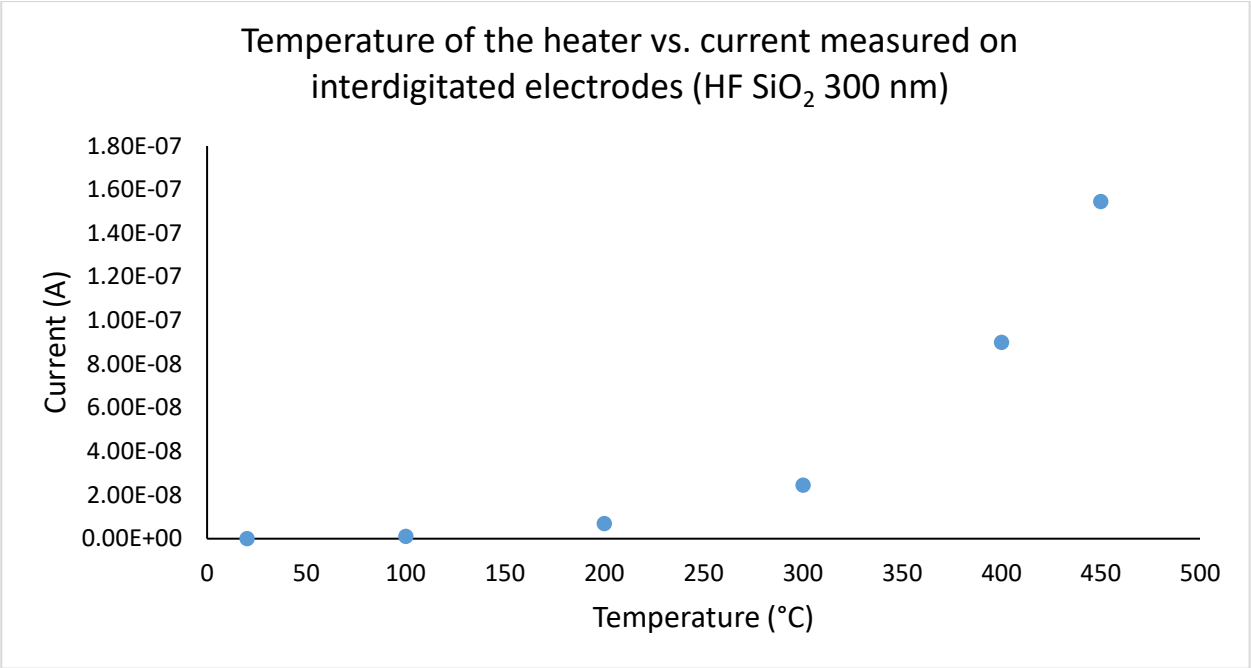

Figure 3.62: Current measured on interdigitated electrodes vs. temperature of the microheater, with a passivation thickness of 300 nm.

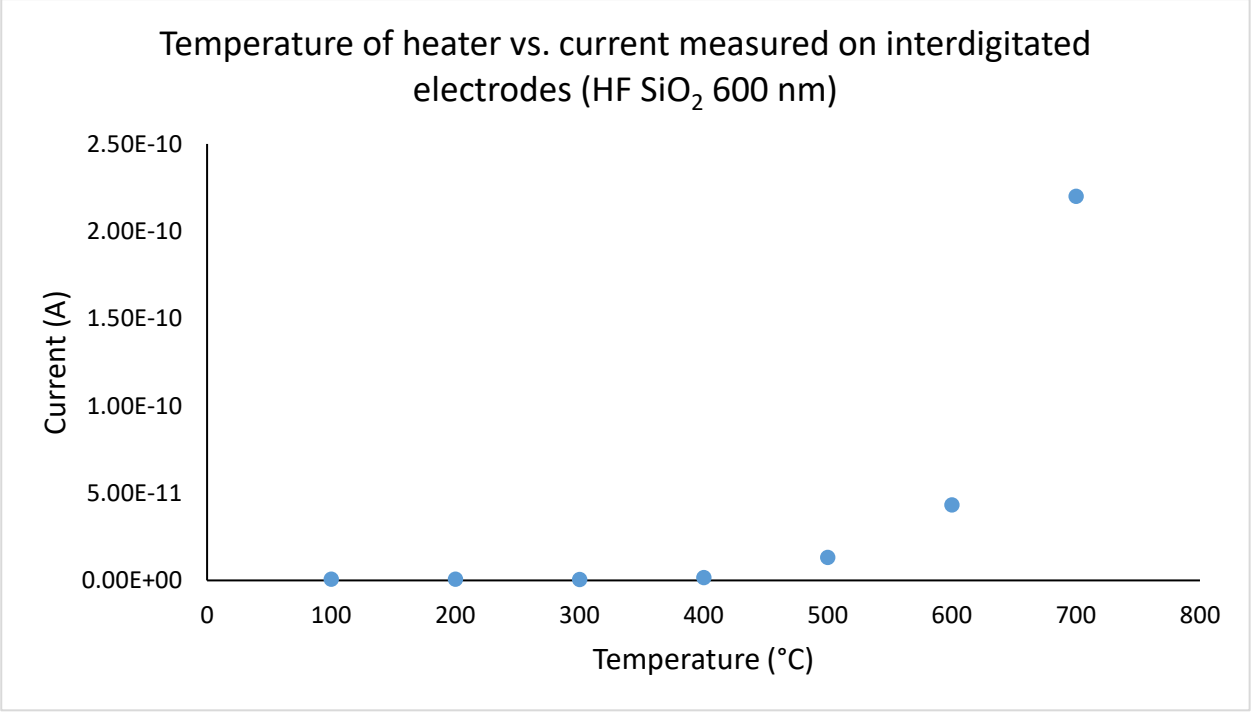

Figure 3.63: Current measured on interdigitated electrodes vs. temperature of the microheater, with a passivation thickness of 600 nm.

As one can observe, the electrical insulation of the passivation layer is strongly influenced by its thickness. With 300 nm of HF SiO_2, the current measured at the electrode pads begins to be relevant by providing the necessary voltage to the heater to reach the temperature of 300°C. At 400°C, this current value was about 0.1 µA, four orders of magnitude higher than MHP with 600 nm of HF SiO_2. Considering that the current circulating in the sensitive film at this temperature, obtained supplying a constant voltage to the electrode of 2.5 V, is of some µA, we have that the current passing through the inter-metal passivation can influence the resistance of the sensing film of about 10%. Therefore,

in the optimized process, it was decided to use an HF SiO_2 thickness of 600 nm, due to its better insulation than the thickness of 300 nm.

3.6 Gas sensing characterizations

In this section will be described the preliminary characterizations carried out on chemoresistive gas sensors, composed by quartz and silicon microheaters. The sensing measurements were carried out by using MHPs of the P1 process. For this investigation, it was decided to use thick films of SnO_2 as a sensing material, which is the most widely used material in gas sensor technology, deposited by means of screen printing technique (section 3.6.1) [3.99]. Our purpose was to verify the stability and operability of microheaters under working conditions of use as substrates for gas sensors. It was therefore not in our interest to test innovative materials coupled with silicon and quartz substrates.

3.6.1 Wafer dicing and sensing material deposition

It is necessary to summarize some studies done regarding the cutting of silicon and quartz wafers and the suitable screen printing deposition compatible with these substrates, before showing the gas sensing characterizations carried out with sensors composed of quartz and silicon substrates. Many works omit these details, which are however fundamental steps for the complete production of a finished sensor.

Concerning wafer dicing, it was first decided to divide the slice into squares containing 7x7 devices. This choice was made in order to have a reasonable number of substrates to use for the deposition, through a single process, of sensing material with screen printing method. To make the printed substrates easily separable from each other, it was also decided to perform head-cut for each individual sensor. The head-cutting is necessary because, once the sensing material has been deposited, it is no longer possible to cut the devices without damaging them. Therefore, a study was carried out on blank wafers in order to identify the suitable thickness of the head-cut, such that the devices could be manually separated from each other, and at the same time that the square formed by the 49 devices was still strong enough to be easy to handle without unwanted breakage.

Figure 3.64: The Disco DAD 3650 Dicing Saw used in FBK for wafers dicing.

Pre-cuttings tested for the quartz wafer, with a thickness of 650 µm, were of 400, 450, 500 and 550 µm. The head-cut that gave optimal results was that of 500 µm. Similarly, for the 300 µm-thick silicon wafers were investigated pre-cuttings of 100, 140, 180 and 220 µm. In this case, 180 µm produced the best result. These pre-cuttings were then used with process wafers.
A shrewdness adopted with the silicon wafers was the use, during dicing, of a transparent film placed on the surface of the wafer, to protect the membranes from the water jet used by the instrument to cool the blade during cutting. Obviously, this was not necessary with quartz, because of its robustness.
As far as screen-printing deposition is concerned, with quartz substrates, the same printing parameters used with alumina were adopted, given their similar mechanical properties.

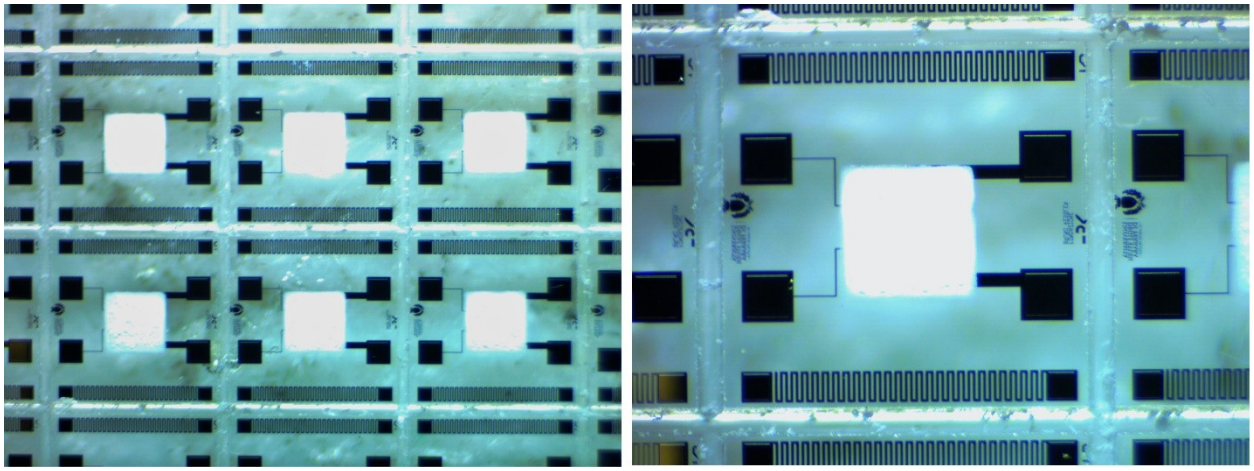

Figure 3.65: Images of quartz microheaters after screen printing deposition of the SnO_2 sensing material. Magnifications of *(left)* 1.1x and *(right)* 1.4x.

For silicon devices, on the other hand, an investigation focused on the rheology of the screen printing paste and on the pressure of the squeeze was carried out, so as not to damage the fragile membranes of the microheaters during the deposition of sensitive material.

Figure 3.66: Stencil Screen Printer Mod. AUREL Mod. VS1520A used in FBK to deposit sensing material on silicon and quartz substrates.

Four different types of deposition pressures were tested, by using a SnO_2 paste, with a standard viscosity for the deposition of a nanostructured semiconductor, and a 250-mesh screen-printing mask [3.98]. Results of depositions were then compared, focusing on the uniformity of the deposition and number of broken membranes (Table 3.7).

Table 3.11: Results obtained of screen printing deposition on silicon substrates.

Squeeze pressure ($Kgcm^{-2}$)	Deposition uniformity	% of broken membranes
1.5	regular	25
1.3	regular	10
1.1	regular	5
0.9	irregular	2

Hence, for silicon sensing devices, was used a squeeze pressure of 1.1 Kg. In comparison, a pressure of 1.5 $Kgcm^{-2}$ was used with quartz substrate in the same conditions.

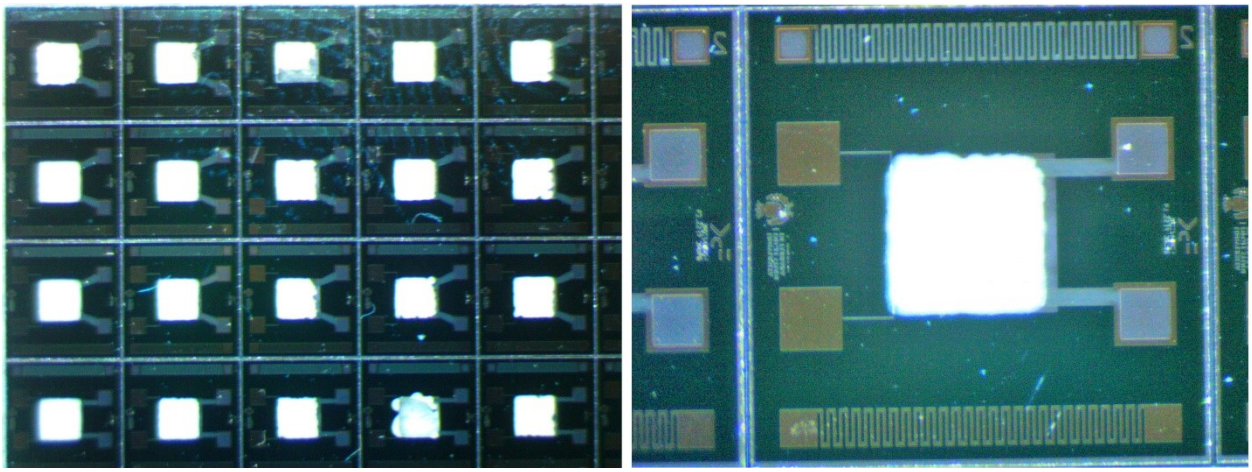

Figure 3.67: Images of silicon microheaters after screen printing deposition of the SnO_2 sensing material. Magnifications of *(left)* 1.0x and *(right)* 1.4x.

The surface of deposition area between silicon and quartz was the same, having utilized the same mask for screen printing deposition. However, the thickness of depositions was slightly different, due to the different pressure of squeeze used. The thickness was measured by an ellipsometric technique, highlighting a thickness of about 6 μm on quartz and 5.2 μm on silicon.

3.6.2 Gas sensing measurements

The electrical characterizations carried out in this section have been performed according to the methods described in paragraph 2.2, about the experimental setup and the calculation of sensor responses.

First, it was decided to characterize the chemical and electrical stability of the substrates in working conditions, without the presence of the sensing material. For this purpose, microheaters of quartz and silicon, which were bonded on T039 supports (see sections 2.2.6), were placed in a gas chamber, and stabilized at a temperature of 450°C. The layout chosen for these characterizations was the L2 both for silicon and quartz. A "bare" alumina substrate has also been inserted in the gas chamber, to compare the behaviour of the different substrates. The resistance of the open circuit, without the sensing material (therefore, the resistance of the insulating material placed on the top of substrates) was read through an operation amplifier, as described in section 2.2.7.3. Working parameters of sensors used are showed in the table below:

Table 3.12: Working parameters of silicon, quartz and alumina substrates.

	V heater (V)	I heater (A)	R heater (ohm)	T (°C)	P heater (W)
Alumina	4.5	0.214	21	450	0.96
Quartz	9.1	0.069	145	450	0.63
Silicon	5.1	0.046	141	450	0.23

It was therefore decided to subject the sensors to quite drastic environmental changes in the gas chamber since a substrate should be chemically inert to variations in gas concentrations in order to perform its function as a transducer optimally. For this purpose, sensors heated to 450°C were first left in an "open" chamber condition for 5 hours, by exposing them to possible interactions with all

gases present in the laboratory air. As can be seen from Figure 3.68, the substrates showed no variations in resistance of the surface insulating film during this time interval.

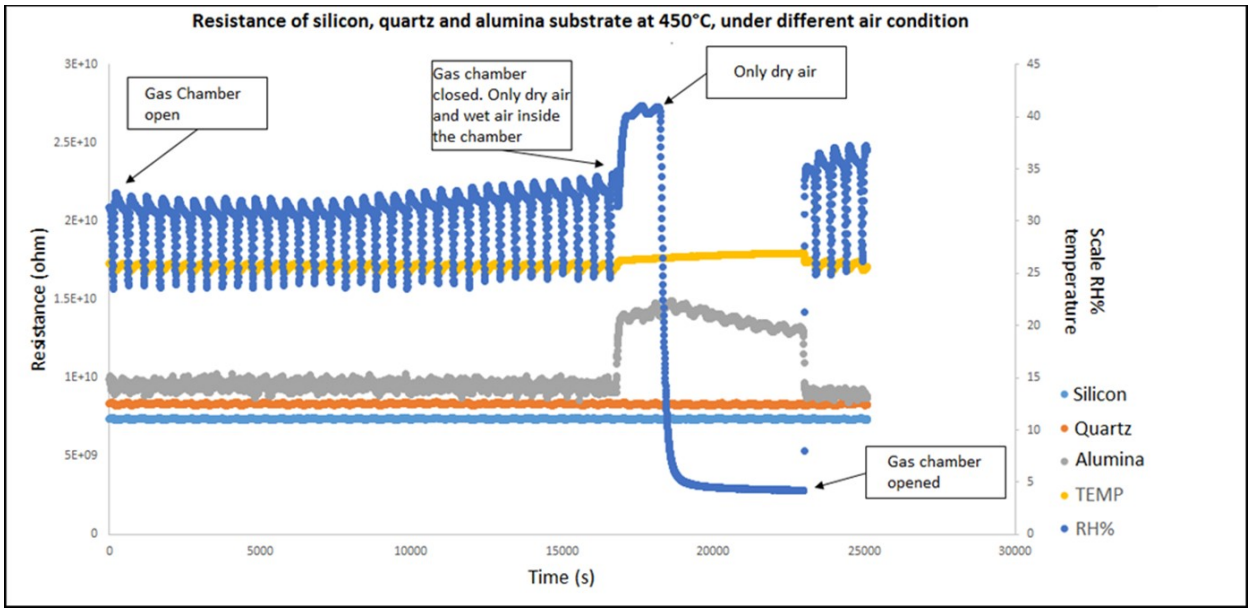

Figure 3.68: Trend of resistance registered in the interdigitated electrodes of substrates without sensing material, at 450°C.

Subsequently, the chamber was closed and only a mixture of dry air and humified dry air was flushed inside (flux of 0.5 $Lmin^{-1}$), in order to keep the humidity value as close as possible to that of the "open" chamber condition. As one can notice, at this condition change, the quartz and silicon MHPs remained insensitive, while the alumina sensor significantly changed its resistance. To check whether the change in resistance of the alumina substrate was due to the slight change of humidity between the two situations, after about 30 minutes the only dry air was injected into the gas chamber, thus decreasing the relative humidity value from 40% to 0%. The alumina substrate resistance has been slightly affected by this variation, while those of silicon and quartz remained stable. The dry air condition was maintained for about 90 minutes. Finally, the initial condition of "open" chamber has been restored. The resistance of the interdigitated electrodes of alumina has returned, to this variation, in its initial value. Throughout the experiment, quartz and silicon substrates remained stable, showing no change in resistance due to changing of the environmental conditions.
The experimental result showed a higher stability of the quartz and silicon substrates than alumina, exposed to the proposed changes in environmental conditions. The difference in alumina resistance may be due to two factors:
- sensor temperature variation due to changing environmental conditions, that may have affected the surface temperature of the substrate;
- a chemoresistive interaction between alumina surface and gold interdigitated electrodes with gases present during the experiment.
As far as the sensor temperature is concerned, it should be pointed out that during the experiment the alumina heater resistance was remained almost constant, let us think that the change of resistance read at the interdigitated electrodes was not due to a change in temperature of the sensor. To verify deeply this point, alumina substrates were exposed to change of dry air flux inside the gas chamber. However, no detectable changes in alumina resistance were recorded. Hence, we can suppose that the alumina substrate behaviour, showed in Figure 3.68, could be due to the interaction of the alumina with the gases that were present in the two different situations of the open and closed chamber. The same goes for the slight resistance change observed with the variation of the relative humidity inside

the closed chamber. In previous works, the chemoresistive behaviour of nanostructured alumina has already been observed, as well as the role of possible chemical catalysis by gold electrodes [3.99-3.101]. The problem of having a substrate that interacts with the gases present in the air lies in the changes of gas concentrations that can interact with the sensing material, compared to the real condition of the surrounding environment. Therefore, this behaviour could affect the response of the sensor.
In any case, this investigation highlighted the stability of quartz and silicon microheaters, developed in this work, to a gaseous environmental change, at a working temperature of 450°C.
The temperature stability of the silicon and quartz substrates was subsequently checked, linked to the resistance of the microheater. For this purpose, silicon and quartz MHPs, bonded on T039 support, were placed in the gas chamber, under a constant air flux. A suitable voltage has been applied to the microheater, in order to heat them up to 450°C. The devices left for one month in this condition, showed a change in heater resistance of less than 0.15%.

At this stage, we decided to verify the sensing responses of SnO_2, synthesized in the laboratories of MNF-FBK, deposited on silicon and quartz substrates by means of screen printing technique (section 3.6.3). In order to evaluate the stability of MHPs in these preliminary measurements, we decided to carry out these electrical characterizations at 450°C, which is a good compromise to verify the thermal stability of the device over time and sensing properties of the SnO_2 thick film [3.102]. The target gas chosen was carbon monoxide (CO). Two silicon and quartz sensors were left to stabilize for 24 hours in the measuring chamber at working temperature before characterizing the sensor responses.

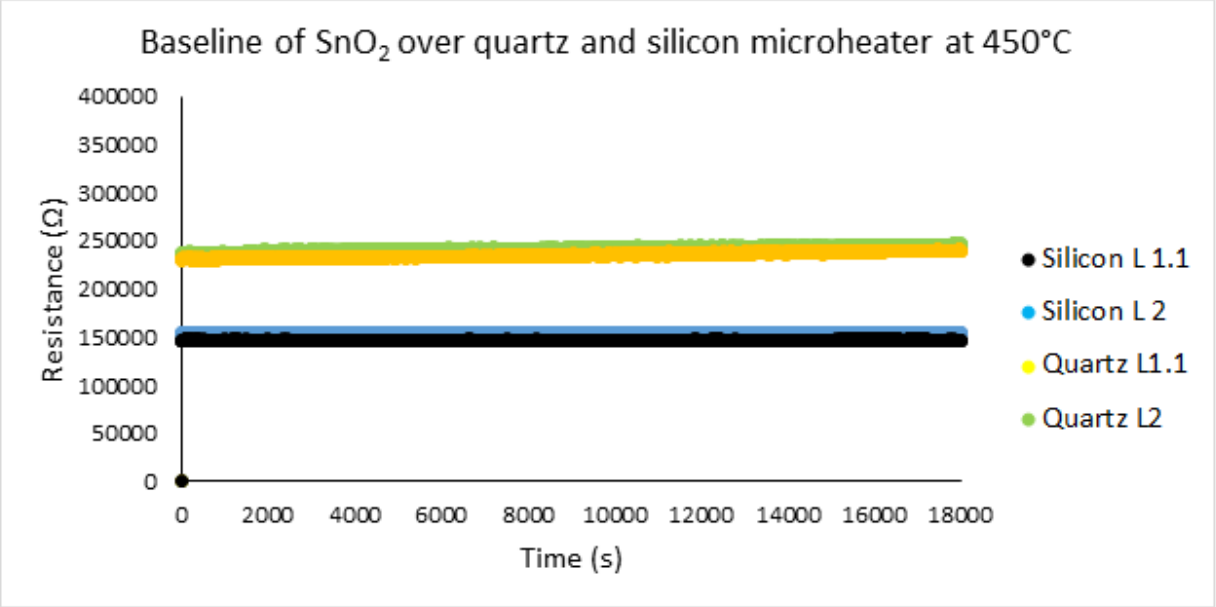

Figure 3.69: Baseline of SnO_2 deposited over silicon and quartz MHP, after 24 hours of stabilization in dry air.

As it can be noticed from Figure 3.69, the baselines of SnO_2 over silicon MHPs were stable after 24 hours, while the baselines in the quartz substrates still had a slight drift. After this time, 20 ppm of carbon monoxide were injected into the gas chamber, under dry air conditions.

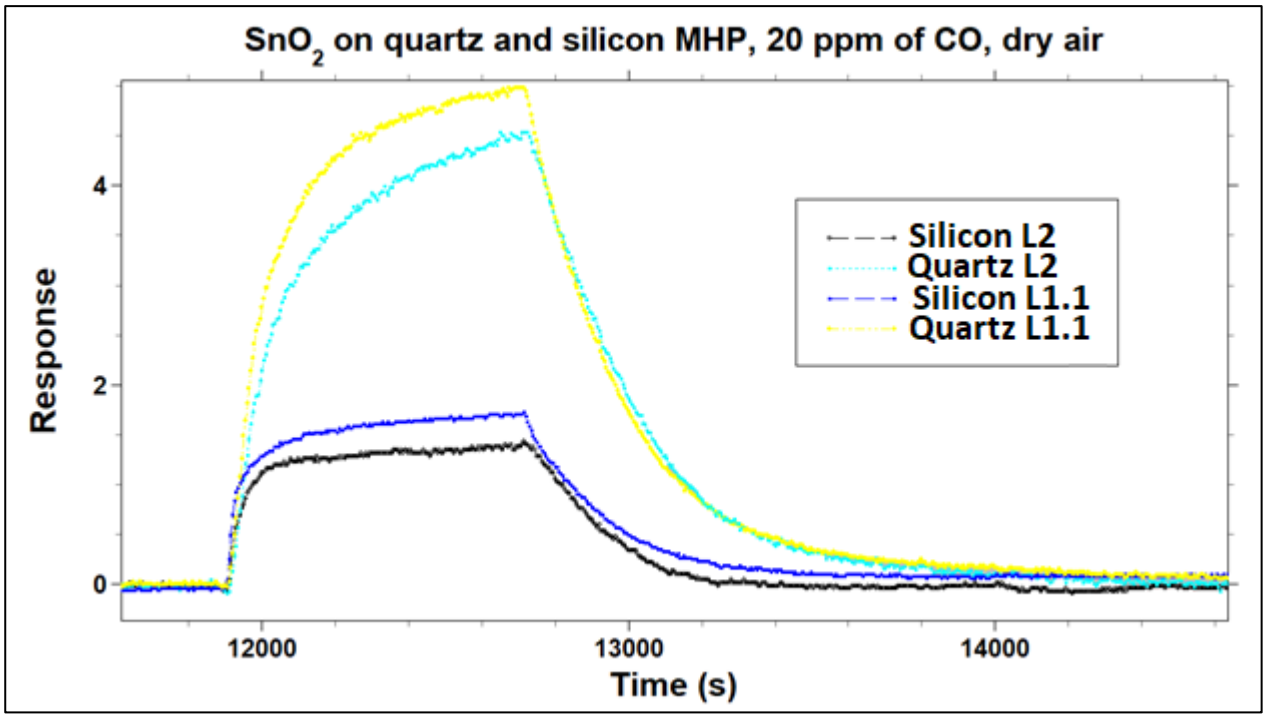

Figure 3.70: Dynamic responses of nanostructured SnO_2 on quartz and silicon MHPs, vs. 20 ppm of CO in dry air.

Figure 3.70 highlighted some interesting features of SnO_2 on the two different substrate types and layouts (L1 and L2). The sensing responses were very similar between identical substrates, but quartz sensors responses were greater than silicon sensors. Moreover, the response and recovery times (calculated as reported in section 2.4.3) also appear to be different between the two substrates, as shown in the table below, which summarises the data obtained for the four devices.

Table 3.13: Response and recovery of nanostructured SnO_2 over silicon and quartz microheaters.

	Quartz L1.1	Quartz L2	Silicon L1.1	Silicon L2
Response time (s)	378	396	259	200
Recovery time (s)	308	315	232	220

For SnO_2 on silicon, reaction kinetics seem to be faster than for quartz, with better response and recovery times. This trend was also verified in subsequent measurements.
A sensitivity measurement was then carried out to determine whether substrates could have an influence on the SnO_2 response to the change in CO concentration.

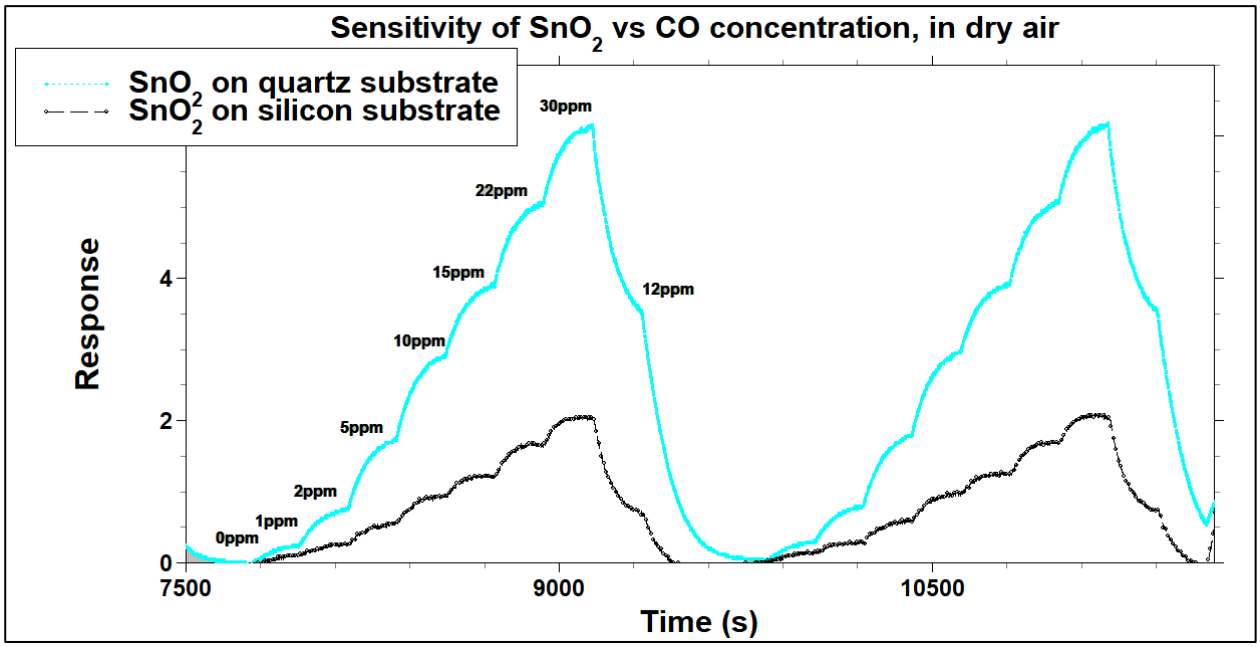

Figure 3.71: Calibration curve of SnO_2 sensors, deposited on the two different MHPs, vs. CO concentration (layout L2).

The two calibration curves showed good repeatability sensing responses for SnO_2 on both substrates, despite a slight drift of the baseline regarding SnO_2 on quartz.

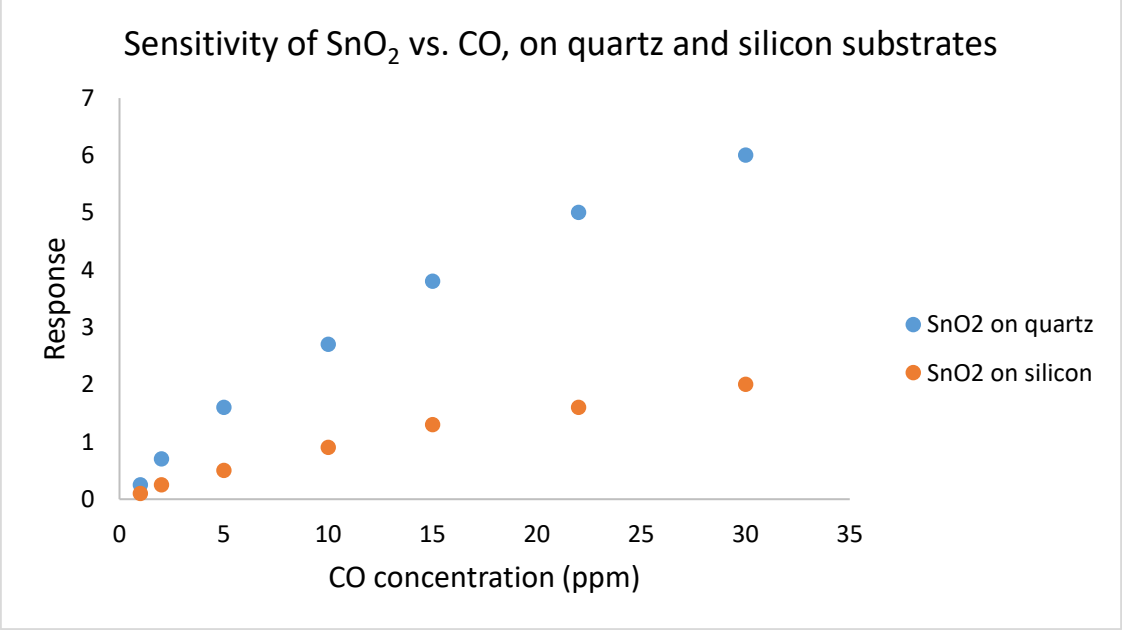

Figure 3.72: Sensitivity of SnO_2 sensing material on silicon and quartz substrates (layout L2), vs CO concentration.

The sensitivity trend is not linear for both sensors, similar to the reported literature for SnO_2 deposited on alumina substrates. Also in this measure, it is evident that quartz has greater responses, but with a slower kinetics than SnO_2 on the silicon substrate.

To investigate the time for SnO_2 on quartz to achieve response stability, further gas sensing measurements carried out leaving the sensor exposed to CO for a longer period.

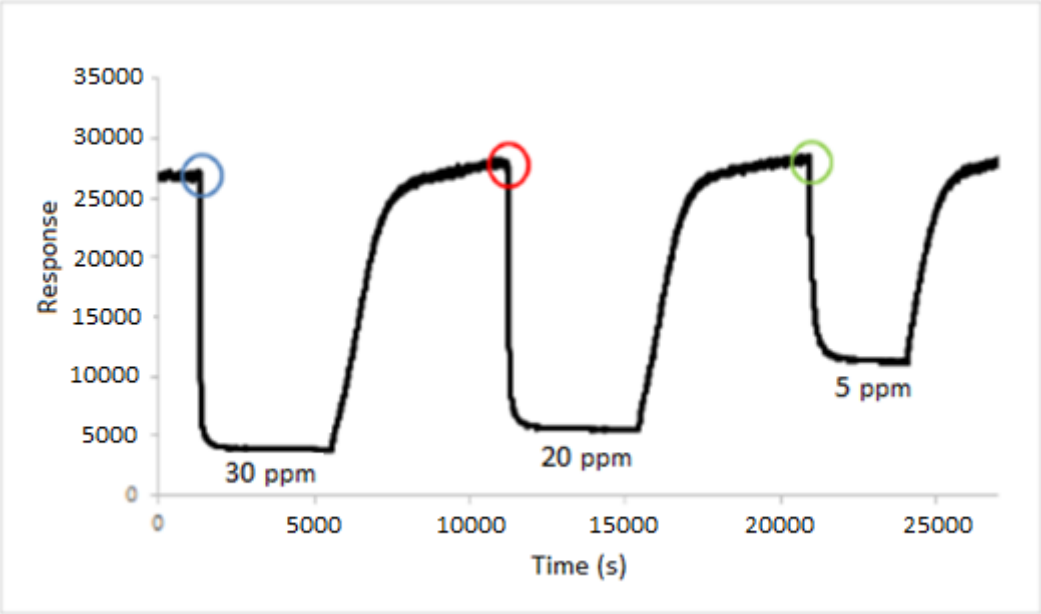

Figure 3.73: Dynamic responses of SnO_2 sensing material on a quartz substrate (layout L2) vs CO concentration. Circled in blue, red and green the baseline trend.

From Figure 3.73, it can be noticed that real sensing responses, of SnO_2 on the quartz substrate, to reach the complete response stability is about 440 seconds, greater than values reported in the table 3.13.

Subsequently, to verify the stability of the device in the presence of humidity, gas-sensing measurements with 20 ppm of CO were carried out in the presence of 30% of relative humidity.

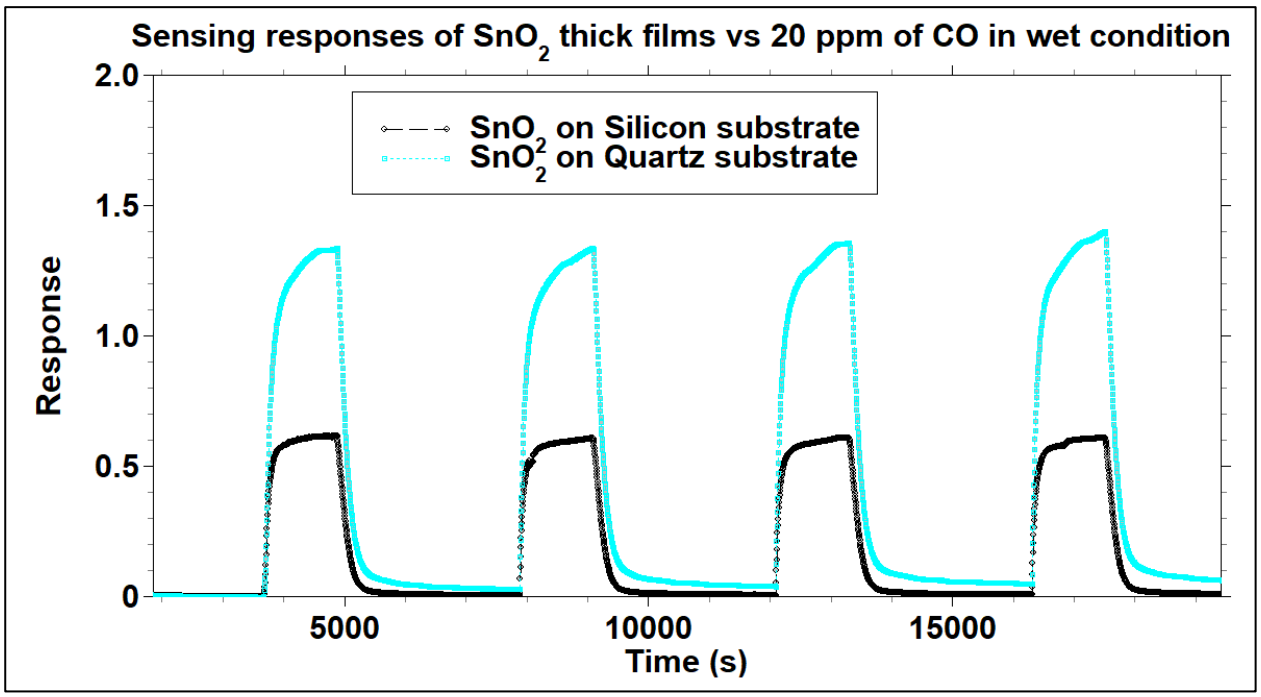

Figure 3.73: Dynamic responses of SnO_2 on quartz and silicon substrates (layout L2) vs. 20 ppm of CO in wet condition (T=25°C).

As it can be observed in Figure 3.73, sensing responses in presence of humidity are lower than in dry air. However, this decrease can be explained by the interference of moisture in the interaction between

CO and SnO_2 surface and is therefore not attributable to silicon and quartz substrates. The responses show good short-term stability, despite the continuous drift of SnO_2 baseline on quartz MHP.
The difference in sensing properties of the SnO_2 film between silicon and quartz substrates, i. e. in baseline stability, response values, response and recovery times, can be due to different parameters. For example, the different thickness of the paste deposited on silicon and quartz could affect the sensing properties of a semiconductor, as well as a difference in temperature between the two substrates [3.103, 3.104]. Further characterizations will be carried out to better understand this behaviour and to investigate whether there may be a role of the two different substrates in these different sensing properties

Finally, SnO_2 sensors on quartz and silicon substrates were subjected to realistic environmental conditions, leaving them exposed to air, in an FBK laboratory for 10 days, thermo-activated at 450°C. To verify their stability, an alumina sensor was also added to the measuring system. The sensing material deposited onto this commercial alumina was the same nanostructured SnO_2 used on silicon and quartz substrate.

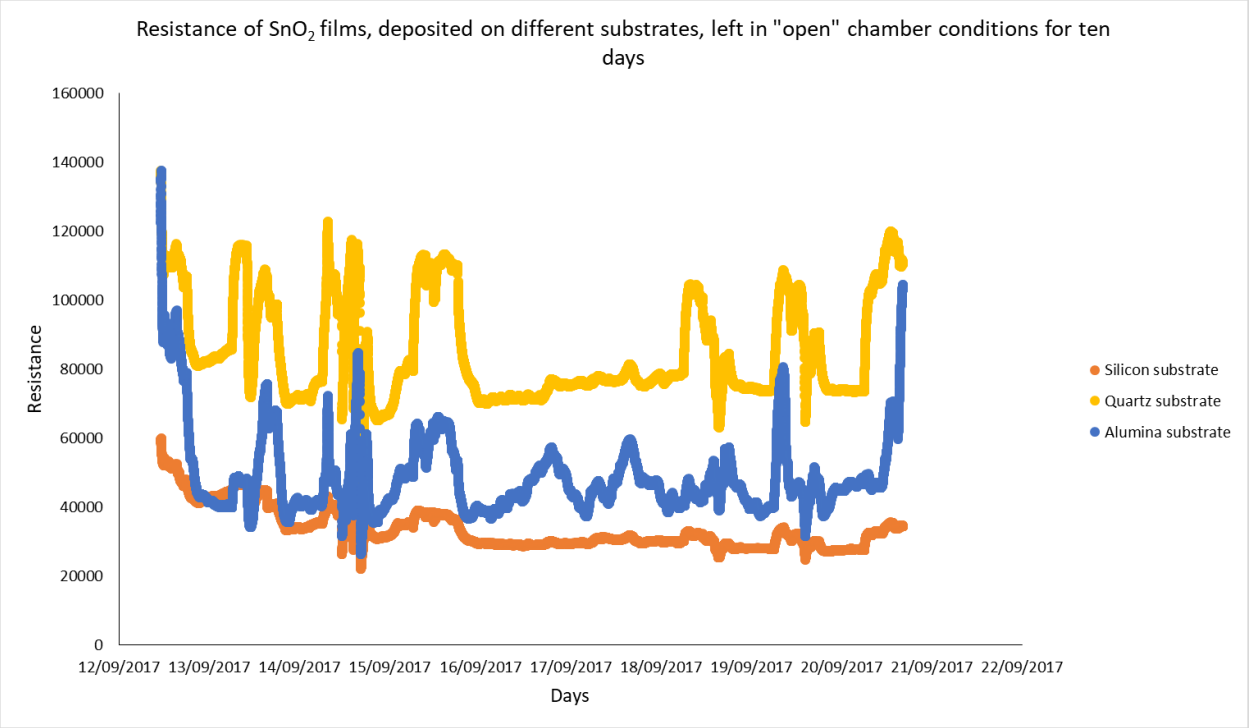

Figure 3.74: Resistance of SnO_2 films, deposited over quartz, silicon and alumina substrates, exposed to "open" chamber conditions.

As can be seen from the Figure 3.74, sensors composed of quartz and silicon substrates have followed a similar trend as alumina sensors. It can be noticed well, for all three sensors, the day and night cycle, due to the change of laboratories conditioning, humidity and the presence of different gases due to the attendance/absence of people in laboratories. It is also possible to observe the greater stability reached by the sensors during the weekend (16-18/9/2017), due to the shutdown of the air conditioning and the constant absence of people inside the laboratory. This stability, as can be seen from the Figure 3.74, was found to be greater for SnO_2 on quartz and silicon substrates than on alumina.

The electrical characterizations carried out in this section, both in the dry and wet air, showed a reasonable sensor trend, similar to what can be achieved with sensors composed of commercial alumina or silicon substrates. These results, obtained at a relatively high working temperature

(450°C), have therefore highlighted the stability of the alumina and silicon substrates developed in this work, which can be used as transducers for the chemoresistive gas sensor. However, the steadiness of these microheaters must be investigated in longer periods and compared with similar commercial sensors, in order to confirm MHPs stability over the time.

Bibliography

[3.1] Mirica, K. A., Weis, J. G., Schnorr, J. M., Esser, B. and Swager, T. M. (2012), Mechanical Drawing of Gas Sensors on Paper. Angew. Chem. Int. Ed., 51: 10740–10745.
[3.2] Claramunt, S., Monereo, O., Boix, M., Leghrib, R., Prades, J.D., Cornet, A., Merino, P., Merino, C., Cirera, A. Flexible gas sensor array with an embedded heater based on metal decorated carbon nanofibers (2013) Sensors and Actuators, B: Chemical, 187, pp. 401-406.
[3.3] Dayan, N.J., Sainkar, S.R., Karekar, R.N., Aiyer, R.C. Formulation and characterization of ZnO:Sb thick-film gas sensors (1998) Thin Solid Films, 325 (1-2), pp. 254-258.
[3.4] Belmonte, J.C., Puigcorbé, J., Arbiol, J., Vilà, A., Morante, J.R., Sabaté, N., Gràcia, I., Cané, C. High-temperature low-power performing micromachined suspended micro-hotplate for gas sensing applications (2006) Sensors and Actuators, B: Chemical, 114 (2), pp. 826-835.
[3.5] N. Taguchi, Method for Making a Gas-sensing Element (1971) US Patent 3 625 756.
[3.6] Gonzalez-Chavarri, J., Parellada-Monreal, L., Castro-Hurtado, I., Castaño, E., Mandayo, G.G. ZnO nanoneedles grown on chip for selective NO_2 detection indoors (2018) Sensors and Actuators, B: Chemical, 255, pp. 1244-1253.
[3.7] Hassan, M., Afify, A.S., Ataalla, M., Milanese, D., Tulliani, J.-M. New ZnO-based glass ceramic sensor for H_2 and NO_2 detection (2017) Sensors (Switzerland), 17 (11).
[3.8] Chen, L.-Y., Hunter, G.W., Neudeck, P.G., Beheim, G.M., Spry, D.J., Meredith, R.D. Packaging technologies for high temperature electronics and sensors (2013) Proceedings for the Joint Conference: MFPT 2013 and ISA's 59th International Instrumentation Symposium, ISA 2013: Sensors and Systems for Reliability, Safety and Affordability, 28 p.
[3.9] T. Seiyama and S. Kagawa, Study on a Detector for Gaseous Components using Semiconductive Thin Films, Analytical Chemistry 38, 1069–1073 (1966).
[3.10] A.C. Pike, Design of chemoresistive silicon sensors for application in gas monitoring. Thesis, University of Warwick 1996.
[3.11] J.L. Vossen and W. Kern, Thin Film Processes, Academic Press, Inc., London, 1978.
[3.12] J.L. Vossen and W. Kern, Thin Film Processes II, Academic Press, Inc., London, 1991.
[3.13] S. Middelhoek and S.A. Audet, Silicon Sensors, Academic Press, London, 1989.
[3.14] J. Brignell and N. White, Intelligent Sensor Systems, IOP Publishing Ltd., London, 1994.
[3.15] R. E. Cavicchi, J. S. Suehle, K. G. Kreider, B. L. Shomaker, J. A. Small, M. Gaitan, and P. Chaparala, **"**Growth of SnO_2 films on micromachined hotplates", Applied Physics Letters, 66, pp.812, 1995.
[3.16] K. Sadek and W. Moussa, **"**Studying the Effect of Deposition Conditions on the Performance and Reliability of MEMS Gas Sensors" Sensors, 7, pp 319-340, 2007.
[3.17] Gas Sensor Technology and Market Report, Yole Developpement, 2016.
[3.18] J. Kang, J. Park, H. Lee, "Pt-doped SnO_2 thin film based micro gas sensors with high selectivity to toluene and HCHO", Sensors and Actuators B, 248, pp. 1011–1016, 2017.
[3.19] Q. Zhou, A. Sussman, J. Chang, J. Dong, A. Zettl, W. Mickelson, "Fast response integrated MEMS microheaters for ultra low power gas detection", Sensors and Actuators A, 223, pp. 67–75, 2015.
[3.20] S. Santra, A. K. Sinha, A. De Luca, S. Z. Ali, F. Udrea, P. K. Guha, S. K. Ray and J. W. Gardner, "Mask-less deposition of Au–SnO2 nanocomposites on CMOS MEMS platform for ethanol detection", Nanotechnology 27, 125502-125511, 2016.
[3.21] S. Z. Ali, F. Udrea, W. I. Milne, and J. W. Gardner, "Tungsten-Based SOI Microhotplates for Smart Gas Sensors", Journal Of Microelectromechanical Systems, Vol. 17, No. 6, pp.1408-1417, 2008.

[3.22] C. Gong, T. Hogan, “CMOS Compatible Fabrication Processes for the Digital Micromirror Device” IEEE Journal Of The Electron Devices Society, 2, NO. 3, pp. 27-32, 2014.
[3.23] J.J. Neumann, K.J. Gabriel, “CMOS-MEMS membrane for audio-frequency acoustic actuation” Sensors and Actuators A, 95, pp. 175-182, 2002.
[3.24] Varel, H., Ashkenasi, D., Rosenfeld, A., Wähmer, M., Campbell, E.E.B.Micromachining of quartz with ultrashort laser pulses (1997) Applied Physics A: Materials Science and Processing, 65 (4-5), pp. 367-373.
[3.25] Rossi, C., Temple-Boyer, P., Estève, D. Realization and performance of thin SiO_2/SiNx membrane for microheater applications (1998) Sensors and Actuators, A: Physical, 64 (3), pp. 241-245.
[3.26] Sebastian, A., Wiesmann, D. Modeling and experimental identification of silicon microheater dynamics: A systems approach (2008) Journal of Microelectromechanical Systems, 17 (4), pp. 911-920.
[3.27] L. Ristic (ed.), Sensor Technology and Devices, Artech House, London, 1994.
[3.28] K.E. Bean, Anisotropic Etching of Silicon, IEEE Trans. Electron Devices, ED-25 (1978) 1185-1193.
[3.29] Bhattacharyya, P. Technological journey towards reliable microheater development for MEMS gas sensors: a review (2014) IEEE Transactions on Device and Materials Reliability, 14 (2), art. no. 6767061, pp. 589-599.
[3.30] G. Delapierre, "Micromachining: a survey of the most commonly used processes", Sensors and Actuators, vol. 17, no. l, pp. 123-138, May 1989.
[3.31] Zhang, H., Kim, E.S. Micromachined acoustic resonant mass sensor (2005) Journal of Microelectromechanical Systems, 14 (4), pp. 699-706;
[3.32] Danel, J.S., Dufour, M., Michel, F. Application of quartz micromachining to the realization of a pressure sensor (1993) Proceedings of the Annual Frequency Control Symposium, pp. 587-596.
[3.33] A. Bose, S. Puri, P. Banerjee. Modern Inertial Sensors and Systems, PHI Learning Pvt. Ltd., Mar 9, 2008 - Technology & Engineering.
[3.34] Zhang, S., Yu, F. Piezoelectric materials for high temperature sensors (2011) Journal of the American Ceramic Society, 94 (10), pp. 3153-3170.
[3.35] https://mnf.fbk.eu/.
[3.36] Jaeger, Richard C. (2001). "Thermal Oxidation of Silicon". Introduction to Microelectronic Fabrication. Upper Saddle River: Prentice Hall. ISBN 0-201-44494-1.
[3.37] Habraken, F.H.P.M. (Ed.), LPCVD Silicon Nitride and Oxynitride Films, Springer-Verlag Berlin Heidelberg, 1991. ISBN: 978-3-540-53954-4.
[3.38] http://www.lithoguru.com/scientist/lithobasics.html.
[3.39] Jaeger, Richard C. (2002). "Lithography". Introduction to Microelectronic Fabrication (2nd ed.). Upper Saddle River: Prentice Hall. ISBN 0-201-44494-1.
[3.40] Willson, C. G., Dammel, R. R., and Reiser, A (1997). "Photoresist materials: a historical perspective". Advances in Resist Technology and Processing XIV: 28.
[3.41] https://news.samsung.com/global/samsung-starts-industrys-first-mass-production-of system-on-chip-with-10-nanometer-finfet-technology;
[3.42] Lin, B. J., "Optical Lithography", SPIE Press, Bellingham, WA, 2009.
[3.43] Selvakumar, N.; Barshilia, Harish C. Review of physical vapor deposited (PVD) spectrally selective coatings for mid- and high-temperature solar thermal applications. Solar Energy Materials and Solar Cells, 2012, 98: 1–23.
[3.44] Hanlon, J. (1992). 1st ed. Handbook of Package Engineering, Lancaster, PA, Technomic Publishing: ISBN 0-87762-924-2.

[3.45] Comini, E., Sberveglieri, G., Guidi, V. Ti-W-O sputtered thin film as n- or p-type gas sensors (2000) Sensors and Actuators, B: Chemical, 70 (1-3), pp. 108-114.
[3.46] Ivanov, P., Stankova, M., Llobet, E., Vilanova, X., Brezmes, J., Gràcia, I., Cané, C., Calderer, J., Correig, X. Nanoparticle metal-oxide films for micro-hotplate-based gas sensor systems (2005) IEEE Sensors Journal, 5 (5), pp. 798-808.
[3.47] He, Zhenping; Kretzschmar, Ilona (18 June 2012). "Template-Assisted Fabrication of Patchy Particles with Uniform Patches". Langmuir. 28(26): 9915–9919.
[3.48] Kelly, P.J., Arnell, R.D. Magnetron sputtering: A review of recent developments and applications (2000) Vacuum, 56 (3), pp. 159-172.
[3.49] Miller, R.A. Current status of thermal barrier coatings - An overview (1987) Surface and Coatings Technology, 30 (1), pp. 1-11.
[3.50] https://en.wikipedia.org/wiki/Plasma-enhanced_chemical_vapor_deposition.
[3.51] http://lnf-wiki.eecs.umich.edu/wiki/Plasma_enhanced_chemical_vapor_deposition.
[3.52] Vlassak, J.J., Nix, W.D. A new bulge test technique for the determination of Young's modulus and Poisson's ratio of thin films (1992) Journal of Materials Research, 7 (12), pp. 3242-3249.
[3.53] Espinosa, H.D., Prorok, B.C., Fischer, M. A methodology for determining mechanical properties of freestanding thin films and MEMS materials (2003) Journal of the Mechanics and Physics of Solids, 51 (1), pp. 47-67.
[3.54] Zhang, Z., Wen, Z., Xu, S., Zhang, Z., Li, K., Huang, S. Poly-silicon micromachined switch (2002) Pan Tao Ti Hsueh Pao/Chinese Journal of Semiconductors, 23 (9), pp. 914-920.
[3.55] Lee, H.K., Ko, S.H., Han, J.S., Park, H. Mechanical properties measurement of silicon nitride thin films using the bulge test (2008) Proceedings of SPIE - The International Society for Optical Engineering, 6798.
[3.56] A. Picciotto, M. Crivellari, P. Bellutti, M. Barozzi, M. Kucharik, J. Krasa, A. Swidlosky, A. Malinowska, A. Velyhan, J. Ullschmied. Fabrication of advanced targets for laser driven nuclear fusion reactions through standard microelectronics technology approaches, Journal of Instrumentation, Vol. 12, 2017.
[3.57] Bagolini, A., Picciotto, A., Crivellari, M., Conci, P., Bellutti, P. PECVD silicon-rich nitride and low stress nitride films mechanical characterization using membrane point load deflection (2015) Journal of Micromechanics and Microengineering, 26 (2).
[3.58] Liu, M.; Peng, J.; et al. Two-dimensional modeling of the self-limiting oxidation in silicon and tungsten nanowires". Theoretical and Applied Mechanics Letters. (2016) 6 (5), 195–199.
[3.59] D.M. Mattox, Handbook of Physical Vapor Deposition (PVD) Processing Noyes Publication, Park Ridge, NJ (1998).
[3.60] Yoshio Nishi, Robert Doering. Handbook of Semiconductor Manufacturing Technology, Second Edition, CRC Press, Jul 9, 2007 - Technology & Engineering.
[3.61] Ruiz, A.M., Gràcia, I., Sabaté, N., Ivanov, P., Sánchez, A., Duch, M., Gerbolés, M., Moreno, A., Cané, C. Membrane-suspended microgrid as a gas preconcentrator for chromatographic applications (2007) Sensors and Actuators, A: Physical, 135 (1), pp. 192-196.
[3.62] Wang, C., Jin, J., Li, Y., Ding, W., Dai, M. Design and fabrication of a MEMS-based gas sensor containing WO_3 sensitive layer for detection of NO_2 (2017) Journal of Micro/ Nanolithography, MEMS, and MOEMS, 16 (1).
[3.63] Ito, S., Murakami, T.N., Comte, P., Liska, P., Grätzel, C., Nazeeruddin, M.K., Grätzel, M. Fabrication of thin film dye sensitized solar cells with solar to electric power conversion efficiency over 10% (2008) Thin Solid Films, 516 (14), pp. 4613-4619.
[3.64] Hong, E., Krishnaswamy, S.V., Freidhoff, C.B., Trolier-Mckinstry, S. Micromachined piezoelectric diaphragms actuated by ring shaped interdigitated transducer electrodes (2005) Sensors and Actuators, A: Physical, 119 (2), pp. 520-526.

[3.65] George, M.A., Glaunsinger, W.S., Thundat, T., Lindsay, S.M. Electrical, spectroscopic, and morphological investigation of chromium diffusion through gold films (1990) Thin Solid Films, 189 (1), pp. 59-72.
[3.66] Schmid, U., Seidel, H. Effect of high temperature annealing on the electrical performance of titanium/platinum thin films (2008) Thin Solid Films, 516 (6), pp. 898-906.
[3.67] S. Bigl, W. Heinz, M. Kahn, H. Schoenherr, and M.J. Cordill, "High-Temperature Characterization of Silicon Dioxide Films with Wafer Curvature", Journal Of Materials, Vol. 67, No. 12, 2015.
[3.68] D.N. Wright, E.S. Marstein, A. Holt, Effect of annealing on PECVD silicon nitride films, 22nd European Photovoltaic Solar Energy Conference, Milano, pp.1652-1655, 2007.
[3.69] P. Lv, Z. A. Tang, J. Yu, F. T. Zhang, G. F. Wei, Z. X. Huang, Y. Hud, "Study on a micro-gas sensor with SnO_2–NiO sensitive film for indoor formaldehyde detection", Sensors and Actuators B, 132, pp.74–80, 2008.
[3.70] A. Picciotto, A. Bagolini, P. Bellutti, M. Boscardin, "Influence of interfaces density and thermal processes on mechanical stress of PECVD silicon nitride", Applied Surface Science, 256, pp. 251–255, 2009.
[3.71] A. Bagolini, A. Stuart Savoia, A. Picciotto, M. Boscardin, P. Bellutti, N. Lamberti and G. Caliano, "PECVD low stress silicon nitride analysis and optimization for the fabrication of CMUT devices", Journal of Micromechanics and Microengineering, 25, pp. 1-11, 2015.
[3.72] R. Bartali, V. Micheli, G. Gottardi, A. Vaccari, M.K. Safeen and N. Laidani, "Nano-hardness estimation by means of Ar+ ion etching", Thin Solid Films, 589, pp. 376–380, 2015.
[3.73] S. J. Bull, "Nanoindentation of coatings", Journal of Physics D: Applied Physics, 38, n. 24, pp. 393-413, 2005.
[3.74] W. C. Oliver, G. M. Pharr, "An improved technique for determining hardness and elastic modulus using load and displacement sensing indentation experiments", Journal of Materials Research, 7, n. 6, pp. 1564-1583, 1992.
[3.75] G.G. Stoney, "The Tension of Metallic Films Deposited by Electrolysis", Proceedings of the Royal Society of London, Series A, 82, pp. 172-175, 1909.
[3.76] M. Ghaderi, G. de Graaf and R. F. Wolffenbuttel, "Thermal annealing of thin PECVD silicon-oxide films for airgap-based optical filters", Journal of Micromechanics and Microengineering, 26, pp. 66-76, 2016.
[3.77] K-S. Chena, X. Zhangb, S-Y. Lina, "Intrinsic stress generation and relaxation of plasma-enhanced chemical vapor deposited oxide during deposition and subsequent thermal cycling," Thin Solid Films, 434, pp. 190–202, 2003.
[3.78] T. Storgaard-Larsen, O. Leistiko, "Plasma-enhanced chemical vapor deposited silicon oxynitride films for optical waveguide bridges for use in mechanical sensors", Electrochemical Society Journal, 144(4), pp. 1505-1513, 1997.
[3.79] J. Thurn and R. F. Cook, "Stress hysteresis during thermal cycling of plasma-enhanced chemical vapor deposited silicon oxide films", Journal of Applied Physics, 91, pp.1988-1992, 2002.
[3.80] F.H.P.M. Habraken, "LPCVD Silicon Nitride and Silicon Oxynitride Films", eds. Springer-Verlag Berlin Heidelberg, project 369, 1, 1991.
[3.81] C. R. Helms, E. H. Poindexter, "The silicon-silicon dioxide system: Its microstructure and imperfections", Reports on Progress in Physics, 57, n. 8, pp. 791-852, 1994.
[3.82] Materials Handbook, ASM desk edition. Materials Park, OH, Nov 1995.
[3.83] E. Bustarret, M. Bensouda, M.C. Habrard, J.C. Bruyère, S. Poulin and S.C. Gujrathi, Configurational statistics in A-Si*x*N*y*H*z* alloys—a quantitative bonding analysis, Physical Review B, 38, pp. 8171–8184, 1988.

[3.84] S. Dauwe, Low-temperature rear surface passivation of crystalline silicon solar cells PhD thesis, University of Hanover, 2004.
[3.85] B. Bharat and L. Xiaodong, "Micromechanical and tribological characterization of doped single-crystal silicon and polysilicon films for microelectromechanical systems devices", Journal of Materials Research, 12, n.1, pp. 54-63, 1997.
[3.86] Jeremy Thurn and Robert F. Cook, Stress hysteresis during thermal cycling of plasma-enhanced chemical vapor deposited silicon oxide films, Journal of Applied Physics, 91, pp.1988-1992, 2002.
[3.87] H. Huang, K.J. Winchester, A. Suvorova, B.R. Lawn, Y. Liu, X.Z. Hu, J.M. Dell, L. Faraone. Effect of deposition conditions on mechanical properties of low-temperature PECVD silicon nitride films, Materials Science and Engineering A, 435–436, pp. 453–459, 2006.
[3.88] A. Bagolini, A. Picciotto, M. Crivellari, P. Conci and P. Bellutti, "PECVD silicon-rich nitride and low stress nitride films mechanical characterization using membrane point load deflection", Journal of Micromechanics and Microengineering, 26, n. 2, pp.1-8, 2016.
[3.89] S. Sundararajan, B. Bhushan, T. Namazu, Y. Isono, "Mechanical property measurements of nanoscale structures using an atomic force microscope", Ultramicroscopy, 91, pp. 111–118, 2002.
[3.90] S. I. Raider, R. Flitsch, J. A. Aboaf and W. A. Pliskin, "Surface Oxidation of Silicon Nitride Films", Journal of the Electrochemical Society: Solid-State Science And Technology, 123, n.4, pp. 560-565, 1976.
[3.91] Shikida, M., Sato, K., Tokoro, K., Uchikawa, D. Differences in anisotropic etching properties of KOH and TMAH solutions (2000) Sensors and Actuators, A: Physical, 80 (2), pp. 179-188.
[3.92] Sato, K., Shikida, M., Yamashiro, T., Asaumi, K., Iriye, Y., Yamamoto, M. Anisotropic etching rates of single-crystal silicon for TMAH water solution as a function of crystallographic orientation (1999) Sensors and Actuators, A: Physical, 73 (1-2), pp. 131-137.
[3.93] http://www.coininginc.com/aluminum_and_silicon_ribbon.asp.
[3.94] http://scipp.ucsc.edu/groups/fermi/electronics/mil-std-883.pdf.
[3.95] Khan, U., Falconi, C. An accurate and computationally efficient model for membrane-type circular-symmetric micro-hotplates (2014) Sensors (Switzerland), 14 (4), pp. 7374-7393.
[3.96] Yang, H., Choi, C.A., Chung, K.H., Jun, C.-H., Kim, Y.T. An Independent, Temperature-Controllable Microelectrode Array (2004) Analytical Chemistry, 76 (5), pp. 1537-1543.
[3.97] Belmonte, J.C., Manzano, J., Arbiol, J., Cirera, A., Puigcorbé, J., Vilà, A., Sabaté, N., Gràcia, I., Cané, C., Morante, J.R. Micromachined twin gas sensor for CO and O_2 quantification based on catalytically modified nano-SnO_2 (2006) Sensors and Actuators, B: Chemical, 114 (2), pp. 881-892.
[3.98] Lin, H.-W., Chang, C.-P., Hwu, W.-H., Ger, M.-D. The rheological behaviors of screen-printing pastes (2008) Journal of Materials Processing Technology, 197 (1-3), pp. 284-291.
[3.99] Eranna, G.; Joshi, B.C.; Runthala, D.P.; Gupta, R.P. Oxide Materials for Development of Integrated Gas Sensors-A Comprehensive Review. Crit. Rev. Solid State Mater. Sci 2004, 29, 111–188.
[3.100] S. Rank, S. Hafner, N. Barsan, and U. Weimar, "The impact of the nature of the electrode material on SnO_2 thick film sensor performance: influence on oxygen adsorption," Procedia Eng., 47, 514–517 (2012).
[3.101] Lee, S.P. Electrodes for Semiconductor Gas Sensors. Sensors 2017, 17, 683.
[3.102] Chiorino, A., Ghiotti, G., Carotta, M.C., Martinelli, G. Electrical and spectroscopic characterization of SnO_2 and Pd-SnO_2 thick films studied as CO gas sensors (1998) Sensors and Actuators, B: Chemical, B47 (1 -3 pt 3), pp. 205-212.
[3.103] Ansari, S.G. Effect of thickness on the H_2 gas sensitivity of SnO_2 nanoparticle-based thick film resistors (1996) Journal of Materials Science: Materials in Electronics, 7 (4), pp. 267-270.

[3.104] Liewhiran, C., Phanichphant, S. Influence of thickness on ethanol sensing characteristics of doctor-bladed thick film from flame-made ZnO nanoparticles (2007) Sensors, 7 (2), pp. 185-201.

Conclusions

This PhD thesis, which is the result of a collaboration between the Department of Physics and Earth Sciences of the University of Ferrara and the Micro-Nano Facilities group of the Bruno Kessler Foundation, was focused on a study of both main components of a chemoresistive gas sensor, i.e. the sensing material, acting as a receptor, and the substrate, which is the transducer of the receptor signal.

Regarding the receptor, the sensing properties of some innovative materials were investigated, both in the photo- and in thermo-activation mode. The choice of analysing materials that have been poorly studied so far has been driven by the limits shown by the common metal oxides used in this research field, including the lack of selectivity and stability in the long-term period. For this reason, gas-sensing properties of these materials were investigated following the "3s" rule, i.e. verifying their Selectivity, Sensitivity and Stability as sensing materials for chemoresistive gas sensors. The semiconductors taken into consideration were metal sulphides, silicon carbide and zinc oxide decorated with gold nanocluster. All these materials were chosen because of their peculiar characteristics, which made them attractive for their characterization from a chemoresistive point of view. Sensing characterizations were performed by testing different gases, belonging from different chemical classes

Concerning metal sulphides, cadmium sulphide and tin disulphide were investigated in this study. Both materials were synthesized at the SSL of the University of Ferrara. This analysis revealed the important role of pH in the synthesis of SnS_2, and of a complexing agent, called o-phenylenediamine, in the controlled synthesis of nanostructures of CdS. The powders synthesized were used as functional materials to obtain thick films, printed through the screen-printing technique onto alumina substrates. The obtained devices were electrically characterized under thermo- and photo-activation modes.

In thermo-activation mode, both metal-sulphides highlighted a high selectivity among the gases tested, in dry air, at the best working temperature of 300°C. The presence of humidity drastically reduces the responses of these sensors, without however affecting their selectivity. CdS showed very peculiar selectivity toward alcoholic molecules with respect to other interfering gases. Furthermore, an increase in CdS sensor responses was observed as the alcohol chain length increased. A sensing mechanism between alcohols and CdS surface was proposed to explain this monotonic increase in the electrical response. Possible applications of this result are of widespread interest, especially in those fields in which separation between alcohols and aldehydes is required, due to the intrinsic selectivity of this material to these groups. SnS_2 showed a good selectivity towards ketones and aldehydes. A further characterization showed a cross selectivity of ketone on aldehyde in the presence of moisture, behaviour that highlighted possible applications of the SnS_2 sensor, including plastic bottle industry and health-based applications with portable devices. A possible gas sensing reaction with acetone was proposed. For both materials, was detect a sensitivity comparable to the films used for gas sensing based on metal oxides. The stability and repeatability of sensing behaviour for both semiconductors were proved for six weeks, under working conditions. After this period, chemical analyses were carried out on the powders used to confirm that they have not undergone any chemical changes, which may impair the operation of the sensors over time. Finally, a comparison between SnS_2 and CdS with their metal-oxide counterparts highlighted some interesting differences, such as better overall chemoresistive properties of CdS than CdO, and a higher baseline stability of SnS_2 than SnO_2. The differences identified brought us to a reflection on the chemical nature of oxides and sulphides. The greater selectivity of sulphides can be brought about by the presence of sulphur, which, being less electronegative than oxygen and having the possibility of expanding the octet, can create a greater number of bonds, thus changing the catalytic characteristics compared to the corresponding metal oxide. At the same time, the improved baseline stability of SnS_2 compared to SnO_2 may be due

to an in-out diffusion of oxygen in the metal oxide. Indeed, in metal sulphides, the presence of sulphur instead of oxygen in the crystalline lattice prevents possible out-diffusion effects. This could lead to the different baseline recorded.

In photo-activation mode, while SnS_2 did not show any appreciable chemoresistive properties, cadmium sulphide showed a clearly photo-catalytic behaviour. The main results obtained consist of the observation and interpretation of the excitation effect of nanostructured CdS films, with different wavelengths, on the surface chemical activity. It was observed that a bandgap-resonant excitation maximized the chemical surface activity of CdS vs. all gases tested. The consequence which is worth to attention is that the wavelength of the incident light can control all those phenomena which are dependent on the surface chemistry. Indeed, it was highlighted that, by using incidence radiation with suitable energy, it is possible to photoinduced chemoresistivity on CdS films. This insight expands knowledge of the mechanisms of solid-gas interactions and the possible applications of them. As an example, related to photoinduced chemoresistivity, a gas sensor based on a CdS film could detect gases at room temperature thus avoiding the problems associated with the high-temperature operation.

Regarding silicon carbide, a commercial powder was purified and deposited on alumina substrates. The material showed, starting at 600°C, an extreme selectivity vs. SO_2, showing no change in resistance in the presence of the other gases analysed. Characterizations highlighted that the presence of humidity increases responses and sensitivity to SO_2, but does not alter the sensor selectivity. The sensitivity of the sensor was found to be comparable to that of common metal oxides, while the stability of the sensing response was confirmed over a relatively long time period. The cross selectivity of the SiC sensors was also verified, showing that, under humidity conditions, the response to SO_2 was not affected by the presence of a common interfering compound, such as H_2S, and very reactive gases such as butanol and acetone. The study of the possible interaction between SO_2 and SiC has shown that at working temperatures of the sensor, a stable core-shell of SiO_2/SiC is formed, due to the surface oxidation of SiC nanoparticles. The formation of core-shell increased the reactivity of silicon carbide. The chemical analysis carried out to identify the heterogeneous reaction between SiO_2/SiC core-shell and SO_2 has shown the formation of SO as a reaction product, resulting in the probable desorption of surface oxygen from the sensing film. The reaction would justify the increased conductivity of the SiC sensor during the exposition to SO_2.

Despite the good gas sensing properties shown in thermo-activation, SiC did not show detectable chemoresistive properties in photo-activation mode.

Concerning Au/ZnO, a study was carried on chemoresistive properties of this material in photo-activation, since it is a semiconductor already widely studied in thermo-activation. With this aim, an in-depth study was carried out on the synthesis of ZnO and Au/ZnO nanopowders, to obtain optimal products. At this stage, was made a comparison between the chemoresistive properties of pure nanostructured ZnO and gold nanoclusters decorated ZnO, at room temperature in photo-activation mode was carried out, by using LEDs as a light source with four incident radiation wavelengths. Both materials showed significant responses to butanol, methanol and sulphur dioxide under an incident radiation wavelength of 385 nm in dry air. This behaviour was probably due to an effective chemoresistive interaction between analytes and semiconductor nanoparticles as the energy of the radiation approaches the ZnO band-gap energy. Indeed, the ZnO photo-enhanced with UV radiation led to a better performance of gas sensors, i.e., greater and faster responses but also a quicker recovery time compared to those obtained for the same analytes by using radiations with lower energies. However, it has been clearly observed that Au/ZnO showed better chemoresistive properties than pure ZnO due to the electric and catalytic effects of gold nanoclusters. More precisely, the sensing responses of Au/ZnO layers were higher and the recovery time was faster with respect to pure ZnO. Furthermore, measurements carried out in wet air highlighted that the sensing responses to butanol and methanol became negligible in case of both metal-oxide semiconductors under evaluation,

whereas the responses to SO_2 of Au/ZnO sensors remained significant up to 80% of relative humidity. Au/ZnO sensors exhibited also an unexpected behaviour with NO_2. It has been observed that in presence of this gas, the response of the sensing material shows a maximum response at a lower energy with respect to the ZnO band gap. This has been correlated with the activation of plasmon effect since the maximum response was observed by using green light (525 nm) source, which has an energy close to the gold plasmon peak. This result opens up to the possibility of detecting selectively NO_2 at room temperature, in particular in dry air

Concerning the transductor, the study carried out at the Micro-Nano Facilities of the FBK allowed the development, during the three years of PhD course, of quartz and silicon micro-hotplates. The purpose of this part of the work was to investigate a stable and reliable process to realize silicon and quartz microheaters with low power consumption, by means of a fabless approach. Indeed, the fabrication of MEMS usually requires a dedicated fabrication line for each device technology, lacking the standardization level of IC fabrication. This study was prompted by the limitations shown by commercial alumina used as a substrate at the SSL of the University of Ferrara. The realization of silicon and quartz devices was possible thanks to a detailed experimental study of the various steps necessary for their production. In order to investigate the effects of the device design on the properties of the microheater, two different types of layouts (L1.1 and L2) and two different production processes (defined horizontal and vertical approaches) were developed for both substrate materials. The geometries of the various levels of the layout were defined by a photolithographic technique. The chosen process flows needed four (vertical approach) and three (horizontal approach) lithographic masks for silicon, while for quartz we used three (vertical approach) and two (horizontal approach) masks.

First, an initial layer of electrical insulator, called ONO, was deposited on silicon, while in quartz its dielectric capacity was directly exploited, without the deposition of an initial insulating layer. The metal circuits deposited on wafers, i.e. the heater and electrodes, were composed by 120 nm of platinum and 10 nm of titanium as an adhesion layer. The fabrication step that most required our attention was the deposition of the inter-metal insulator. In fact, having at its disposal a low-temperature technique to deposit this passivation layer (PECVD), it was first necessary to define a suitable recipe for obtaining an insulator with high thermal stability and low stress. With this aim, residual stress, refractive index and elastic modulus were measured and compared with the literature. The layers were annealed at different temperatures up to 700°C to simulate the thermal load of the microfabrication process and the curing of the sensor's chemical paste. Best performing layers were employed in the fabrication of microheater gas sensors, to test their resistance to the fabrication process thermal load and subsequent curing. SiO_2 deposited using a high-frequency plasma generator was the sole material to withstand the complete process. As far as silicon is concerned, the last step was a TMAH wet etching of the silicon bulk, in order to obtain a final thin membrane useful to minimize the thermal dispersion of the device during heating.

Devices thus realized have been fully characterized. The study of the I/V curves of heaters and TCR showed that the power consumption of the L1.1 layout was lower than the one of the L2 layout for both quartz and silicon devices. The power consumption of quartz MHPs was about 0.55 W, while for silicon were developed microheaters with a consumption of 0.2 W (small membrane) and 80 mW (large membrane), at 450°C. The consumption of microheaters in quartz, although it is higher than in silicon, is about 35% lower than those in alumina, also having a robustness comparable to the latter. Concerning the inter-metal passivation, was verified that 600 nm of HF SiO_2 provide optimal electrical insulation between heater and electrodes, recording a current of 10^{-10} A in the pads of electrodes, providing the necessary voltage to the heater to heat MHPs up to 650°C. Both silicon and quartz devices highlighted thermal stability at temperatures above 650°C.

Finally, the microheaters were tested in working conditions, depositing SnO_2 as sensing material on them by means of screen-printing technique. The obtained results, by detecting carbon monoxide with the sensors thus prepared, have shown a good stability of the devices at a working temperature of 450°C, both in dry and wet conditions.
In conclusion, both the nanostructure materials tested as sensing layers and the MHPs developed in this work have shown interesting properties, making them suitable for use as receptors and transducers in chemoresistive gas sensors.

Outlook

The results obtained in this work are a good starting point for an in-depth study of the materials and substrates investigated. The collaboration between UNIFE and FBK aims to create optimised and energy-efficient chemoresistive systems through in-depth analysis of innovative sensing materials and fine-tuning of transducers.

Concerning receptors, a broader analysis must be carried out in order to verify the long-term stability of semiconductors analysed. A wide-ranging study of the motivations leading to chemoresistive characteristics in the materials investigated, combined with the knowledge gathered over the years on common metal oxides, can be useful to build a model that helps to better understand the mechanisms of operation of these semiconductors as chemoresistive gas-sensing materials. Investigated materials should also be tested on sensor devices under real-life conditions, such as systems developed at SSL for medical analysis and monitoring of agricultural crops, to verify their actual functionality in these applications and increase the amount of information collected about their behaviour. Among our future objectives, there is also the investigation about effects of dimensional structures and metal nanoparticle decorations on the sensing behaviour of investigated materials. In particular, 2-D nanostructures, which showed a better stability for metal oxides than 1- and 3-D nanostructures could allow for interesting future developments.

The catalytic properties recorded in photo-activation, on the other hand, open to the development of a low power consumption system, in which various sensitive materials can be excited with different wavelengths of radiation via LEDs. The advantage of such a system would be, in addition to low power consumption, its possible use in conditions where the high temperature of sensors in thermo-activation can lead to problems, such as the analysis of explosive gases.

Among the future objectives for developed microheaters is to study their long-term stability. New layouts will be investigated that could allow lower energy consumption for both quartz and silicon devices. Concerning silicon, the development of a platform containing several sensing materials on a single chip is envisaged, in order to obtain a small sensor system, with low power consumption, through a single fabrication process. For quartz, on the other hand, it will be study a possible experimental set up that allows the use of this MHP with materials having both chemoresistive and optical properties, with the aim of constructing a prototype in which a double information can be obtained from the same sensing material, thanks to transparency property of quartz to certain radiation wavelengths.